MICROSTRUCTURAL EVOLUTION OF ADIABATIC SHEAR BANDS IN STEEL BY IMPACT

BY

SOLOMON BOAKYE-YIADOM

A Thesis Submitted to the Faculty of Graduate Studies of

The University of Manitoba

in Partial Fulfillment of the Requirements for the Degree of

DOCTOR OF PHILOSOPHY

Department of Mechanical Engineering

University of Manitoba

Winnipeg, Manitoba

Canada

ABSTRACT

Structural materials such as steel are easily susceptible to strain localization which results in the formation of Adiabatic Shear Bands (ASBs) during impact. It is generally agreed that the initiation and development of ASBs are manifestations of damage in metallic materials subjected to high strain rates and large strains of deformation and may lead to catastrophic failure instantaneously. There have been several experimental and theoretical investigations on ASBs since it was first reported by Zener and Hollomon in 1944. However, because of the complexity of the problem of formation of ASBs, their very narrow nature in the microstructure (~1 to 350μm), and the rapid rates of deformation, it is virtually impossible to observe their evolution and mechanism of formation during impact. In this study, it is hypothesized that a systematic study of the microstructure of a material prior-to, and after impact can be used to track the microstructural changes that occur during the evolution of ASBs. This research, is initiated to systematically study the microstructure of AISI 4340 steel prior to impact, after impact and after post-impact annealing to determine the effect of the pre-deformation microstructure on the nucleation and initiation of ASBs, and the mechanism of evolution of ASBs during impact.

This study used state-of-the-art microstructural characterization techniques such as the FIB and STEM/HRTEM to reveal that initial microstructural inhomogeneity produces nucleation sites for the initiation of ASBs during impact. It was observed that double misfit interfaces and boundary layers, formed around precipitated carbides (interface between reinforcements and matrix), increased the volume fraction of dislocation sources within the pre-impact specimens. It is demonstrated that the intersection of an activated dislocation source with the direction of maximum shear (regions of stress concentrations) within the specimens during impact, is a necessary condition for the points of intersection to act as possible sites for the nucleation and

initiation of ASB depending on the rate of dislocation generation, local strain and strain rate. In addition, the structure that evolves after strain localization starts out with elongation of the grains in the shear direction with the initiation of random and transverse dislocation boundaries along the elongated grains. The elongated grains break along the initiated dislocation boundaries as strain/strain rate increases resulting in the creation of smaller elongated-broken grains and nanograins. Boundary refinement of the broken grains occurring through grain rotation and adiabatic heating results in the evolution of refined grains, subgrains and nanograins. The presence of elongated grains, broken grains, refined grains, subgrains and nanograins within the evolved shear band structures demonstrate that the local deformation is dependent on the imposed local strain and strain rate and that these mechanisms occur concurrently during impact. Also, plastic deformation of precipitated carbides results in carbide fragmentation creating residual carbide particles which are redistributed within the ASBs. The residual carbide particles trap and pin dislocations and contribute to increase in local hardening in the shear bands. The results obtained, which are specific to the behavior of BCC ferritic Pearlitic hardenable steels, lead to the conclusion that the evolution of ASBs is a simultaneous layering of microstructures initially driven by dislocations which produce the final structures observed in the shear bands at the end of passage of the stress wave.

ACKNOWLEDGEMENTS

I would like to thank my advisor, Professor Nabil Bassim, for giving me the opportunity to work on this project. I couldn't have asked for a better advisor. The persistent support, advice, encouragement and the exposure he gave me is what led to the success of this research. I am most grateful.

I thank the Natural Sciences and Engineering Research Council of Canada (NSERC) for the funds they provided for this research. I also thank the Department of National Defense (DND) and Defense Research and Development Canada (DRDC) for their financial support. I thank the University of Manitoba for providing me with UMGF and other scholarships including the Edward R. Toporeck Graduate Fellowship in Engineering. I thank Prof. Gregory Glinka from the University of Waterloo for his time and support in reading my thesis and all the useful recommendations. My sincere gratitude goes to Prof. Dimos Polyzois, Prof. Norman Richards and Prof. Olanrewaju Ojo for their time, support and advice in making this project a success.

I am most grateful to Dr. Abdul Khan for the support and useful discussions throughout this research. I am very grateful to Dr. Akindele Odeshi and Mr. J. P. Burak for their technical support during the high strain rate experiments. I appreciate the help and support from my friend and colleague Ian Polyzois throughout this project. I also thank Jeff Delorme and Emmanuel Abrokwah for their invaluable discussions. My gratitude goes to all the staff and technicians at the department of Mechanical and Manufacturing Engineering for their help and support throughout this project. My sincere gratitude also goes to all my committee members for their support and advice in making this project a success. Finally, I thank my mum Cynthia Agnes Rothe, Dr. Sylvia Yiadom-Boakye and Pastor Benjamin Fiifi Karikari for their love, prayers, encouragement and support throughout this project.

DEDICATION

I dedicate this doctoral dissertation to

the Source of Wisdom

and

all the wonderful mothers out there especially

Cynthia Agnes Rothe and Dr. Sylvia Yiadom-Boakye

Table of Contents

LIST OF FIGURES

LIST OF TABLES

COPYRIGHT PERMISSIONS

Figure 2-2: Source – S. Boakye-Yiadom And M. N. Bassim, Materials Science And Engineering A 546 (2012) 223– 232. Reprinted with permission from RightsLink / Elsevier 15th May, 2014.

Figure 2-4: Source – Y. Xu, J. Zhang, Y. Bai And M. A. Meyers, Metallurgical And Materials Transactions A 39 (2008) 811-841. Reprinted with permission from RightsLink/Springer 15th May, 2014.

Figure 2-5(a) : Source – P. W. Leech, Metallurgical Transactions A 16 (1985) 1900-1903. Reprinted with permission from RightsLink/Springer 10th July, 2014.

Figure 2-5(b) : Source – W. S Lee, T. H. Chen, C. F. Lin And G. T. Lu, , Materials Transactions 51 (2010) 1216 – 1221. Reprinted with permission from The Japan Institute of Metals and Materials 16th July, 2014.

Figure 2-6 : Source – M. A. Meyers, B. Y. Cao, V. F. Nesterenko, D. J. Benson And Y. B. Xu, Metallurgical And Materials Transactions A 35 (2004) 2575-2586. Reprinted with permission from RightsLink/Springer 15th May, 2014.

Figure 2-7 : Source – C. Z. Duan, Y. J. Cai, M. J. Wang And G. H. Li, Journal Of Material Science 48 (2009) 897–902. Reprinted with permission from RightsLink/Springer 10th July, 2014.

Figure 2-8 : Source– Y. Yang, F. Jiang, B. M. Zhou, X. M. Li, H. G. Zheng And Q.M. Zhang, Materials Science And Engineering A 528 (2011) 2787–2794. Reprinted with permission from RightsLink / Elsevier 15th May, 2014.

Figure 2-9 : Source – J. A. Hines And K. S. Vecchio, Acta Materialia 45 (1997) 635-649. Reprinted with permission from RightsLink / Elsevier 13th June, 2014.

Figure 2-10 : Source – Y. Xu, J. Zhang, Y. Bai And M. A. Meyers, Metallurgical And Materials Transactions A 39 (2008) 811-841. Reprinted with permission from RightsLink/Springer 15th May, 2014.

Figure 2-11 : Source – M. T. Perez-Prado, J. A. Hines And K. S. Vecchio, Acta Materialia 49 (2001) 2905-2917. Reprinted with permission from RightsLink / Elsevier 13th June, 2014.

Figure 2-12 : Source – M. T. Perez-Prado, J. A. Hines And K. S. Vecchio, Acta Materialia 49 (2001) 2905-2917. Reprinted with permission from RightsLink / Elsevier 13th June, 2014.

Figure 2-13 : Source – Y. Xu, J. Zhang, Y. Bai And M. A. Meyers, Metallurgical And Materials Transactions A 39 (2008) 811-841. Reprinted with permission from RightsLink/Springer 15th May, 2014.

LIST OF INITIALS AND ACRONYMS

ASBs	Adiabatic Shear Bands
AISI	American Iron and Steel Institute
TEM	Transmission Electron Microscopy
STEM	Scanning Transmission Electron Microscopy
HRTEM	High Resolution Transmission Electron Microscopy
HAADF	High-Angle Annular Dark-Field
XRD	X-Ray Diffraction
EPMA	Electron Probe Micro Analyzer
SEM	Scanning Electron Microscopy
OM	Optical Microscopy
FIB	Focused Ion Beam
SPD	Severe Plastic Deformation
ECAE/ECAP	Equal Channel Angular Extrusion/ Equal Channel Angular Pressing
HPT	High Pressure Torsion
DIHPB	Direct Impact Hopkinson Pressure Bar
HRC	Rockwell C
HV	Vickers Pyramid Number
LMIS	Liquid Metal Ion Source
BCC	Body Centered Cubic
SADPs	Selected Area Diffraction Patterns
EELS	Electron Energy Loss Spectroscopy
EDS	Energy Dispersive Spectroscopy

WDS	Wavelength Dispersive Spectroscopy
BSE	Backscattered Electron
SE	Secondary Electron
BF	Bright Field
DF	Dark Field
SZ	Stretch Zones
PSBs	Persistent Slip Bands
RX	Recrystallization
DR	Dynamic Recovery
DRX	Dynamic Recrystallization
PriSM	Progressive Subgrain Misorientation
GPA	Geometric Phase Analysis
EDM	Electrical Discharge Machine
FT	Fourier transform
FFT	Fast Fourier transform

CHAPTER 1
INTRODUCTION

1.1 Background

Inhomogeneous plastic deformation at high strain rates and large strains results in strain localization which leads to the concentration of deformation within narrow bands called Adiabatic Shear Bands (ASBs) [1-6]. The formation of ASBs is the 'fingerprint' of deformation in materials at large strains and high strain rates such as in ballistic impact, foreign object damage, explosive welding/forming, crashworthiness, high-speed-impact-cutting and machining [7-13]. Generally, these bands are manifestations of damage because they are susceptible to crack nucleation and propagation due to their high internal stresses [2-8]. On the other hand, the potential of Severe Plastic Deformation (SPD) processes such as Equal Channel Angular Extrusion (ECAE) and High Pressure Torsion (HPT) are being used for production of bulk nanostructured materials with special physical and mechanical properties [12, 14]. The nanostructured materials produced by SPDs processes have similar physical appearance and properties to those reported for ASBs. Therefore, it is important to understand in detail the entire process of evolution and formation of ASBs from localization to failure during deformation at high strain rates and large strains.

While efforts have been made in including studies on the characteristics and properties within shear bands, as well as response of engineering material under high strain rates of deformation, there are uncertainties because of inadequate experimental evidence regarding where within materials that ASBs initiate and how they evolve during deformation [3-5, 8-11]. In addition, thermomechanical and/or microstructural mechanisms which have been used to describe the formation of ASBs are unable to satisfactorily explain the measured properties and the observed

structure within evolved adiabatic shear bands. Rittel reported that the physical picture on the phenomenon of ASBs is inadequate because there is no connection between reported mechanical quantities and microstructural observations [15-16]. Moreover, Dynamic Recovery (DR) and Dynamic Recrystallization (DRX) have been generally used to explain the evolution of ASBs because of the extent of the deformation and associated temperature rise, due to the conversion of plastic work to heat, which investigators believe is adequate to produce new recrystallized grains as has been observed in some shear bands [6, 10, 14-16]. However, it has been reported that DR and DRX by themselves do not adequately explain the structure within the evolved shear bands and does not provide satisfactory relation between measured properties and observed structure within the shear bands [7, 16-18].

Because of the rapid rates of deformation during impact, controlled recovery experiments have been used to provide a link between observed microstructures and initial states during dynamic loading. Also, the small width of ASBs makes microscopic examinations more difficult and limits the amount of information that can be obtained to fully understand the formation of ASBs. To better understand the nucleation and evolution of ASBs, combination of systematic experimental methodologies and simulations are required. Post-deformation microstructure characterization and measurements of the microstructure need to be pursued further.

1.2 Problem Statement and Research Objectives

Although there have been several experimental and theoretical investigations on ASBs, the mechanism of their nucleation and evolution remain less understood. This is due in part to the complexity of the problem of formation of ASBs, their very narrow nature in the microstructure

(~1 to 350μm), and the rapid rates of deformation which makes it virtually impossible to observe their evolution during dynamic loading. In this study, it is hypothesized that, because of the rapid rate of deformation during impact, a systematic study of the microstructure of a typical heat-treatable steel prior-to, and after impact can be used to determine the initiation of ASBs and track the microstructural changes that occur during the evolution of ASBs. The objectives of this research were to systematically and comprehensively study the microstructure of AISI 4340 steel prior to impact, after impact and after post-impact annealing to determine the effect of the pre-impact microstructure on the nucleation and initiation of ASBs and the mechanism of evolution of ASBs during impact. This systematic study would increase our understanding of the susceptibility of structural materials to shear strain localization and the mechanism of evolution of ASBs during dynamic loading.

1.3 Research Methodology

The process to achieve the objectives of this study was grouped into three major parts. Firstly, a Body-Centered Crystal (BCC) metal, namely AISI 4340 steel, which is known to be susceptible to the formation of ASBs, was selected. An initial investigation of appropriate heat treatment to determine the proper conditions that favor the formation of ASBs were performed. This was followed by a comprehensive microstructural characterization and measurements to determine the morphology and constituents of the heat-treated specimens prior to impact and also used as a baseline for comparison to the microstructure that evolves after impact. Secondly, the Direct Impact Hopkinson Pressure Bar (DIHPB) was used to systematically impact the heat treated steel specimens under predetermined high rate loading conditions. Standard metallographic techniques were used to document the presence of ASBs in the impacted specimens. Additionally, the

microstructural changes that occur during post-deformation annealing processes which may relate to understanding of the mechanism of formation of ASBs were also investigated. This study used state-of-the-art microstructural characterization techniques including X-ray Diffraction Analysis (XRD), Electron Probe Microanalysis (EPMA), Scanning Electron Microscopy (SEM), Transmission/High Resolution Transmission Electron Microscopy (T/HRTEM), and Scanning Transmission Electron Microscopy (STEM) to reveal the microstructure within the pre-impact, impact and post-impact annealed steel specimens. A Focused Ion Beam (FIB) was used to cut the impacted specimens for electron microscopy analyses without adding more stresses or distortions to the specimens. The careful use of these techniques and equipment allows a systematic and detail study of the microstructure of the steel specimens in order to determine the effect of the pre-impact microstructure on the nucleation and initiation of ASBs, and to determine the mechanism of evolution of ASBs during impact. This would increase our understanding of the susceptibility of structural materials to the formation of ASBs and provide the knowledge needed to tailor materials to be resistant to the formation of ASBs during dynamic loading.

1.4 Summary of Findings

On the mechanism of evolution of ASBs, the current study revealed that, concurrent occurrence of emergence of dislocations, texture development, breaking of elongated grains, grain rotations and refinements result in the observed structure within ASBs in impacted 4340 steel specimens. It was observed that the structure of the shear bands that evolve after strain localization starts out with elongation of the grains due to grain reorientation in the shear direction with the initiation of random and transverse dislocation boundaries along the elongated grains. For higher strain

rates/strains during impact, the elongated grains break along the initiated dislocation boundaries resulting in the creation of smaller elongated broken grains and nanograins. Boundary refinement of the broken grains occurring through grain rotation and adiabatic heating results in the evolution of refined grains, subgrains and nanograins. The sizes and types of the grains present within the evolved ASB after the initiation of strain localization is dependent on the ensuing strain and strain rate during impact. The presence of elongated grains, broken grains, refined grains, subgrains and nanograins within the shear band structures demonstrate that these mechanisms occur concurrently during impact. Additionally, fragmented and redistributed residual carbide particles trap and pin dislocations and contribute to increase in local hardening within the shear bands in the quenched-tempered 4340 steel specimens. It was demonstrated that the occurrence of Dynamic Recovery (DR) and Dynamic Recrystallization (DRX) alone is not sufficient to explain the observed microstructure within the evolved ASBs in 4340 steel specimens after impact because of the presence of refined sub-grains and nanograins with high density of dislocations, and the high local hardness associated with the shear band microstructures when compared to regions outside the shear bands. It is concluded that the evolution of ASBs in quenched-tempered 4340 steel during impact is a simultaneous layering of microstructures initially driven by dislocations which produce the final structure observed in the shear bands at the end of passage of the stress waves. The current observations agree well with recent findings on the mechanism of evolution of ASBs in Tantalum (Ta) and Tantalum–Tungsten (Ta-W) alloys. It also agrees well with the mechanism of grain refinement during Severe Plastic Deformation Processes (SPDs) such as Equal Channel Angular Extrusion (ECAE) and High Pressure Torsion (HPT) which are used to produce bulk materials with ultrafine grains.

On the nucleation and initiation of ASBs, it was demonstrated that initial microstructural inhomogeneities within the pre-impact 4340 steel specimens, as established by the amount, sizes and defects around precipitated carbides, produce nucleation sites for the initiation of ASBs during impact. Double misfit interfaces and boundary layers, with random arrangement of atomic columns formed around precipitated carbides, increase the volume fraction of dislocation sources within the pre-impact specimens. It was demonstrated that the intersection of an activated dislocation source with the direction of maximum shear (regions of stress concentrations) within a specimen during impact, is a necessary condition for the point of intersection to act as a possible site for the nucleation and initiation of ASBs. At a constant carbide volume fraction, the higher susceptibility of the tempered specimens to the initiation of ASBs is attributed to the volume fraction of points of intersection between activated dislocation sources and the direction of maximum shear (regions of stress concentrations) within the specimen during impact. Even though there is no experimental data in the literature on regions within a steel's microstructure where ASBs can nucleate and initiate from during impact, it agrees well with some numerical models such as the Feng and Bassim model that predicts the formation of ASBs. The results from the current study provide the knowledge and understanding to model and design structural steels and Metal Matrix Composites (MMCs) with higher resistance to the formation of ASBs by controlling the shape, sizes and distribution densities of reinforcements (carbides) within the materials. Plastic theoretical and numerical models which take into account these complex microstructures and better depict the microstructures of materials used for structural applications can be developed using the data from this research.

1.5 Thesis Organization

This dissertation is structured into six chapters. The following are summaries of the chapters:

- Chapter 1 introduces the concept of ASBs as a damage mechanism and presents the problem statement and objectives for the research.
- Chapter 2 reviews the physical appearance and properties of ASBs, and factors that influence the formation of ASBs. A thorough review of proposed mechanisms of formation of ASBs is also presented in this chapter.
- Chapter 3 describes the material and experimental procedures used in this research. A detail description of the equipment and procedure used for the impact tests, and the metallographic and microscopic examinations are presented.
- Chapter 4 provides comprehensive observations of the microstructures of the specimens prior to impact, after impact and after post-impact annealing.
- Chapter 5 discusses the main findings in this research based on the results of the microstructural observations of the specimens. The Final section of this chapter discusses how the results from this research can be applied in tailoring and designing microstructures that are resistant to the formation of ASBs.
- Chapter 6 presents a summary of the results and conclusions from this study. In addition, references and research contributions are presented at the end of this thesis.

CHAPTER 2
LITERATURE REVIEW

2.1 Introduction

This chapter consists of seven sections, section 2.2 to 2.8. The phenomenon of Adiabatic Shear Bands (ASBs), and their properties are introduced in section 2.2. The factors that influence the formation of ASBs as reported in the literature are presented in section 2.3 while section 2.4 provides a review of the structure of the two types of ASBs. A comprehensive review of the proposed mechanisms of formation of ASBs as well as debates surrounding these proposed mechanisms are presented in section 2.5. Section 2.6 reviews the microstructure of hardenable steels and the mechanism of heat treatment which is used for hardening. Specimen preparation for microstructural characterization using the Focused Ion Beam (FIB) is reviewed in section 2.7. Finally, the scope and objectives of this research is presented in section 2.8.

2.2 The Characteristics of Adiabatic Shear Bands (ASBs)

When materials are subjected to large strains and high strain rates of deformation such as impact, Adiabatic Shear Bands (ASB's) of intense plastic shear evolve in the microstructure of the materials. The initiation and development of ASBs are manifestations of damage because they are susceptible to crack nucleation and propagation resulting in fracture and fragmentation due to high internal stresses [1-7]. Whether or not the formation of narrow zones of highly localized deformation is accompanied by fracture, strain localization generally implies failure of the structural component through an essentially complete loss in the load-carrying capacity of the highly deformed material within the shear band [7-11]. Two types of ASBs reported in

the literature based on their appearance under the optical microscope are the dark-etching shear bands, called deformed bands, and the white-etching shear bands called “transformed” bands as shown in figure 2-1 [19].

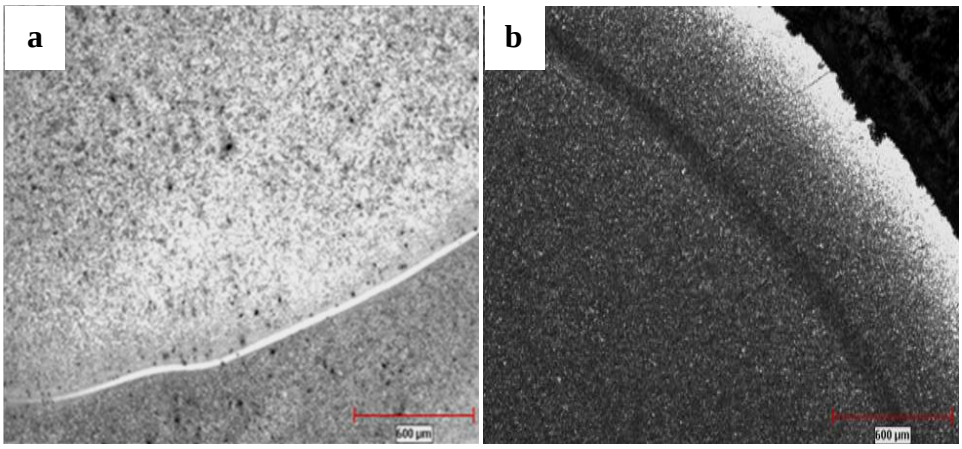

Figure 2-1: : Optical micrograph of (a) transformed band (b) deformed band [19].

ASBs are hard and brittle when compared to the surrounding material creating a hardness gradient within the deformed material [6, 17, 19]. However, the white-etching shear bands are harder and more brittle compared to the dark-etching shear bands as shown in figure 2-2 [20].

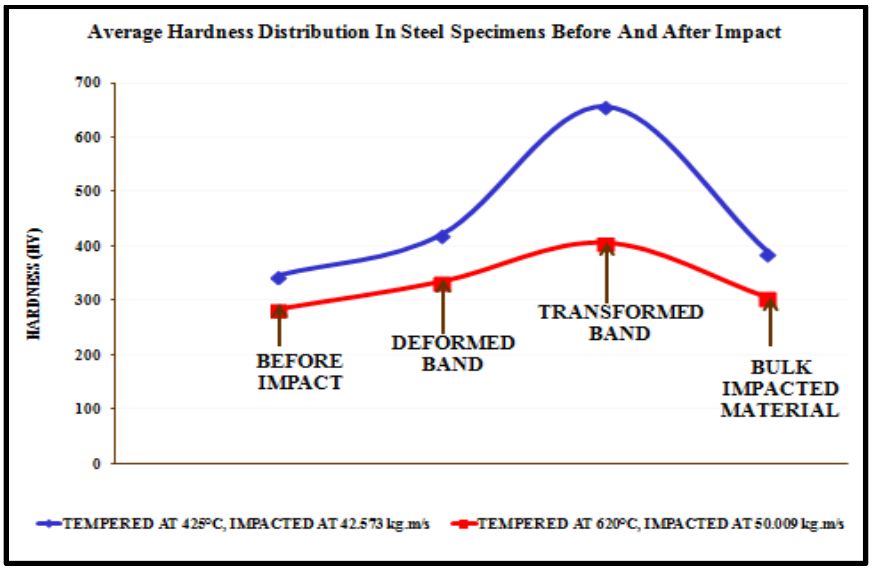

Figure 2- 2: Hardness within and outside ASBs in rolled homogeneous alloy steel after high velocity impact [20].

The hard nature of ASBs and their high internal stresses make them brittle and hence act as precursors and preferential sites for the nucleation and propagation of cracks [21-25]. However, the transformed ASBs are more susceptible to crack nucleation and propagation due to their very high hardness and internal stresses as shown in figure 2-3 [19].

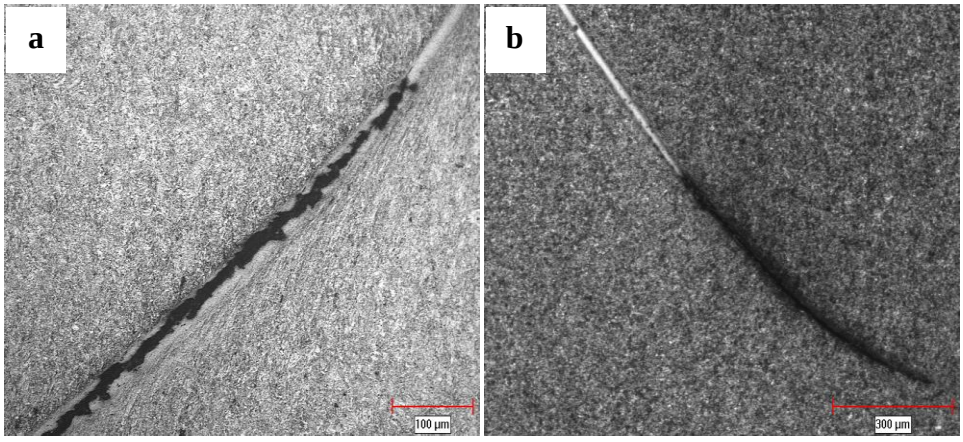

Figure 2- 3: Cracks propagating within transformed ASBs [19].

2.3 Factors that Influence the Formation of Adiabatic Shear Bands (ASBs)

Factors that have been reported in the literature to influence the susceptibility of materials to the formation of ASBs can be grouped under mechanical and material factors. Some of the material factors that have been considered in the literature are the physical appearance and microstructural properties of the material under dynamic deformation. Backmann and Finnegan [11] studied the metallurgical effects of selected materials at high strain rates and reported that the microstructure of a material has an influence on the formation of ASBs. Bassim et al. [21, 24] also reported that the occurrence, morphology, width and cracking susceptibility of ASBs are

dependent on the strength and microstructure of the material. It has been reported that BCC metals exhibit an increased propensity to ASB when their grain sizes are reduced into the ultrafine-grain and nano-crystalline regime [7, 12-13]. This is attributed to the associated changes in the strength, strain hardening behavior and strain rate sensitivity when the grain size changes [12]. Also, it has been observed that the ASBs associated with FCC metals, such as aluminum and copper, are diffused and exhibit a plastic flow phenomenon [26].

Mechanical factors such as impact momentum, loading conditions, strain rate and strains have been reported to affect the formation of ASBs during dynamic loading [21, 24]. Also, factors including thermal sensitivity, work hardening, microstructure of the parent material, tempering temperature and deformation temperature have been reported to influence the type of ASB formed during dynamic loading [17, 19]. The influence of these mechanical and material factors on the formation of ASBs during dynamic loading makes the phenomenon of ASBs very complex.

2.4 Structure of Transformed and Deformed Adiabatic Shear Bands

Several investigators have tried to establish the structure and constituents of the white-etching shear bands, usually called “transformed” bands. The transformed ASBs have received much attention because of their high susceptibility to crack nucleation and propagation which leads to fracture and fragmentation during dynamic loading. It has often been speculated that phase transformation occurs in the white-etching shear bands; hence the name “transformed” bands [17, 19, 21]. It has been reported that the transformed ASBs have very fine equiaxed grains and

sub-grains that are different from the surrounding matrix [8, 17]. Figure 2-4 shows an ultrafine-grain sized structure within shear band in Al-Li alloy [6].

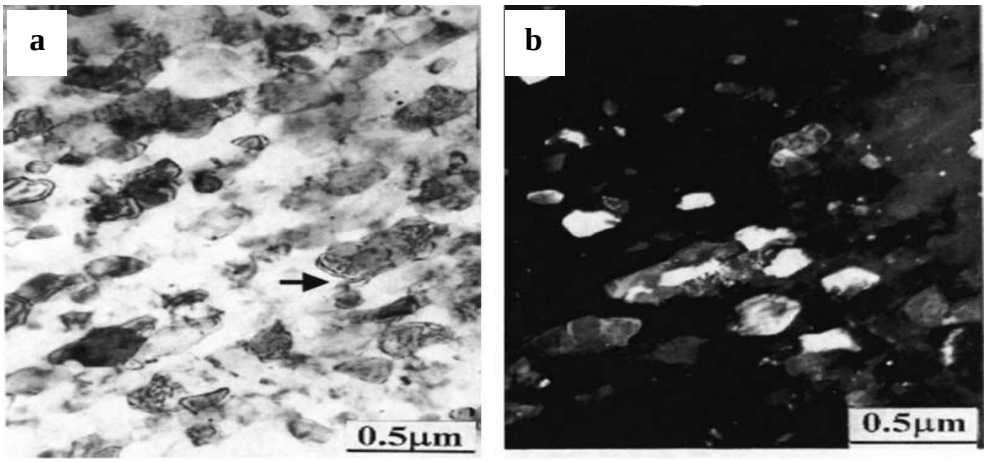

Figure 2- 4: (a) Bright- and (b) dark-field TEM showing ultrafine-grain sized structure within shear band in Al-Li alloy [6].

Zhang et al. [27] also reported that the white-etching ASBs possess nearly equiaxed fine sub grains whereas the neighboring deformed matrix has characteristics of the lath type microstructure. On the other hand, other investigators have reported of a combination of fine grains, subgrains, elongated grains and dislocation structures within the transformed ASBs. Chen et al. [28] reported of highly elongated narrow sub-grains extending in the shear direction within the transformed ASBs as well as the observation of fine equiaxed cells. Wingrove [29] observed that the white-etching shear bands had a high dislocation density with cell boundaries, a microstructure which did not resemble a typical martensite observed in steel even though the diffraction patterns indexed to martensite. Upon tempering of the white-etching zones, extra spots appeared in the diffraction patterns, an indication of carbide precipitation, and small precipitates after imaging under dark-field conditions [29].

On the other hand, it has been shown that the deformed ASBs have much larger sub-grains than those in the transformed ASBs [22-23, 30-32]. They appear as highly distorted grains with regions of intense plastic deformation in the form of plastic flow localization of the original material as shown in figure 2-5 [31-32].

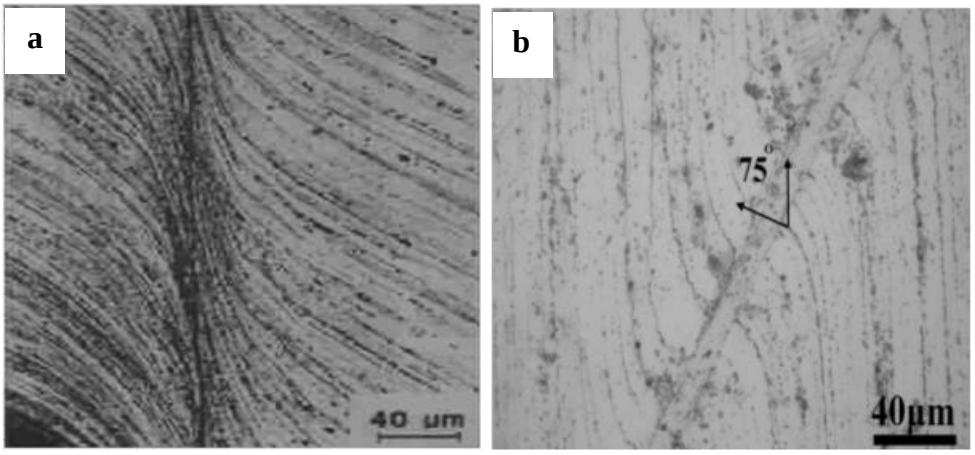

Figure 2- 5: (a)A deformed shear band in 7039 aluminium alloy [31] (b) A deformed shear band in Al-Sc alloy specimens deformed at strain rates of 6.2 $x10^5$ s^{-1} [32].

The difference in appearance and structure of the deformed and transformed ASBs has been attributed to the crystal structure of the material under dynamic loading and the amount of strain within the evolved ASBs [17]. Also, some investigators report that the initial tempering conditions of martensitic steels have an influence on the type of ASB formed [27, 33]. It was proposed that the higher the tempering temperature, the higher the tendency for the occurrence of deformed ASBs rather than transformed bands. Zhang et al. reported that the microstructure of evolved deformed ASBs in steel had tempered martensite sub-grains and readily formed in the specimens tempered at higher temperatures [27]. Other investigators have reported of the

formation of both deformed and transformed ASBs in the microstructure of a single material after deformation under high strain rates [24, 30, 34].

Even though the physical appearance and characteristics of the ASBs are well documented in the literature, their mechanism of nucleation and evolution are still under investigation. This is due in part to the complexity of the problem of formation of ASBs, the narrow widths of the evolved ASBs and the fact that there is not enough time to measure or observe the actual changes in properties in-situ due to the short duration between deformation and failure. This has given rise to many proposed mechanisms of formation of ASBs that have resulted in much debate in the field of high strain rates. The following sections review some of the proposed mechanisms of formation of ASBs and the questions surrounding these propositions.

2.5 Mechanisms of Formation of Adiabatic Shear Bands during Dynamic Deformation

Investigations on high strain rate deformations have been carried out from two main perspectives, mechanical and material (microstructural) [35]. The mechanical investigations characterize the properties of the material and its performance under high strain rates of deformation and use mechanical models to explain the occurrence of ASBs [3, 9, 17, 35]. On the other hand, some investigators study the properties of the material and its microstructure under high strain rates of deformation and use microstructural models to predict the mechanism of formation of ASBs [6, 8, 17]. Based on these investigations, the mechanisms of formation of ASBs can be been grouped into two main parts:

(a) Thermomechanical mechanisms

(b) Microstructural mechanisms

In 2009, Rittel [16] reported that the physical picture on the phenomenon of ASBs is inadequate because there is no connection between the reported mechanical quantities and microstructural observations. Recently, Panin et al. [36] reported that ASBs are mesoscale features, which are two-dimensional, and are caused by thermodynamical nonequilibrium instabilities. They proposed that ASBs are in the same category as dislocations, dislocation structures and disclinations. Bassim [7] in 2011, reported that the apparent features observed microscopically in ASBs resemble those observed in low-cycle fatigue with the occurrence of persistent slip bands (PSB) and in ductile fracture with the presence of stretch zones (SZ). In some cases, these features have been related to the macroscopic behavior of materials exposed to loading leading to fatigue or fracture. In the case of impact behavior, the situation is much more complicated. The two main mechanisms for the presence of ASBs in materials after deformation at high strain rates and large strain are discussed into detail in the subsequent sections.

2.5.1 Thermomechanical Mechanisms for the Formation of Adiabatic Shear Bands

Extensive investigation and analyses using mostly theoretical and some experimental considerations have made the thermomechanical mechanisms of formation of ASBs clearer as compared to the microstructural mechanisms. This is partly due to the difficulty in characterizing the shear band microstructure because of the very rapid rate at which the deformation proceeds and the narrow nature of the ASBs [17, 35]. The main characteristic of the thermomechanical model is that the formation of ASBs is driven by dislocation multiplication and the conversion of plastic work to heat resulting in thermomechanical instabilities during dynamic deformation [6, 17, 37].

In 1944, Zener and Hollomon described a phenomenon of adiabatic heating and the effects of strain hardening and thermal softening leading to strain localization and formation of ASBs at high strain rates of deformation [5]. They proposed that thermal softening brings the material to a point where it can no longer harden and losses its stability leading to localization. Since the inception of the concept of strain hardening and thermal softening, it has been the prevailing assumption in the emergence of ASBs and current models rely on perturbation analyses of the hardening and/or thermal or mechanical fields [8, 17, 19, 21]. Bassim reported that the mechanism of formation of ASBs is the concurrent effects of strain hardening followed by thermal softening due to significant rise in temperature which results in the occurrence of large strains within a narrow, mesoscale shear band [24, 26].

The proponents of strain hardening and thermal softening as a mechanism for the formation of ASBs suggest that during plastic deformation, there is competition between the two processes [6, 7, 8, 21, 35, 38]. On strain hardening, it has been shown that the dislocation density in a metal increases with deformation due to dislocation multiplication or the formation of new dislocations. It has been reported that work-hardening result from the interaction of dislocations and that the creation, interaction and movement of dislocations lead to a build up at grain boundaries during the early stages of the deformation [39]. Gilman [38] demonstrated that dislocation avalanches may lead to shear banding just like the collision cascade mechanism proposed by Holden [40]. Dislocation pile-ups have been used to explain the increase in strength with increasing deformation; strain hardening [41-42]. On the other hand, a large percentage of the work done during plastic deformation of metals is converted into heat that leads to thermal

softening; adiabatic heating [6-7, 17, 39]. It has been reported that at high strain rates of deformation, there is insufficient time for the dissipation of this heat from the material to the atmosphere or the surroundings [39]. This leads to a localized increase in the temperature of the material. The heat produced is retained in the regions or zones where it was created leading to stress collapse and hence strain localization in narrow bands [1, 3-4, 30]. Bassim and Odeshi reported that during high strain rate deformations, there is no plastic deformation in the early stages, then there is a competition between strain hardening and thermal softening at a later stage in the deformation process [21]. They reported that in the final stages of the deformation process, thermal softening predominates leading to viscoplastic instability and the formation of ASBs [21, 24].

Some investigators have conducted experiments to monitor the real time temperature of impacted specimens in order to understand the thermomechanical conversion and its efficiency during deformation. Costin et al. [43] in 1979 are known to be the first to measure the temperature history of shear localization. Hartley et al. [44] in 1987, Marchand [45] and Duffy [46] in 1984 and 1988 respectively, used improved infrared techniques and measured the temperature distribution and history within shear bands during dynamic deformation. In 1990, Wittman et al. [25] developed a finite-difference heat flow model to describe the thermal history of shear bands and reported of a temperature rise of 800^0C. The model was used to calculate temperature rises of up to 1000^0C occurring in the shear bands. In 1992, Duffy and Chi [47] performed experiments to study the process of ASB initiation and formation in steels. They employed an array of small high-speed infrared detectors, which provide a plot of temperature as a function of time and position to measure the local temperature in the shear band and measured temperatures

as high as 600°C within the shear band regions. Around this same time, Dodd and Bai [35] reported temperatures as high as 1200K in steels deformed at high strain rates. Feng and Bassim [48] developed a finite element model for the formation and evolution of adiabatic shear bands in 1999 and reported that during the initial stages of the deformation process the temperature is constant, and then as adiabatic heating continues thermal softening prevails, resulting in a temperature rise of up to 250^0C. In 2005, Chen et al. [28] obtained analytical solutions for the ballistic perforation performance of a fully clamped circular plate struck by a blunt projectile. They reported that the temperature in the localized shear zone increases sharply from 430^0C to 1527^0C for some of the tested plates and that the maximum temperature of T=1527^0C reaches the melting temperature, Tm, of the Weldox 460 E steel which was being analyzed. During failure analyses of the ferry Estonia in 2009, Johnson and Smith reported that adiabatic shear resulted in heating of the shear band areas to temperatures between 699^OC to 721^OC during rapid shear failure deformation [49]. All these analyses lend credence to the fact that there is a significant rise in temperature during deformations at high strain rates which may account for the thermal softening as proposed by the various investigators.

In addition, several empirical and phenomenological constitutive models have been reported in the literature which are either based on strain hardening and/or thermal softening mechanisms described here under the thermomechanical models. These constitutive models usually describe the thermo-viscoplastic behavior of metals under high strain rates and large strains of deformation. However, the basic concept behind most of these models is either strain hardening and/or thermal softening. The empirical Johnson-Cook model has been proven to be useful for predicting the thermo-viscoplastic behavior of metals that show constant rate of hardening at

increasing strain rates or for metals that show increasing rates of strain hardening at higher strain [50-51]. The dislocation mechanics model by Zerilli and Armstrong considers the crystal structure, presence of solutes, temperature, grain size, and initial dislocation density of the material and couples the strain rate and temperature during deformation to predict the behavior of metals under high strain rates of deformation [4, 52]. Also, the Anand model, which uses a single internal scalar state variable to represent the material's average resistance to plastic flow, has been adopted for use as a general thermo-viscoplastic material model for large deformation with relatively low elasticity [53]. In addition, the Feng and Bassim model takes advantage of the single internal scalar state variable in the Anand's model to predict the occurrence of ASBs in steel under high strain rates of deformation[48, 54-55]. All these models are based on the conversion of plastic work to heat which results in thermal softening leading to strain localization and the formation of ASBs under high strain rates of deformation.

However, other investigators have used infrared techniques and computer simulations to suggest that the temperature rise is not significantly high as has been reported and that the observed temperatures are inadequate to affect the mechanical properties of the material [15-16, 18, 56-58]. These investigators discussed that the conversion of plastic work to heat leading to thermal softening can affect the mechanical properties of the material only when the rise in temperature is at least equal to the homologous temperature of the material during deformation [16, 57-58]. Thus, even though there is conversion of plastic work to heat which results in a rise in temperature during dynamic deformation, this rise in temperature would have to be at least equal to half of the melting temperature of the material (homologous temperature) under deformation before any significant effect can occur on the mechanical properties of that material. Hines et al.

[18, 58] conducted liquid nitrogen temperature tests and reported that temperature did not play a major role in the emergence of the shear bands. Rittel et al. [15, 56-57] carried out experiments to characterize the rise in temperature in the gauge section of an impacted specimen for various metals and reported that for a pure α-iron specimen deformed at $\dot{\varepsilon}\sim 8000s^{-1}$, the recorded temperature reached 431K at $\varepsilon\sim 0.7$ corresponding to a homologous temperature of 0.24. They reported that the recorded temperature rise was more moderate at lower strain rates which demonstrated that β was rate-sensitive. Their work on pure polycrystalline tantalum showed a temperature rise of 378K at a plastic strain $\varepsilon_p\sim 0.3$ irrespective of strain rate corresponding to a homologous temperature of 0.15 [56]. An annealed commercial Ti6Al4V alloy resulted in a temperature rise of 350K at $\varepsilon\sim 0.27$, $\dot{\varepsilon}\sim 3000s^{-1}$, corresponding to a homologous temperature of 0.19 [16]. Again, Rittel and Wang reported a localization temperature of 323K at $\varepsilon\sim 0.17$, $\dot{\varepsilon}\sim 3000s^{-1}$, for a cast magnesium (AM50) alloy corresponding to a significant homologous temperature of 0.46 with the temperature measurement carried out until full localization and fracture of the ASB [57]. Even though a softening mechanism is observed by all these investigators based on the stress-strain response of the materials under dynamic loading, it is argued that it may not be thermal softening because the rise in temperature is not significant to cause any mechanical effect on the materials during dynamic deformations.

2.5.2 Microstructural Models and Mechanisms of Formation of Adiabatic Shear Bands

In the thermomechanical mechanisms for the formation of ASBs, the microstructure is not distinctly considered because it is assumed that the strain is limited only in the shear bands and that the occurrence of ASBs is attributed to thermomechanical instabilities. Conversely, the microstructural mechanisms of formation of ASBs are more complicated and are not clear

because of the very rapid rate at which the deformation proceeds and the narrow nature of the ASBs. The microstructural models assume that there is a significant change that occurs to the initial microstructure of the material during the passage of the stress waves when the material is deformed at high strain rates and large strain [17]. The deformation starts out with an original microstructure and its constituents which may be very complex and it changes very rapidly during the passage of the stress waves leading to a new microstructure due to the absorption of the strain energy [27-28]. Investigators report that after the conversion of plastic work to heat, the remainder is stored in the material microstructure [6, 17, 57, 59]. It has been reported that the stored strain energy which remains in the material after removal of the external load is an essential feature of the deformed material and represents the change in internal energy of the metal [17, 56-57]. Two main mechanisms for the microstructural models include:

(a) Phase Transformation model

(b) Dynamic Recovery (DR)/Recrystallization (DRX) model

These models are based on observations of the post-deformation microstructure after dynamic loading. The subsequent sections discuss these models in detail.

2.5.2.1. Phase Transformation as a Mechanism of Formation of ASBs

As microstructural modelling was considered, phase transformation and/or melting were considered to be associated with the formation of ASBs. Some researchers proposed that a phase transformation from martensite to austenite to untempered martensite occurs in the white-etching ASBs due to the high temperature rise that occurs in the shear bands during deformation [60]. It

has been demonstrated that during the fast punching of steels, the temperature of the shear zones become sufficiently high enough to locally austenitize the steel, turning into martensite when the surrounding material quenches the shear zone and concluded that if the local plastic shear-rate is adequately high, the local cooling-rate would be exceeded by the heating rate leading to adiabatic instability as the plastic resistance of the material decreases [5, 38]. In addition, Glenn and Leslie [60] studied shear bands in 0.6% carbon steel produced by ballistic impact and reported a gradual transition from the white etching region to the matrix with the electron diffraction patterns changing from a diffuse ring to a solid Body-Centered Tetragonal (BCT) ring pattern. They proposed that the white etching region was very rapidly quenched martensite. Also, Wingrove [29] reported that the white etching shear bands did not temper in a manner typical of martensite, and did not have the type of structure usually associated with high-carbon martensites. Nevertheless, they had lattice spacing that matches that of martensite. He concluded that the white etching shear bands are martensite though their structures are different from that of normal martensite for the steels used. Meyers et al. [10] in 2004 reported of the formation of an amorphous region in Fe-Cr-Ni monocrystal deformed dynamically (strain rate ~10^4 s^{-1}) by the collapse of an explosively driven thick-walled cylinder under prescribed initial temperature and strain conditions as shown in figure 2-6. They asserted that the formation of the amorphous region was due to melting and very high rate resolidification. They discussed that the cooling rate within shear bands was extremely high and could possibly lead to resolidification in the glassy state from the melt resulting in the formation of the amorphous region.

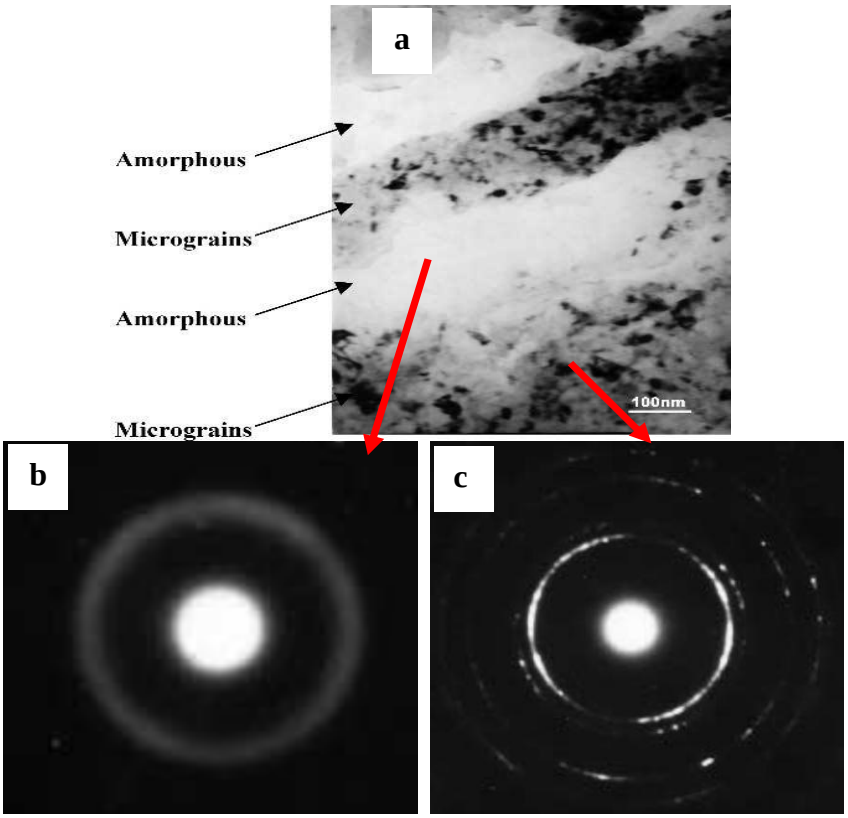

Figure 2- 6: (a) Transmission electron micrograph of ASB showing microcrystalline and amorphous regions. (b) Diffraction rings from the amorphous phase. (c) Diffraction rings from the microcrystalline zones [10].

In 2009, Duan et al. [61] used X-ray diffraction to assess the possible occurrence of a diffusionless phase transformation in ASBs when they studied the microstructure of serrated chips generated during high-speed machining of hardened 30crNi3MoV steel. They reported that the undeformed specimen contained only the body-centered cubic α-ferrite phase and carbides but the shear band in the machined chip had a mixture of α-phase and face-centered cubic γ-phase together with carbides because the (111) and (220) diffraction peaks of γ-phase appear as shown in figure 2-7. They reported that there was a transformation of the α-phase to γ-phase due to the generation of high temperature within the shear bands followed by subsequent quenching

to martensite in the form of diffusionless phase transformation during the machining. They estimated a temperature rise of approximately 750^{O}C.

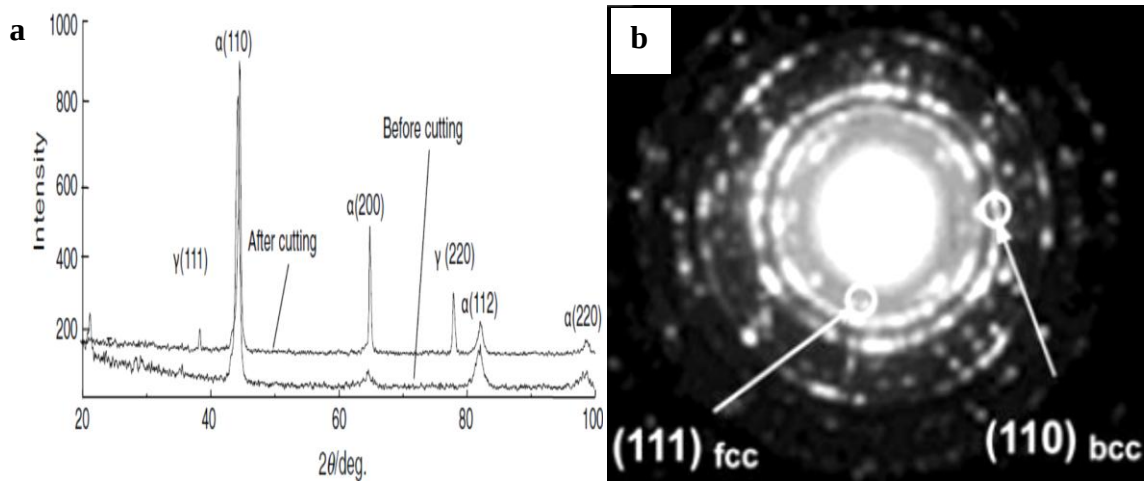

Figure 2- 7: (a) X-ray diffraction peaks of the ASB in the serrated chip in comparison with uncut specimen (b) diffraction pattern of center of ASB [61].

In 2011, Yang et al. [62] reported of an athermal phase transformation of β to ω within ASBs in a beta-Ti alloy when they investigated the microstructure and evolution mechanism of ASBs in a near beta-Ti alloy as shown in figure 2-8. They reported that the shear band offers thermodynamic and kinetic conditions for the $\omega_{(althermal)}$ phase formation beside the high alloying content of this material.

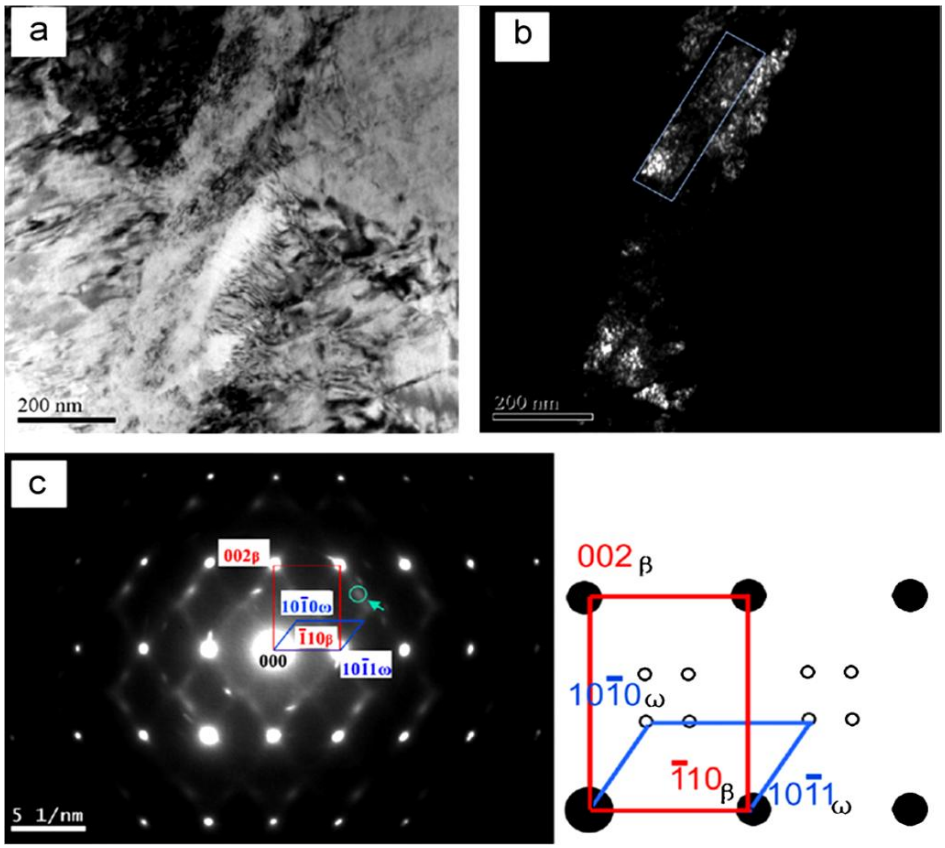

Figure 2- 8: TEM micrographs showing: (a) Bright-Field (BF) micrograph of ASB (b) Dark-Field (DF) micrograph obtained by the spot marked by green arrow and (c) corresponding diffraction pattern and indexed diffraction pattern [62].

However, other researchers differ in their opinion about this phase transformation in the shear bands. Zhang et al. [27] in their studies on ASBs in impact wear using low-alloy steel reported that if phase transformation from tempered martensite to austenite occurs in the narrow bands, then a high percentage of that austenite should remain in the narrow bands when cooled by the surrounding matrix. They however reported in their studies that no apparent austenite was detected in the diffraction patterns of the evolved ASBs. Wittman et al. [25] reported of the absence of austenite in the shear bands since in splat quenching from austenitic phase, the presence of austenite is very common. They reported that there was no change in hardness when

the sample was super cooled in liquid nitrogen that lends credence to the fact that there was no retained austenite, hence any phase transformation.

2.5.2.2 Dynamic Recovery (DR) and Dynamic Recrystallization (DRX) as a Mechanism of Formation of ASBs

Dynamic recovery/recrystallization is a popular and important mechanism used to explain the formation of adiabatic shear bands under the microstructural model. The initial observation of recrystallization in ASBs was by Glass et al. [9] in 1961 during analyses on an explosively loaded steel cylinder. Recrystallization in shear bands during dynamic loading is widely accepted due to the extent of the deformation and associated conversion of plastic work to heat during dynamic loading which investigators believe is adequate to produce new recrystallized grains in the shear bands [6, 17]. Prado et al. [63] reported that the characteristics of recrystallization is a combination of large misorientation and refined-faceted grain boundaries. However, there was no evidence to indicate if the recrystallized microstructure developed concurrently with deformation (dynamic recrystallization (DRX)) or subsequent to deformation (static recrystallization). Recently, some investigators have demonstrated that the refined microstructure within ASBs develop simultaneously with deformation [6, 16-17].

Several investigators have reported of recrystallization arising from dynamic loading conditions and the presence of equiaxed recrystallized grains within ASBs [12, 15, 58, 61, 64]. It has been reported that fine equiaxed grains with low dislocation density and well-defined grain boundaries are the microstructural characteristics of DRX [6, 17]. DRX has been defined as a structural rearrangement as a result of refinement of initial grain structures of materials to a point where

new nanograins form and grow [17, 65]. Accumulated strain and temperature drives static recrystallization while DRX has been reported to be an athermal phenomenon entailing successive grain refinement where thermal activation is not a pre-requisite to initiation [15-16]. Based on dynamically stored energy of cold work, DRX has been used to establish a link between mechanical phenomenon and material microstructure [15-16].

The density of dislocations in nanocrystalline specimens have been reported to saturate because of recovery due to the annihilation of dislocations into the grain boundaries [41]. Dynamic recovery is known to occur during severe plastic deformation [101-103]. It is often reported that due to the conversion of plastic work to heat, recovery produces ultrafine grains having both low-angle and high-angle grain boundaries [41-42, 66]. It has been shown that the competition between the generation of dislocations during plastic deformation and the annihilation during recovery determines the steady state dislocation density [41]. In 1993, Cho et al. [23] ascribed dynamic recovery mechanisms as the main cause of the fine equiaxed grains observed in the center region of a shear band in HY-100 steel rather than DRX. In addition, Rittel [15-16] reported that the stored energy of cold work is the driving force for microstructural rearrangement by dynamic recrystallization (DRX) which results in ASBs and that it is an athermal phenomenon observed at the early stages of the dynamic deformation process, while thermal effects are insignificant.

The explanations of the mechanisms for dynamic recovery and dynamic recrystallization that leads to the formation of ASBs during dynamic loading are presently unclear. Several nucleation mechanisms including Strain Induced Boundary Migration (SIBM), rotation and subgrain

coalescence and Progressive Subgrain Misorientation (PriSM) have been proposed to explain the mechanism of DR and DRX. Strain Induced Boundary Migration (SIBM), initially proposed by Bailey and Hirsch in 1962 suggests that recrystallization occurs as a result of differences in dislocation density across an existing high-angle grain boundary in a cold worked metal [67]. They discussed that the driving force associated with the strain energy difference causes a portion of the high angle grain boundary to migrate into the subgrain with the higher dislocation density. As the high-angle boundary sweeps through the deformed microstructure, it eliminates the dislocations creating a small, strain-free nucleus which will continue to grow through grain boundary migration as shown in figure 2-9 [58].

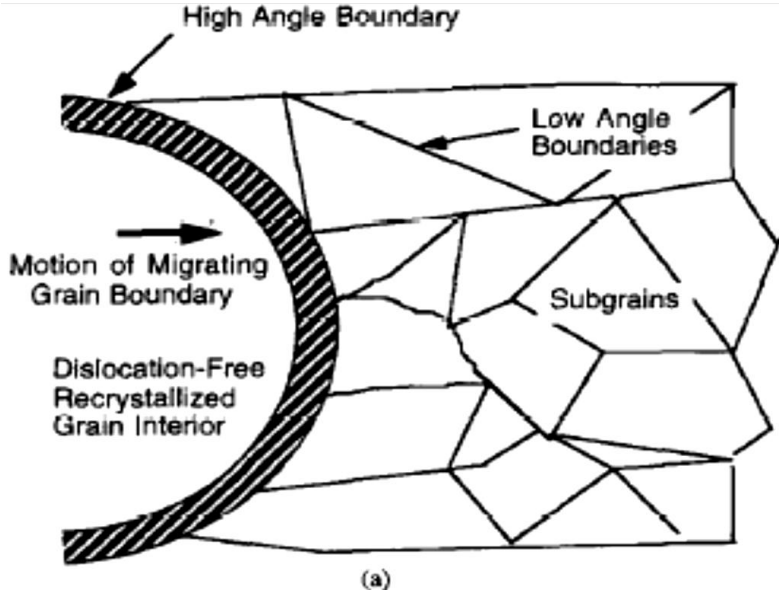

Figure 2- 9: Schematic diagram of recrystallization by high angle boundary migration through a partially recovered microstructure [58].

Rotation and coalescence of subgrains as a mechanism of recrystallization have been studied in detail by Li in 1962 [68] and Hu in 1963 [69]. They reported that it is energetically feasible for the rotation of subgrains with respect to neighboring grains if the direction of rotation favors the elimination of low-angle boundaries over that of high-angle boundaries, twist/asymmetric boundaries over that of the tilt/symmetric boundaries and large-area boundaries over that of the small-area boundaries. Li and Hu discussed that, in the subgrain rotation and coalescence model, two adjacent subgrains with a small misorientation between them will attempt to lower their surface energy by rotating into coincidence, thereby eliminating the low angle boundary that separates them as shown in figure 2-10 [6, 68].

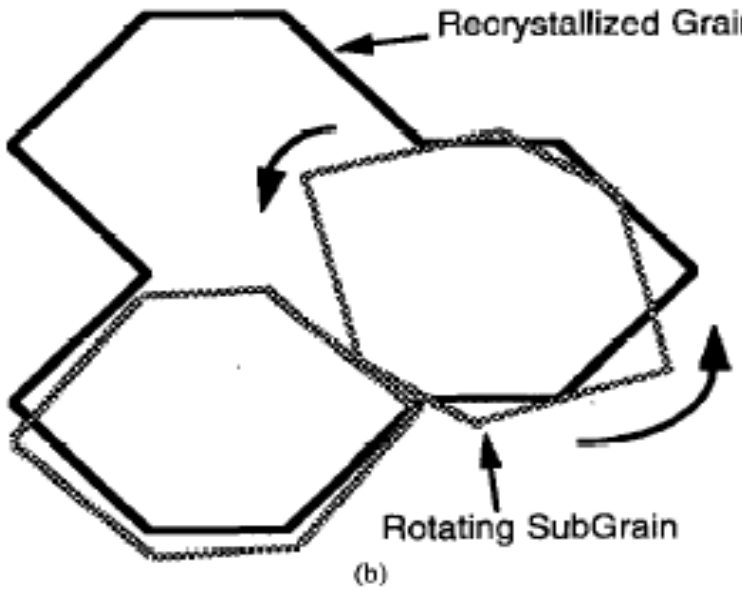

Figure 2- 10: Schematic diagram of recrystallization by subgrain rotation and coalescence [6].

Most of the experiments which were used to establish the theories of grain boundary migration and subgrain rotation and coalescence as mechanisms of recrystallization were carried out under

static annealing conditions. It has been reported that these classical mechanisms do not adequately account for the structure within ASBs and do not explain the mechanism of formation of ASBs [17-18, 58]. Progressive Subgrain Misorientation (PriSM) is the only model found in the literature which was established based on high strain rate deformations. Hence, it is reviewed into detail in the subsequent section.

2.5.2.2.1 Progressive Subgrain Misorientation (PriSM)

Hines in 1997 [58] and Hines et al. in 1998 [18] reported that classical recrystallization mechanisms are inadequate to account for the observed grain sizes during high strain rates by comparing the kinetics of high angle boundary migration and subgrain coalescence with the time-temperature profile determined for ASBs. They were unable to explain their observations of ASBs using the diffusion based recrystallization models of grain boundary migration, and subgrain rotation and coalescence [18, 58]. This was attributed to the presence of heavily dislocated cells, deformation texture due to rotation of the cells since substructural subdivision could no longer accommodate deformation, and the presence of comparatively high misorientation in Ta and Ta alloys. They concluded that the kinetics of the existing recrystallization models were too slow than the deformation time and/or the cooling time of the shear bands as shown in figure 2-11 [63].

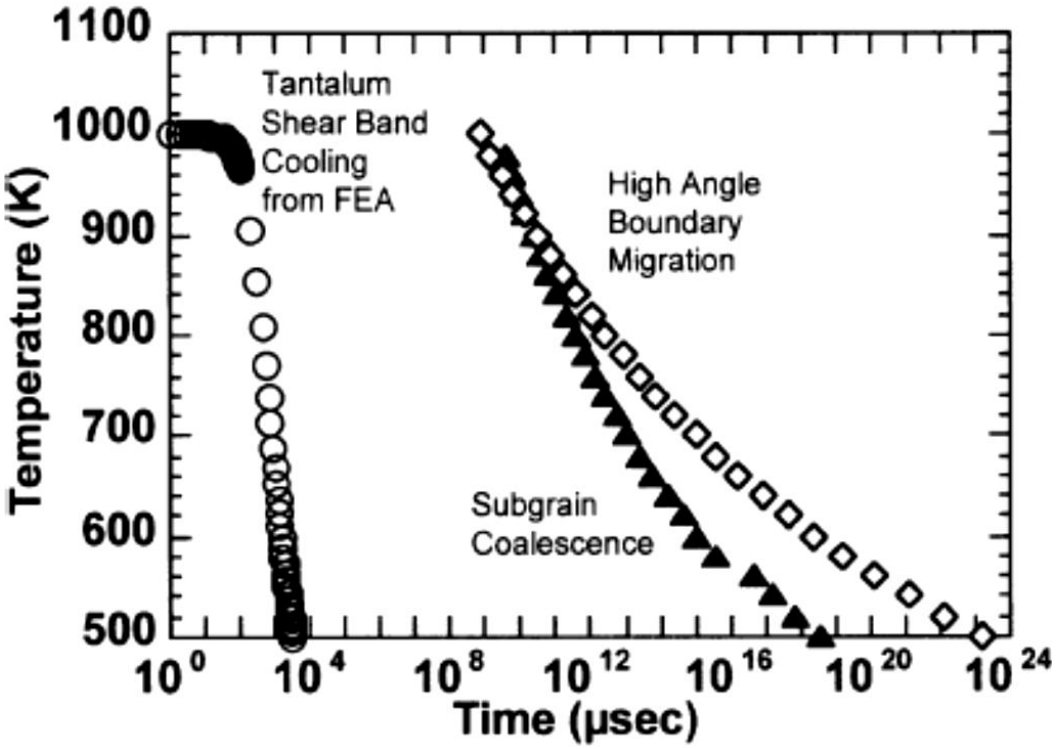

Figure 2- 11: A comparison of mechanism kinetics for high angle boundary migration model and subgrain coalescence model with shear band cooling rate for a tantalum specimen tested at an initial temperature of 298K [63].

In addition, Hines et al. [63] conducted liquid nitrogen temperature tests on copper and reported that temperature did not play a major role in dynamic recrystallization. These findings led to the proposal of the Progressive Subgrain Misorientation (PriSM) recrystallization model as depicted in the figure 2-12 [63]. According to the PriSM model of recrystallization developed by Hines et al. [63], cell subdivision takes place at the onset of shear band formation along the direction of shear which results in the breakup of the original grains into a cell structure to accommodate the strain. This results in a reduction in the size of cell structures, becoming narrower and evolving into subgrains through dynamic recovery processes. They discussed that at a critical cell size (approximately 0.2 μm), substructural subdivisions are unable to accommodate any more deformation leading to subgrain rotation which results in higher misorientation angles between

subgrains. They reported that the final state is through the occurrence of boundary refinement during cooling through dislocation annihilation which results in the final observed structure [18, 58, 63].

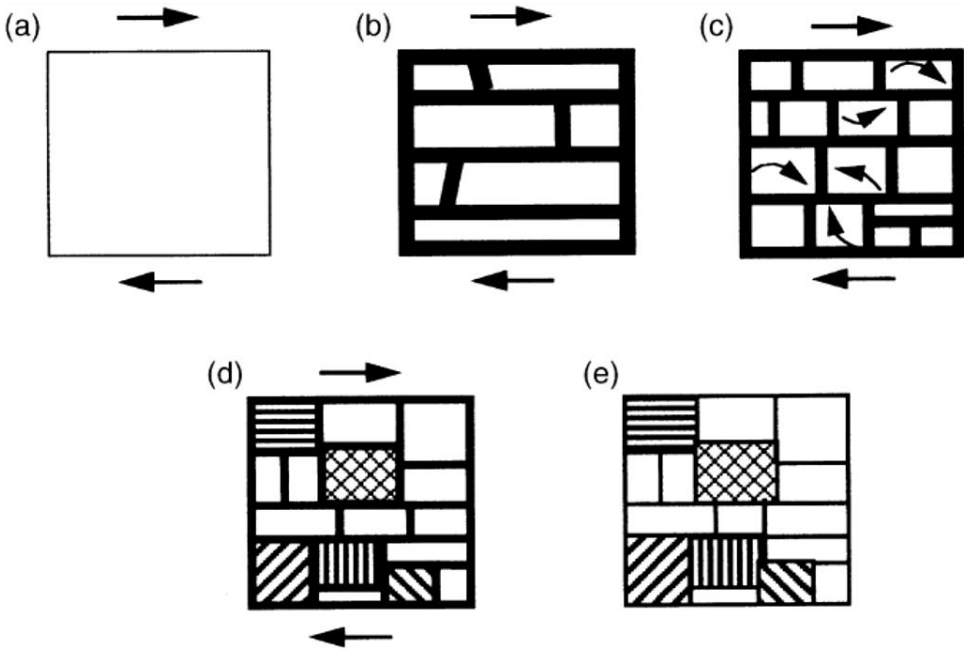

Figure 2- 12: PriSM model (a) starting single crystal (b) formation of elongated subgrains (c) rotation of equiaxed subgrains (d) high angle misorientation between some subgrains (e) boundary refinement during cooling (63).

Hines et al. [18, 58, 63] demonstrated that this recrystallization model is based on mechanically-assisted subgrain rotation that is kinetically feasible in the stringent time and temperature profile of an adiabatic shear band and may enable dynamic recrystallization to progress at very high strain rates with little or no thermal assistance. They reported that the PriSM model shows that the observed recrystallized grains present in shear bands are due to the rotation of the recovered

microstructure with subsequent dislocation annihilation responsible for the transformation of subgrain dislocation walls to grain boundaries [17, 18, 58, 63, 70-71]. Hines et al. [18, 58, 63] concluded that only dynamic recovery occurs within the highly-localized deformation regions of Ta and Ta-10wt% W and did not observe any dynamically recrystallized grains in the shear bands because the temperature rise associated with the shear band region was insufficient to achieve dynamic recrystallization. This conclusion brings into the question "what triggers dynamic recrystallization? Dynamic recrystallization has been reported to be an athermal process and that temperature has little or no effect on the mechanism of DRX [15-16]. This conclusion also contradicts the liquid-nitrogen temperature tests on copper by Hines et al. [18, 58, 63] in which they observed dynamically recrystallized grains since they concluded that temperature did not play a role during DRX. Rittel also reported that the stored energy of cold work is the driving force for microstructural rearrangement by dynamic recrystallization (DRX) which results in adiabatic shear bands [15-16]. High density of dislocations and dislocation structures have also been observed within ASBs which cannot be explained based on the characteristics of recrystallization [28-29].

The differences in observations and measurements of the structure and properties of ASBs, coupled with the associated proposed mechanisms of formation of ASBs which do not adequately relate the observed structure to the measured properties has limited our understanding of the mechanism of formation of adiabatic shear bands during dynamic loading. To better understand the mechanism of formation of ASBs, post-deformation microstructure characterization and the measurement and systematic observations of the microstructure of materials under dynamic deformation need to be pursued further. Structural steels in their

hardened conditions are readily susceptible to the formation of ASBs during dynamic deformation. The subsequent section reviews the microstructure of typical hardenable steels used for structural applications and the mechanism used in strengthening the steels.

2.6 Physical Appearance and Properties of Hardenable Steel

Body-Centered Cubic (BCC) metals such as steel are easily susceptible to the formation of ASBs than Face-Centred Cubic (FCC) metals [17, 30]. FCC metals under high strain rates of deformation usually exhibit plastic flow and texture development [6, 8, 17]. Hardenable steel was chosen for this study because it can be heat treated to achieve different mechanical and microstructural properties and it is easily susceptible to the formation of ASBs. Steel is also used frequently for structural applications and loadings that subject it to high strain rate and large strains of deformation. The subsequent sections review the physical appearance and properties of hardenable steels and and the mechanism used in strengthening the steels for structural applications.

2.6.1 Constituents and Phases of Steel

Steel is an alloy of iron (Fe) and carbon (C) with the carbon content ranging between 0.2% and 2.1% by weight [72-73]. Investigations on steel has proved that carbon strengthens steel and gives it the ability to be hardened by heat treatment with the iron and carbon atoms having approximate diameters of 0.258nm and 0.154nm respectively [73]. Other alloying elements reportedly used in addition to carbon in steel include manganese, chromium, vanadium, and tungsten [72-73]. It has been shown that iron atoms are arranged in either a Body-Centered

Cubic (BCC) or a Face-Centered Cubic (FCC) crystal structure [73-74]. A phase possesses characteristic structure, properties, and assumed chemical uniformity in a material [73-74]. Through a process called phase transformation, an existing phase can change to another and the transformation temperature is the temperature at which this occurs [74]. In steel, Iron (Fe) and Carbon (C) exist together in several different phases, dependent on the carbon content, alloying elements and temperature. The type and amount of alloying elements determines the transformation temperature [73]. Some important single-phases of steel include, γ-austenite, α-ferrite, δ-ferrite, Fe_3C-cementite or iron carbide [73-74].

2.6.2 Austenite

Studies on steel have shown that pure iron assumes a Face-Centered Cubic (FCC) crystal structure known as austenite from approximately $1394^{O}C$ to $912^{O}C$ [73]. Designated as γ, austenite is a non-magnetic solid solution of carbon and iron, and has high formability, characteristic of the FCC crystal structure [73-74]. It has been demonstrated that carbon atoms fit into interstitial spaces in FCC better than BCC and this allows the FCC crystal structure to hold a high proportion of carbon in single-phase solid solution approximately between 0.8% at $723^{O}C$ and 2.08% at $1148^{O}C$ [74, 75]. Investigators have shown that properties of austenite such as low strength, high ductility and chemical uniformity make austenite very useful during hot forming of steels [73, 75]. During phase transformation, depending on the rate of cooling and alloy composition, austenite either breaks down into α-ferrite and iron carbide (cementite) or undergoes a slight crystal lattice distortion known as martensitic transformation [72-73]. To be able to form any phase or a mixture of phases with certain desired properties in steel, the

specimen would have to be heated to the austenitic temperature where austenite exists as a single phase and then cooled by the appropriate means to form the desired phase(s) [73, 75].

2.6.3. Ferrite

Two types of ferrite, δ-ferrite and α-ferrite have been reported to occur at different temperatures in the microstructure of steel [73]. Alpha ferrite (α-ferrite) has been shown to be stable form of iron at temperatures approximately below $912^{O}C$ and is commonly referred to as ferrite [74]. The α-ferrite is a Body Centered Cubic (BCC) form of iron in which a small amount of carbon (approximately a maximum of 0.021% at $910^{O}C$ and only 0.008% at room temperature) is dissolved [74-75]. Studies has shown that the dissolution of carbon in BCC ferrite is less than that of FCC austenite because the BCC crystal structure has much less interstitial space than the FCC crystal structure and the carbon atoms cannot fit into interstitial spaces in the BCC ferrite structure as they can in the FCC austenite structure [74]. As a result, there is usually the creation of a two-phase mixture in most steels due to the limited number of carbon that BCC structures can hold compared to FCC structures in the steel [74]. At room temperature, the most stable form of iron is ferrite (α-Fe) [72-75].

2.6.4. Cementite (Iron Carbide)

Cementite or iron carbide with the formula Fe_3C is an intermetallic compound and has an orthorhombic crystal structure [72-75]. Several investigators have established that cementite is hard and brittle and contains approximately 6.7% carbon [72-75]. Structural investigations have established that alloys or phases with high amounts of cementite tend to be brittle and all the

cementite dissociate prior to melting [74-75]. Phase changes investigations has established that in carbon steel, when austenite is formed, all the carbon dissolves in the austenite and as carbon rich austenite cools, the iron attempts to change its crystal structure from the FCC austenite to the BCC ferrite, but the BCC ferrite can only contain 0.021% carbon in solid solution [73-75]. During this structural change, when ferrite forms, the excess carbon that ferrite cannot contain are rejected which results in some areas having excess of carbon [75]. The excess carbon forms the carbon-rich intermetallic known as cementite or iron carbide. Thus, the precipitation of cementite is a mechanism by which carbon atoms can leave the austenitic structure leaving behind iron that is pure enough to take the form of ferrite, creating a cementite-ferrite mixture [72-75]. The net reaction is shown in equation 2-1 below [73]:

$$\text{Austenite}_{0.77\%C}\text{,(fcc)} = \text{Ferrite}_{0.021\%C}\text{, (bcc)} + \text{Cementite}_{6.67\%C} \quad \text{.....2-1}$$

2.6.5. Heat Treatment of Steel

Several studies on the structure of metallic materials have established that the mechanical properties of metals, especially steel, are extremely dependent on the microstructure, crystal structure and elemental composition [73-77]. It has been established that controlled heating and cooling can be used to change the structure and properties of materials through heat treatment [76-77]. Heat treatment can be used to change the structural arrangements of atoms and the crystallographic structure of materials, which can cause changes in properties such as resistance to corrosion, machinability, resistance to wear, toughness and strength without concurrent change in the shape of the material [73-74]l. Most of the heat treatment on steel begins by forming the homogeneous single-phase high temperature austenite structure [72-77]. The final

properties of the heat-treated material mostly depend on the cooling rate, cooling temperature and the alloying elements [74-77]. During heat treatment, mechanisms including solid solution, grain size refinement, precipitation hardening, dispersion hardening, and phase transformations have been shown to improve the strength of steels [39, 73, 75]. Dispersion hardening is obtained by scattering stronger second-phase particles throughout a base material or matrix such as the distribution of cementite in ferrite [73, 75-77].

2.6.6. Martensite and its structure

Several investigations on martensite and martensitic structures have established that martensite is a hard unique phase that forms in steel and has a Body-Centered Tetragonal (BCT) crystal structure in which some carbon is dissolved [74-77]. It has been shown that austenite is the parent phase that transforms to martensite on quenching or rapid cooling [78-81]. During heating above the critical hardening temperature, the FCC austenite forms and all the carbon atoms present are dissolved in the austenite structure [73, 75, 78]. During rapid cooling or quenching, the FCC austenite is converted into a body centered cubic (BCC) crystal structure [73]. However, all the carbon atoms that were dissolved in the FCC austenite are retained and trapped in the octahedral sites of the BCC structure stretching the BCC crystal structure into a BCT crystal [73, 77]. The FCC lattice of austenite is distorted into the BCT structure of martensite without the loss of its contained carbon atoms such that the crystal structure is slightly longer than before in one dimension (c-parameter) and shorter in the other two (a-parameters) [74, 78-84].

Studies on phase transformation on steels have established that the rapid cooling or quenching makes the martensitic transformation a diffusionless process and as such, martensite has the

same composition as its parent austenite phase [73-75]. Defect analyses has established that the distortions in the BCT crystal structure of martensite results in a high amount of dislocations (linear defects) and high internal stresses [74, 78-82]. These dislocations make martensitic structures extremely hard and resistant to shear stresses. Structural investigations has shown that martensite appear as laths or plates on the microscope [75, 78-81].

It has been shown that the carbon content of the parent austenite phase determines the formation of either a lath martensite, plate martensite or a mixture of the two [73-81]. In iron-carbon alloys, it is reported that alloys with 0%C-0.6% C form lath martensites, alloys with 1%C-1.4%C form plate martensites and alloys with 0.6%C-1%C form mixed lath and plate martensite [73-75]. A comparison between lath and plate martensites in general, shows that lath martensites have higher toughness and ductility but lower strengths, while plate martensites have higher strengths but are more brittle [74]. Under the light microscope, units of plate martensites can be seen and retained austenite in the plate martensites in high carbon steels helps in sharply defining the plates while many of the individual units of lath martensite are below the resolution limit of the light microscope [74-75].

Investigators have demonstrated that lath martensite units are finer but are suggestive of the characteristic acicularity of martensitic microstructures and typical of them is the tendency for many laths to align themselves parallel to one another in large areas of the parent austenite grain [73, 74, 85-87]. These regions of parallel lath alignment are referred to as packets and they develop most prominently in low-carbon alloys [78-81, 88]. Numerous investigators have reported that lath martensites are long, approximately 0.5μm, and are typically grouped together

in the packets with low angle boundaries between each lath while very few might be separated by high angle boundaries [82]. Packets are delineated as a result of the different etching characteristics of the different variants or orientations of the laths in the various packets [85-86]. Laths in a packet of low-or-medium carbon martensite are very fine in sizes, with most of the laths having widths smaller than 0.5μm, and might not be revealed by light microscopy [73-76]. However, larger martensite laths might be visible in the light microscope.

Crystallographic investigations on lath martensites has shown that there are 24 variants of laths in a packet of lath martensite but one variant tends to be dominant meaning that most of the laths separated by low-angle boundaries or retained austenite have the same crystal orientation and that a packet may be considered as a single grain or crystal, albeit a grain divided by many low-angle boundaries and containing fine structures of many dislocations [73, 83-88]. Blocks are packets with martensite crystals of the same habit plane and same crystallographic orientation in low-carbon steel and iron-nickel alloys [85-88].

Studies have shown that the packet structure of lath martensite is important in determining mechanical properties and fracture behavior of the martensite that forms in low-and medium-carbon steels [73, 78, 87-88]. Dislocations are the major fine structural component in lath martensite including fine transformation twins [39, 86-88]. A dislocation density of approximately $10^{12}/cm^2$ in a low carbon lath martensite has been reported by Speich [89]. Tangled dislocations and dislocation cells have also been reported in the fine structure of lath martensite in a 0.2%C alloy [39, 73, 89-90].

2.6.7 Tempering Of Martensitic Steel

From the principles of phase transformations, the metastable phase martensite, present because carbon diffusion has been suppressed by rapid cooling or quenching, can break down into a mixture of ferrite and cementite when the martensite is heated to a temperature where the carbon atoms gain mobility and diffuse out of the octahedral sites of the BCT structure [72-76, 87-94]. This process is known as tempering and the final structure is usually referred to as tempered martensite [94]. It has been established that during tempering, the high internal stresses associated with martensite are relieved because the carbon atoms diffuse out and reduce the tetragonality of the BCT structure [87-94]. Tempering affects the microstructure and the mechanical properties of the steel such that toughness is improved while strength and hardness decreases [75, 87-96].

Several investigations have established that carbon atoms dispersed in martensite, form carbide precipitates of increasing size during tempering [73, 75]. The stages of tempering as summarized by [73-75, 83] are, the formation of a transition carbide and reduction of carbon content in the martensite matrix, the transformation of retained austenite to ferrite and cementite, and the replacement of the transition carbide and low-carbon martensite with cementite and ferrite. During the preliminary stages of tempering, it has been shown that carbon atoms segregate to various defects in the microstructure, martensite is converted to a low carbon martensite, and transition carbides are formed [72-75, 83-84]. The formation of transition carbides reduces the carbon content of the martensitic matrix and in the final stages of tempering, transition carbides dissolve and are replaced by cementite when the tempering temperatures are increased [73, 75].

The microstructure of a tempered martensite may consist of retained austenite, martensite, ferrite and cementite depending on the tempering conditions [73-75, 83-84, 97]. Investigations has shown that tempering steels used for engineering applications that require high strength and fatigue resistance (medium-carbon steels) and where the primary loading is compressive as in bearings and gears (high-carbon steels) in the range of 150^{O}C to 200^{O}C produces modest increase in toughness [73, 75]. In addition, it has been reported that tempering above 425^{O}C produces a significant improvement in toughness with a subsequent decrease in hardness and strength [73-74]. Toughness may decrease during tempering in the range of 260^{O}C to 370^{O}C [92]. This decrease in toughness is referred to as tempered martensite embrittlement [74]. It has been shown that during heat treatment of steels, lower strength and hardness leads to higher ductility and toughness of a microstructure unless embrittlement occurs [73]. In general, embrittlement is a reduction in the normal toughness of steel due to a microstructural change and chemical effects during tempering [74]. Tempered martensite embrittlement is thought to result from the combined effects of cementite precipitation on prior austenite grain boundaries or interlath boundaries and the segregation of impurities at prior austenite grain boundaries [92-93]. The reduced impact toughness associated with tempered martensite embrittlement is associated with three different modes of fracture that depend on the various carbon and phosphorus contents of the hardened steels. These are ductile, cleavage, and intergranular modes of fracture [92-95]. A general cause of tempered martensite embrittlement is attributed to the formation of carbide films from the interlath austenite after tempering [74, 83-84, 97]. Tempering hardened carbon and low alloy steels for relatively long times or cooling slowly through the temperature 375^{O}C to 575^{O}C may lead to temper embrittlement [93-96]. Other studies show temper embrittlement

occurs in the temper range 400^{O}C to 600^{O}C [92-94]. Temper embrittlement is caused by the presence of specific impurities such as manganese, Mn, and phosphorus, P, in the steel, which segregate to prior austenite grain boundaries during heat treatment [74, 94]. When embrittlement occurs, ductility and toughness are reduced as hardness and strength decreases [92-97].

It has been reported that in the tempering of oil-quenched AISI 4340 steel, at temperatures above 200^{O}C, yield strength and tensile strength decrease continuously and elongation and reduction of area increase with increasing tempering temperature [73, 74-75]. It has been shown that strong carbide formers such as chromium, molybdenum and vanadium, in addition to increasing the hardenability of iron-carbon alloys help to retard the rate of softening during tempering [96]. Without these elements, iron–carbon alloys and low-carbon steels soften rapidly with increasing tempering temperature [95-97]. Grange et al. [96] show that this softening is due to rapid coarsening of cementite with increasing tempering temperature, which is dependent on the diffusion of iron and carbon. They however reported that the carbide forming elements not only retard softening but also forms fine alloy carbides that produce a hardness increase at higher tempering temperatures through a process referred to as secondary hardening [92-97]. Even though temperature is a major variable during tempering, the structural changes responsible for the property changes are thermally activated and therefore dependent on both temperature and time [92-96]. A recent study demonstrated that during tempering at 315^{O}C and 425^{O}C of as-quenched AISI 4340 steel, the tempering time is as significant as the tempering temperature because the dynamic impact properties of the tempered steels were influenced by the duration of the tempering [33].

2.7 Preparing Specimens from Regions within ASBs for Microstructural Characterization using the Focused Ion Beam (FIB)

Because of the rapid rate of deformation during dynamic loading, recovery experiments including microstructural characterization of the post-deformation specimens are used to make predictions on the mechanism of formation of ASBs. During microstructural characterization, a carefully prepared specimen interacts with either a probe of X-ray radiation, visible light, a sharp-flexible needle or a high-energy electron beam to reveal information about the microstructural features within the specimens [98]. A myriad of advanced microstructural characterization techniques include Atomic Force Microscopy (AFM), X-ray Diffraction (XRD), Scanning Electron Microscopy (SEM), Transmission Electron Microscopy (TEM) and Scanning Transmission Electron Microscopy (STEM).

Recently, advanced microstructural characterization techniques are being employed to reveal into detail the structure within the evolved ASBs after dynamic deformation [6, 12, 17, 14]. However, due to the very narrow nature of the evolved ASBs (~1 to 350μm), preparing and collecting data from the deformed specimens are very difficult and result in distortion of data in most cases. This is due in part to the equipment used for the characterization processes, and how specimens are to be prepared before usage. In TEM, electron waves interact with carefully prepared thin specimens approximately, 10nm to 1μm thick, and provides great detail of the microstructure features within the specimen [99-100]. High-resolution TEM/STEM requires thin specimens typically less than 100nm to transmit electron beams through the specimens [100]. Hence, specimen preparations for TEM/STEM/HRTEM investigations are critical because the specimens would have to be thin enough and contain the defects and features to be investigated

without any added distortions. During microstructural analyses of ASBs, conventional preparation of thin foil specimens for TEM/STEM/HRTEM investigations is difficult because the perforation produced using conventional techniques such as double-jet polishing and ion milling generally do not coincide with the shear band area because of the small widths of the shear bands. Specimens with easily observable shear bands are electro-polished to produce a perforation within the specimen through which the electron wave is passed. As the electron wave passes through the perforation, the edges of the perforation would be thin enough to transmit the electron waves through the specimens and reveal the underlying microstructural features. However, most of the perforations produced using the conventional techniques do not coincide with the evolved ASBs as shown in figure 2-13 [6, 101]. When this happens, the electro-polished specimens are ion milled to gradually enlarge the perforation until it intersects the shear band.

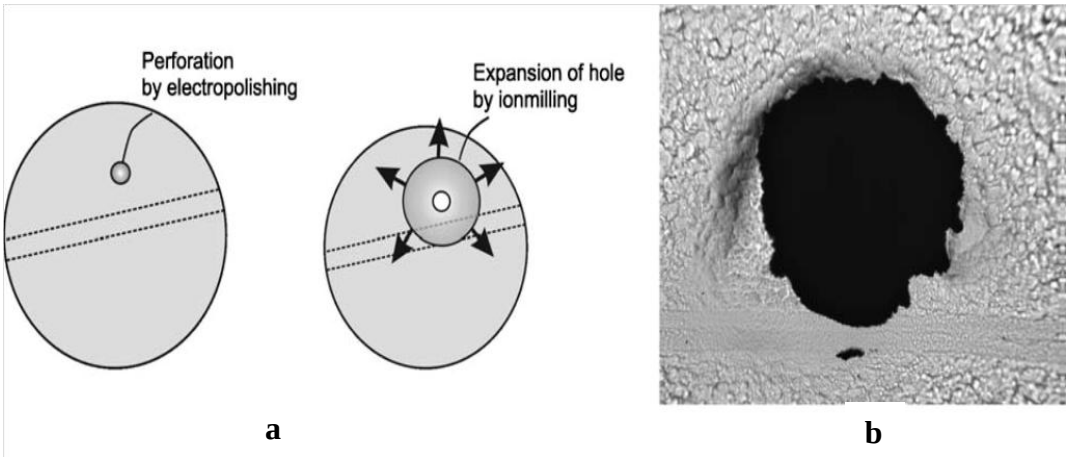

Figure 2- 13: (a) Sequential electropolishing and ion-milling technique and (b) shear band in Zircaloy at edge of perforation [6].

Besides bending, cracking and distorting the microstructural features within the ASBs when using these conventional specimen preparation techniques, most of the ASBs are only visible

under the optical microscope in the polished and etched conditions. This renders specimen preparation from ASBs for microscopic analyses even more difficult and limits the information that can be obtained during post-deformation analyses.

Recently, the Focused Ion Beam (FIB) instrument has become an important technology for circuit editing, TEM specimen preparation, microstructural analysis and nano/micromachining [99, 102]. FIB microscopy provides the opportunity for novel specimen imaging, sectioning, specimen preparation and micromachining [102]. The FIB consists of an ion source, sequence of electrostatic lenses and a scan generator [102]. The Liquid Metal Ion Source (LMIS) is the type of ion source used on most FIB instruments because it provides the brightest and most focused ion beam [99]. The basic function of the FIB is imaging and sputtering with an ion beam. The FIB microscope uses the technique of raster scanning similar to the SEM except that an ion beam is rastered over the specimen [99]. Ga ions are used in most of the commercially available FIB columns, and their sputtering action enables precise machining of specimens. The electrostatic lenses shape the ion beam while the scan generator guides the beam onto the specimen with a moving stage [102]. Generated secondary electrons, upon interaction of the ion beam with the surface of the specimen, are used to obtain high-spatial resolution images. The dual-beam FIB instrument has the FIB column which uses the ion beams while the SEM column uses the generated secondary electrons [99]. It also has gas-injection capabilities for local chemical vapor deposition which enable ion-beam activated depositions and enhance etching [102]. Thin foils from the adiabatic shear bands for TEM/STEM/HRTEM investigations can be prepared using the FIB microscopy because it can better select the shear band regions, and prevent bending and cracking that occurs during conventional thin foil preparations. This will

increase the accuracy of the data that can be retrieved from post-deformation specimens and would results in providing a more accurate and detail understanding of the structure within the narrow ASBs.

2.8 Scope and Objectives of Current Research

Although there have been several experimental and theoretical investigations on ASBs, the mechanisms of their nucleation and propagation remain less understood. This is due in part to the complexity of the problem of formation of these shear bands, their very narrow nature in the microstructure (~1 to 350μm), and the fact that they occur so rapidly that it is almost impossible to observe the actual changes in properties due to the short duration between deformation and failure. These factors have limited the information that can be obtained in order to improve our understanding of the mechanism of formation of ASBs and have resulted in scientific questions that have not been satisfactorily answered. Additionally, numerical models in the literature that include the formation of ASBs such as the work by Erlich et al. [103] assume a blank pre-deformation microstructure and applies to materials with simple microstructures. However, most of the materials used for structural application that are susceptible to the formation of ASBs have complex microstructures with constituents including carbides, solutes and hard particles/second phases within a matrix. Thus, these numerical models do not adequately predict the microstructures of materials used for structural applications.

Because of the rapid rate of deformation during impact, a systematic study of the microstructure of a typical heat-treatable steel prior-to, and after impact can be used to determine the initiation of ASBs and track the microstructural changes that occur during the evolution of ASBs. The

objectives of this research was to systematically and comprehensively study the microstructure of AISI 4340 steel prior to impact, after impact and after post-impact annealing to determine the effect of the pre-impact microstructure on the nucleation and initiation of ASBs and the mechanism of evolution of ASBs during impact. A new approach using the FIB was applied for preparing thin foil sections from ASBs in the impacted steel specimens for comprehensive electron microscopy examinations without distorting the structure within the ASBs. Furthermore, the present study also includes the structural changes that occur during post-deformation annealing processes which clarifies understanding of the mechanisms of formation of ASBs. Details of the methodology employed to achieve the objectives of this research are presented in the next chapter.

CHAPTER 3
MATERIAL AND EXPERIMENTAL PROCEDURE

3.1 Introduction

In this research, it is proposed that because of the rapid rate of deformation during impact, a systematic study of the microstructure prior-to, and after impact can be used to track the microstructural changes that occur during the evolution of Adiabatic Shear Bands (ASBs). Thus, the objectives of this research are to study the microstructure of AISI 4340 steel prior to impact, after impact and after a post-impact annealing, to determine the effect of the prior-deformation microstructure on the nucleation and initiation of ASBs, and to deduce the mechanism of evolution of ASBs during impact. The process to achieve the objectives of this study is grouped into three major parts:

a. First, an initial heat treatment of AISI 4340 steel followed by a comprehensive microstructural characterization and measurements to determine the morphology and constituents of the heat-treated specimens prior to impact.
b. Secondly, impact of the heat treated steel specimens using the Direct Impact Hopkinson Pressure Bar (DIHPB) under predetermined high rate loading conditions followed by standard metallographic techniques to study the impacted specimens.
c. Thirdly, cutting thin sections from impacted steel specimens using Focused Ion Beam (FIB) followed by comprehensive microstructural characterization techniques using optical and electron microscopy to determine the evolved structure within the ASBs.

In this study, the structural changes that occur during a post-deformation annealing process which may relate to understanding of the mechanism of formation of ASBs is also investigated.

A detailed study of the initial morphology and constituents of the steel prior to impact was required as a baseline for comparison to the final microstructure after impact. The Direct Impact Hopkinson Pressure Bar was used because of its ability to induce high strain rates and large strains of deformation in the specimens tested. Standard metallographic techniques were used to document the presence of ASBs in the impacted specimens. Specimens containing metallographically observable ASBs were examined using X-ray diffractometry and electron microscopy techniques. The current study uses a Focused Ion Beam (FIB) to cut the impacted specimens for electron microscopy analyses without adding more stresses or distortions to the prepared specimens. The following sections describe into detail the material and experimental procedures used in order to achieve the objectives of this research. Section 3.2 deals with the steel selected for this study and the reasons why it was selected. Section 3.3 describes in detail the experimental procedures used while 3.4 describes the procedure used for analyzing Selected Area Diffraction Patterns (SADPs) and Geometric Phase Analysis (GPA).

3.2. MATERIAL

AISI 4340 steel was used for this study. It is a low alloy heat treatable steel containing nickel, chromium and molybdenum. It can develop high strength when heat-treated as well as fatigue resistance. It is used in structural applications including aircraft transmission gears, power transmission gears, power shafts and other structural parts. AISI 4340 steel was selected for this study because it can be heat treated to achieve different mechanical and microstructural properties and it is easily susceptible to the formation of ASBs. Because of these properties, it can be used to study the pre-impact and after-impact microstructures in order to follow the microstructural changes that occur during impact.

Specimens were cut from the as-received rolled AISI 4340 steel bar and machined to specifications. The chemical composition of AISI 4340 steel as received from the manufacturer in weight percent (weight %) is given in table 3-1. The machined specimens had a diameter of 9.5mm and a height of 10.5mm as shown in figure 3-1.

Table 3- 1: Chemical Composition of AISI 4340 steel (weight %)

Chemical Composition	Minimum (%)	Maximum (%)
Carbon	0.37	0.44
Silicon	0.10	0.35
Manganese	0.55	0.90
Nickel	1.55	2.00
Chromium	0.65	0.95
Molybdenum	0.20	0.35
Phosphorus	0	0.04
Sulphur	0	0.04

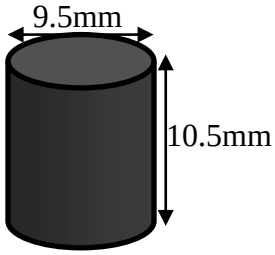

Figure 3- 1: Schematic of the cylindrical specimens used for the study.

3.3 Description of Experimental Procedure

The experimental procedure used to achieve the objectives of this research are outlined in the following subsections. Section 3.3.1 describes the procedure used for the pre-impact heat treatments of the steel specimens. Section 3.3.2 provides information on the impact tests, and the

post-impact annealing whereas section 3.3.3 presents the metallographic and microstructural characterization techniques used to study the pre-impact, impact and post-impact steel specimens. Figure 3-2 shows a flow chart of the experimental procedure and the number of specimens used for each stage of the experiment from the initial heat treatment to the impact tests.

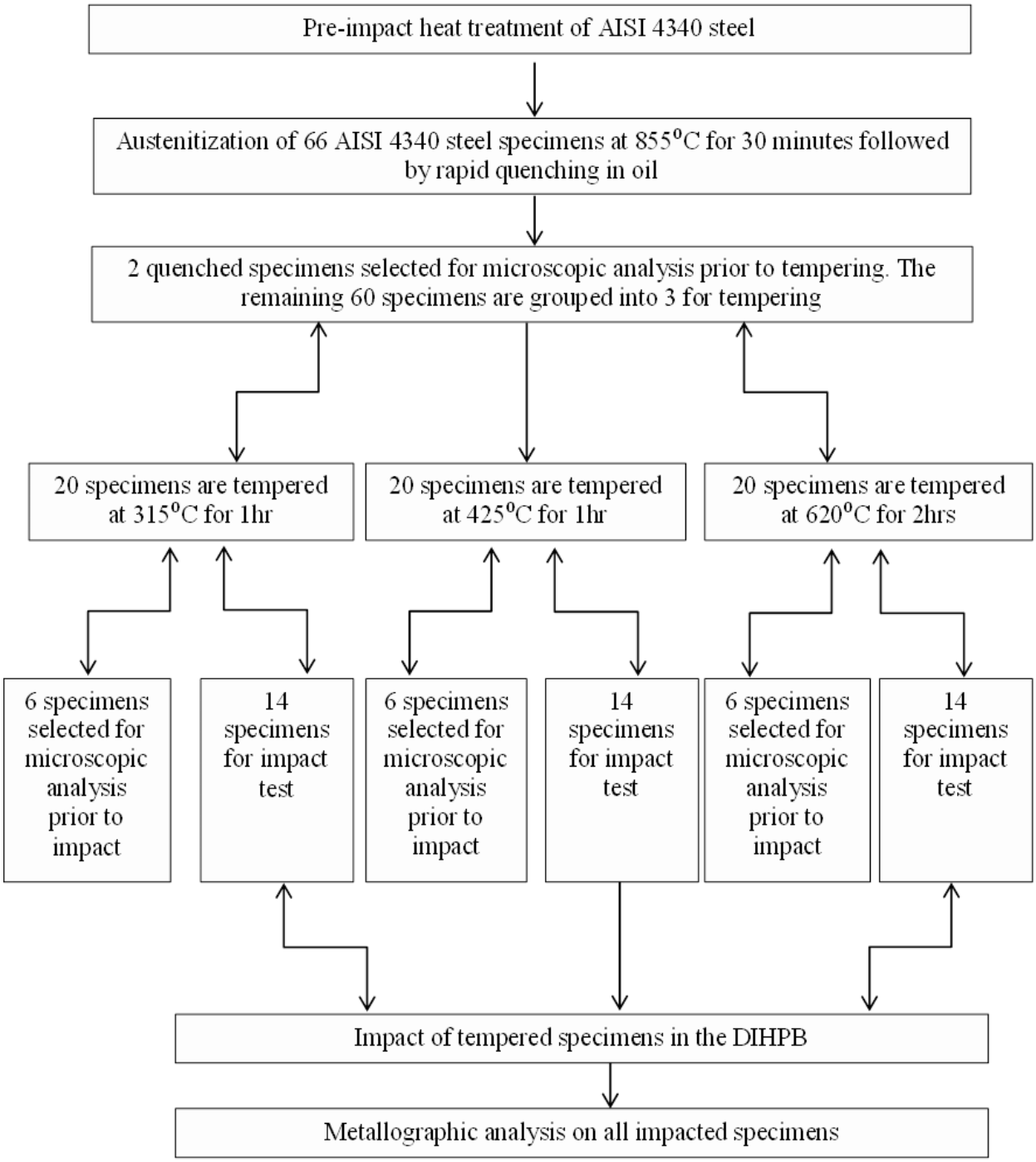

Figure 3- 2: Flow chart of experimental procedure from the initial heat treatment to the impact tests.

3.3.1 Heat Treatment of the As-received AISI 4340 Steel Specimens Prior to Impact

Sixty-two machined cylindrical steel specimens were heat-treated prior to impact. The heat treatment was carried out by an austenitize-quench-and-temper procedure. All the specimens were austenitized at $855^{O}C$ for 30 minutes followed by rapid quenching in oil to produce martensite. Two selected martensitic specimens were metallographically studied to confirm the formation of martensite and any other present phases. Sixty quenched specimens were then put into three groups of twenty specimens in each group and tempered at $315^{O}C$, $425^{O}C$, and $620^{O}C$ to produce a tempered martensite structure. The first two groups were tempered at $315^{O}C$, and $425^{O}C$ for 1 hour each followed by air-cooling. The twenty specimens in the last group were tempered at $620^{O}C$ for 2 hours followed by air-cooling. Detailed metallographic and microscopic analyses was carried out on six selected specimens from each group using Optical Microscopy (OP), Scanning Electron Microscopy (SEM), X-ray Analysis (XRD), Electron Probe Microanalyses (EPMA) and Transmission Electron Microscopy (TEM) techniques. The purpose of this process was to study the morphology and the constituents of the tempered specimens prior to impact in order to have a basis for comparison with specimens after the impact. Table 3-2 shows the list of groups of specimens prior to impact and the conditions for their pre-impact heat treatments.

Table 3- 2: List of Groups of Specimens and their Pre-impact Heat Treatments

Name of Group	Number Of Specimens	Tempering Temperature	Tempering Time	Specimens For Pre-Impact Microstructural Analysis
Martensite	2	Not Tempered	Not Tempered	2
315^{O}C-1hr	20	$315\ ^{O}$C	1hr	6
425^{O}C-1hr	20	$425\ ^{O}$C	1hr	6
620^{O}C-2hr	20	$620\ ^{O}$C	2hrs	6

3.3.2 Impact Tests and Post-impact Annealing

This section describes the equipment and the procedure used to impact the steel specimens at high strain rates and large strains. The final part of the section describes the post-impact annealing processes which were performed on selected impacted specimens with distinct ASBs.

3.3.2.1 Impact Test

A modified form of the Hopkinson Pressure Bar, Direct Impact Hopkinson Pressure Bar (DIHPB), was developed at the University of Manitoba. It applies large strains and strain rates as high as 10^4/sec in compression. This equipment was used to impact the steel specimens because of its advantages in ensuring homogeneous compression while extensively impacting the material at high strain rates to ensure that ASBs are formed in the steel specimens. Further accurate determination of the dimensions of the specimens was carried out. A summary of the dimensions of the pre-impact specimens and impact conditions is given in table 3-3. The impact tests were conducted at increasing impact momentum as indicated on table 3-3. Since the weight

of the projectile is constant (18.67 N), an increase in impact pressure results in increase in impact momentum and strain rate.

Table 3- 3: Dimensions of Pre-impact Steel Specimens and Impact Conditions

Specimen	Name of group	L_O (mm)	D_O (mm)	Area (mm^2)	L_F (mm)	Pressure (KPa)	Velocity (m/s)	Impact Momentum (kg.m/s)
1	315^OC-1hr	10.51	9.49	70.70	8.51	160	21.0	41
2	315^OC-1hr	10.46	9.48	70.58	8.41	180	22.0	43
3	315^OC-1hr	10.50	9.49	70.66	6.50	190b	22.6	44
4	315^OC-1hr	10.46	9.48	70.51	6.57	200b	23.0	45
1	425^OC-1hr	10.51	9.50	70.88	8.31	180	22.0	43
2	425^OC-1hr	10.47	9.50	70.88	8.11	200	23.0	45
3	425^OC-1hr	10.48	9.50	70.81	6.96	220b	24.0	46
4	425^OC-1hr	10.42	9.53	71.33	6.73	260	25.8	50
5	425^OC-1hr	10.55	9.50	70.88	5.75	280b	26.7	52
1-A	620^OC-2hrs	10.55	9.50	70.88	7.63	140	20.0	39
2-B	620^OC-2hrs	10.54	9.47	70.44	7.32	160	21.0	41
3-C	620^OC-2hrs	10.54	9.49	70.73	6.99	180	22.0	43
4-D	620^OC-2hrs	10.50	9.50	70.81	6.90	200	23.0	45
5-E	620^OC-2hrs	10.50	9.50	70.81	6.73	230	24.4	47
6-F	620^OC-2hrs	10.47	9.51	71.03	6.21	260	25.8	50
7-G	620^OC-2hrs	10.44	9.51	71.03	6.08	260	25.8	50
b = fractured								

3.3.2.2 The Direct Impact Hopkinson Pressure Bar (DIHPB)

The DIHPB consists of a cylindrical projectile, timer, Transmitter bar, strain gage, hollow gun barrel, control box and accumulator, and firing chamber. The accumulator contains compressed air that provides pressure that accelerates the cylindrical projectile to strike the sample at high impact velocities. Attached is a pressure gage that is used to set and control the firing pressure. An accumulator pressure button controls the firing pressure. The strain gage is mounted on the transmitter bar and is used in conjunction with a differential amplifier and a digital oscilloscope to monitor the strain during the impact test. The "Control Box" serves as the control center of the Direct Impact Hopkinson Pressure Bar. It has a power switch button that is used for switching the set up on. There is a retract reset button which brings the cylindrical projectile to the start point before firing. The projectile is a solid cylinder machined out of AISI 4340 steel and weighs 18.67 N. It is accelerated using an air operated gas gun. A hollow cylinder guides the projectile to strike the sample at high strain rates. A charge button on the control box initiates pressure charging. A fire button fires the projectile after charging to the required pressure. Two light beams connected 250mm apart are attached. This is used to calculate the projectile velocity by measuring the time the projectile travels a distance of 250mm. A schematic of the DIHPB used for this research is shown in figure 3-3.

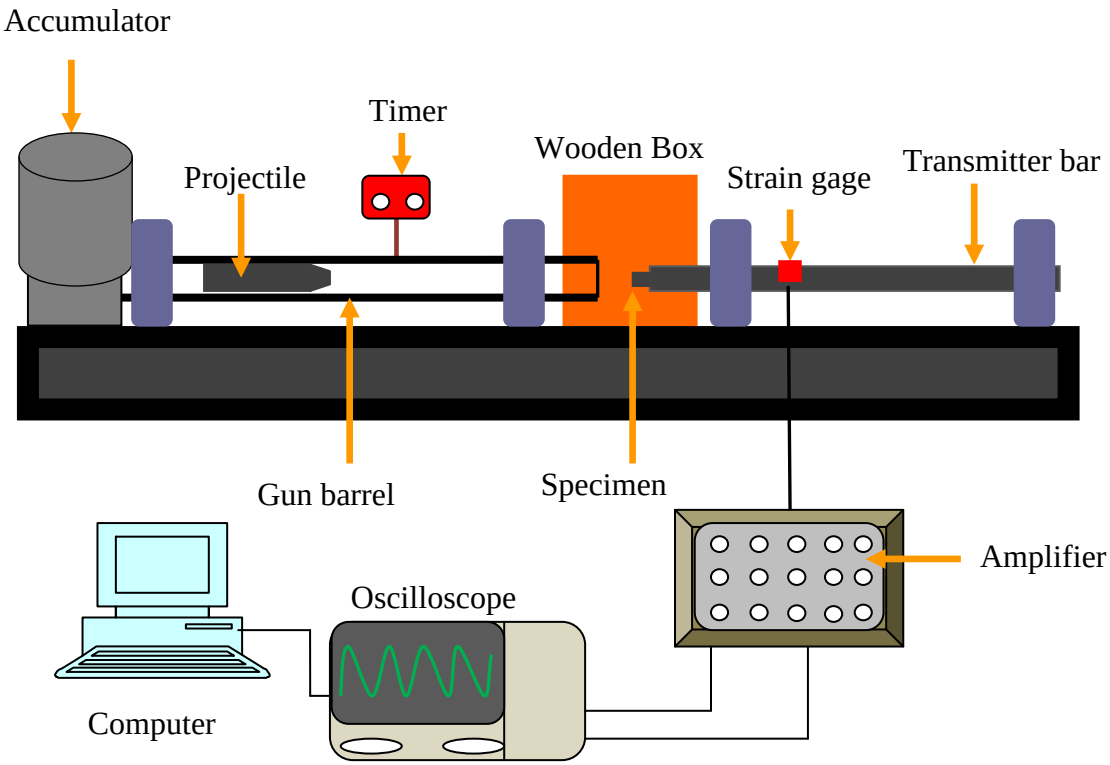

Figure 3- 3: A schematic of the Direct Impact Hopkinson Pressure Bar (DIHPB).

3.3.2.3 Impact Procedure

During the impact, the heat treated steel specimens were attached to the center of the front face of the transmitter bar. This was done by applying a high viscous gel on the flat faces of the specimens. Friction at the specimen-bar interface prevents spreading of material leading to barreling during deformation. The high viscous gel reduces the friction at the specimen-bar interface and ensures uniform deformation of samples during impact. A wooden box was fixed around the specimen to reduce noise and prevent flying parts when specimens fracture during deformation. A high velocity cylindrical projectile made from AISI 4340 steel was used to impact the specimens. The hardness value of the projectile was 47 HRC. An air operated gas gun fires the cylindrical projectile through a hollow barrel .The projectile strikes the attached specimens at the center of the front face of the transmitter bar at a very high impact velocity.

This impact generates a compressive pulse (elastic waves) which travels through the specimen and is transmitted into the output bar. A strain gage and a strain pulse amplifier are attached to the transmitter bar. The generated elastic waves during deformation are captured by the strain gage and a signal is sent to the strain pulse amplifier that amplifies the signals and sends it to an oscilloscope. The strain wave data is stored in the form of voltage and time by the oscilloscope. The firing pressure was varied to obtain different impact momentum during the deformation process. Calibration of the transmitted bar with the strain gages shows that, with the current strain gage and bar, the relationship between the measured voltage and the load is:

$$P = 0.021796\ V \quad \text{.....3-1}$$

where P is the load in Kilo Newton (kN) and V is the corresponding measured voltage in milli Volt (mV).

Considering that metals are essentially incompressible, their volume will remain constant during plastic deformation. Assuming a linear variation of displacement with time and constant strain rate, the true stress, σ, and the true strain, ε, at time t during the deformation are given by:

$$\sigma_{(t)} = \frac{P(t)}{Ai}\ \frac{Li-(Li-Lf)(t/tf))}{Li} \quad \text{.....3-2}$$

$$\varepsilon_{(t)} = In\ \frac{Li}{Li-(Li-Lf)(t/tf))} \quad \text{.....3-3}$$

where Li is the initial length and Lf is the final length of the steel samples.

The maximum strain in a specimen is directly proportional to the strain rate, έ, and the length of the striker bar, *l*, by the relation:

$$\acute{\varepsilon} = \frac{C}{2l}\,\varepsilon \quad \text{.....3-4}$$

where C is the longitudinal wave propagation velocity in the transmitter bar. Dynamic stress strain curves were generated for the steel specimens under direct impact using the above equations. The global strain rates for each test were calculated as a function of total strain using the above equation.

3.3.2.4 Post-Impact Annealing Heat Treatment

Six impacted specimens with distinct ASBs without microcracks were annealed at $350^{O}C$ to $650^{O}C$ for periods ranging from 30 minutes to 4 hours. Soaking the impacted specimens at the higher temperatures was done for shorter periods whilst soaking at the lower temperatures were done for longer periods. This provided information on how different temperatures and time affect the properties of the shear bands and the surrounding material. Each annealing process was followed by air cooling and subsequent microstructural analysis to study the ensuing properties and structure of the shear bands and the surrounding material. The 6 impacted specimens which were used for the post impact annealing and their post impact annealing conditions are shown on table 3-4.

Table 3- 4: Conditions for post-impact annealing

Name of Specimen	Tempering Temperature/Time Prior to Impact	Impact Momentum	Annealing Temperature/Time
A-(Impacted	425 ^{O}C	45kg.m/s	350 ^{O}C for 2hrs
B-(Impacted)	425 ^{O}C	50kg.m/s	450 ^{O}C for 2hrs
C-(Impacted)	425 ^{O}C	52kg.m/s	650 ^{O}C for 0.5hrs, 2hrs
A-315^{O}C	315^{O}C	44kg.m/s	350 ^{O}C for 2hrs
A-425^{O}C	425^{O}C	45kg.m/s	350 ^{O}C for 2hrs
A-620^{O}C	620^{O}C	50kg.m/s	350 ^{O}C for 2hrs, 4hrs

3.3.3 Metallographic and Microstructural Analyses

Standard metallographic techniques for microstructural studies including sectioning, mounting, grinding, polishing, etching and microscopic analyses were used to study 20 specimens prior to impact, 40 specimens after impact and 6 specimens after post-impact annealing. Selected specimens were mounted, ground, polished and etched to reveal their microstructure. Microscopic analyses were performed using an Optical Microscope (OM), Scanning Electron Microscope (SEM), Transmission Electron Microscope (TEM), Electron Probe Microanalysis (EPMA), and X-Ray Diffractometry (XRD).

3.3.3.1 Metallographic Specimen Preparations

To reveal the microstructure of the steel specimens under the microscope, the specimens were mounted in Bakelite, ground, polished and etched. The specimens were mounted using an

automatic mounting press for easier handling during grinding and polishing the mounted specimens were ground using emery papers. Polishing was done on a 6-micron diamond wheel and a 1-micron diamond wheel until a mirror surface was obtained. A 2% Nital solution consisting of 100 ml Ethanol and 1-20 ml Nitric acid was used to etch the polished specimens. Figure 3-4(a) shows an image of a steel specimen prior to impact, an impacted and fractured specimens while figure 3-4(b) shows a mounted specimen after etching.

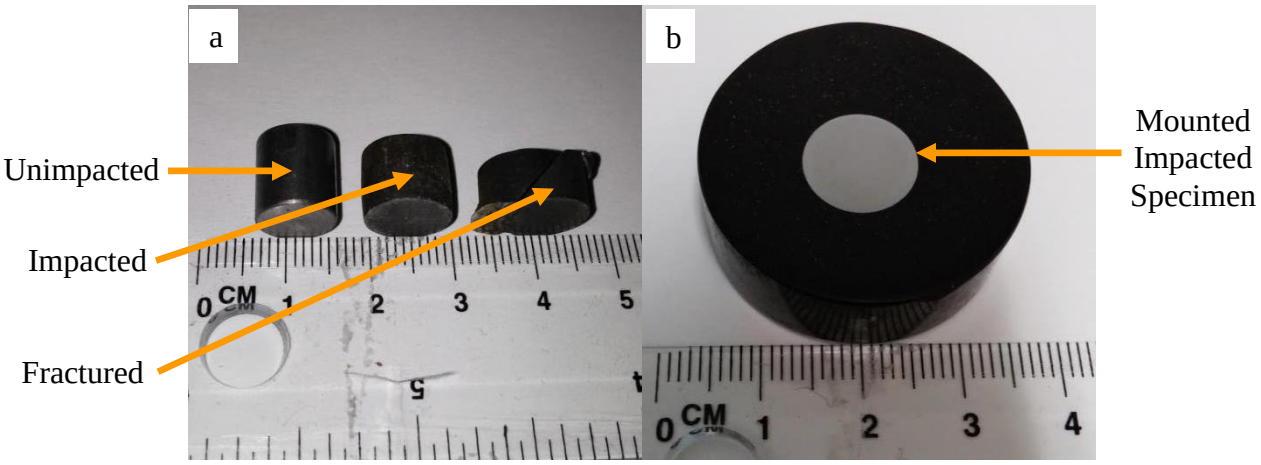

Figure 3- 4: (a) Image of an untested, impacted, and fractured specimens (b) Image of a mounted specimen after etching.

3.3.3.2 Optical Microscopy (OM), Scanning Electron Microscopy (SEM), Electron Probe Microanalysis (EPMA) and Microhardness Measurements

ZIESS Axiovert 25 inverted-reflected light microscope, equipped with CLEMEX Vision 3.0 image analysis software and a JEOL 5900 scanning electron microscope (SEM) equipped with an Oxford (Oxford Instruments) ultra-thin window energy dispersive spectrometer (EDS) were used to study the morphology and constituents of the mounted specimens. The optical

microscope was used to study the structure of the impacted specimens to document the presence of ASBs. The SEM was used to study the morphology of the martensitic structures in both Secondary Electron (SE) and Backscattered Electron (BSE) imaging modes. Spectroscopic analysis was carried out on the pre-impact, impact and post-impact annealing specimens using a CAMECA SX 100 Electron Probe Microanalyzer (EPMA). Microhardness measurements were performed with a Buehler micro-hardness machine on the steel specimens, prior to impact, after impact and after post-impact annealing by applying a 300 gram-force (2.942N) for 15 seconds to form indents in the specimens as shown in figure 3-5(a). All specimens were properly ground and polished by using standard metallographic techniques prior to the hardness testing. A total of 20 hardness values (Vickers Hardness, HV) were recorded for regions within and away from the shear bands and their average values calculated. The thickness of the evolved shear bands after impact was also measured on the optical microscope as shown on figure 3-5(b). Forty measurements were made across the length of the shear bands and the average was calculated.

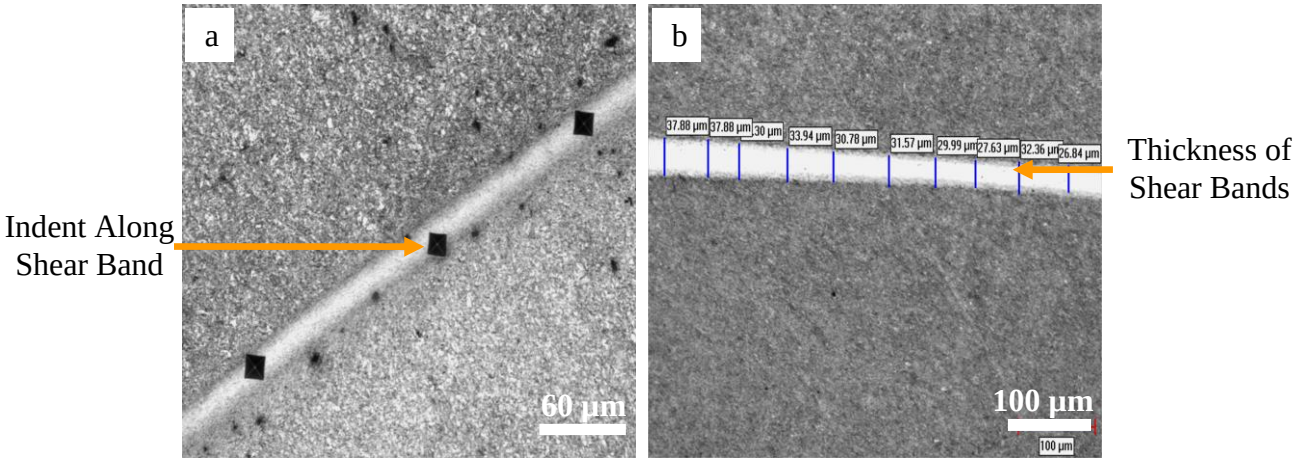

Figure 3- 5: Optical micrographs of (a) indents formed in the shear bands (e) how the thicknesses of the shear bands were measured.

3.3.3.3 X-Ray Diffraction Analyses On the Steel specimens

A Bruker D8 Discover with GADDS and a super speed HI-STAR detector was used to obtain diffraction spectra of the steel specimens prior to impact, after impact and after post-impact annealing. It has a rotating anode, uses copper radiations and is operated at 50kV and 60mA. A 0.5mm collimator was used for the current study on all the steel specimens. Each analysis was performed by collecting three data frames at 2θ positions that overlapped to allow data merging during analysis and an hour for the three frame collections. The three detector positions for the three frames were at 2θ positions of $49^{O}\pm15^{O}$, $74^{O}\pm15^{O}$ and $99^{O}\pm15^{O}$. The specimen to detector distance was 15cm which determined the range across the detector.

3.3.3.4 Specimen Preparation for Transmission/Scanning Transmission Electron Microscopy (TEM/STEM)

Detailed microstructural studies were conducted on the pre-impact and impacted steel specimens using a JEOL 2100F TEM/STEM located at the University of Manitoba and JEOL 2010F located at the Material Research Institute of Pennsylvania State University. Two specimen preparation techniques, standard thin foil preparation using electropolishing and the Focused Ion Beam (FIB) were used to prepare thin foils for TEM/STEM analyses. Details of the two preparation techniques used in this research are outlined in the following subsections.

3.3.3.4.1 Standard Thin Foil Preparation

An electrical discharge machine (EDM) was used to cut 0.5mm circular thin foils of sections perpendicular to the impact direction. The circular thin foils were thinned down mechanically to a thickness of 0.2mm after which 3mm diameter discs were punched out from the 0.2mm thin foils using a Gatan Disc Punch Model 659. The 3mm diameter discs were further thinned down mechanically to 0.08mm before dimpling with a Gatan Dimple Grinder Model 659 to a thickness of 0.03mm in the center. This was followed by electro polishing of the discs in a solution of 10% perchloric acid and ethanol in a Struers Tenupol-3 Jet Polisher at a voltage of 30V and a temperature of $-40^{O}C$. The electrolyte was cooled by passing a liquid nitrogen coolant into the tank. The flow rate of the electrolyte was adjusted to ensure that the jets met at the center of the foil in order to ensure that the foils are not deformed by the jets. As soon as a tiny hole is created in the thin foil, the specimens were removed and rinsed thoroughly in ethanol before proceeding to the TEM for analysis.

3.3.3.4.2 Focused Ion Beam (FIB) Thin Foil Preparation of Shear Bands

The small width of the shear bands renders conventional preparation of thin foil cross sections for transmission electron microscopy (TEM) difficult because the perforation produced using techniques such as double-jet polishing and ion milling generally do not coincide with the shear band area. To better select the shear band regions for preparing thin foils for transmission electron microscopy (TEM) examinations without adding more stresses or distortions, an FEI Quanta 200 3D Dual Beam Focused Ion Beam (FIB) located at the Materials Research Institute of Pennsylvania State University was used to specifically select and prepare 6 shear band regions

for TEM analyses. The FEI Quanta 200 3D Dual Beam Focused Ion Beam (FIB) permits fast, reliable preparation of high-quality, site specific specimens. The basic function of the FIB is imaging and sputtering with an ion beam. Gallium (Ga) ions are used in the FIB column, and their sputtering action enables precise machining of specimens. The ion source type in the FEI Quanta 200 3D Dual Beam Focused Ion Beam (FIB) is a Ga-based blunt needle liquid metal ion source (LMIS). Figure 3-6 shows the orientation of the TEM specimen prepared with respect to the impact direction and shear band normal. The impact direction was parallel to the fibbed surface used for the TEM analysis. Indents were made across the length of the shear bands in order to make the selection of shear band regions more visible and accurate on the FIB/SEM.

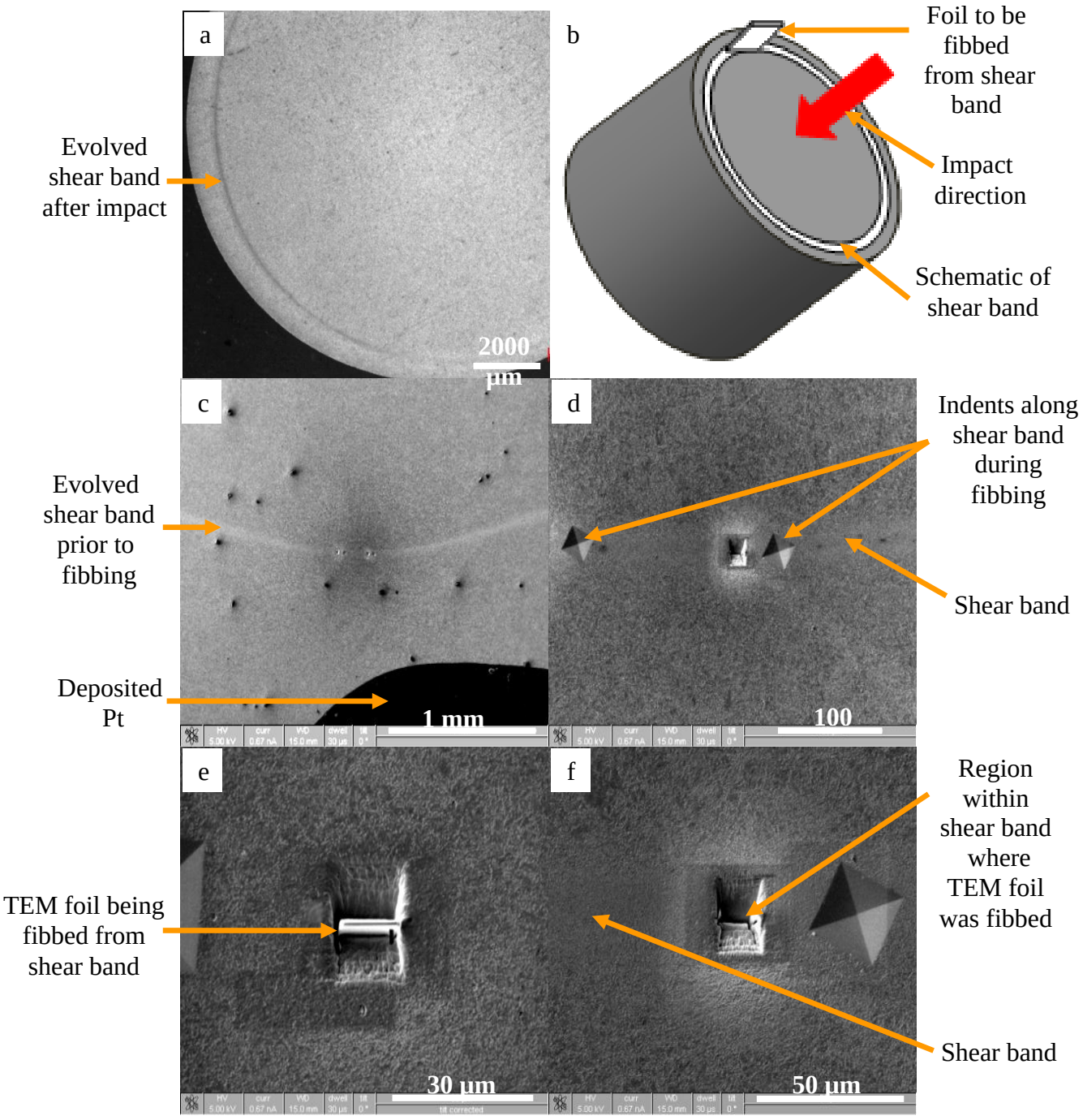

Figure 3- 6: (a) optical micrograph of evolved shear band (b) schematic of impacted specimen showing the impact direction and direction of TEM foil to be fibbed. Secondary Electron Images of (c) shear band prior to fibbing (d) indents along shear band (e) TEM foil during fibbing (f) Region where TEM foil was fibbed.

During operation, Ga flows from a reservoir to the needle tip (with an end radius of about 10 μm), where it is extracted by field emission. A large negative potential between the needle and an extraction electrode generates an electric field of magnitude 10^{10} V/m at the needle tip. The balance between the electrostatic forces and the Ga surface tension wetting the tapered W needle geometry results in the formation of a single Taylor cone at the needle tip. The ion beam column consists of condenser and objective lenses to define the beam and then focus it on the specimen. It also has beam defining apertures that select the beam diameter and current, deflection plates to raster the beam over the specimen surface, stigmation poles to ensure a spherical beam profile, and a high-speed beam blanker to deflect the beam off the specimen onto a beam stop. Focusing and steering are performed using electrostatic components rather than the electromagnetic components used for the electron. The beam that is rastered over the specimen by the FIB instrument is an ion beam rather than electron beam as in the SEM. As the ion beam interacts with the specimen surface, secondary electrons are generated which are used to obtain high-spatial resolution images. Because of the sputtering action of the ion beam, the FIB can be used to locally remove or mill away material.

In the current study, selected 620^{O}C-2hrs tempered steel specimens impacted at 42.6 to 50 kg.m/s were prepared for TEM analysis using the focused ion beam. Due to the dense nature of the steels, while selecting shear band sites for thin foil preparation was easy and accurate, it was not a rapid preparation technique since specimens had to be milled for longer hours. To prepare the specimens using the FEI Quanta 200 3D Dual Beam Focused Ion Beam (FIB), the steel specimen and an omniprobe grid were loaded in a specified holder. The area of the specimen where lift out was to be performed was located and its eucentric height obtained. To protect the

surface of the specimen from any damage during ion milling, a Pt layer was deposited on the surface. An e-beam Pt deposition box (in E-beam image) with dimensions approximately x: 24 μm, y: 4 μm, and z: 20 μm was drawn. With the specimen at zero tilt degree, the Pt needle was inserted and warmed up. The e-beam current was increased to 37nA (maximum current) and the voltage was decreased down to 1kV. The voltage was only increased when it is difficult to focus the image at 1kV. The Pt was then deposited for at least 10 minutes.

A Pt layer is also deposited in I-beam. The specimen was tilted to 52^{O} and a deposition box (in I-beam image) with dimensions approximately x: 12.5 μm, y: 1.5 μm, and z: 20 μm was drawn. Using a 10ρA, the box was aligned directly over the center of the Pt pad. The current was increased to approximately 2-10ρA/μm^2 , thus 0.1nA according to the appropriate deposition rate after pausing the image. A reduced area box in the ion image was opened, moved over a distinguishable feature and the image unpaused. The WD was adjusted to 30mm and the stigmators adjusted till the image was crisp. The reduced area box was closed and a snapshot of the ion image was taken. The deposition box was readjusted so that it was centered over the pt pad. The Pt was deposited until the layer appears to be ~3 μm thick in E-beam image as shown in figure 3-7.

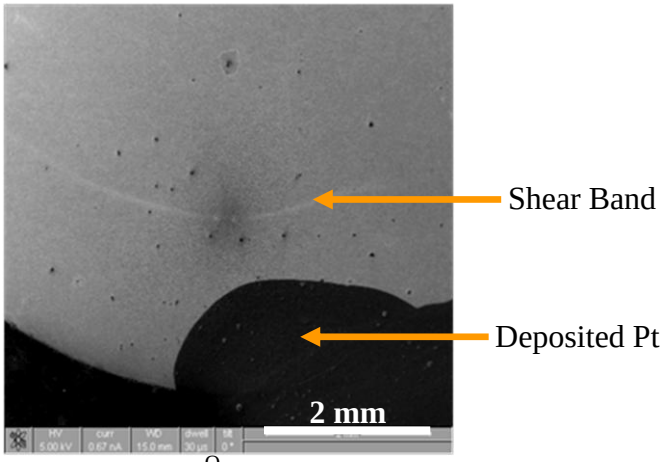

Figure 3- 7: Deposited Pt on an impacted 620^{O}C-2hrs tempered steel specimen during fibbing.

Due to the dense nature of the steel, a pre-made cross section pattern of 20 nA was used. The ion image was paused and the current was changed to 20 nA. A reduced area box was opened in the ion image, moved over a distinguishable feature and the image was unpaused and the stigmators adjusted until the image was crisp. The area box was closed and a snapshot of the ion image was taken. The patterns were aligned by selecting both cross section boxes and moved so that they were equal distance from the Pt strip. The z-dimension was changed to 7 µm. Milling of the pattern was started and refreshed every few seconds in E-beam image. The milling continued until the pattern appears black in E-beam even after increasing contrast.

To clean the cross section for the first time, a pre-made cross section pattern of 7 nA was used due to the dense nature and the slow mill-rate of the steel. The ion image was paused and the current was changed to 7 nA. A reduced area box was opened in the ion image, moved over a distinguishable feature and the image was unpaused and the stigmators adjusted until the image was crisp. The area box was closed and a snapshot of the ion image was taken. The patterns were aligned by selecting both cross section boxes and moved so that they were equal distance

from the Pt strip. The z-dimension of the pattern was changed to 1.5 μm (1/3 of the previous z value). The y-dimension was adjusted until the cross section extended into the already milled holes. Patterning was started and ran until it was finished.

A pre-made cross section pattern of 3 nA was used for the second cleaning. The ion image was paused and the current was changed to 3 nA. A reduced area box was opened in the ion image, moved over a distinguishable feature and the image was unpaused and the stigmators adjusted until the image was crisp. The area box was closed and a snapshot of the ion image was taken. The patterns were aligned by selecting both cross section boxes and moved so that they were equal distance from the Pt strip. The z-dimension of the pattern was changed to 1.5-2 μm because the steel was not milling quickly. The y-dimension was adjusted until the cross section extended into the already milled holes. Patterning was started and ran until it was finished.

To cut out the cross section, the stage was then tilted from 52^{O} to 7^{O}. With ion quad selected, the scan rotation was adjusted to 180^{O}. The shift in E-beam and I-beam were adjusted so that liftout specimen was in the center of both images. A pre-made 3 nA cutout pattern was selected and adjusted to fit the liftout specimen accordingly. The z-dimension of the pattern was changed to ~4 μm. Patterning was started till the specimen was milled though as shown in figure 3-8.

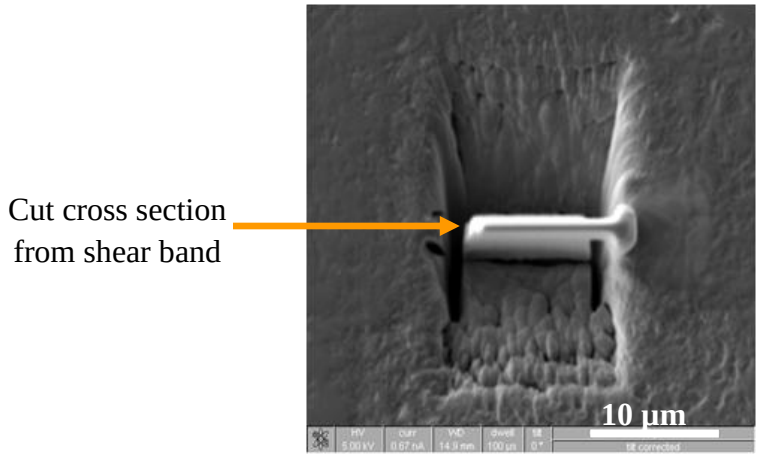

Figure 3- 8: A cut cross section from shear band prior to lift out in an impacted 620^{O}C-2hrs tempered steel specimen during fibbing.

To attach the omniprobe, the stage was moved back to a zero tilt. The ion beam current was decreased to 30 pA for safer imaging. The Pt deposition needle was inserted followed by the Omniprobe. Using Omniprobe control program on a support computer, the probe was lowered to the edge of the specimen. Due to the stage orientation, movement in z was visible in the ion image and movement in x-y was visible in the electron image. Once the omniprobe was touching the top edge of the specimen, the ion beam Pt deposition (x = y = z = 1.5 µm) was attached. If omniprobe does not appear attached, more Pt was deposited until it was attached. To lift the fibbed specimen out, the section of the foil that was still attached to the bulk specimen was cut. A rectangle with x=700 nm, and z= 2 µm was drawn with the y adjusted accordingly. The rectangle was positioned and rotated until it covered the piece of material attaching the specimen. The ion image was paused and the current was changed to 0.3 nA. A reduced area box was opened in the ion image, moved over a distinguishable feature and the image was unpaused and the stigmators adjusted until the image was crisp. The area box was closed and a snapshot of the ion image was taken to ensure that the milling rectangle was properly positioned. Milling was

started, and the ion image was refreshed until the material was free. The free specimen was then lifted out by increasing the z in the omniprobe software. Once the specimen was lifted out, the omniprobe was moved to park and taken out of the chamber. The Pt needle was then taken out of the chamber as well. Figure 3-9 shows the procedure for lift out.

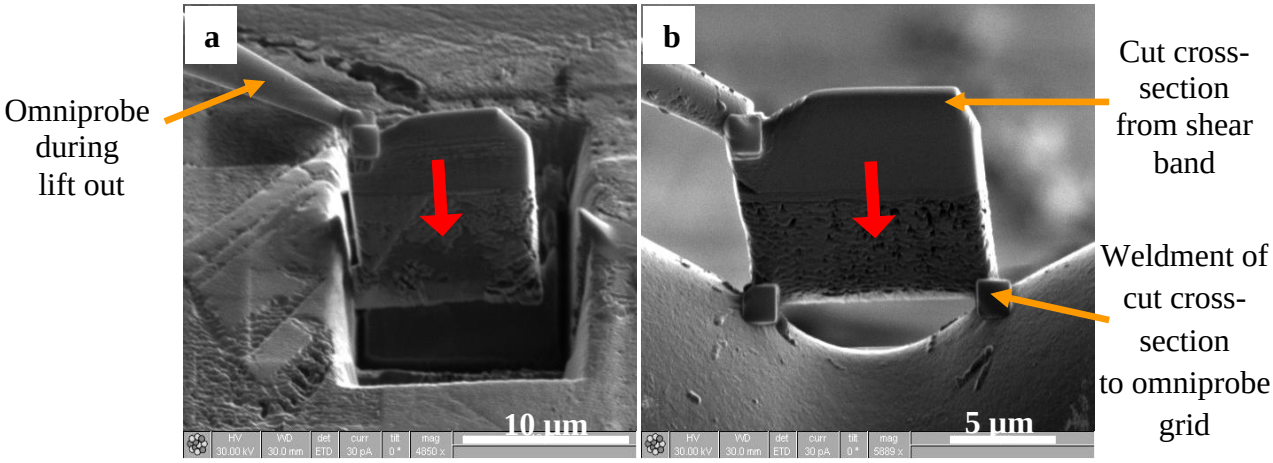

Figure 3- 9: (a) Specimen lift out by omniprobe (b) specimen weld to omniprobe grid.

To attach the specimen to the Tem grid, the TEM grid was moved on the specimen in the chamber. The xt align feature was used so that the grid was horizontal in the E-beam image with rounded edge on top. The eucentric point was located, and the Pt needle was reinserted followed by the omniprobe. The Omniprobe was lowered towards the grid and once the specimen touches the grid, deposit Pt to adhere it to grid using 30 pA. Once attached, the omniprobe was cut off using an ion current of 1.0 nA. Once the Omniprobe was released, it was moved to park and out of the chamber followed by the Pt needle. Figure 3-10 shows the final specimen for TEM analysis.

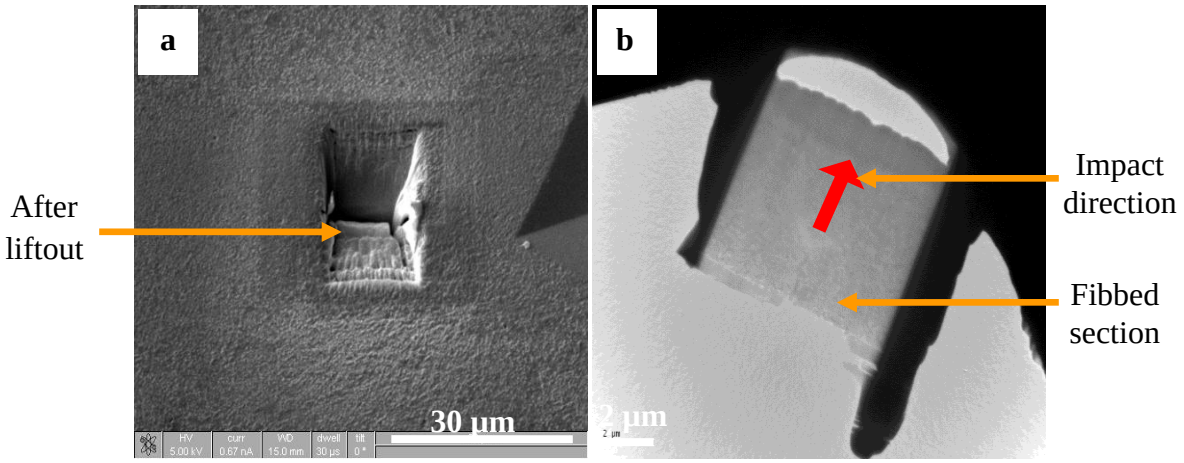

Figure 3- 10: (a) Bulk specimen after lift out (b) specimen welded to omniprobe for TEM analysis.

To clean the cross sections using 1.0 nA, the xt align was used to adjust the specimen to be horizontal and then it was tiled to 52^{O}. The scan rotation in the ion image was changed to 0^{O}. The specimen was then tilted and cleaning cross section was drawn by setting z to 1 µm, adjusting x so that cross section covers length of specimen inside of Pt grips and adjusting y so that cross section covered the entire width of the specimen. A reference E-beam image in Quad 3 was taken and cleaning begun. The E-beam image was frequently refreshed and the patterning stopped when Pt layer begun depleting. The relative tilt was changed back to 0^{O}, the specimen was rotated 180^{O} (compucentric) and the other side cleaned using the same procedure. The same procedure was used to clean the cross sections at 0.3 nA and 0.1 nA by using the appropriate offset angles and 0.3 nA and 0.1 nA ion beam currents respectively. The specimen was always rotated in order to clean both sides until brighter areas appear on the specimen after cleaning at 0.1 nA indicating electron transparency. The final cleaning was done with an accelerating voltage of 5 kV and a current of 29 ρA. The tilt angle was corrected and a rectangular cross section drawn over the entire specimen. Milling was started while monitoring the E-beam image.

The milling was stopped when the entire Pt had been removed. The specimen was rotated 180^{O}, the tilt angle corrected and the milling continued. The milling was stopped when the appearance of the specimen changes in the E-beam image. The specimen is returned to zero degree tilt, the chamber vented and the specimen removed. This was followed by TEM examinations. A summary of the fibbing procedure is shown in figure 3-11.

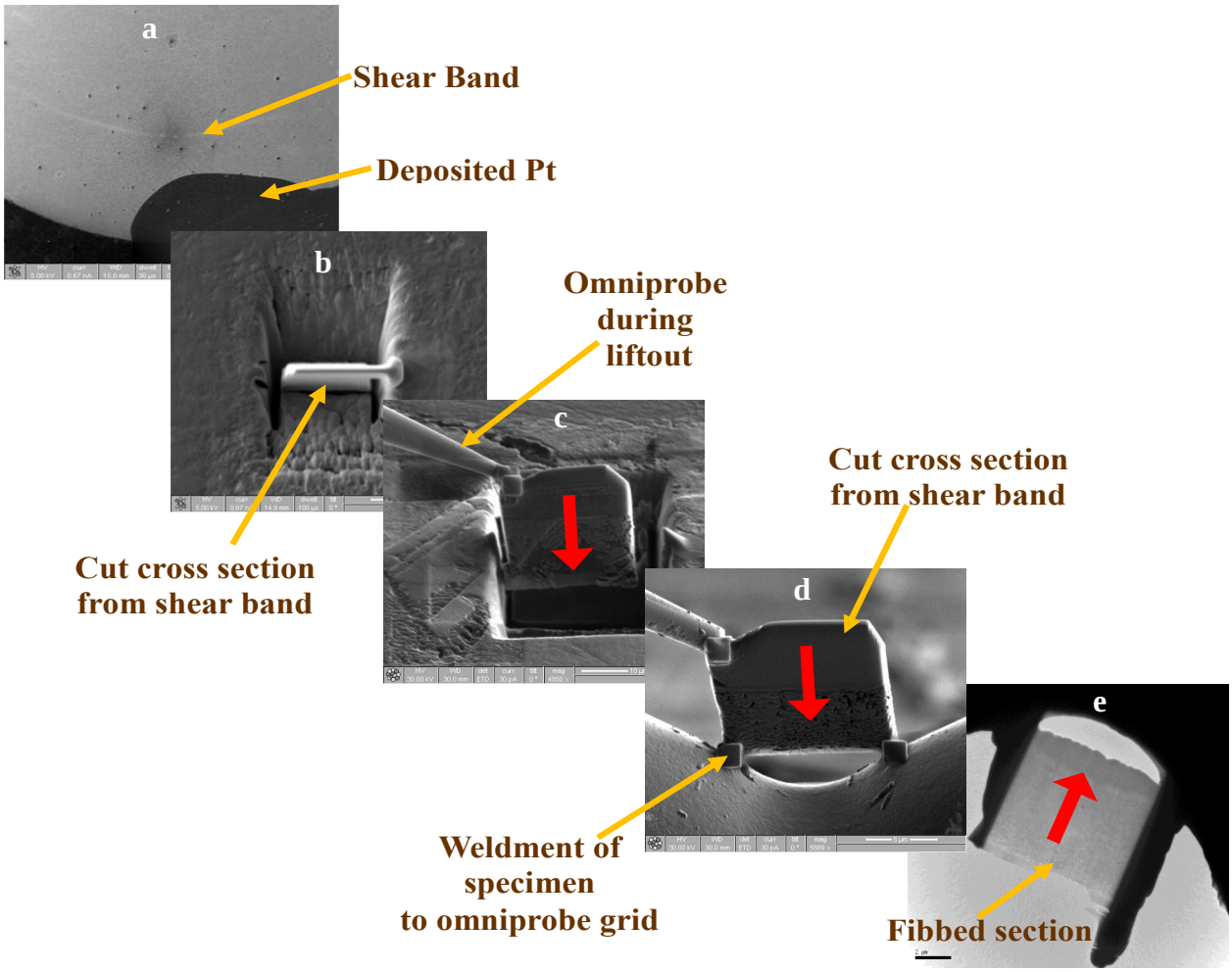

Figure 3- 11: Typical images showing the stages during fibbing prior to TEM analysis. Big arrows show the direction of impact relative to the TEM foil.

3.4 Analysis of Selected Area Diffraction Patterns and Geometric Phase Analysis

Electron diffraction analysis was performed to verify the crystal structures of the specimens. Selected Area Diffraction Patterns (SADPs) were obtained from different zone axes and analyzed. Gatan digital micrograph software, DM3, was used to take the images and diffraction patterns in DM3® format in order to directly measure the d-spacing and angles between different planes. During the analysis, all the d-spacings of the different diffraction patterns and angles between the different planes were measured. A MATLAB® code was written which calculated the d-spacing and the angles between planes for the different crystal structures. This program was used to confirm the measured d-spacings and angles between the different planes on the diffraction patterns. The diffraction patterns were indexed and then simulated using EDA® software and web-EMAPS® to confirm the indexed diffraction patterns and their respective zones axes.

Geometric Phase Analysis (GPA) was used to analyze High Resolution Transmission Electron Microscope (HRTEM) images of regions within the evolved ASBs. GPA is a technique developed by Hÿtch [104] and coworkers [105-106] for mapping crystallographic lattice displacements and strain fields from typical HRTEM images. The presence of strong Bragg-reflections which characterizes an HRTEM lattice image in its Fourier transform are related to the 2-Dimensional unit cell that describes the projected crystalline structure [105, 107]. GPA, based on centering a small aperture on a strong reflection in the Fourier transform of an HRTEM lattice image, and finding its inverse Fourier transform, has been shown to provide information on local displacements of crystallographic lattice planes and two dimensional displacement fields [104-106]. It has been shown that the selection of two non-collinear reciprocal lattice vectors in the Fourier transform indirectly defines a 2-D lattice in the HRTEM image to which all

variations can be referred [105-106]. Quantitative measure of the two-dimensional strain tensors for each point in the field of view of the image can be obtained [104, 106, 108].

The basic assumption of the GPA technique is that the lattice fringes in the experimental image should not be displaced by the imperfect contrast transfer of the TEM [106, 108]. In addition, Hÿtch and Plamann [106] assumed that the specimen should have inversion symmetry (centrosymmetric structures). Technically, the recorded HRTEM image should include a localized strained area (deformed configuration) and an unstrained region (perfect-crystal reference area). However, it has been shown that strain gradients break inversion symmetry and GPA of structures with rapidly varying displacement fields produces error implications [106, 108]. Thus, the strained and the unstrained regions should have slowly varying displacement fields. However, a single HRTEM image of a shear band region and a region outside the shear band would have rapidly varying displacement fields because of strain localization within the ASBs which would break inversion symmetry. For these reasons, separate GPA was performed for images taken from carbides, and ferrite matrix in the specimens prior to impact and compared with GPA from regions within evolved ASBs after impact. GPA of the experimental HRTEM images was accomplished using the software tool, STEM_CELL, which uses routines for data analysis and image processing recently developed by Grillo et al. [109-110]. DiffTools from DigitalMicrograph® was used to analyze the HRTEM images by calculating and analyzing the FFTs and Inverse FFTs from the entire images [107].

The use of these techniques and equipment provide comprehensive description of the possible sites within the pre-impact specimen for the initiation of ASBs and to determine the changes in the microstructure after impact and the mechanism of evolution of ASBs in 4340 steel.

CHAPTER 4
EXPERIMENTAL RESULTS

4. Introduction

The results from the current study are presented in this chapter. The chapter is made up of three main sections, 4.1 to 4.3. Section 4.1 presents the results of microstructural analysis on the pre-impact steel specimens. It identifies the morphology and the constituents of the original microstructure prior to impact. Section 4.2 documents the response of the tempered steel specimens to impact, the presence and properties of observed ASBs within the impacted specimens. Section 4.3 presents a comprehensive microstructural analysis of regions within and outside the evolved ASBs and how the original microstructure has been altered due to the passage of the stress waves through the specimens. This section also presents the microstructure that evolves during post-impact annealing heat treatments.

4.1 Initial Microstructure of Tempered Steel Specimens Prior to Impact

To establish a basis for comparison with the microstructure of the impacted steel specimens, the pre-impact specimens were thoroughly studied using Optical Microscopy (OM), Scanning Electron Microscopy (SEM), Transmission Electron Microscopy (TEM), Scanning Transmission Electron Microscopy (STEM), High Resolution Transmission Electron Microscopy (HRTEM), X-Ray Diffraction (XRD) and Electron Probe Microanalyzer (EPMA). This section presents the results of the microstructural analysis on the pre-impact steel specimens. The section consists of six subsections, 4.1.1 to 4.1.6. Section 4.1.1 analyzes the microstructure of the steel specimens after austenitization and rapid quenching prior to tempering. Section 4.1.2, 4.1.3, and 4.1.4 presents the detailed microstructure of the pre-impact steel specimens in the 315^{O}C-1hr

tempered, 425^{O}C-1hr tempered and 620^{O}C-2hrs tempered groups respectively. Section 4.1.5 and 4.1.6 presents the XRD and EPMA analyses of the pre-impact specimens.

4.1.1 Microstructure of the As-quenched Specimen Prior to Tempering

The morphology of the machined as-received specimens prior to heat treatment consisted of spheroidized carbides in a ferrite matrix as shown in the Backscattered Electron (BSE) micrograph in figure 4-1(a). This is due to the high temperature used in rolling the steel bars during processing. The microstructure of the as-quenched specimen was studied prior to tempering as a baseline for comparison with the microstructure that evolves after tempering. Figure 4-1(b) shows the BSE micrograph of the as-quenched martensite prior to tempering while figure 4-1(c) to (f) shows TEM/STEM micrographs of the as-quenched martensite. Typically, the as-quenched martensite consisted of lath structural units (martensite laths) oriented parallel to each other within groups generally referred to as packets. The martensite laths within a packet were separated by low angle boundaries and dense dislocations producing the dark contrast as shown in figure 4-1(c) and (d). The packets were separated by high angle boundaries as shown in figure 4-1(e). The average width of the martensite laths in the as-quenched specimen prior to tempering was 155nm.

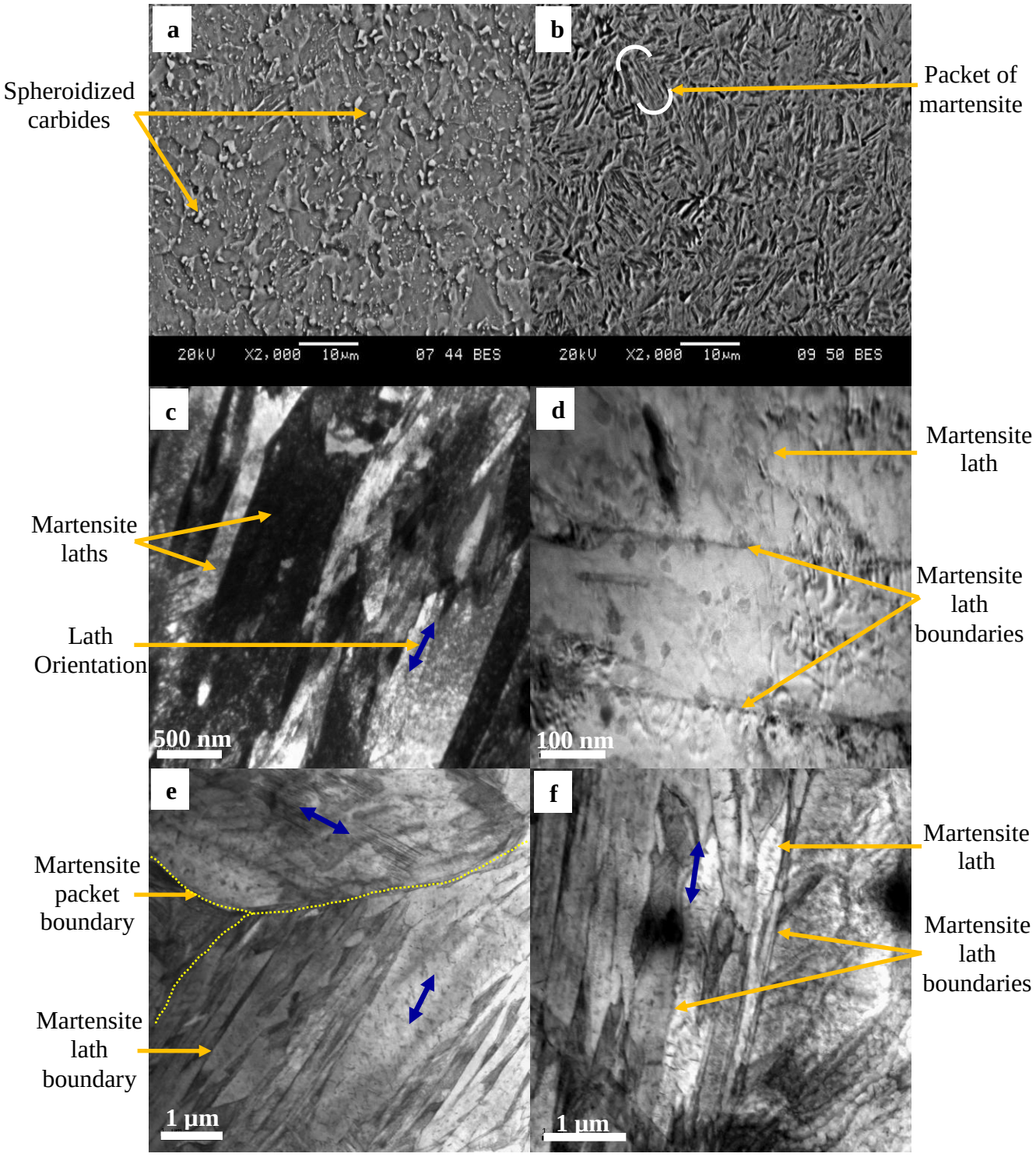

Figure 4-1: SEM micrographs of (a) as-received specimen (b) as-quenched martensite. TEM Bright Field (BF) micrographs of (c) martensite laths (d) martensite laths and lath boundaries. STEM micrographs of (e) martensite lath and packet boundaries (f) martensite lath boundaries.

The dense dislocations which produce the dark contrast were evident under 2-Beam conditions as shown in figure 4-2(a) and (b). Most of the dislocations were concentrated on the martensite lath and packet boundaries. Analysis of Selected Area Diffraction Patterns (SADPs) confirmed that the martensite laths had Body-Centered Tetragonal (BCT) crystal structures as shown on figure 4-2(c) to (f) close to the [-311], [-3-31], [11-1] and [-2-20] zone axes respectively. The martensitic transformation is a diffusionless shear transformation process which produces dislocations that remain in the structure when the transformation is complete [72-74, 78]. During the rapid cooling or quenching, all the carbon atoms that were dissolved in the Face-Centered Cubic (FCC) austenite are retained and trapped in the octahedral sites of the Body-Centered Cubic (BCC) structure stretching the BCC crystal structure into a BCT crystal [73, 78]. The distortions in the BCT crystal structure of martensite results in a high amount of dislocations and high internal stresses [72-74, 78]. These dislocations make martensitic structures extremely hard and brittle.

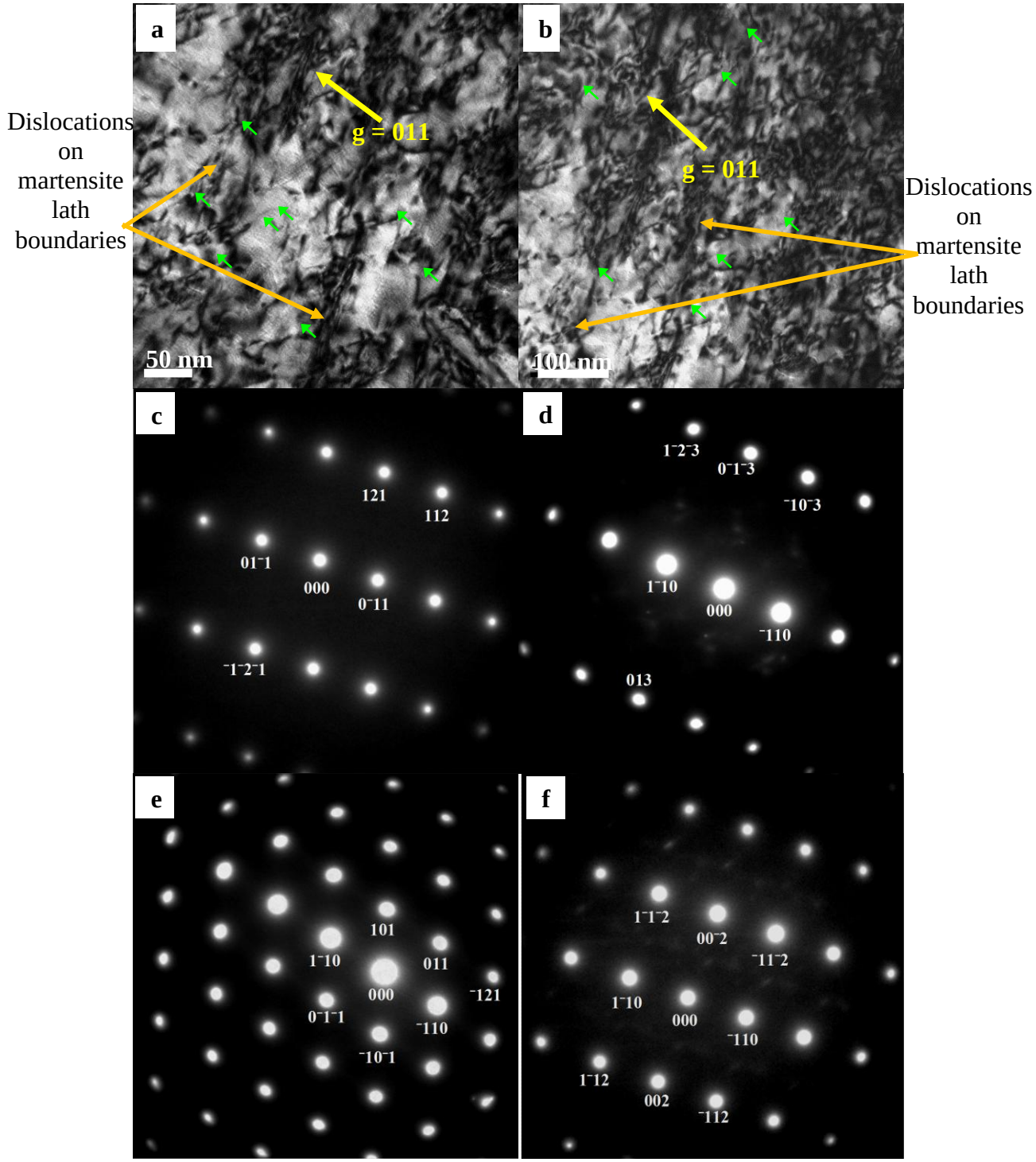

Figure 4- 2: (a), (b) TEM micrographs in 2-Beam conditions of the as-quenched martensite showing dislocations and dislocation networks within and along the lath boundaries. SADPs of the lath martensite close to the (c) [-311] (d) [-3-31] (e) [11-1] and (f) [-2-20] zone axes.

4.1.2 Microstructure of the 315^{O}C-1hr Tempered Specimens Prior to Impact

Twenty as-quenched specimens were tempered at 315^{O}C for 1 hour followed by air cooling to produce a tempered martensite structure. The specimens in this group were labeled 315^{O}C-1hr tempered specimens. The morphology of the tempered specimens consisted of thin precipitated platelet and spherical carbides immersed in lath matrix as shown in figure 4-3. With the exception of the precipitated carbides, the tempered microstructure was comparable to the as-quenched martensite but with larger packets and lath structures. Carbon atoms dispersed in the as-quenched martensite form carbide precipitates of increasing size during tempering [72-73, 78]. Thus, carbon atoms are able to diffuse out of the martensitic structure by forming carbide precipitates. The average width of the individual lath units (lath matrix) was 209nm, representing approximately a 35% increase in size compared to the widths of the as-quenched specimens. The growth in lath sizes during tempering is attributed to the movement of lath boundaries and the elimination of lath boundaries due to the movement and/or annihilation of dislocations at the boundaries [76]. The precipitated platelet carbides were distributed within the lath matrix (intralath platelet carbides) and along the lath/packet boundaries (interlath platelet carbides) as shown in figure 4-3(c) to (e). The average length and width of the intralath platelet carbides were 214nm and 32nm respectively representing an aspect ratio of 6.7. The average width of the interlath platelet carbides was 41nm. The platelet carbides were rich in Carbon (C) and Iron (Fe) as shown by the Electron Energy Loss Spectroscopy (EELS) in figure 4-3(f).

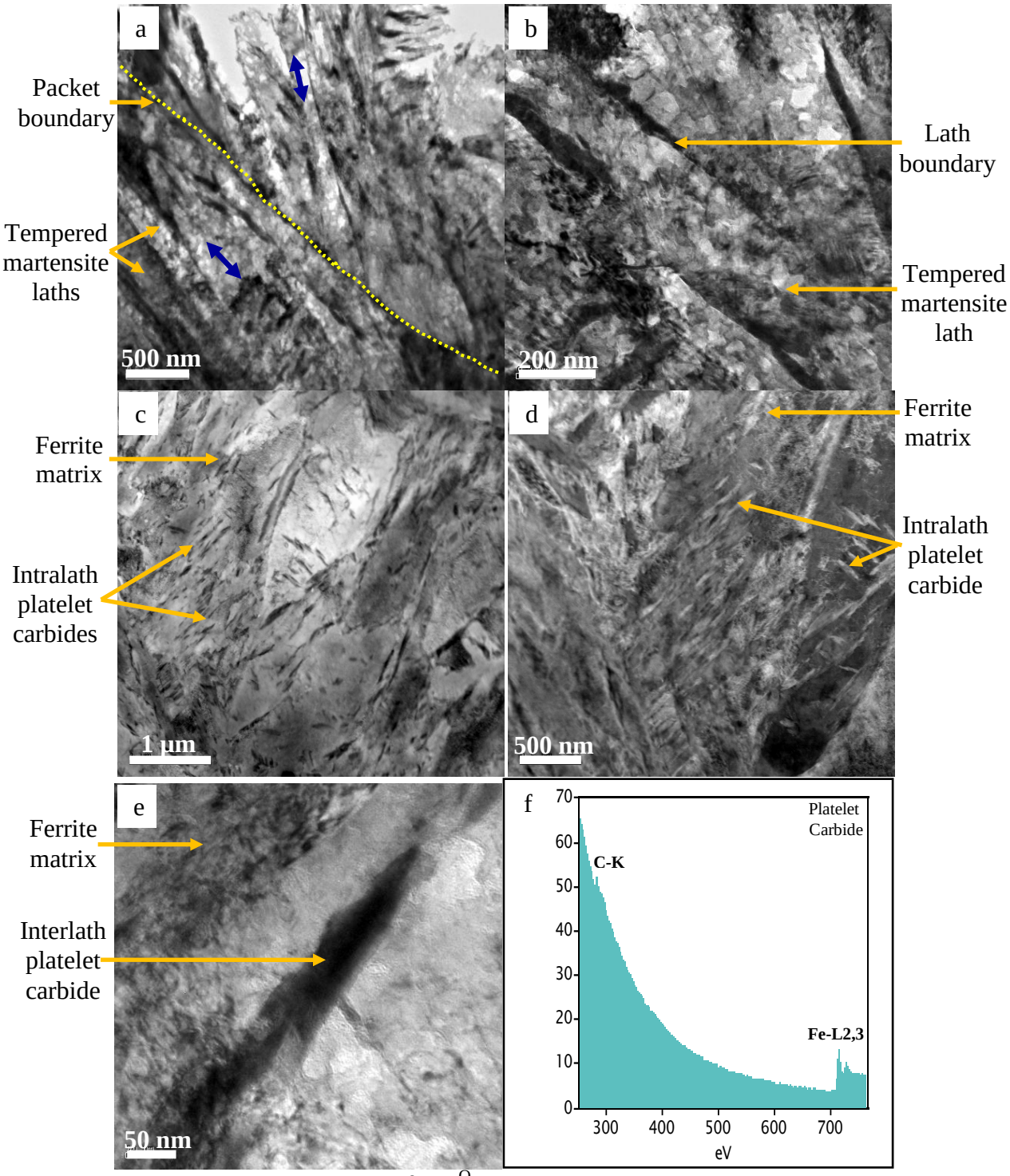

Figure 4- 3: TEM BF micrographs of 315^{O}C-1hr tempered specimen showing (a) martensite laths and packet boundary (b) tempered martensite lath and lath boundary. (c) STEM micrograph of platelet carbides (d) High Angle Annular Dark Field (HAADF) micrograph of platelet carbides (e) TEM BF of platelet carbides on lath boundary (f) EELS of the platelet carbides.

Even though the platelet carbides were predominant within the tempered structure, the spherical carbides were relatively larger with an average diameter of 299nm as shown in figure 4-4(a) and (b). Analysis of SADPs of the spherical carbides confirmed that they were typical M_3C (M=Cr, Fe) carbides with orthorhombic crystal structure as shown by the SADP in figure 4-4(c) close to the [001] zone axis. EELS on the M_3C spherical carbides revealed that they were rich in Chromium (Cr), Iron (Fe) and Carbon (C) as shown in figure 4-4(d). Analysis of the lath matrix confirmed that the matrix was ferrite with a BCC crystal structure as indicated by the SADPs in figure 4-4(e) and (f) close to the [011] and [311] zone axes respectively.

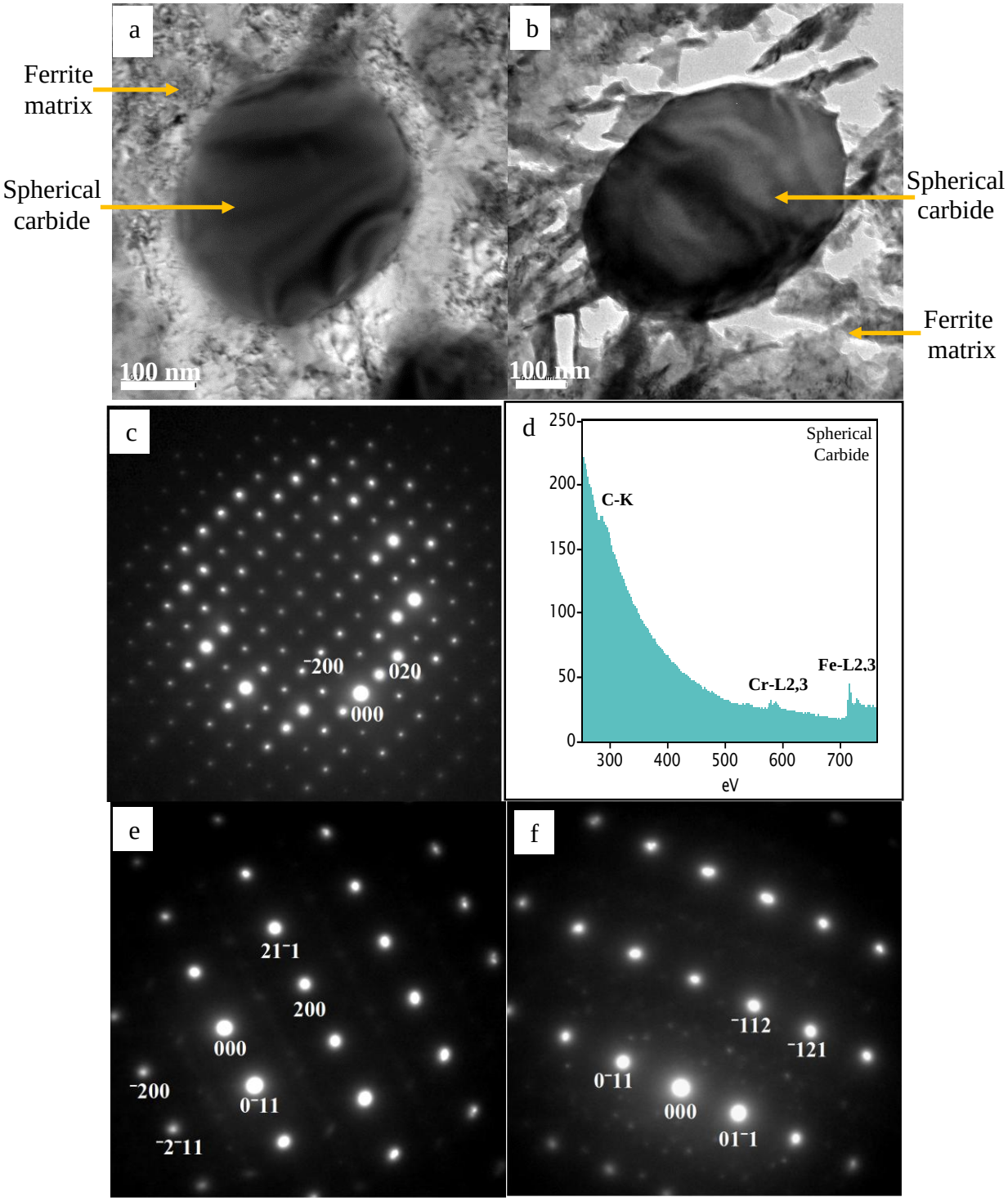

Figure 4- 4: (a), (b) TEM BF micrographs showing spherical carbides (c) SADP of spherical carbide close to the [001] zone axis (d) EELS on the spherical carbide. SADPs of the ferrite matrix close to the (e) [011] and (f) [311] zone axes in the 315^{O}C-1hr tempered steel specimens.

The metastable phase martensite, present because carbon diffusion has been suppressed by the rapid cooling or quenching, breaks down into a mixture of ferrite and cementite when the martensite is heated to a temperature where the carbon atoms gain mobility and diffuse out of the octahedral sites of the BCT structure [73-76]. During tempering, some of the pre-existing dislocations within the as-quenched martensite structure are annihilated. However, most of the dislocations still remain in the tempered structure as shown by figure 4-5 due to the associated tempering temperature and time. The interlath and intralath platelet carbides within the tempered specimen were surrounded by relatively high density of dislocations as shown in figure 4-5(a) and (b). However, the lath matrix (ferrite) was relatively not highly dislocated when compared to the boundaries and regions around the precipitated carbides as shown by figure 4-5(c) and (d). Tempering reduces the density of the pre-existing dislocations and residual stresses associated with the martensitic structure. This was established based on the reduction in microhardness of the tempered specimens and the appearance of the observed microstructures. However, presence of the pre-existing dislocations within the tempered specimens demonstrates that the microstructure retains most of the dislocations and residual stresses that were introduced into the specimens during the rapid quenching prior to tempering.

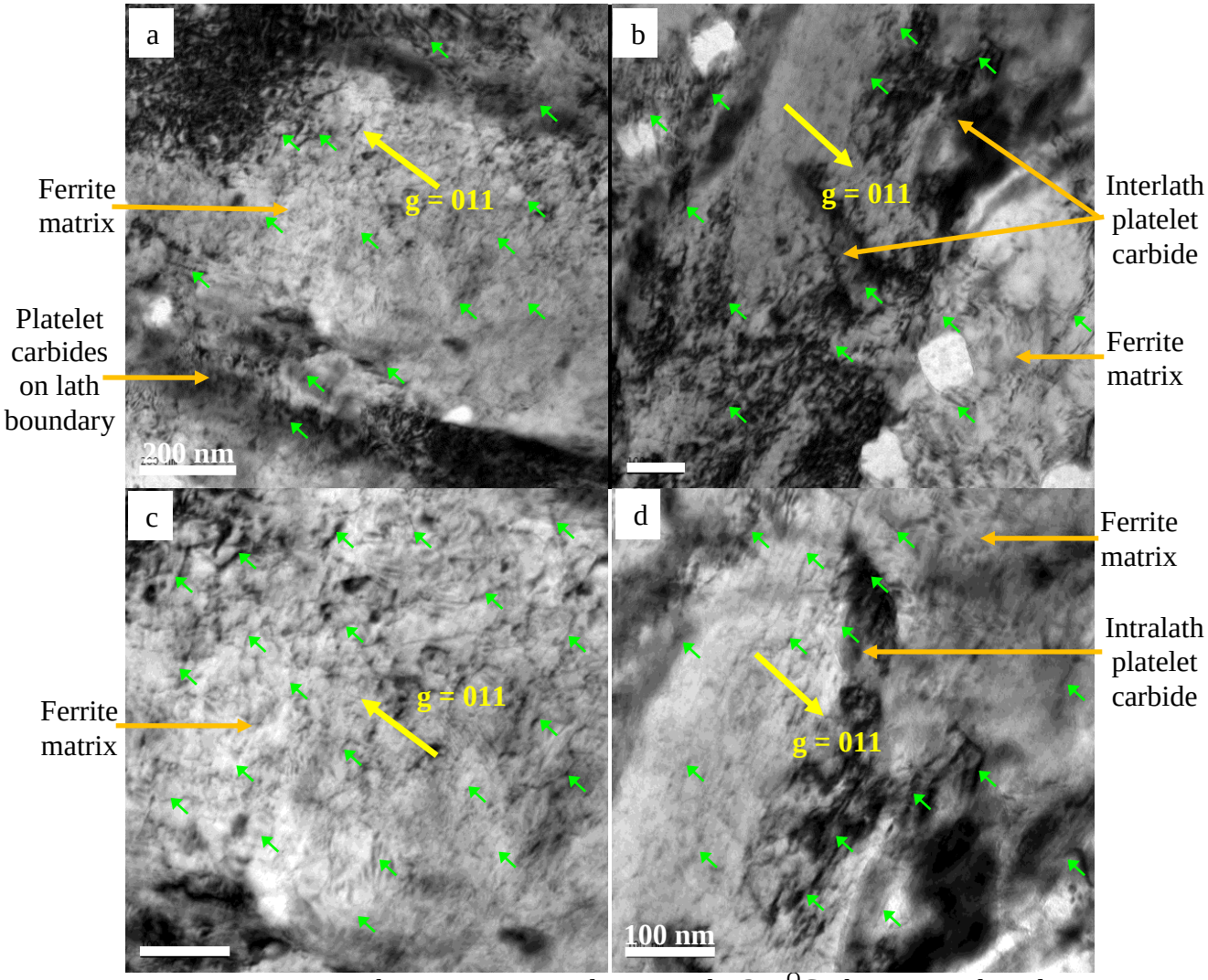

Figure 4- 5: TEM micrographs in 2-Beam conditions in the 315^{O}C-1hr tempered steel specimens showing dislocations (a) around platelet carbides on lath boundaries (b) around platelet carbides on lath boundaries and within ferrite matrix (c) within ferrite matrix (d) around platelet carbides within ferrite matrix.

High Resolution Transmission Electron Microscopy (HRTEM) micrographs of the precipitated spherical and platelet carbides are shown in figure 4-6(a) and (b) respectively. It was observed that the carbides were surrounded by thin boundary layers with an average thickness of 8nm as shown in figure 4-6(c)-(d). Tilting the carbides to different zone axes confirmed the existence of

the boundary layers and revealed that the boundary layers were not overlapping regions between the matrix and the carbides. The existence of the boundary layers around the carbides creates two distinct misfit interfaces: the 1st and 2nd interfaces. The 1st misfit interface is the interface between the carbide and the boundary layer while the 2nd misfit interface is between the boundary layer and the ferrite matrix as shown in figure 4-6(c)-(d). Further analysis on the boundary layers revealed that their atomic columns were almost randomly arranged as shown by the HRTEMs in figure 4-6(f) when compared to the carbides and the ferrite matrix. Figure 4-6(h), (i) and (j) are the Fast Fourier Transforms (FFTs) of the ferrite matrix in 4-6(e), the boundary layer in 4-6(f) and the carbide in 4-6(g) respectively. The loss of lattice fringes in the HRTEM images demonstrates the disorder in the arrangement of the atomic columns within the boundary layers. During the preliminary stages of tempering, carbon atoms segregate to various defects in the microstructure, martensite is converted to a low carbon martensite, and transition carbides are formed [73-78]. The structural changes that occur are thermally activated and dependent on both temperature/time. When the martensite is heated to a temperature where the interstitial carbon atoms gain mobility, atom-by-atom transfer across interfaces occurs. In this study, it is inferred that the boundary layer is a diffusion barrier across which the atomic transfers occur. The random arrangement of atomic columns that exists within the diffusion barriers may reduce by increasing the tempering temperature and/or time. This increases the size of the precipitated carbides because of the associated increase in diffusion rate when the tempering temperature/time is increased. The random arrangement of the atomic columns creates high density of local defects within the boundary layers. The presence of the two misfit interfaces in addition to the high density of local defects within the boundary layers accounts for the observed dislocations around the carbide/ferrite interfaces as was shown in figure 4-5.

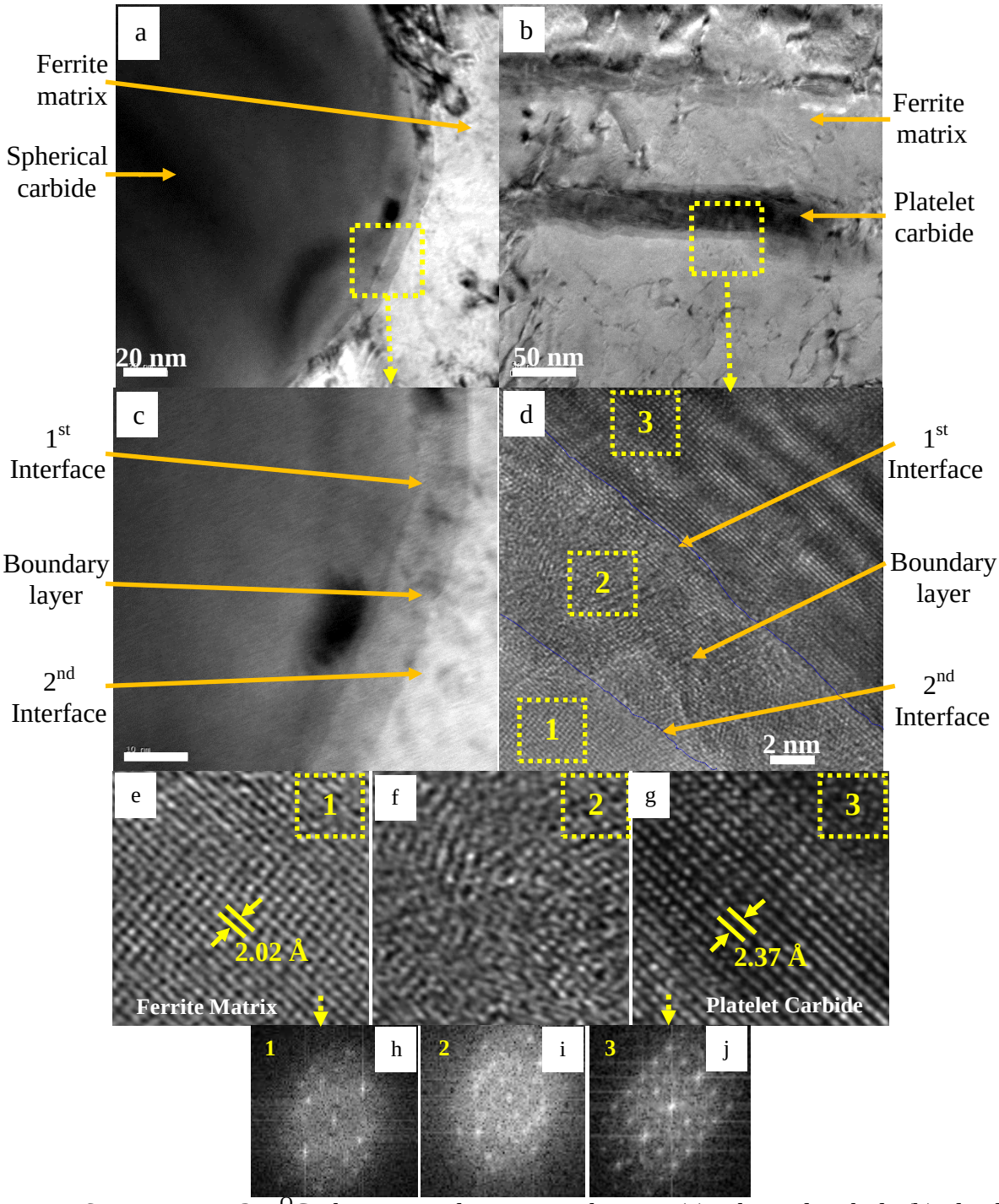

Figure 4- 6: HRTEM in 315^{O}C-1hr tempered specimen showing (a) spherical carbide (b) platelet carbide (c) spherical carbide showing the 1st and 2nd interfaces (d) platelet carbide showing the 1st and 2nd interfaces (e) ferrite matrix (f) boundary layer (g) platelet carbide. (h), (i), (j) are FFTs of (e), (f), and (g) respectively.

4.1.3 Microstructure of the 425^{O}C-1hr Tempered Specimens Prior to Impact

The microstructure of the specimens within this group were comparable to the structure in the 315^{O}C-1hr tempered specimens except the difference in the sizes of the precipitated carbides, lath matrix, and the relative distribution density of the carbides as shown in figure 4-7. The average width of the lath matrix in the 425^{O}C-1hr tempered specimens was 238 representing approximately a 14% increase in size compared to the widths of the lath matrix in the 315^{O}C-1hr tempered specimens. The intralath platelet carbides were 181nm in length and 50nm in width representing an approximate aspect ratio of 3.6. This corresponds to a 46% reduction in aspect ratio of the intralath platelet carbides when compared to those within the 315^{O}C-1hr tempered specimens. Nonetheless, the intralath platelet carbides in the 425^{O}C-1hr tempered specimens were shorter but wider (approximate 2D surface area of 9050nm^2) while the 315^{O}C-1hr tempered specimens were longer but thinner (approximate 2D surface area of 6848 nm^2). The shorter/wider intralath platelet carbides were sparsely distributed within the matrix when compared to the distribution of the longer/thinner carbides in the 315^{O}C-1hr tempered specimens. Additionally, the average width of the interlath platelet carbide was 46nm representing a 12% increase in size when compared to the width of the interlath platelet carbides in the 315^{O}C-1hr tempered specimens. Thus, the increased tempering temperature for the specimens in this group resulted in increase in the size of the lath matrix and the precipitated carbides and a reduction in the distribution density of the carbides within the matrix. The platelet carbides were rich in Carbon (C) and Iron (Fe) as shown by the EELS in figure 4-7(f).

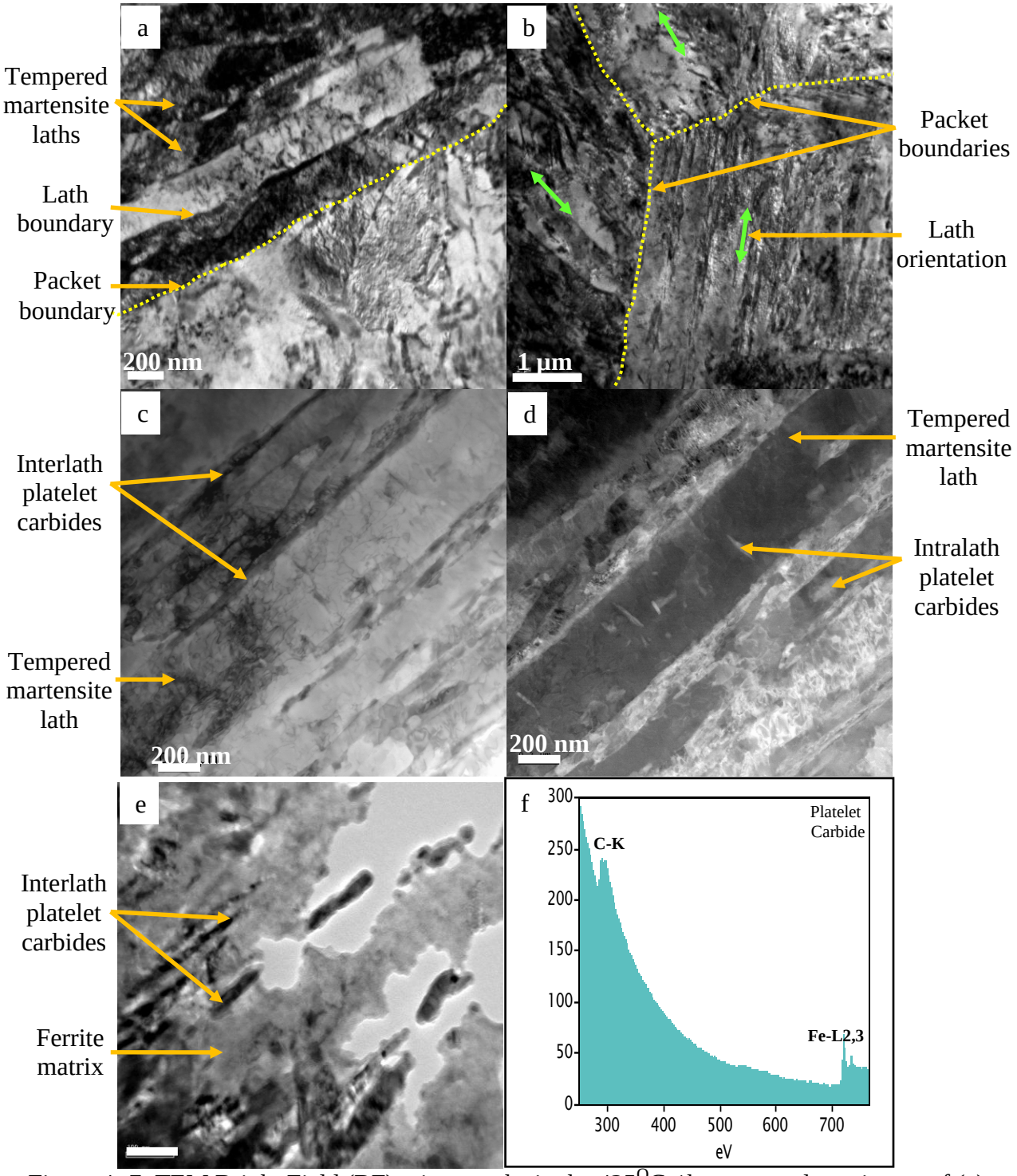

Figure 4- 7: TEM Bright Field (BF) micrographs in the 425^{O}C-1hr tempered specimens of (a) tempered martensite laths and lath/packet boundaries (b) packet boundaries (c) STEM micrograph of platelet carbides on lath boundaries (d) HAADF micrograph of platelet carbides (e) TEM BF of platelet carbides on lath boundaries (f) EELS of platelet carbides.

Larger spherical carbides with an average diameter of 376nm were observed within the tempered specimens in this group as shown in figure 4-8(a) and (b). This represents approximately a 26% increase in size when compared to the diameter of the spherical carbides in the 315^{O}C-1hr tempered specimens. EELS analysis on the spherical carbides indicated that they were rich in Chromium (Cr), Iron (Fe) and Carbon (C) as shown in figure 4-8(c). SADPs of the spherical carbides confirmed that they were typical M_3C (M=Cr, Fe) carbides with an orthorhombic crystal structure as shown in figure 4-8(d) to (f) close to the [-220], [-420] and [31-1] zone axes. It is concluded that the precipitation of the spherical carbides occurs after the platelet carbides are fully developed and concentrated in the ferrite matrix. In addition, increasing the tempering temperature increases the precipitation of the spherical M_3C carbides. Again, the microstructure of the specimens within this group was also decorated with high density of dislocations as shown by the 2-Beam conditions and the STEM micrographs in figure 4-9. The regions surrounding the precipitated carbides were decorated with relatively higher densities of dislocations when compared to the regions within the ferrite matrix. Moreover, the dislocations appeared to be emanating from the carbides and the lath boundaries into the matrix as shown by figure 4-9(e) and (f).

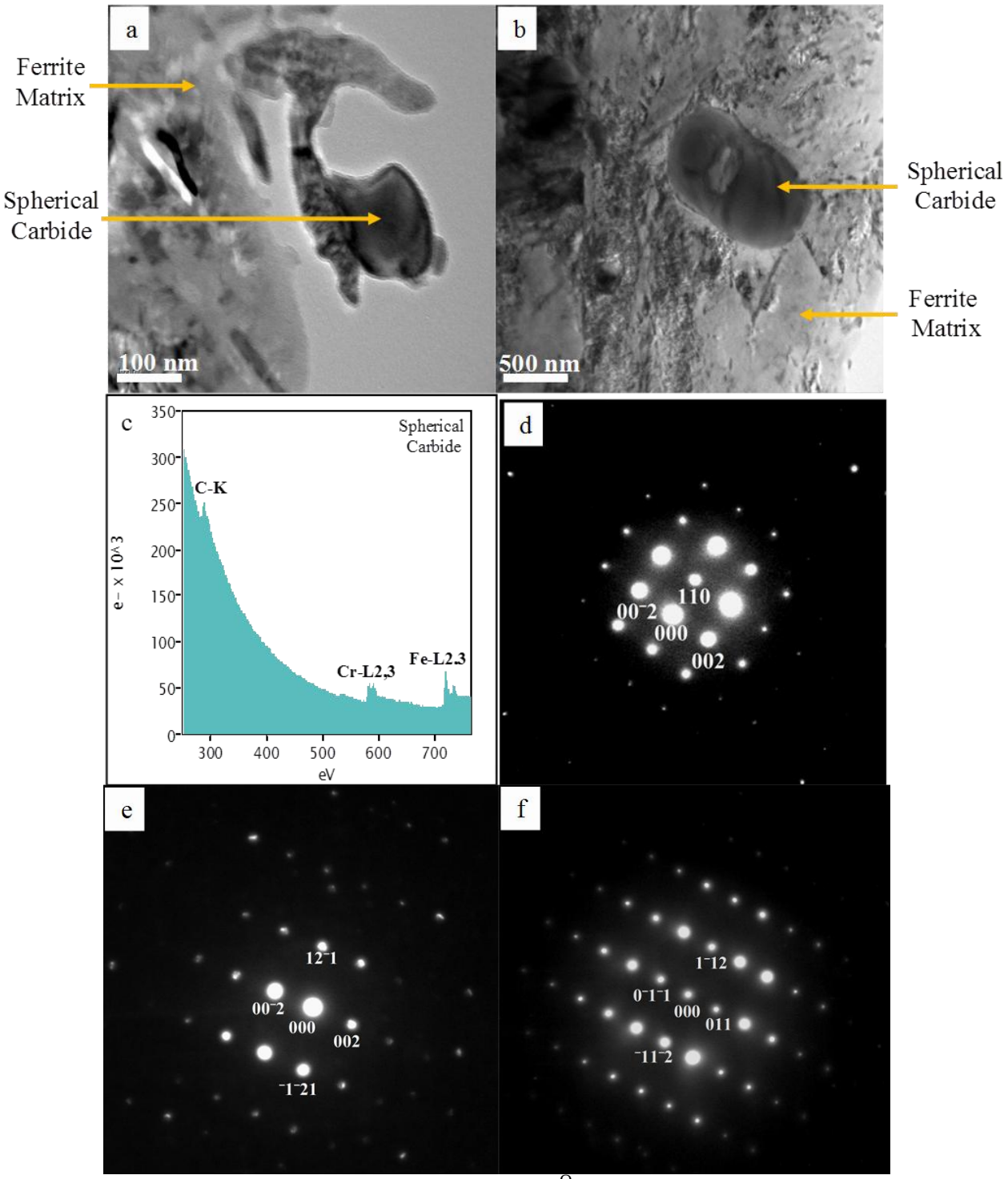

Figure 4- 8: (a), (b) TEM BF micrographs of the 425^{O}C-1hr tempered specimens of spherical carbides (c) EELS analysis on the spherical carbides. SADP of the M_3C (M=Cr, Fe) spherical carbide close to the (d) [-220] (e) [-420] and (f) [31-1] zone axes.

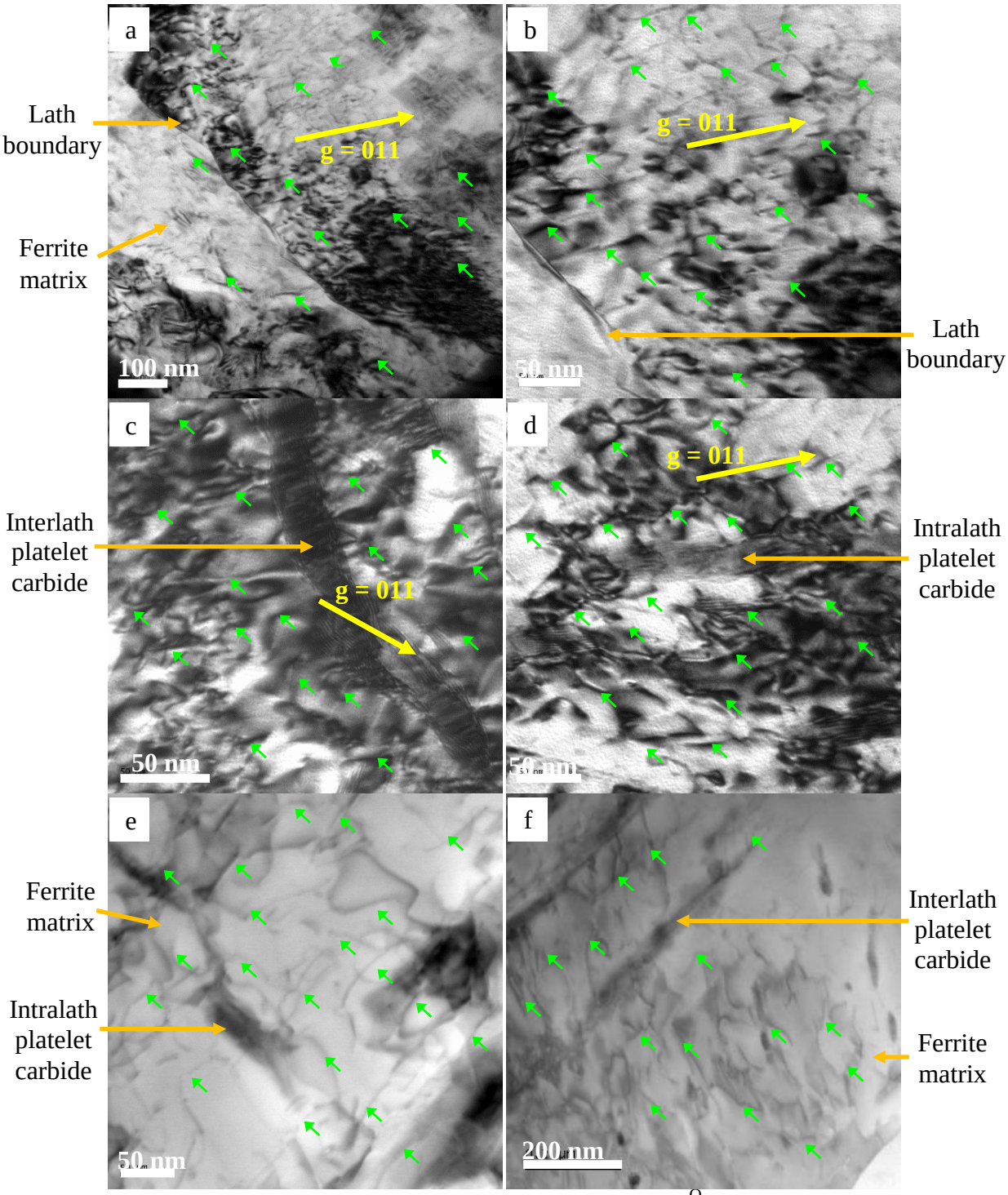

Figure 4- 9: TEM micrographs in 2-Beam conditions in the 425^{O}C-1hr tempered specimens showing dislocations (a) around lath boundaries (b) in regions close to lath boundaries (c) around interlath platelet carbides (d) around intralath platelet carbides. STEM micrographs showing dislocations (e) within ferrite matrix (f) emanating from interlath platelet carbides.

4.1.4 Microstructure of the 620^{O}C-2hrs Tempered Specimens Prior to Impact

Figure 4-10 shows typical micrographs of the 620^{O}C-2hrs tempered specimens prior to impact. The size of the lath matrix and the precipitated carbides were larger than those observed in the other groups. In addition, the relative distribution density of the carbides within the matrix was relatively lower than the distribution of the carbides in the other tempered groups. The existence of the relatively larger carbides is attributed to the occurrence of static recrystallization and/or complete carbide precipitation during tempering under this condition (620^{O}C for 2hrs). The average width of the lath matrix was 565nm while the average width of the interlath platelet carbides lining the lath matrix was 74nm. The platelet carbides within the lath matrix (intralath platelet carbides) had an average length of 203nm and a width of 51nm representing an approximate aspect ratio of 4. The average diameter of the spherical carbides observed in the tempered specimens was 400nm. SADPs from the spherical carbides showed that the carbides were of the M_3C (M= Fe, Cr) carbide type with an orthorhombic crystal structure as shown by the SADP in figure 4-10(e) close to [11-1] zone axis. The SADP in figure 4-10(f) close to the [0-26] zone axis shows that the matrix is a body centered cubic (BCC) ferrite matrix.

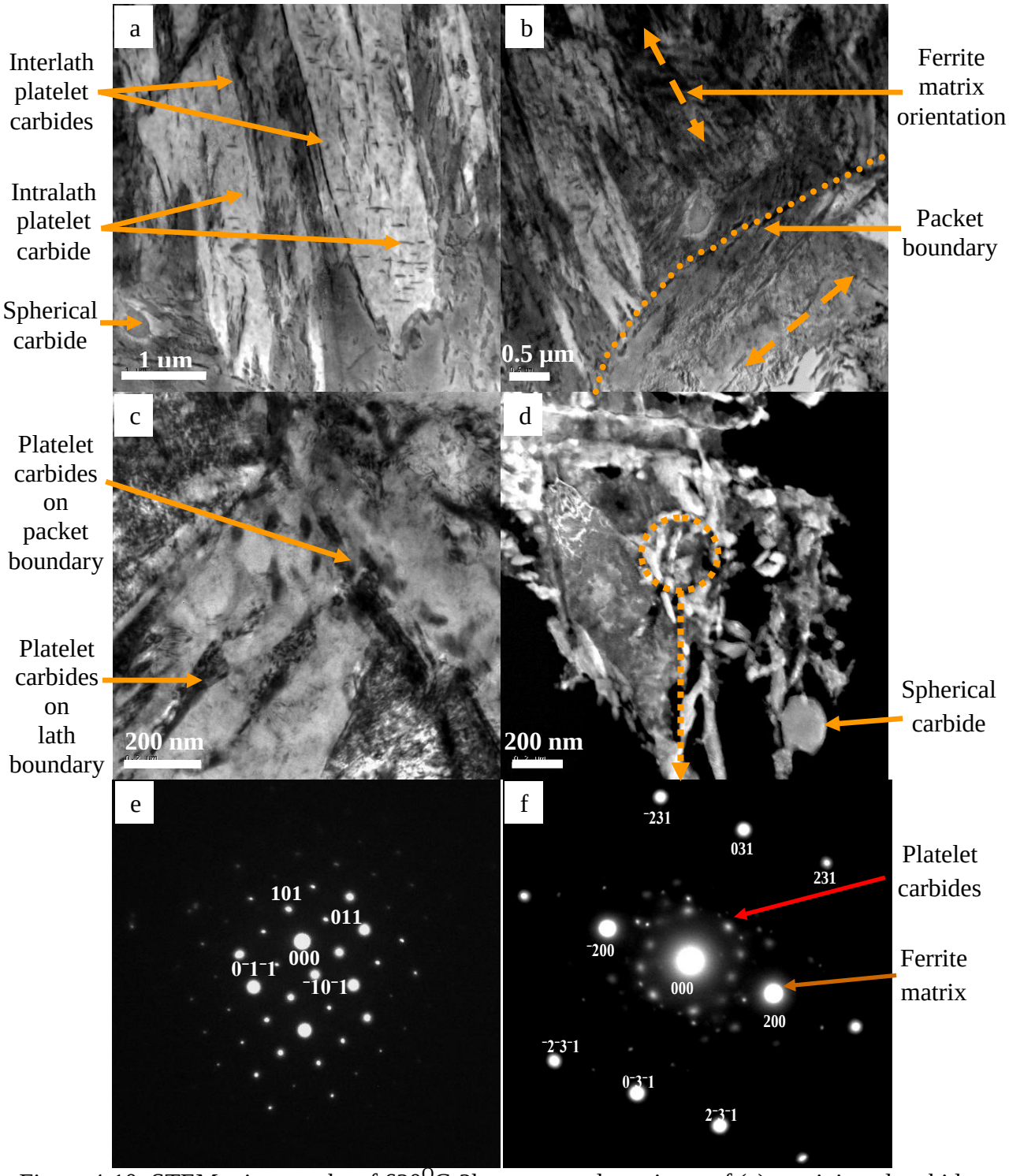

Figure 4-10: STEM micrographs of 620^{O}C-2hrs tempered specimen of (a) precipitated carbides (b) martensite packet. (c) TEM BF micrograph of platelet carbides (d) HAADF micrograph of carbides. SADPs close to (e) [11-1] M_3C carbide and (f) [0-26] ferrite zone axes.

Figure 4-11(a) and (b) show High Angle Annular Dark Field (HAADF) micrographs of the precipitated platelet and spherical carbides respectively. Figure 4-11(c) shows the EELS analysis of the platelet carbide while figure 4-11(d) shows the EELS analysis of the ferrite matrix. The platelet carbides were rich in Iron (Fe) and carbon (C). Figure 4-11(e) shows the EELS of the spherical carbides while table 4-1 and figure 4-11(f) show the Energy Dispersive Spectroscopy (EDS) of the spherical carbide. The spherical carbides were rich in chromium (Cr), iron (Fe) and carbon (C).

Table 4- 1: EDS Analysis on the spherical carbide in the 620^{O}C-2hrs tempered specimens

Element	Weight%	Atomic%
C K	6.13	23.08
Cr K	15.58	13.55
Fe K	78.29	63.37
Totals		100.00

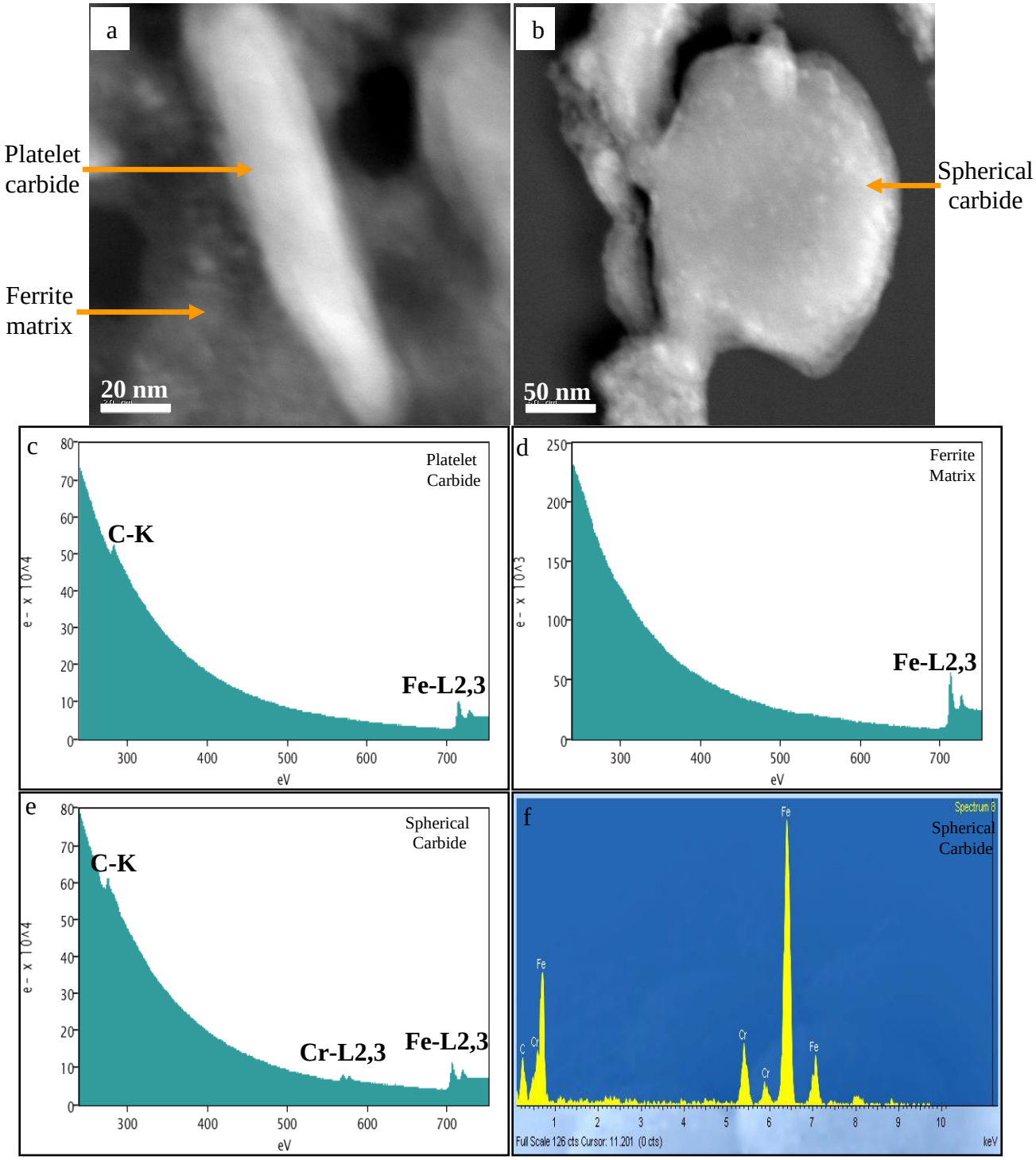

Figure 4- 11: HAADF micrographs of (a) platelet carbide (b) spherical carbide. EELS analyses on (c) platelet carbide (d) ferrite matrix (e) spherical carbide. (f) EDS analysis on spherical carbide

The regions surrounding the precipitated carbides on the lath boundaries and within the lath matrix were decorated with relatively higher densities of dislocations when compared to regions away from the carbides and the boundaries as shown in figure 4-12. The pre-existing dislocations appear to be emanating from the carbides on the boundaries into the matrix as shown by the 2-Beam conditions in figure 4-12(a) to (c).The presence of dislocations within the tempered structure shows that, regardless of the occurrence of static recrystallization, the structure retains a lot of the dislocations that were induced in the as-quenched martensite structure due to the shear martensitic transformation process.

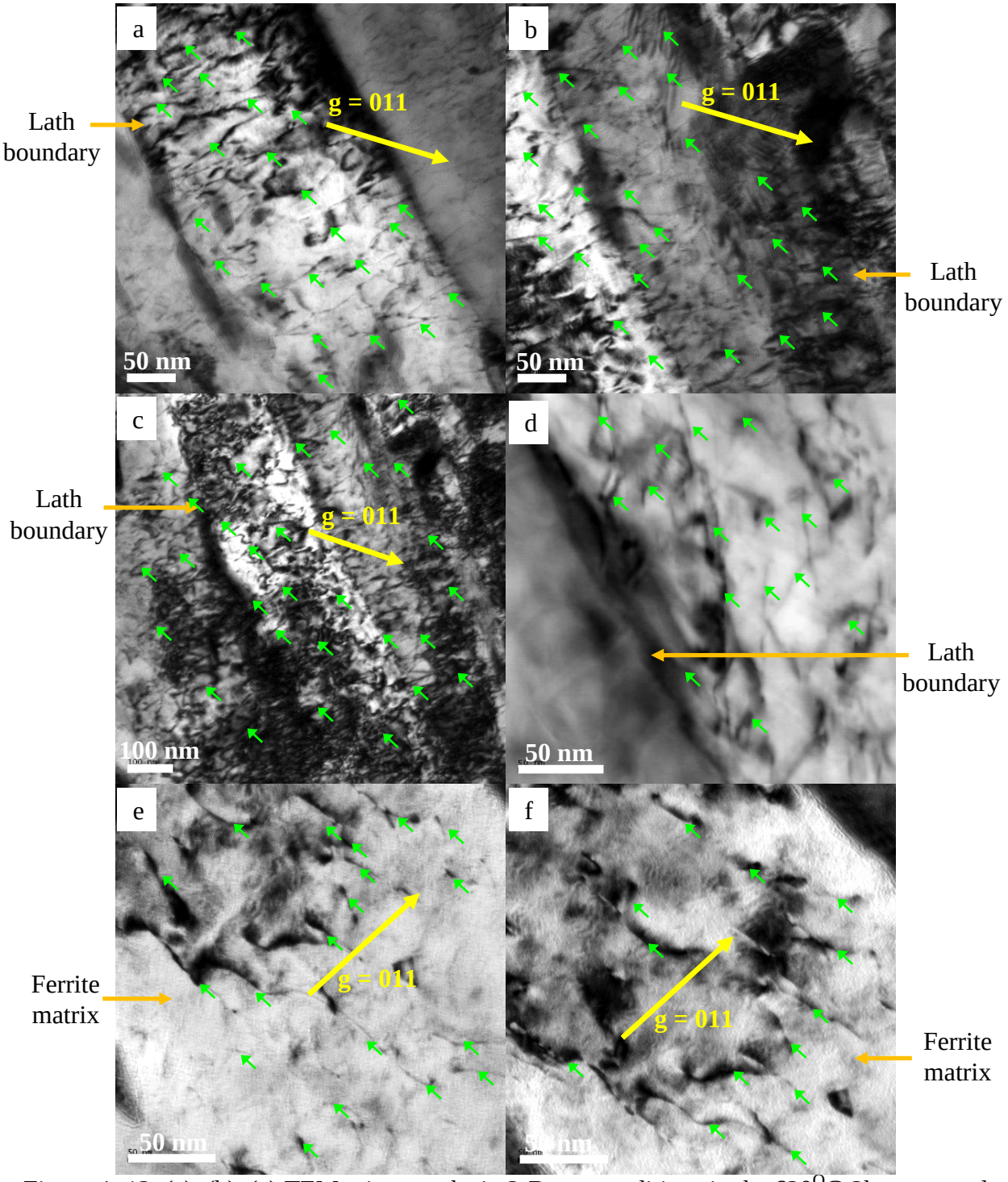

Figure 4- 12: (a), (b), (c) TEM micrographs in 2-Beam conditions in the 620^{O}C-2hr tempered specimens showing dislocations emanating from lath boundaries into the ferrite matrix. (d) STEM micrograph of dislocations emanating from lath boundary. (e), (f) 2-Beam conditions of dislocations within the ferrite matrix

The thin boundary layers that were observed around the precipitated carbides in the other tempered specimens, were also observed in the specimens within this group. Figure 4-13 shows typical HRTEM micrographs of the precipitated carbides within the ferrite matrix. The carbides were surrounded by boundary layers which were approximately 6nm thick as shown by figure 4-13(a) and (b). The 1st and 2nd misfit interfaces were also observed as delineated by the blue lines. The existence of two misfit interfaces increases the number of misfit dislocations present within the microstructure when compared to an interface with no boundary layer. The loss of lattice fringes in the HRTEM micrographs shown in figure 4-13(d) and in the FFT in figure 4-13(g) demonstrate the random arrangement of the atomic columns within the boundary layer. This is evident when compared to the ferrite matrix and precipitated carbides. Thus, besides the dislocations at the misfit interfaces, the random arrangements of atomic columns within the boundary layers create high density of local defects and increase the dislocations around the interfaces. This was evident in the micrographs under 2-Beam conditions when the dislocations appeared to be emanating from the regions around the precipitates into the matrix. The schematic in figure 4-13(i) shows the random arrangement of the columns of atoms within the boundary layer when compared to the atomic columns within a carbide precipitate and matrix. Generally, lower stresses are required during plastic deformation for the nucleation and multiplication of dislocations when dislocation sources are present within a microstructure. Thus, it is easier to nucleate and multiply dislocations within the microstructure during plastic deformation when dislocation sources are activated. It is inferred that the carbide/ferrite interfaces could act as dislocations sources when they are activated during impact because of the presence of dislocations at the interface. The activation of dislocation sources during impact would enhance the emergence and multiplication of dislocations within the specimens.

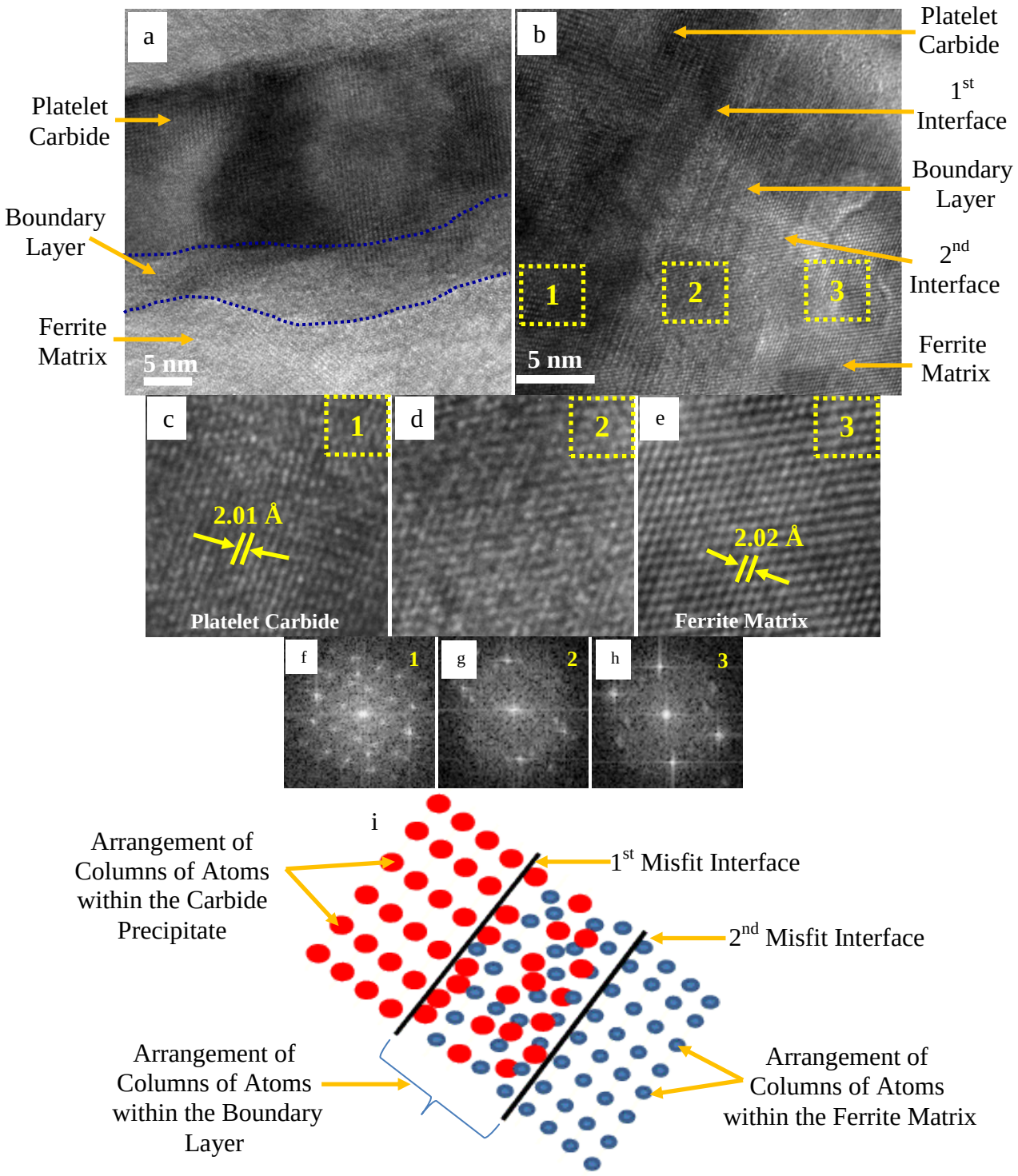

Figure 4- 13: HRTEM micrographs in 620^{O}C-2hrs tempered specimen of (a) platelet carbide (b) platelet carbide showing the 1st and 2nd interfaces. HRTEM micrographs of (c) platelet carbide (d) boundary layer (e) ferrite matrix. (f), (g), (h) are FFTs of (c), (d), and (e) respectively. (i)Schematic of the random arrangement of the columns of atoms within the boundary layer.

4.1.5 The X-Ray Diffraction (XRD) Analyses of the Tempered Pre-impact Steel Specimens

The X-ray diffraction spectra of the specimens before impact in figures 4-14 to 4-16 show increasing peak height and decreasing peak width (Full Width at Half Maximum-FWHM) as the tempering temperature increases. The peak width, β in radians, measured at FWHM is inversely proportional to the crystallite size L_{hkl} perpendicular to the hkl plane according to the Scherrer equation [111-112]:

$$L_{hkl} = \frac{\lambda}{\beta \cos\theta} \quad \text{.....4-1}$$

The increase in peak width or line broadening in x-ray diffraction profiles have been attributed to small crystal sizes/dislocations and peak broadening to variations in d-spacing caused by microstrain [111-112]. The Body Centered Tetragonal (BCT) crystal structure of martensite has a high amount of dislocations and high internal stresses due to the diffusionless shear transformation process [73,75-76]. However, during tempering the structure of the steel becomes more homogeneous and the density of dislocations is reduced due to dislocation annihilation, static recovery and static recrystallization processes. Reduction in dislocation densities and defects due to tempering could give rise to the sharp peaks with high intensities from the various reflecting planes as observed in figures 4-14 and 4-15. The amounts of defects and/or dislocations/strains in the steel specimens decrease with increasing tempering temperature as indicated by increasing peak heights in the x-ray diffraction spectra in figure 4-15.The sizes of laths and packets of laths in the steel specimens increases with tempering temperature as indicated by decreasing peak widths (FWHM) in figure 4-16.

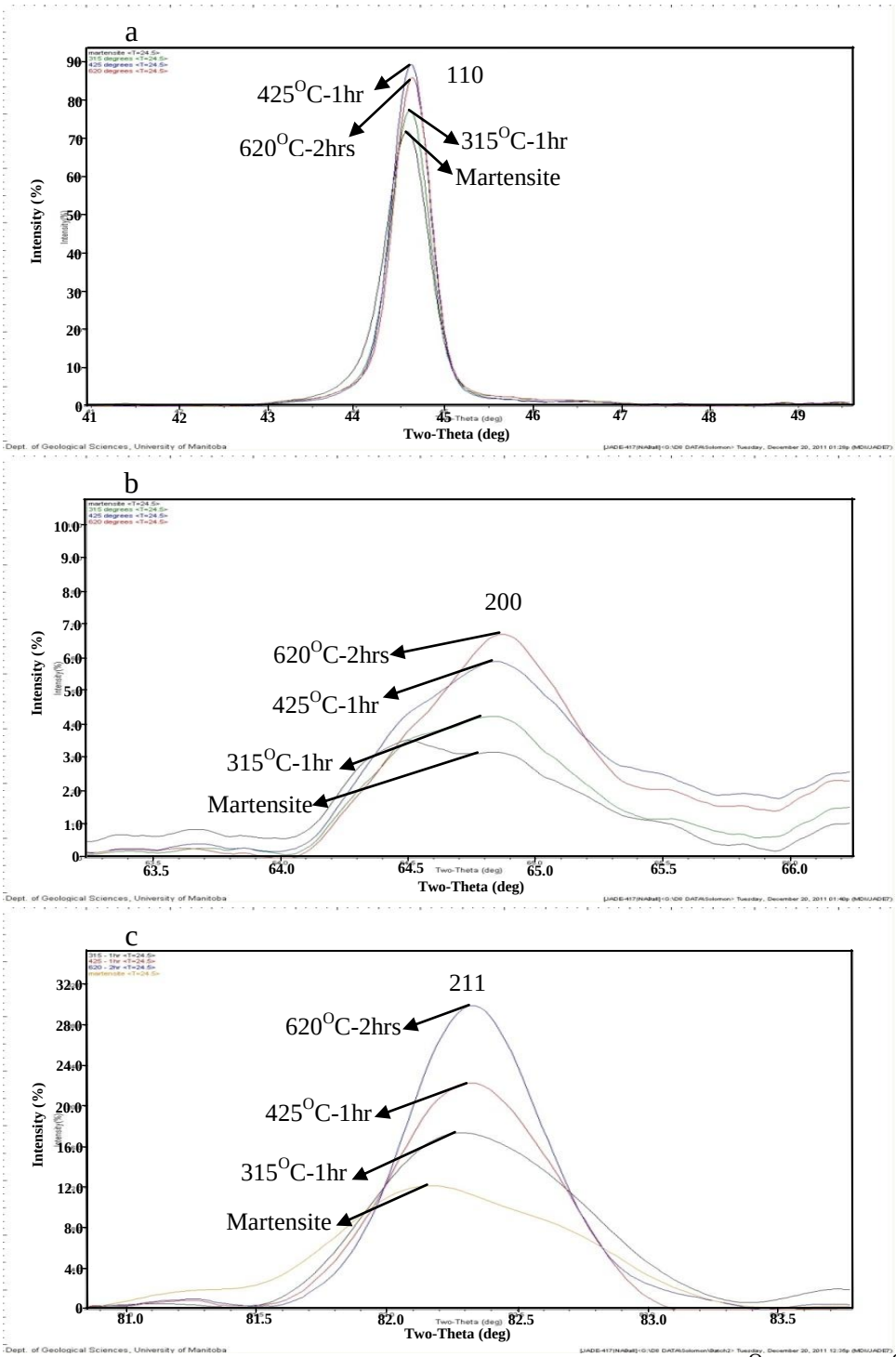

Figure 4- 14: X-ray diffraction spectra of the as-quenched martensite, 315^{O}C-1hr, 425^{O}C-1hr and 620^{O}C-2hrs tempered specimens superimposed on each other on (a) (110) (b) (200) and (c) (211) reflecting planes prior to impact.

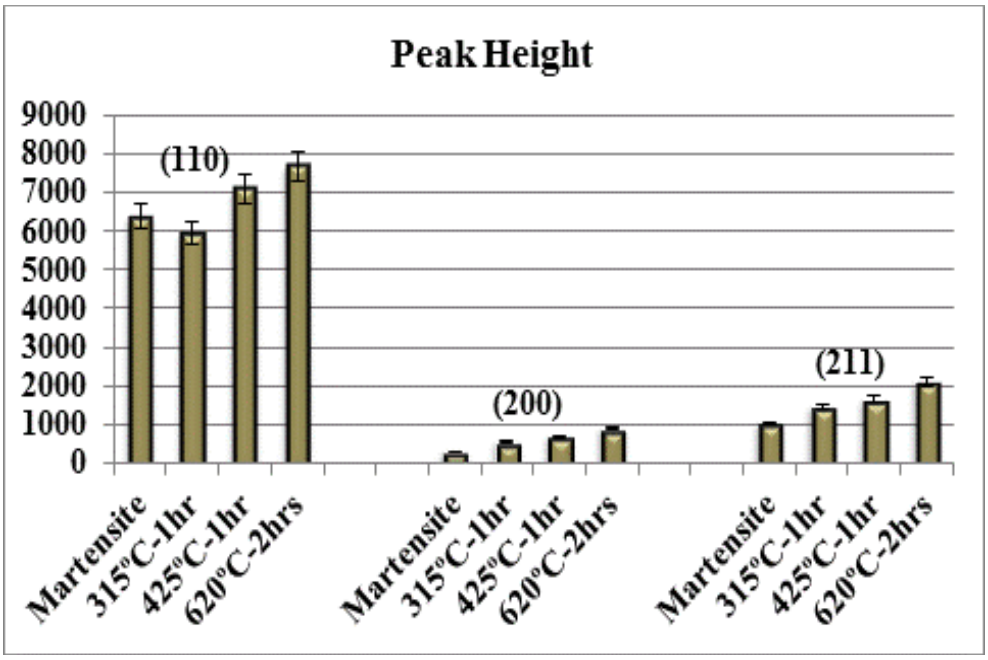

Figure 4- 15: A graph depicting increasing peak height of x-ray diffraction spectra with increasing tempering temperature on different reflecting planes.

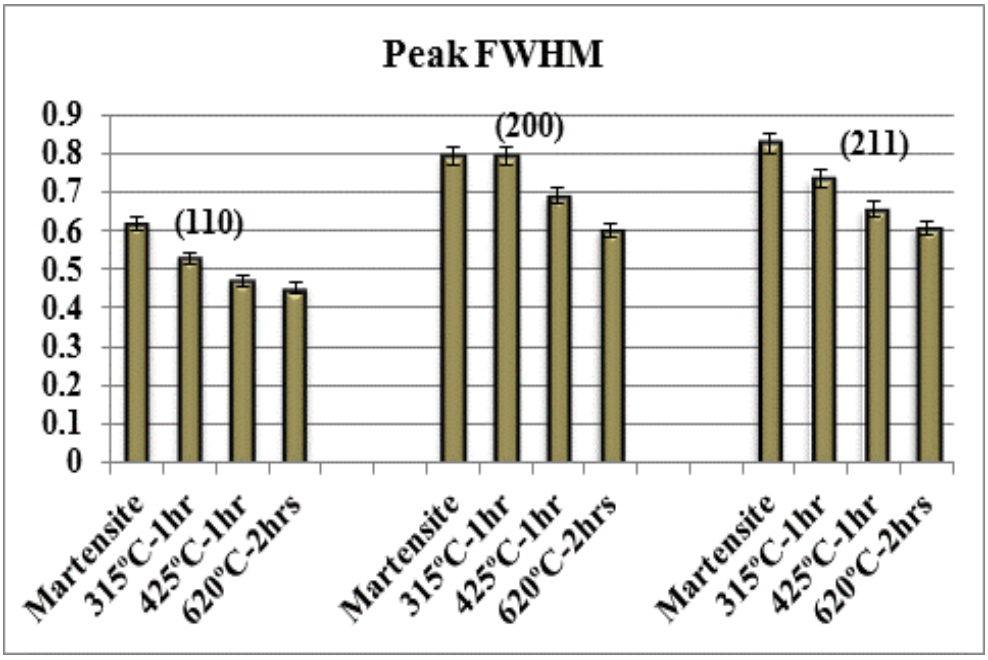

Figure 4- 16: Graph depicting decreasing peak width of x-ray diffraction patterns with increasing tempering temperature at different reflecting planes.

4.1.6 Chemical Analysis and Microhardness Distribution of the Pre-impact Steel Specimens

It was observed that increasing the tempering temperature increases the clustering of carbide-forming elements such as chromium (Cr), Manganese (Mn) and Molybdenum (Mo) within the matrix as shown on figure 4-17, and table 4-2 and 4-3. These carbide-forming elements diffuse to carbon rich regions due to their higher affinity for carbon within the matrix [73-74, 76]. In addition, it is easier for these heavy elements to diffuse into the carbides at relatively higher temperatures. In 2012, Lim et al. [113] reported that grouping of carbon atoms in the martensite matrix occurs prior to the precipitation of transition carbides during tempering of AISI 4340 steel. Cr and Mo are known to increase the stability of supersaturated iron-carbon solid solution while Mn decreases its stability [73, 76, 113]. Nevertheless, Cr and Mo alloying elements reduce the coarsening of cementite which accounts for the presence of the platelet carbides (Fe_3C) even at relatively higher tempering temperatures [113].

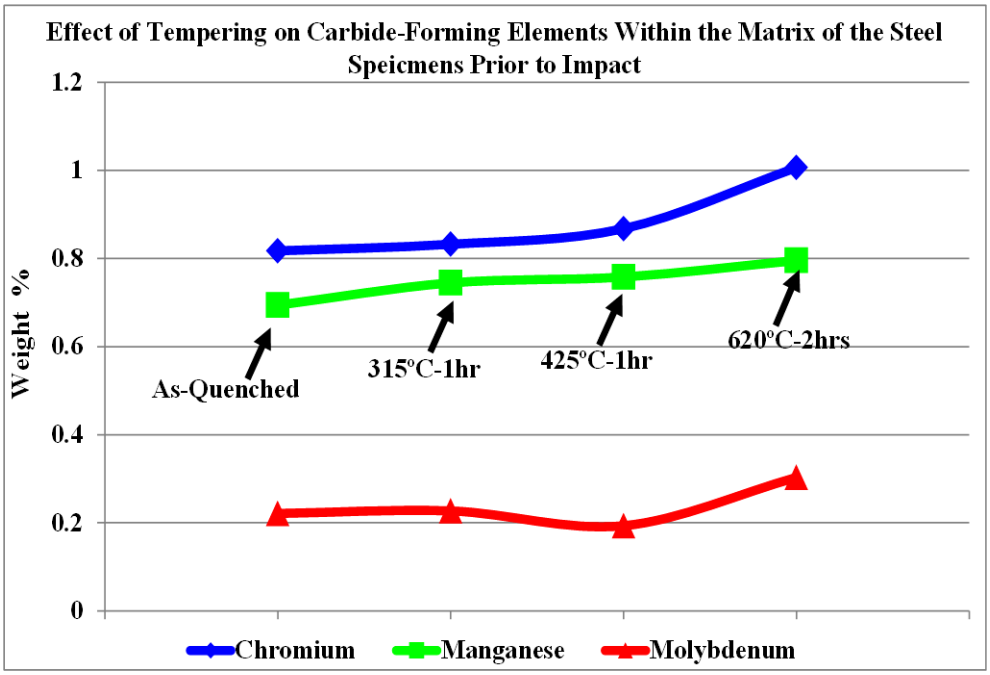

Figure 4- 17: Wavelength Dispersive Spectroscopy (WDS) on the pre-impact specimens.

Table 4- 2: Wavelength Dispersive Spectroscopy (WDS) of the Pre-impact steel specimens

Weight%					
Specimen	Si	Cr	Mn	Ni	Mo
Martensite	0.24052	0.8177	0.69436	1.7717	0.22138
315°C-1hr	0.231967	0.832533	0.744933	1.7685	0.2271
425°C-1hr	0.2912	0.867967	0.758267	1.841667	0.193467
620°C-2hrs	0.24735	1.0067	0.79572	1.6226	0.3033

Table 4- 3: Standard deviation of the WDS analysis of the Pre-impact steel specimens

Standard Deviation wt%					
	Si	Cr	Mn	Ni	Mo
Martensite	0.06094	0.01262	0.08858	0.0505	0.07284
315°C-1hr	0.025067	0.0127	0.033367	0.050433	0.038467
425°C-1hr	0.0261	0.0129	0.033567	0.0513	0.036867
620°C-2hrs	0.0235	0.0138	0.03432	0.04825	0.04375

Hardness of the steel specimens decreased as the tempering temperature increased as shown on figure 4-18 and table 4-4. This shows that the high residual stresses associated with the martensitic transformation reduce considerably as the tempering temperature and/or time increases. Carbide precipitation during tempering coupled with the occurrence of static recrystallization at high tempering temperatures account for the significant reduction in hardness.

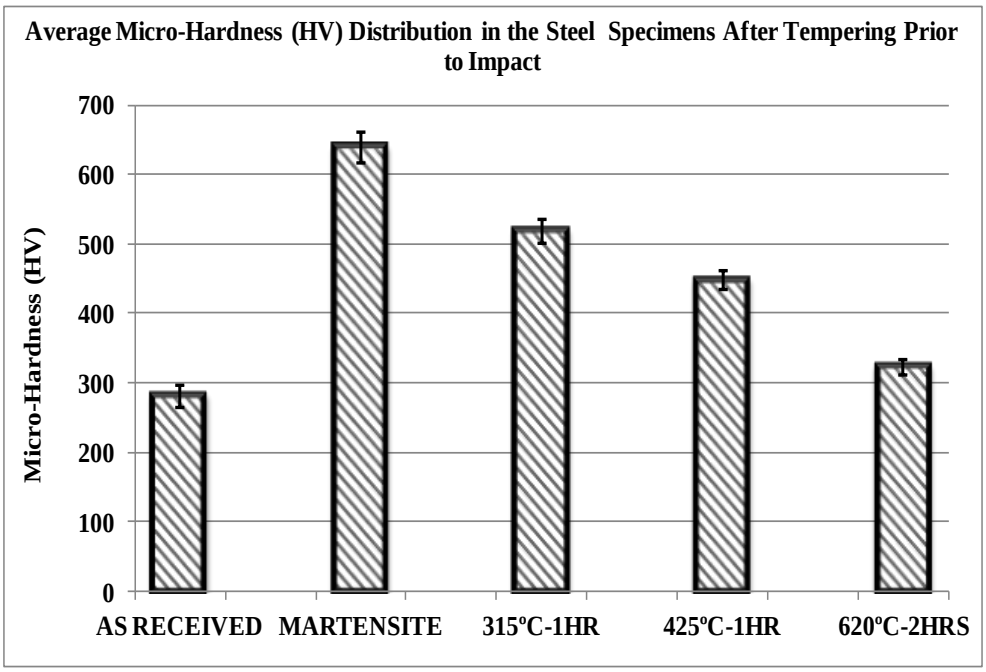

Figure 4- 18: Microhardness (HV) distribution of the pre-impact steel specimens.

Table 4- 4: Microhardness (HV) distribution of the pre-impact steel specimens

Group of Specimen	Average Microhardness (HV)
As-Received	281±16
As-Quenched Martensite	639±21
315^{O}C-1hr Tempered Specimens	518±16
425^{O}C-1hr Tempered Specimens	447±14
620^{O}C-2hrs Tempered Specimens	322±11

4.2 Results and Analysis following Impact

The tempered steel specimens were impacted at high strain rates and large strains using the Direct Impact Hopkinson Pressure Bar (DIHPB). The response of the specimens to impact was monitored and standard metallographic techniques were used to document the occurrence of Adiabatic Shear Bands (ASBs) within the impacted specimens. This section is has four subsections, 4.2.1 to 4.2.4. Subsection 4.2.1 presents the response of the steel specimens to impact and the calculated impact properties. Subsection 4.2.2 compares the documented ASBs in the 315^{O}C-1hr, 425^{O}C-1hr and 620^{O}C-2hrs tempered groups and their susceptibility to the formation of ASBs. SEM and XRD results of the structure within and outside ASBs are presented in subsection 4.2.3 while subsection 4.2.4 analyzes the effect of impact properties on the properties of ASBs.

4.2.1 Response of the Tempered Steel Specimens to Impact

Figure 4-19 shows typical impact resistance curves of the 620^{O}C-2hrs tempered specimens. The impact resistance curves are indicative of the behavior of the specimens and their respond to the impact. In general, in response to the impact, flow stress increases initially with strain, reaches a maximum and decreases with subsequent increase in strain irrespective of the initial conditions of the specimen or the amount of deformation. This trend for the flow stress was prevalent in all the impacted specimens regardless of the condition of the specimen prior to impact, impact momentum or the strain rates. Higher impact momentum results in higher strain during the impact and the higher the strain rate, the higher the flow stress. Furthermore, the area covered by the impact resistance curves can be approximated as the amount of deformation demonstrating that the deformation energy and the amount of deformation increases as the strain rate increases.

Table 4-5 shows the calculated impact properties of the steel specimens. At a constant strain rate, the maximum strain in a specimen is directly proportional to the strain rate and the length of the projectile, L [114]. The length of the projectile, L, and the speed of the elastic wave, C, transmitted through the specimen to the transmitter bar were used to calculate the impact properties indicated on table 4-5. The results demonstrate that the impact momentums influence the maximum strain and strain rates in the specimen during the impact.

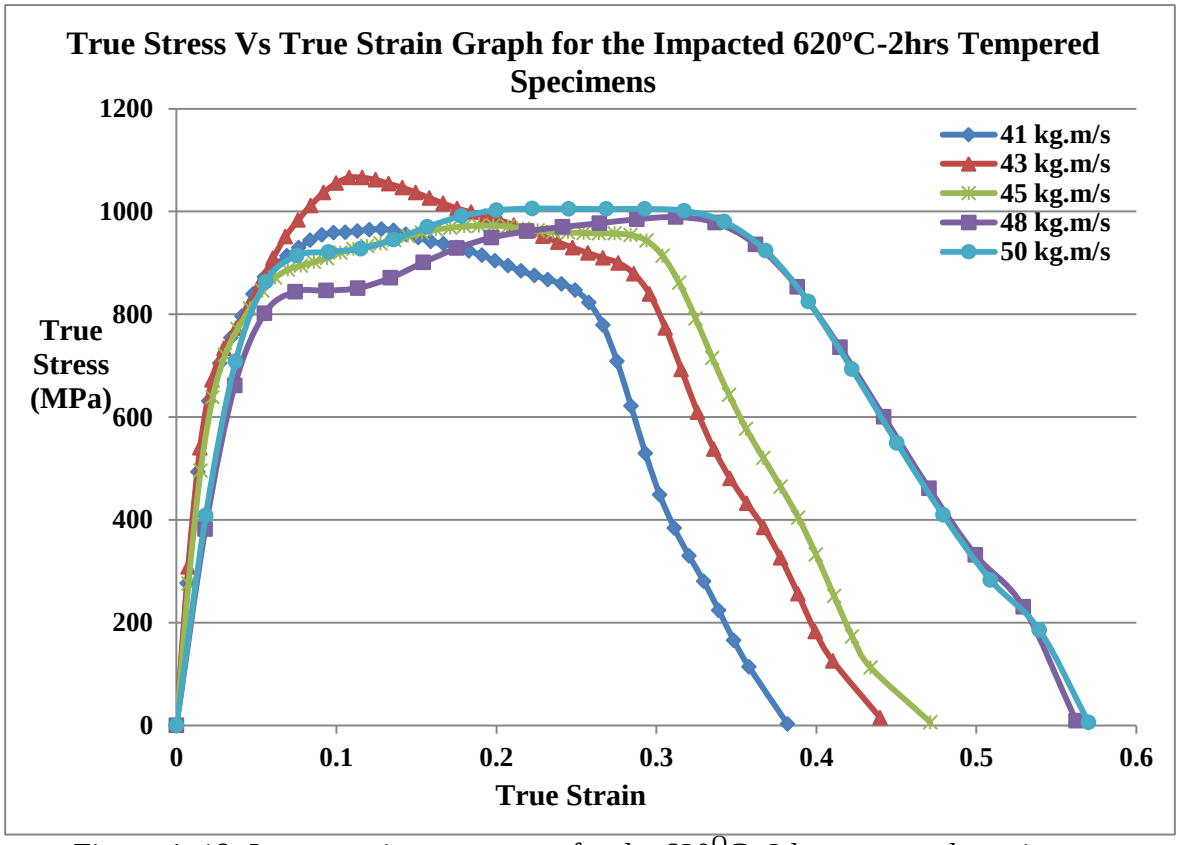

Figure 4- 19: Impact resistance curves for the 620^{O}C- 2 hrs tempered specimens.

Table 4- 5: Calculated impact momentum and strain rates of the impacted steel specimens

Specimen	Tempering Temperature And Time	Pressure (KPa)	Velocity (m/s)	Impact Momentum (kg.m/s)	L_O-L_F (mm)	Maximum Strain	Strain Rate (S^{-1})
1	315^{O}C-1hr	160	21.0	41	2.00	0.1903	1802
2	315^{O}C-1hr	180	22.0	43	2.05	0.1960	1856
3	315^{O}C-1hr	190b	22.6	44	4.00	0.3810	3521
4	315^{O}C-1hr	200b	23.0	45	3.89	0.3719	3607
1	425^{O}C-1hr	180	22.0	43	2.20	0.2093	1982
2	425^{O}C-1hr	200	23.0	45	2.36	0.2254	2134
3	425^{O}C-1hr	220b	24.0	46	3.52	0.3359	3180
4	425^{O}C-1hr	260	25.8	50	3.69	0.3541	3353
5	425^{O}C-1hr	280b	26.7	52	4.80	0.4550	4308
1-A	620^{O}C-2hrs	140	20.0	39	2.92	0.2768	2620
2-B	620^{O}C-2hrs	160	21.0	41	3.22	0.3112	2946
3-C	620^{O}C-2hrs	180	22.0	43	3.55	0.3368	3189
4-D	620^{O}C-2hrs	200	23.0	45	3.60	0.3429	3246
5-E	620^{O}C-2hrs	230	24.4	48	3.77	0.3590	3400
6-F	620^{O}C-2hrs	260	25.8	50	4.26	0.4069	3853
7-G	620^{O}C-2hrs	260	25.8	50	4.36	0.4176	3954

* At a constant strain rate, the maximum strain in a specimen is directly proportional to the strain rate and the length of the striker bar, l, by: $\acute{\varepsilon} = \frac{C}{2l}\ \varepsilon$ [114]

4.2.2 Susceptibility of the Tempered Steel Specimens to the Formation of Adiabatic Shear Bands during Impact

Impact of the steel specimens at high strain rates and large strains followed by the metallographic analysis as outlined in the experimental procedure showed that the 315^{O}C-1hr tempered specimens were more susceptible to the formation of ASBs when compared to the tempered specimens in the other groups. Figure 4-20 shows the optical micrographs of ASBs observed in impacted 315^{O}C-1hr tempered specimens. The impact momentum where the first metallographically observable shear band appeared in the microstructure of the impacted specimens in this group was at 43kg.m/s corresponding to a strain rate of $1856S^{-1}$. In addition, the shear bands in this group readily developed cracks even if fracture and fragmentation did not occur. Furthermore, multiple ASBs were observed propagating with cracks in the fractured specimens.

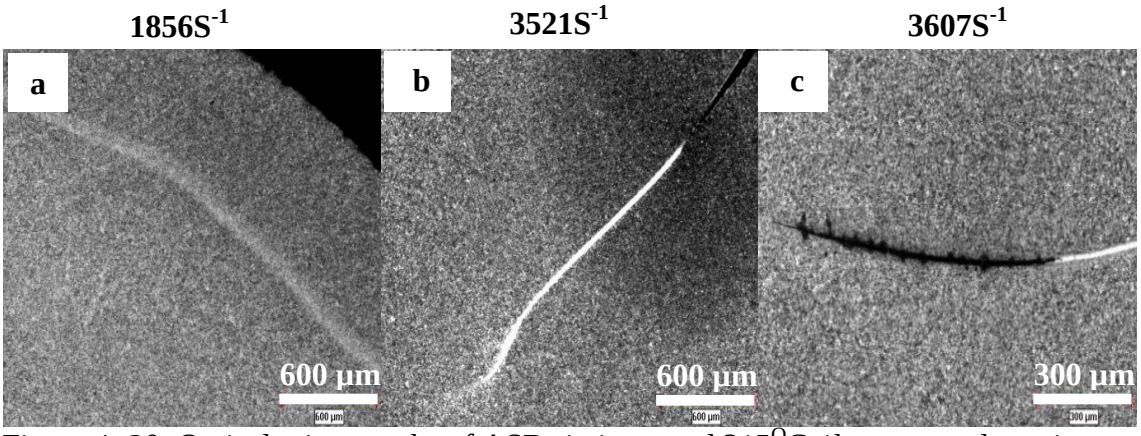

Figure 4- 20: Optical micrographs of ASBs in impacted 315^{O}C-1hr tempered specimens.

It was observed that even though the average hardness of the regions within the shear bands was higher than the regions outside the ASBs, the hardness increased as the impact momentum (strain rate) increase as shown in figure 4-21 and table 4-6. The first metallographically observable shear band (in the specimen impacted at 43kg.m/s) had approximately a 13% increase in hardness when the regions within the shear bands were compared to the pre-impact specimen. Also, there was approximately a 20% increase in hardness when the pre-impact specimen is compared to the hardness of the regions within the shear bands which were first observed with cracks (in the specimen impacted at 44kg.m/s). Thus, approximately a 13% increase in hardness of the pre-impact specimen (518±16HV) resulted in the evolution of a shear band region with comparable hardness while a 20% increase in hardness resulted in a shear band region with a crack during impact of the 315^{O}C-1hr tempered specimens.

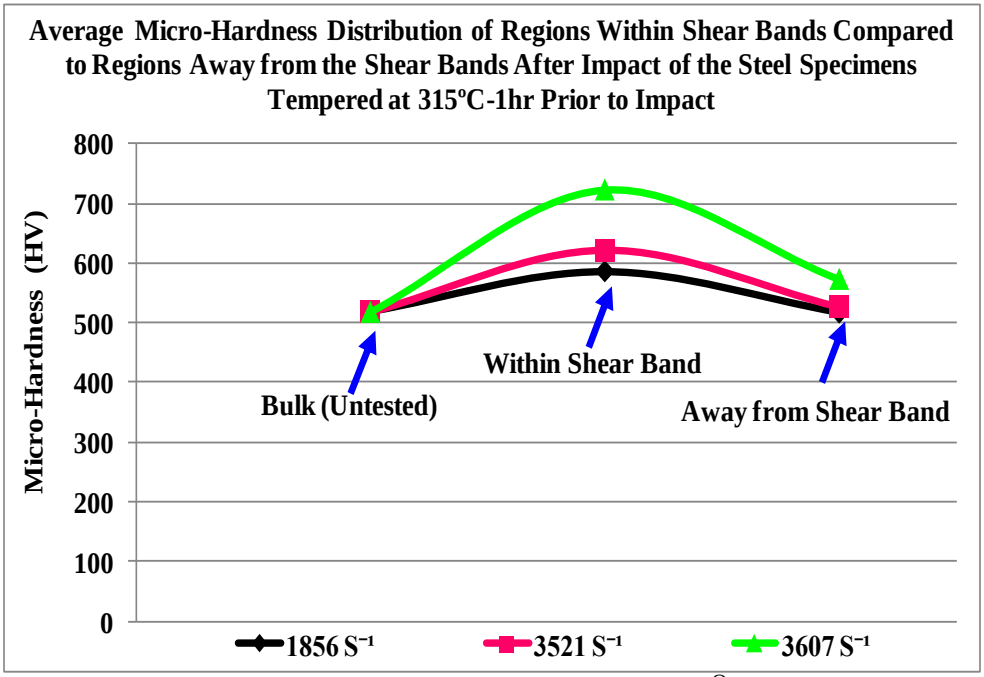

Figure 4- 21: Microhardness (HV) distribution in impacted 315^{O}C-1hr tempered specimens.

Table 4- 6: Microhardness (HV) distribution of the regions within and outside evolved ASBs in the impacted 315^{O}C-1hr tempered specimens

315^{O}C-1hr Tempered Specimens		
Impact Momentum (Strain Rate)	Average microhardness (HV)	
	Shear Band Region	Region Outside ASB
Untested	518±16	
43 kg.m/s (1856/S)	586±15	517 ±5
44 kg.m/s (3521/S)	621±21	527±9
45 kg.m/s (3607/S)	723±35	574±24

Figure 4-22 shows the optical micrographs of evolved ASBs in impacted 425^{O}C-1hr tempered specimens. It was observed that the structure and thickness of the shear bands become metallographically distinct as the impact momentum (strain rate) is increased. The impact momentum where the first metallographically observable shear band appeared in the microstructure of the impacted specimens in this group was at 43kg.m/s corresponding to a strain rate of $1982S^{-1}$. This observed shear band was metallographically diffused and indistinct from the surrounding regions when compared to the first observable shear band in the 315^{O}C-1hr tempered specimen also impacted at 43kg.m/s. Further increase in the impact momentum (strain rate) increased the damage through the evolution of a more-distinct ASB as shown on figure 4-22. This shows that the ASB structure evolves and becomes well-defined when the strain rate (impact momentum) increases till cracks initiate and propagate through the specimen to failure.

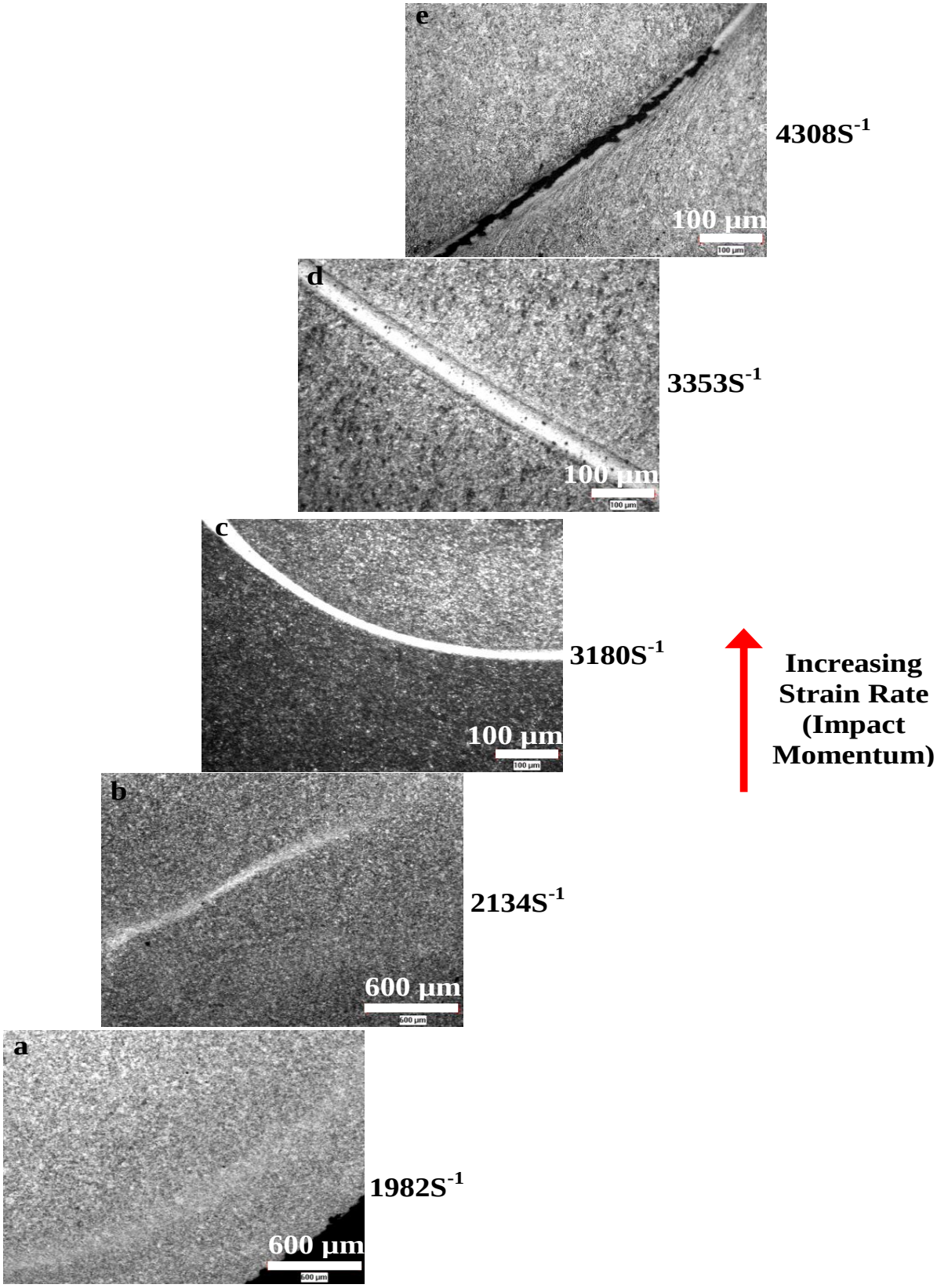

Figure 4- 22: Optical micrographs of ASBs in impacted 425^{O}C-1hr tempered specimens.

The average microhardness distribution of the evolved shear bands in the impacted 425^{O}C-1hr tempered specimens compared to the regions outside the ASBs is shown in figure 4-23 and table 4-7. There was approximately a 17% increase in hardness for regions within the shear bands in the specimen impacted at 43kg.m/s when compared to the hardness of the pre-impact specimen. In addition, approximately a 62% increase in hardness was observed for the regions within the shear bands with cracks that evolved after impact at 52kg.m/s when compared to the pre-impact specimen. This shows that excessive amount of damage would have to occur to the material in this group for cracks to initiate and propagate within the shear bands when compared to the relatively brittle specimens in the 315^{O}C-1hr tempered group.

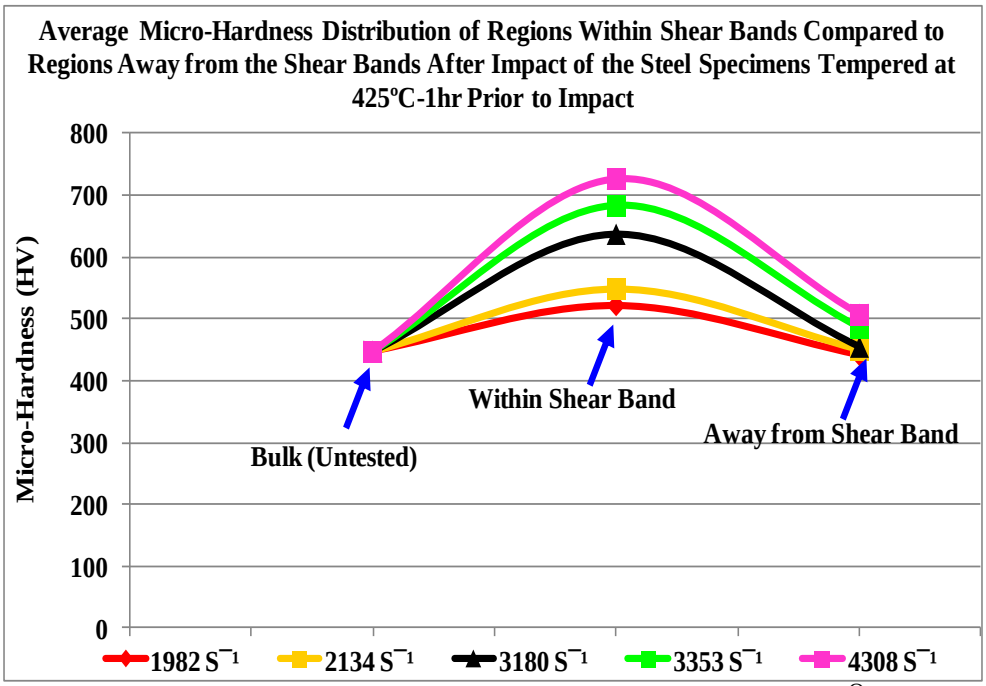

Figure 4- 23: Microhardness (HV) distribution of ASBs in impacted 425^{O}C-1hr tempered specimens.

Table 4- 7: Microhardness (HV) distribution of the regions within and outside evolved ASBs in the impacted 425^{O}C-1hr tempered specimens

425^{O}C-1hr Tempered Specimens		
Impact Momentum (Strain Rate)	Average Microhardness (HV)	
	Shear Band Region	Region Outside ASB
Untested	447±14	
43 kg.m/s (1982/S)	522±9	441 ±11
45 kg.m/s (2134/S)	549±6	450±12
46 kg.m/s (3180/S)	637±64	454±18
50 kg.m/s (3353/S)	683±51	489±7
52 kg.m/s (4308/S)	726±50	507±12

The 620^{O}C-2hrs tempered specimens were the least susceptible to the formation of ASBs during impact. Figure 4-24 shows the evolution of ASBs as a function of strain rate in five impacted specimens. There was no observed shear band in the specimens impacted at the strain rates of $2620S^{-1}$ and $2946S^{-1}$. The strain rate where a metallographically observable ASB appears in the microstructure of the impacted specimens was at 3189/S which corresponds to figure 4-24(a). It was observed that the structure and thickness of the ASBs become metallographically more-defined and distinct as the strain rate/strain is increased. It must be noted that at the strain rate of 3189/S, a metallographically-diffused ASB had already been formed (signifying an already damaged material because of the presence of ASB) and any further increase in strain rate/strain increases the damage through the evolution of a more distinct ASB.

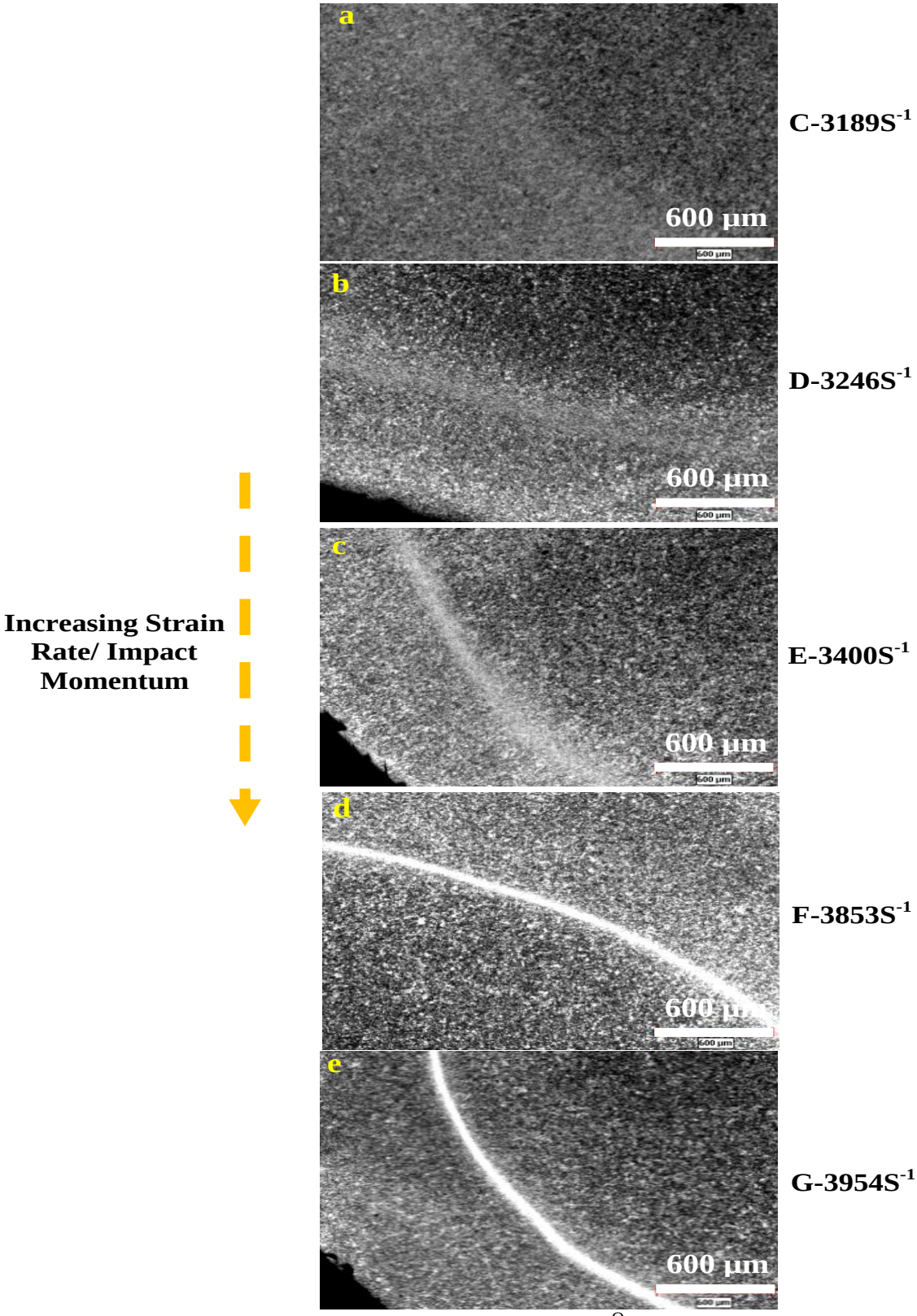

Figure 4- 24: Optical micrographs of ASBs in impacted 620^{O}C-2hrs tempered specimens.

As expected, micro-hardness of the regions within the ASBs increase as the strain rate/strain increases as shown in figure 4-25 and table 4-8. There was an approximate 27% increase in hardness for the evolved shear band after impact at 3189/S and an 8% increase in hardness in the regions outside the ASBs compared to the hardness of the untested steel specimen. In addition, there was a 41% increase in hardness for the evolved shear band after impact at 3954/S and a 7% increase in hardness of the regions outside the ASBs compared to the untested specimen. Moreover, there was approximately a 12% increase in hardness within the shear bands after impact at 3189/S to 3954/S. This demonstrates that most of the deformation energy is concentrated within the narrow regions where the shear band evolves and increasing the deformation energy during impact increases this effect within the shear bands because of the imposed local strain and strain rate.

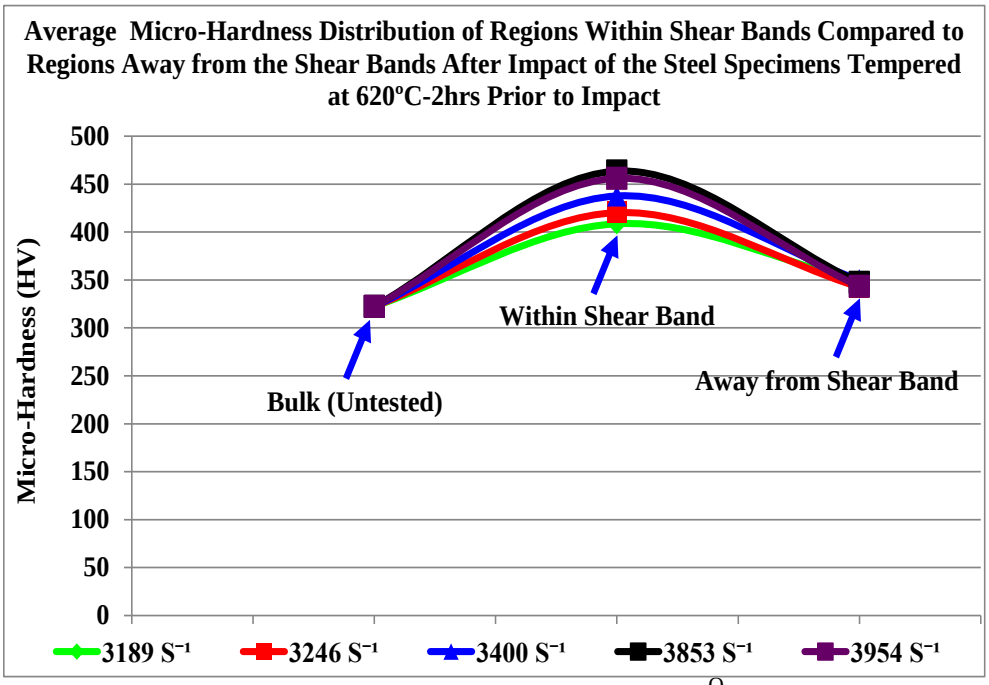

Figure 4- 25: Microhardness (HV) distribution in impacted 620^{O}C-2hrs tempered specimens.

Table 4- 8: Microhardness (HV) distribution of the regions within and outside evolved ASBs in the impacted 620^{O}C-2hrs tempered specimens

Impact Momentum (Strain Rate)	Average Microhardness (HV)	
	Shear Band Region	Region Outside ASB
Untested	323±11	
43 kg.m/s (3189/S)-C	409±12	349±13
45 kg.m/s (3246/S)-D	420±17	343±8
47 kg.m/s (3400/S)-E	438±21	350±9
50 kg.m/s (3853/S)-F	464±22	348±7
50 kg.m/s (3954/S)-G	456±20	344±9

4.2.3 Scanning Electron Microscopy (SEM) and X-ray Diffraction (XRD) Analyses on ASB

The concept of strain localization which precedes the formation of ASBs is more prominent on the Backscattered Electron (BSE) micrograph in figure 4-26, which shows a highly strained region within the ASB compared to regions outside the shear band. The finer regions within the ASB (figure 4-26(b)) are more apparent when compared to the regions outside the ASB (figure 4-26(c)) because the imposed strain and strain rate are not uniformly distributed within the specimen during the impact (inhomogeneous plastic deformation).

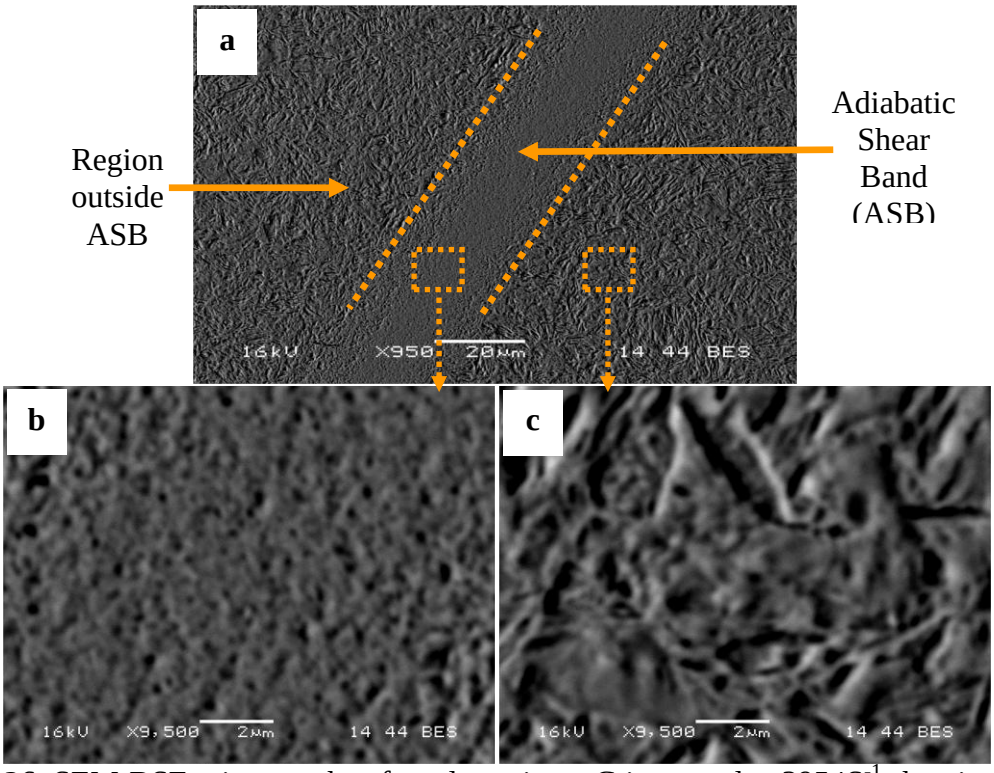

Figure 4- 26: SEM-BSE micrographs of steel specimen G impacted at $3954S^{-1}$ showing (a) ASB and surrouding regions (b) regions within ASB (c) regions outside ASB.

Figures 4-27 and 4-28 show a comparison of the X-ray diffraction spectra of the steel specimen G before and after impact showing the various reflecting planes of (110), (200) and (211). It was observed from figure 4-27 that there was a continuous decrease in average crystallite sizes based on the Scherrer equation using the increasing peak width at FWHM and the decreasing peak heights. The increasing peak width and decreasing peak height, which was very typical of all the ASBs when compared to the regions outside the ASBs and the pre-impact specimens, is attributed to the evolution of smaller grains, and high strains due to strain localization that occurs during the impact. The decreasing peak heights from regions outside the ASBs to the shear band regions is attributed to decreasing homogeneity which confirms that the shear band regions are highly inhomogeneous compared to the regions outside the ASBs.

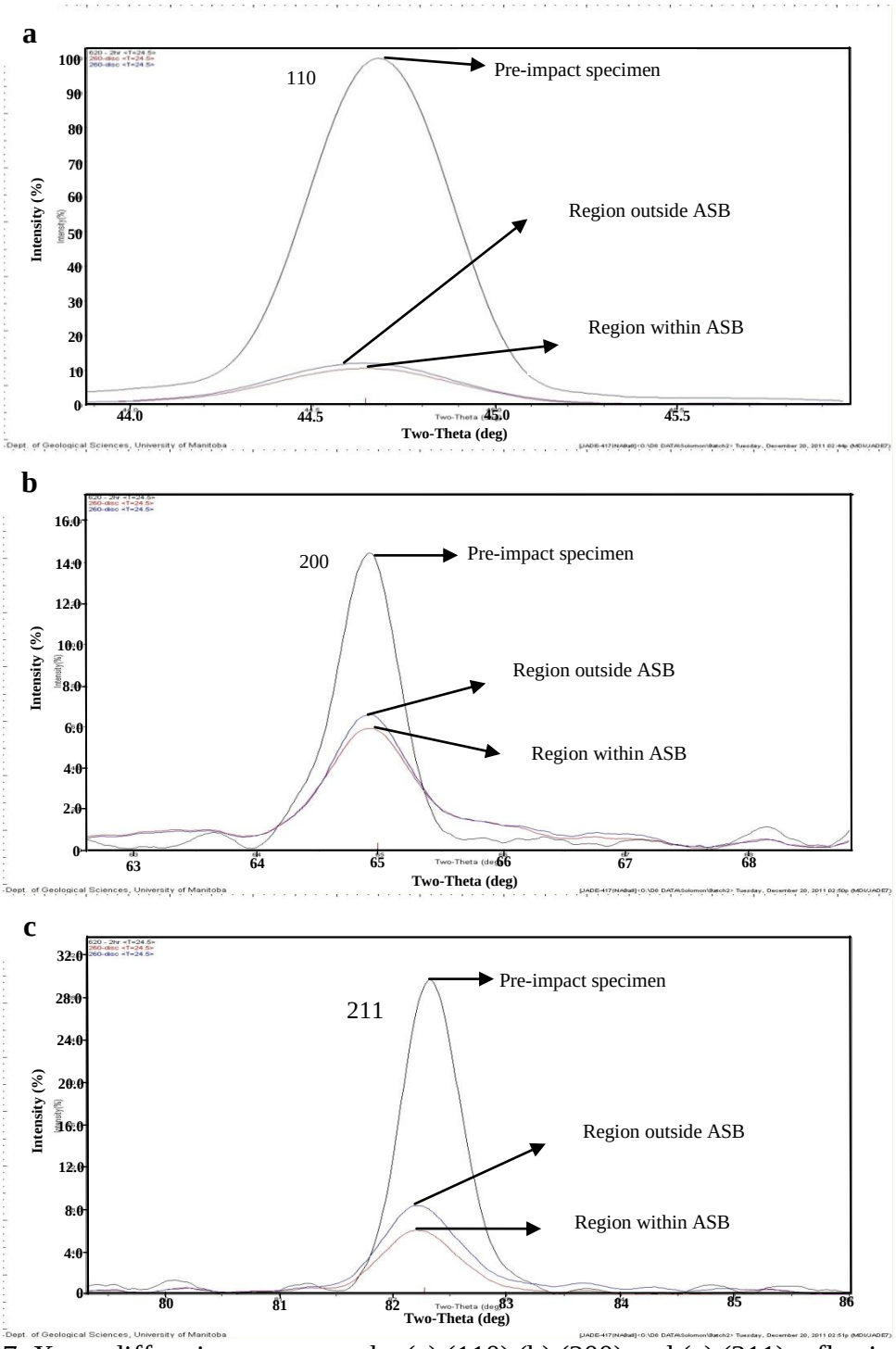

Figure 4- 27: X-ray diffraction spectra at the (a) (110) (b) (200) and (c) (211) reflecting planes of specimen G impacted at $3954S^{-1}$ compared to the pre-impact specimen.

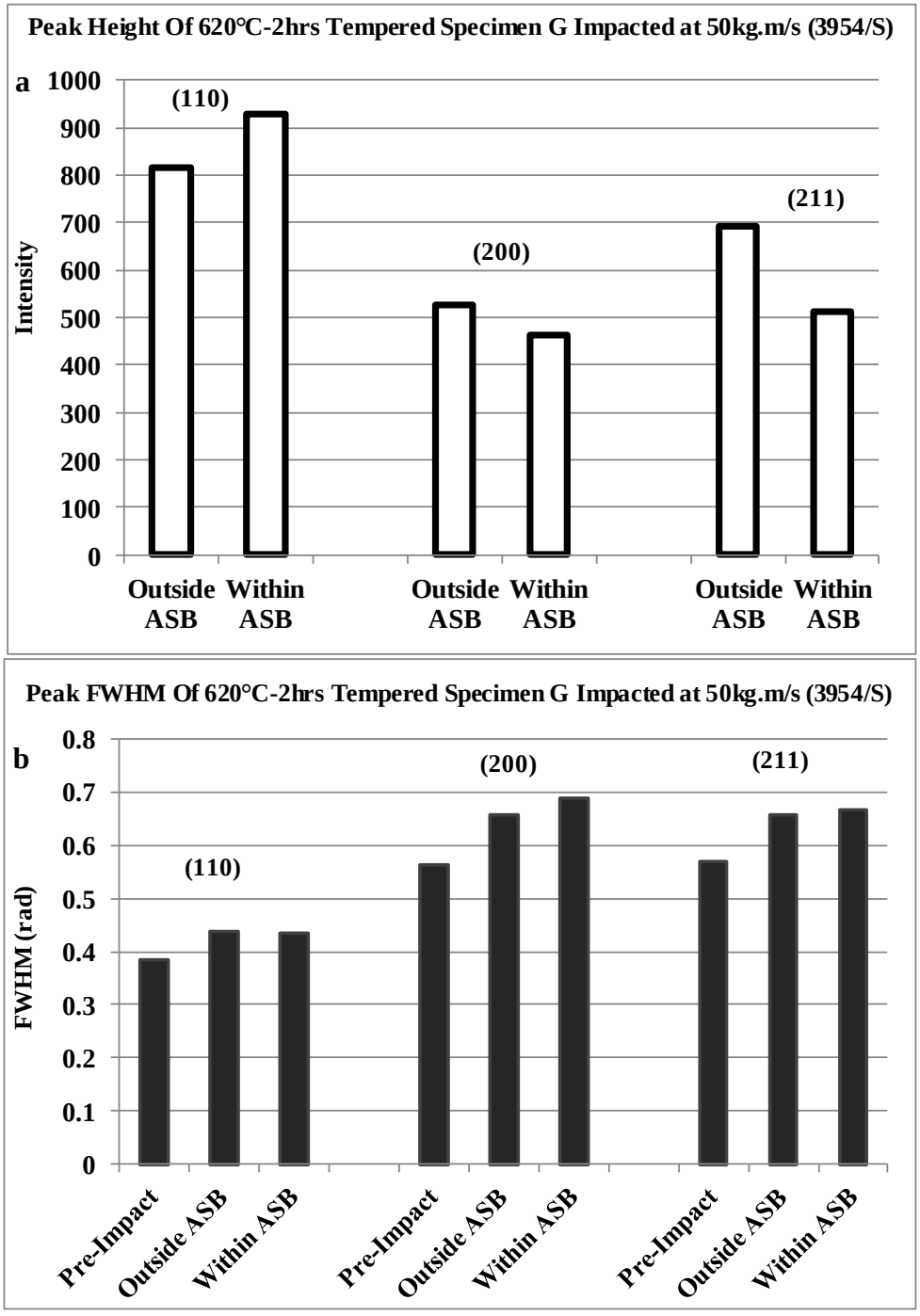

Figure 4- 28: (a) Peak height and (b) peak width at FWHM of X-ray diffraction spectra of specimen G impacted at $3954S^{-1}$ compared to the pre-impact specimen.

4.2.4 Effect of Strain Rate on Thickness and Hardness of Evolved Adiabatic Shear Bands

During impact of the steel specimens with the same pre-impact conditions (within the same group), it was observed that increasing the strain rate decreases the thickness of the evolved ASBs. In addition, the microhardness of the regions within the shear bands increases as the thickness decrease. Figure 4-29 illustrates the effect of strain rate on thickness and microhardness (HV) of evolved ASBs during impact of the tempered specimens from the three groups. A 315^{O}C-1hr tempered specimen impacted at a strain rate of $1856S^{-1}$ resulted in the formation of ASB with an average thickness of 146μm and a hardness of 586HV whereas another specimen from the same group produced ASB with a thickness of 10μm and a hardness of 723 when it was impacted at $3607S^{-1}$ as shown on table 4-9. From the documentation of the occurrence of ASBs, it was observed that the ASB structure evolved from a metallographically diffused band to a distinct band as the strain rate (impact momentum) is increased. The current results show that the thickness and structure of the evolving shear bands are influenced by the initial conditions (starting microstructure) of the pre-impact specimens and the ensuing strain rates during impact. Increasing the strain rate during impact increases the damage evolution through localization due to the concentration of higher strains within narrower bands. Thus, for specimens with the same initial conditions, the structure and appearance of each evolved ASB is more dependent on the prevailing strain rate during impact. Nevertheless, on the average, the steel specimens tempered at lower temperatures had relatively narrower shear bands than the steel specimens tempered at higher temperatures as shown on table 4-9.

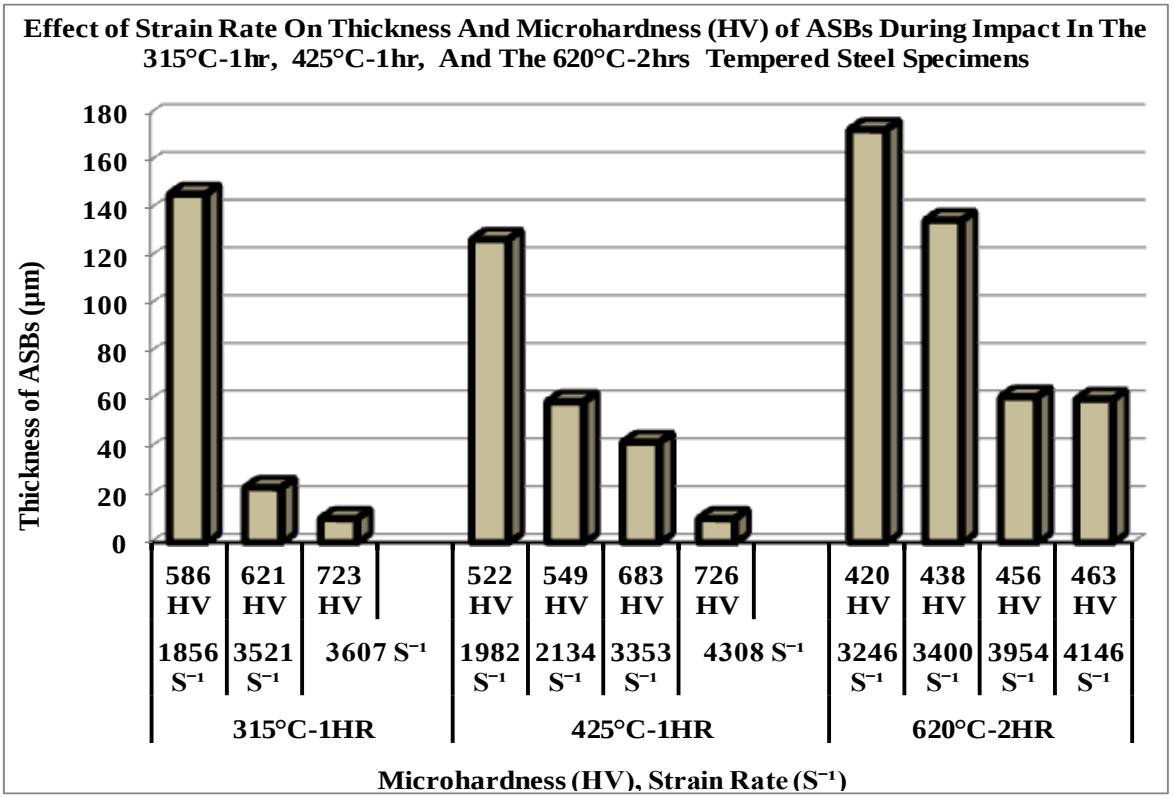

Figure 4- 29: Effect of strain rate on thickness and microhardness (HV) of ASBs in impacted 315°C-1hr, 425°C-1hr, and 620°C-2hrs tempered specimens.

Table 4- 9: Impact properties, thickness, and microhardness of evolved ASBs

	315°C-1hr			425°C-1hr				620°C-2hrs			
Momentum (kg.m/s)	43	44	45	43	45	50	52	45	47	50	50
strain rate (S^{-1})	1856	3521	3607	1982	2134	3353	4308	3246	3400	3954	4146
Thickness of ASBs (µm)	146	23	10	127	59	42	10	173	135	61	60
Microhardness of ASBs (HV)	586	621	723	522	549	683	726	420	438	456	463

Table 4-10 shows the quantification of the average sizes of the martensite laths, and precipitated carbides within the pre-impact steel specimens. The lower the tempering temperature, the smaller the average size of the lath martensite in the pre-impact specimens. The average lengths of the platelet carbides and their aspect ratios within the pre-impact specimens are shown in figure 4-30. The higher susceptibility of the 315°C-1hr tempered steel specimens to shear strain localization is attributed to the relatively high aspect ratios and distribution density of the precipitated carbides within the tempered pre-impact specimens. In addition, the properties of the evolved ASBs after impact can be related to the size and distribution of the martensite laths and precipitated carbides within the tempered specimens prior to impact. Figure 4-31 shows the relation between the widths of the lath matrix prior to impact and the thickness of evolved ASBs after impact. At the same impact momentum, the smaller the width of the lath matrix, the smaller the thickness of the evolved ASBs. In addition, it was observed that the smaller the width of the precipitated interlath platelet carbides within the pre-impact specimens, the smaller the thickness of the evolved ASBs after impact at the same momentum as shown on figure 4-32. This demonstrates that even though the prevailing strain rate/strain determines the structure and appearance of the evolved ASBs during impact, the microstructure of the specimen prior to impact contributes to the nucleation and propagation of ASBs. Thus, the pre-impact microstructure influences not only the susceptibility of the specimen to shear strain localization but also the properties of the evolved shear bands after impact.

Table 4- 10: Quantification of the average sizes of the grains, and precipitated carbides in the pre-impact steel specimens

Tempered Groups	Martensite lath	Platelet carbides within lath (Intralath)		Platelet carbides along lath boundaries (Interlath)	Spherical carbides
	Width (nm)	Length (nm)	Width (nm)	Width (nm)	Diameter (nm)
Martensite	155				
315°C-1hr	209	214	32	41	299
425°C-1hr	238	181	50	46	376
620°C-2hrs	565	203	51	74	400

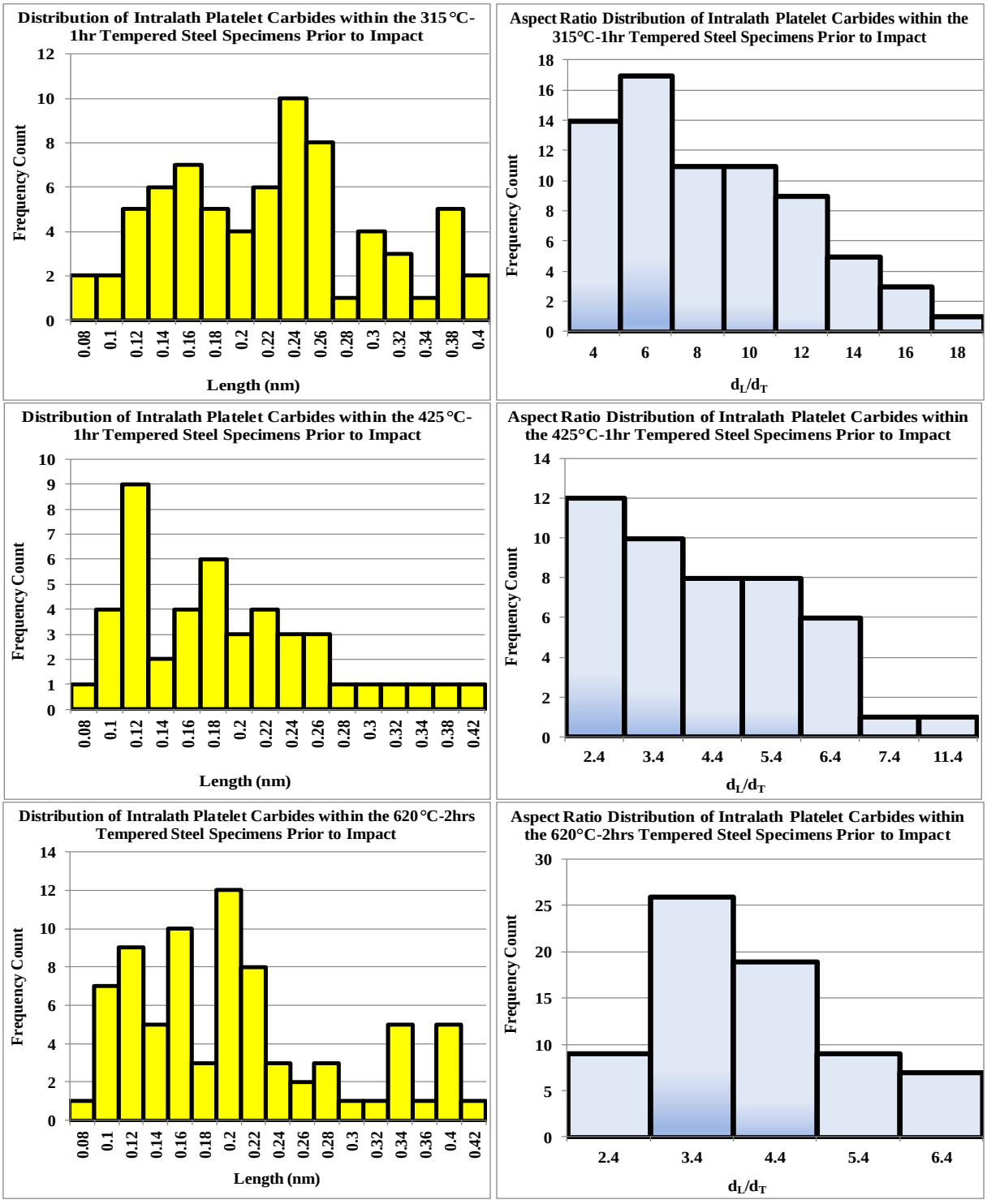

Figure 4- 30: Distribution of intralath platelet carbides and their aspect ratios (d_L/d_T) within (a),(b)315^{o}C-1hr (c),(d) 425^{o}C-1hr (e),(f) 620^{o}C-2hrs tempered specimens respectively.

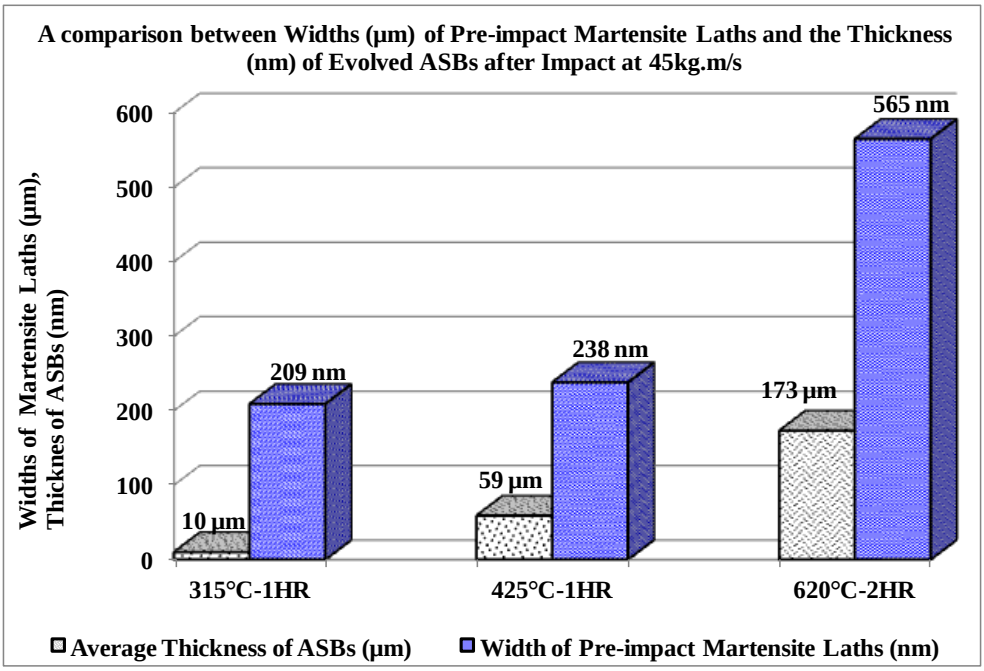

Figure 4- 31: Widths (µm) of martensite laths in the pre-impact specimens and thickness (nm) of evolved ASBs after impact at 45kg.m/s.

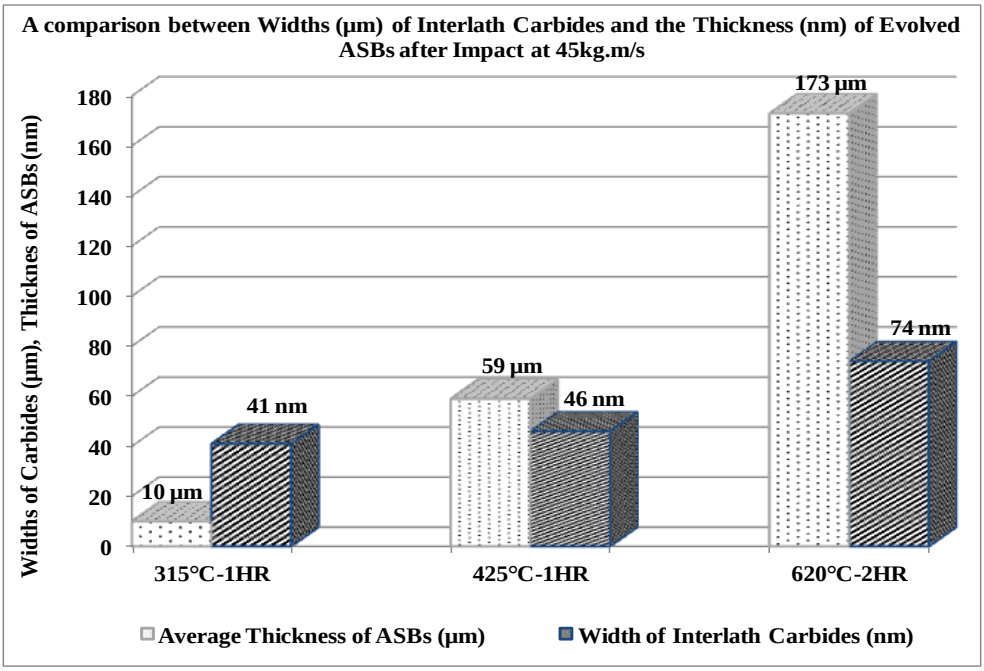

Figure 4- 32: Widths (µm) of interlath carbides in the pre-impact specimens and thickness (nm) of evolved ASBs after impact at 45kg.m/s.

4.3 Transmission Electron Microscopy (TEM) and Scanning Transmission Electron Microscopy (STEM) Analysis of Impacted Steel Specimens

This section presents the microstructural analysis of regions within and outside the evolved ASBs and how the original microstructure has been altered due to the passage of the stress waves through the specimens during the impact tests. There are five subsections in this section. Subsection 4.3.1 presents the TEM/STEM analysis of regions within ASBs that evolved after impact at increasing strain rates/strains. Subsection 4.3.2 presents the microstructure of regions outside ASBs in the impacted specimens while carbide fragmentation and redistribution within the impacted specimens is presented in subsection 4.3.3. Mapping of strain fields within ASBs is presented in subsection 4.3.4. Finally subsection 4.3.5 presents the microstructural changes during post-impact annealing of the ASBs.

4.3.1 Microstructure of Regions within ASBs in the Impacted Steel Specimens

TEM foils were prepared from regions within the evolved ASBs in figure 4-24(a)-d) corresponding to the ASBs in the 620^{O}C-2hrs tempered specimens impacted at increasing strain rates/strains for TEM/STEM analyses. The steel specimens used for this analysis were labelled C, D, E and F corresponding to the strain rates $3189S^{-1}$, $3246S^{-1}$, $3400S^{-1}$, and $3853S^{-1}$ respectively as was shown in figure 4-24. The subsections 4.3.1.1 to 4.3.1.4 systematically describe the observations of the microstructures within the ASBs as a function of strain rate/strain. Subsection 4.3.1.5 presents quantification and statistical analyses of the evolved grains within the ASBs in the impacted specimens.

4.3.1.1 Structure of ASBs in Specimen C after Impact at 3189/S

Figure 4-33 shows typical TEM micrographs of the steel specimen after impact at 3189/S which corresponds to the shear band in figure 4-24(a). This was the first metallographically observable diffused shear band of the impacted specimens within the 620^{O}C-2hrs tempered group as shown by the insert in figure 4-33(b) (the optical micrograph of the diffused ASB in specimen C). The structure within the shear band exhibits the presence of elongated grains with initiated transverse dislocation boundaries as indicated by the short green arrows in figure 4-33(a) to (d). The boundary regions of the elongated grains were well defined as shown by figure 4-33(e). Selected Area Diffraction Pattern (SADP) from the region within the shear band showed that there was some degree of texture as indicated by the arrows in figure 4-33(f).

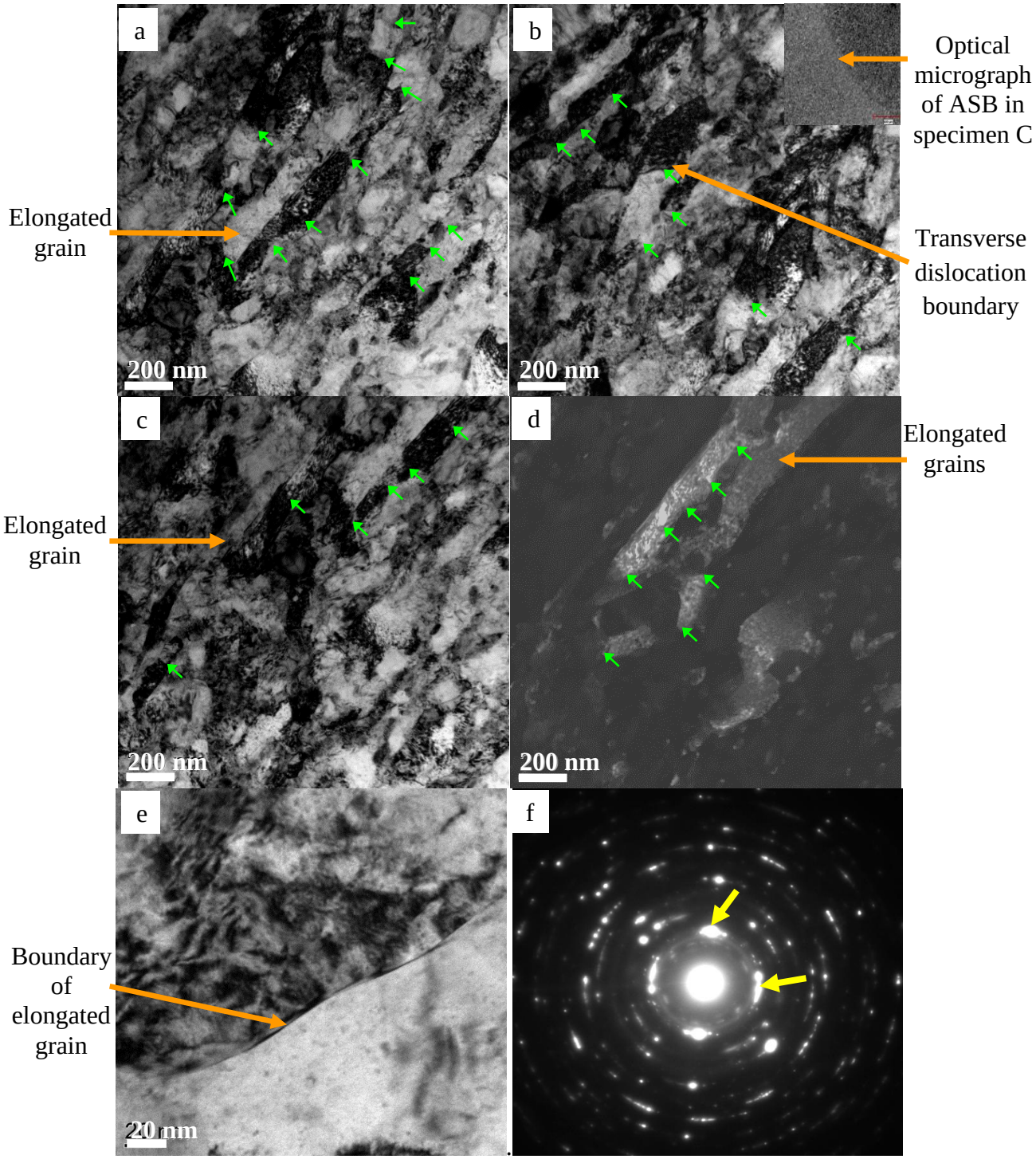

Figure 4- 33: TEM micrographs of the steel specimen C after impact at 3189/S. (a), (b), (c) are BF of the elongated grain structures with transverse dislocation boundaries (indicated by green arrows) (d) DF of (c) showing elongated grains, (e) bright field of an elongated grain with no platelet carbides on the boundary (f) SADP from the shear band.

The elongated grains were decorated with dislocation structures including clusters of dislocations along the predominant transverse boundaries as shown in figure 4-34(a) and (b). Even though the transverse dislocation boundaries were prevalent within the elongated grains, there were also initiated random dislocation boundaries. Figure 4-34(c) is a STEM image of an elongated grain with random dislocation boundaries (delineated by dashed lines) while figure 4-34(d) shows a High Angle Annular Dark Field (HAADF) image of an elongated grain with a transverse dislocation boundary. It is believed that the early stages of breaking of the elongated grains starts with the initiation and arrangement of dislocations into dislocation boundaries (both the random dislocation boundaries and transverse dislocation boundaries) which eventually serve as routes for the breaking up of the elongated grains into smaller grains with increased strain and strain rate. Hence the schematic in figure 4-34(e) and (f) are two suggested possible routes for the breaking of the elongated grains into smaller grains based on the observed arranged dislocation boundaries.

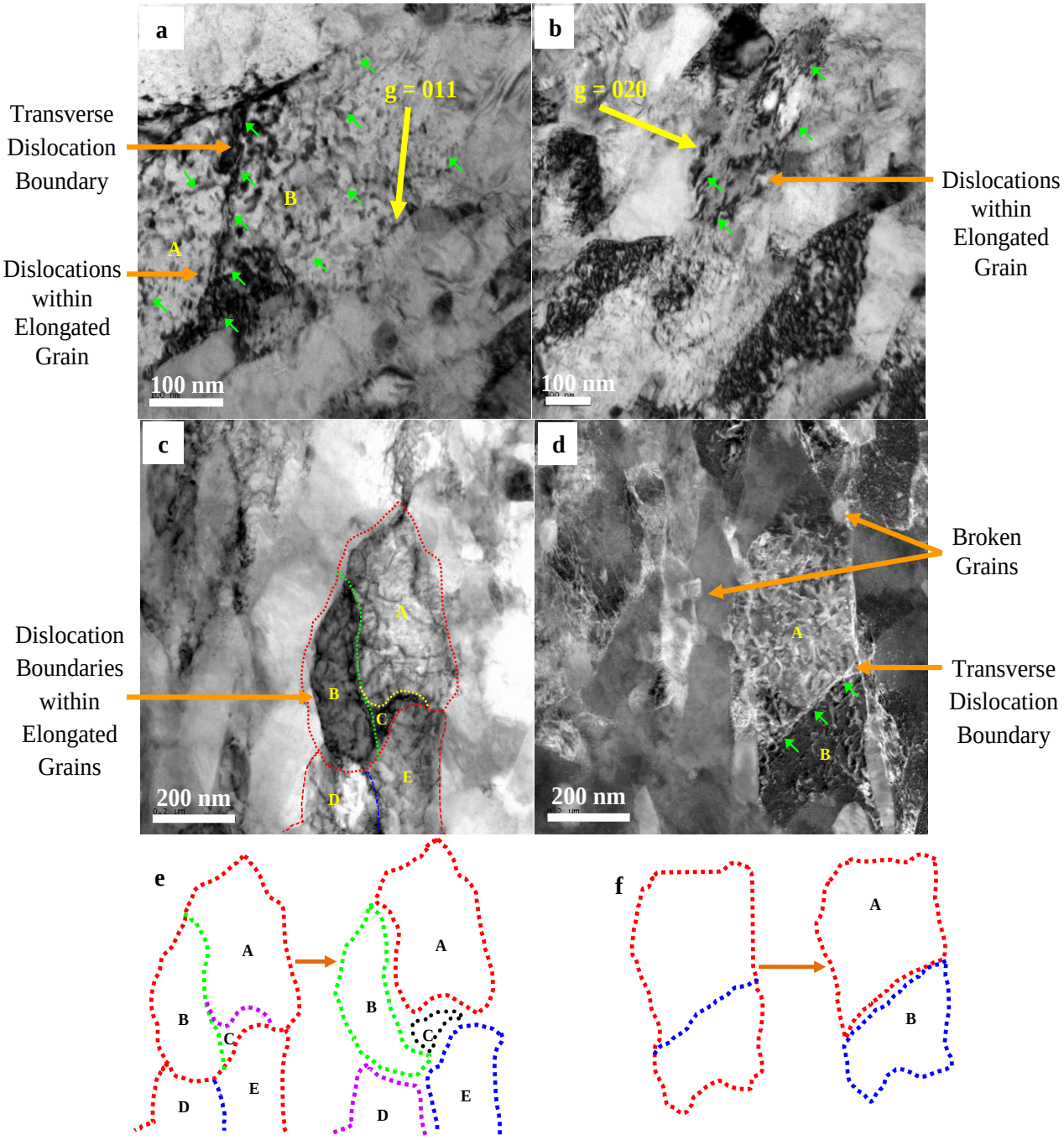

Figure 4- 34: 2-Beam condition of elongated grains showing (a) transverse dislocation boundary with dislocation structures (b) dislocation network within an elongated grain (c) STEM image of an elongated grain with dislocation boundaries (delineated by dashed lines) (d) HAADF image of elongated grain with transverse dislocation boundaries (e), (f) possible routes for grain refinement based on the dislocation boundaries in the steel specimen C after impact at 3189/S.

4.3.1.2 Structure of the ASB in Specimen D after Impact at 3246/S

Typical TEM/STEM micrographs of the steel specimen after impact at 3246/S is shown in figure 4-35, which corresponds to the shear band in figure 4-24(b) The optical micrograph of the ASB is inserted in figure 4-35(a). The structure within the shear band consists of a mixture of broken grains and elongated grains as shown in figure 4-35(a). However, the elongated grains were not as much as those observed within the shear band that evolved after impact at 3189/S. The size of the broken grains was smaller compared with the elongated grains. Some of the broken grains were observed as undergoing boundary refinement due to rotation of the grains as shown in the STEM image in figure 4-35(b) (details on grain rotation under the quantification section). The refinement of the boundaries of the broken grains occurs along the initiated transverse dislocation boundaries which serve as routes for breaking of the grains as shown in figure 4-35(b). Figure 4-35(c) is a bright field micrograph of the mixture of elongated and broken grains while figure 4-35(d) is a dark-field micrograph of (c) showing the stages of broken grain boundary refinement. There is a mixture of thick and thin transverse dislocation boundaries as shown in figure 4-35(e) with the thick boundaries having more dislocations clustered on them than the thin boundaries. SADP from the region within the shear band shows that the orientations of the grains are becoming more random as shown in figure 4-35(f).

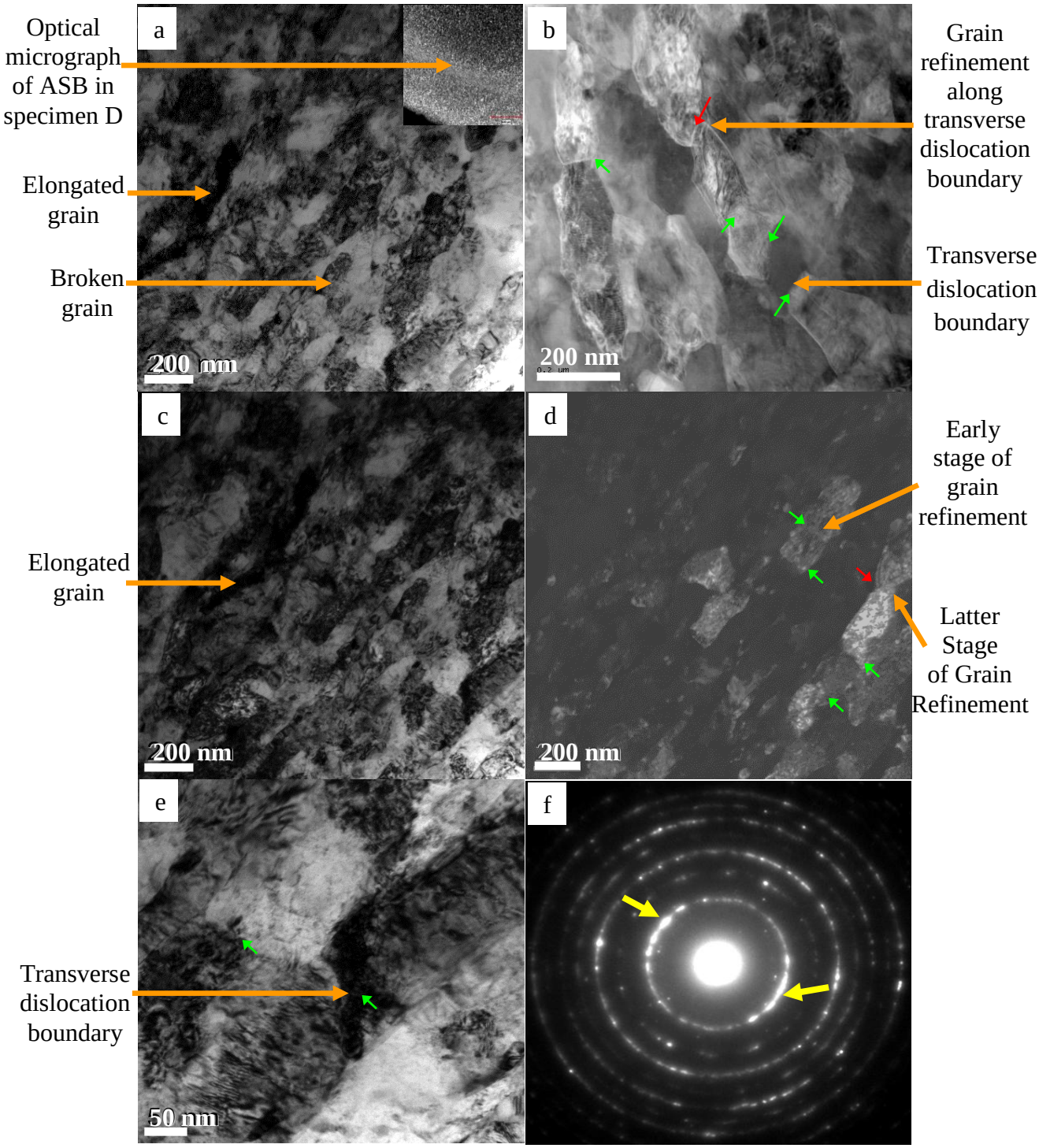

Figure 4- 35: TEM micrographs of the steel specimen D after impact at 3246/S. (a) BF of mixed elongated and broken grains (b) STEM image of grain refinement along transverse dislocation boundaries (c) BF of the elongated and broken grains (d) DF of (c) showing the stages of grain refinement (e) transverse dislocation boundaries (f) SADP from the shear band.

The broken grains were smaller in size and had square or straight boundaries. Figure 4-36(a) and (b) show a broken grain under 2-Beam conditions. Most of the dislocations are within the broken grains compared to the elongated grains which had the dislocations aligned on the boundaries. Figure 4-36(c) shows a STEM image of an elongated grain with random boundaries (delineated by dashed lines) and dislocations within the elongated grain. The dislocations were not aligned on the random boundaries as was observed in the previous structure. Figure 4-36(d) to (f) show broken grains that are under different stages of boundary refinement due to grain rotation.

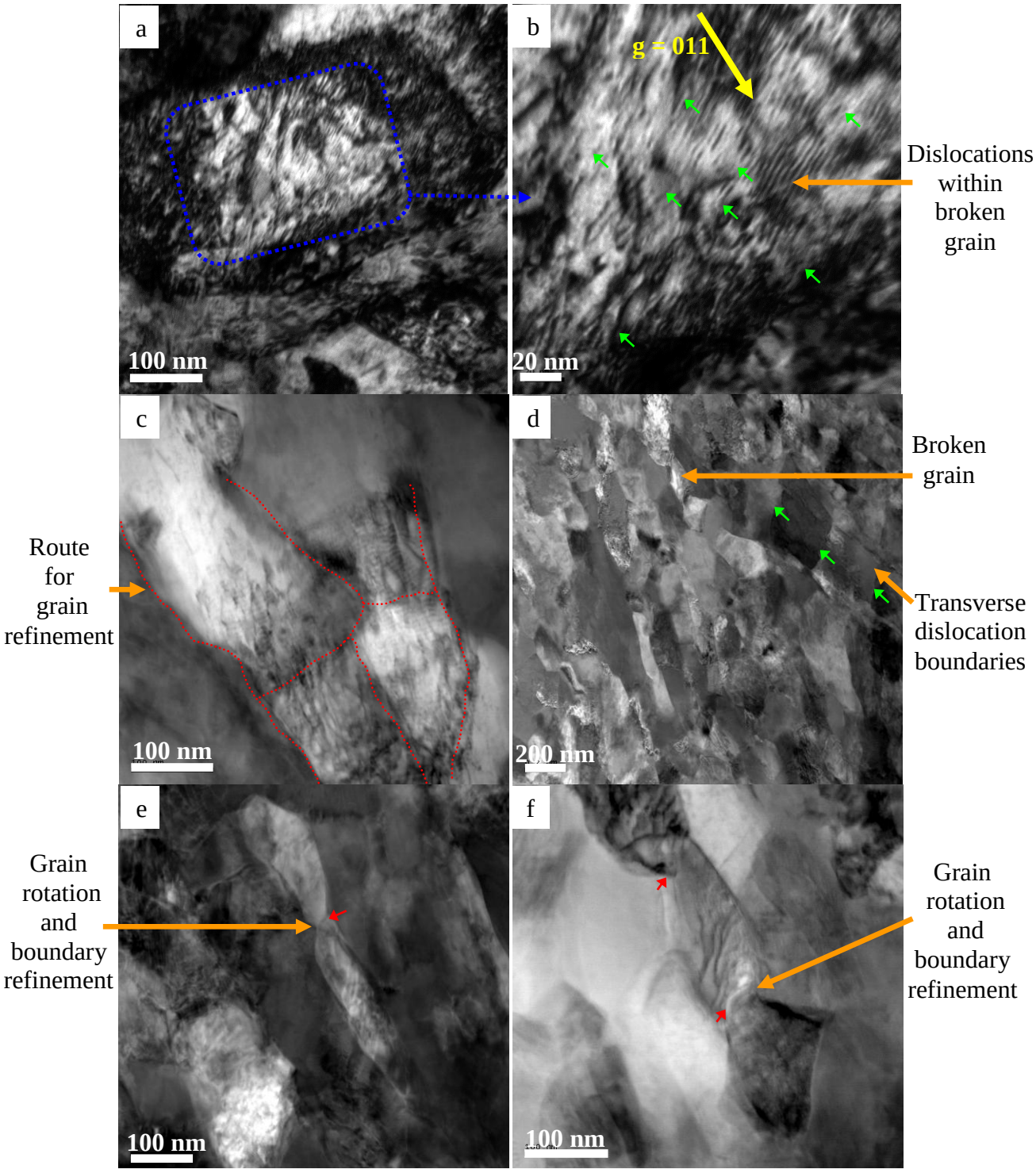

Figure 4- 36: (a), (b) Broken grain under 2-Beam conditions (c) STEM of an elongated grain with dislocation boundaries (d) HAADF of elongated grains with transverse dislocations, broken grains and refined grains (e) HAADF and (f) STEM of boundary refinement along transverse dislocation boundaries in specimen D after impact at 3246/S.

4.3.1.3 Structure of the ASB in Specimen E after Impact at 3400/S

The structure of the shear band that evolved in the steel specimen after impact at 3400/S, corresponding to the shear band in figure 4-24(c), consisted of broken grains coexisting with evolved nanograins as shown in figure 4-37(a)-(d). The optical micrograph of the shear band is inserted in figure 4-37(a). The most distinguishing features of the broken grains were their relatively small sizes and straight boundaries (square edges). The broken grains were predominant in this structure compared to the evolved nanograins. Subgrains were also observed within some of the grains as shown in figure 4-37(e). SADP from the region within the shear band showed that the orientation of the grains were more random as shown on the ring-like diffraction pattern in figure 4-37(f).

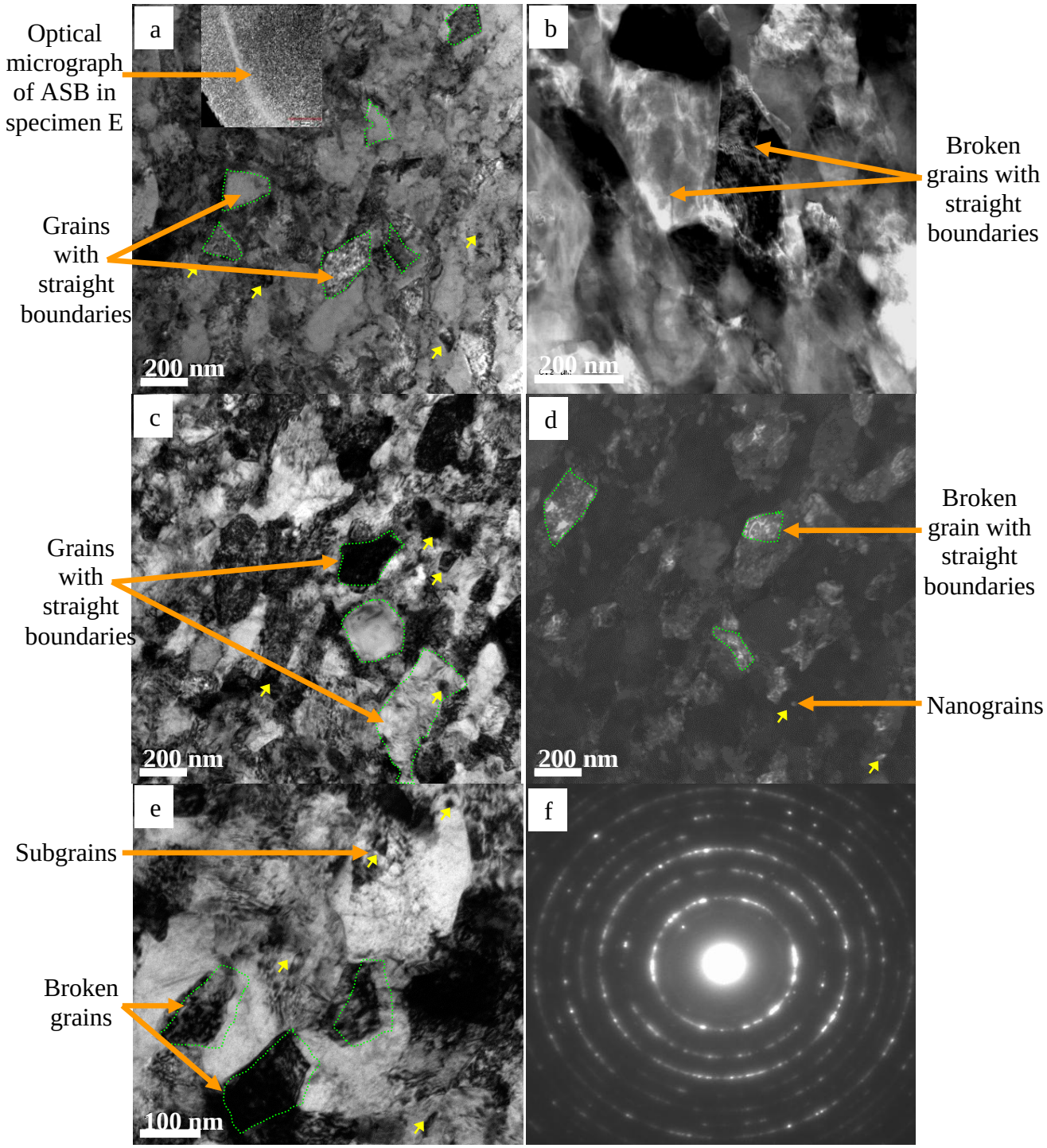

Figure 4- 37: TEM micrographs of steel specimen E after impact at 3400/S. (a) BF micrograph of mixed broken and nanograins (b) HAADF image of broken grains with straight boundaries (c) BF micrograph of mixed broken and nanograins (d) DF micrograph of (c) showing the broken grains (e) BF micrograph showing broken grains and subgrains (f) SADP from ASB.

Figure 4-38(a) and (b) show two broken grains under 2-Beam conditions. The dislocation structures were predominant within the broken grains than on the grain boundaries. The STEM image in figure 4-38(c) also confirms that most of the dislocations are within the grains than on the boundaries. In addition, broken grains under boundary refinement are also common within this structure as shown by figure 4-38(d).

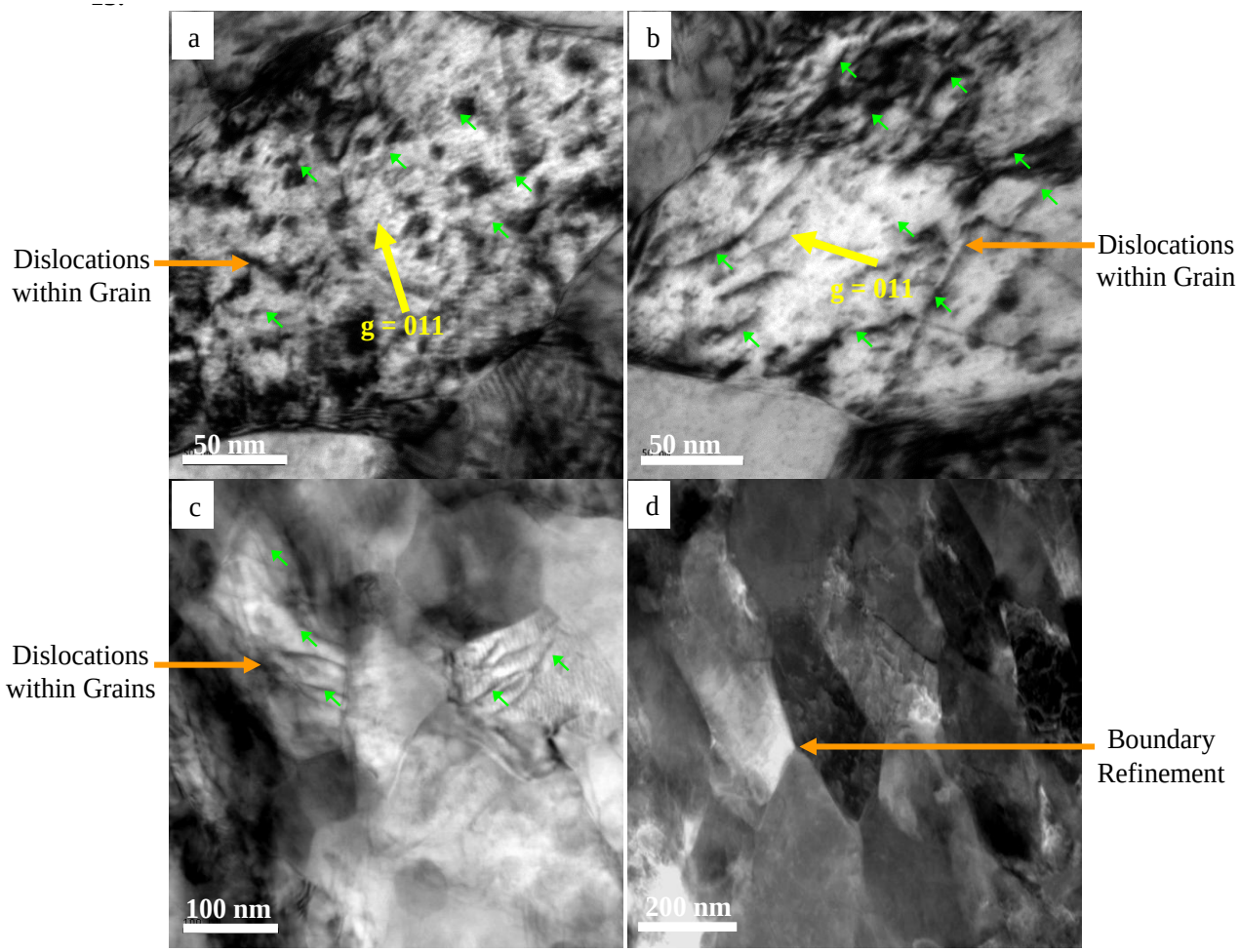

Figure 4- 38: (a), (b) Dislocations within broken grains under 2-beam condition (c) STEM image of broken grains with dislocations (d) HAADF image of broken grains during boundary refinement in the steel specimen E after impact at 3400/S.

4.3.1.4 Structure of the ASB in Specimen F after Impact at 3853/S

Refined grains coexisting with evolved nanograins and subgrains characterize the structure within the shear band that evolved after impact at 3853/S (corresponding to the shear band in figure 4-24(d)) as shown on the micrographs in figure 4-39. The optical micrograph of the ASB is inserted in figure 4-39(a). The refined grains are relatively smaller than the broken grains and have round boundaries as indicated by the arrows in figure 4-39(a)-(c). The presence of the evolved nanograins is evident from figure 4-39(d) which is a dark-field image of figure 4-39(c). The nanograins were smallest, followed by the subgrains and then the refined grains as shown by figures 4-39(d) and (e). SADP in figure 4-39(f) also suggests a more random grain orientation within the shear band. This shear band appeared very bright under the optical microscope as shown on figure 4-24(d) than the previous evolved shear bands.

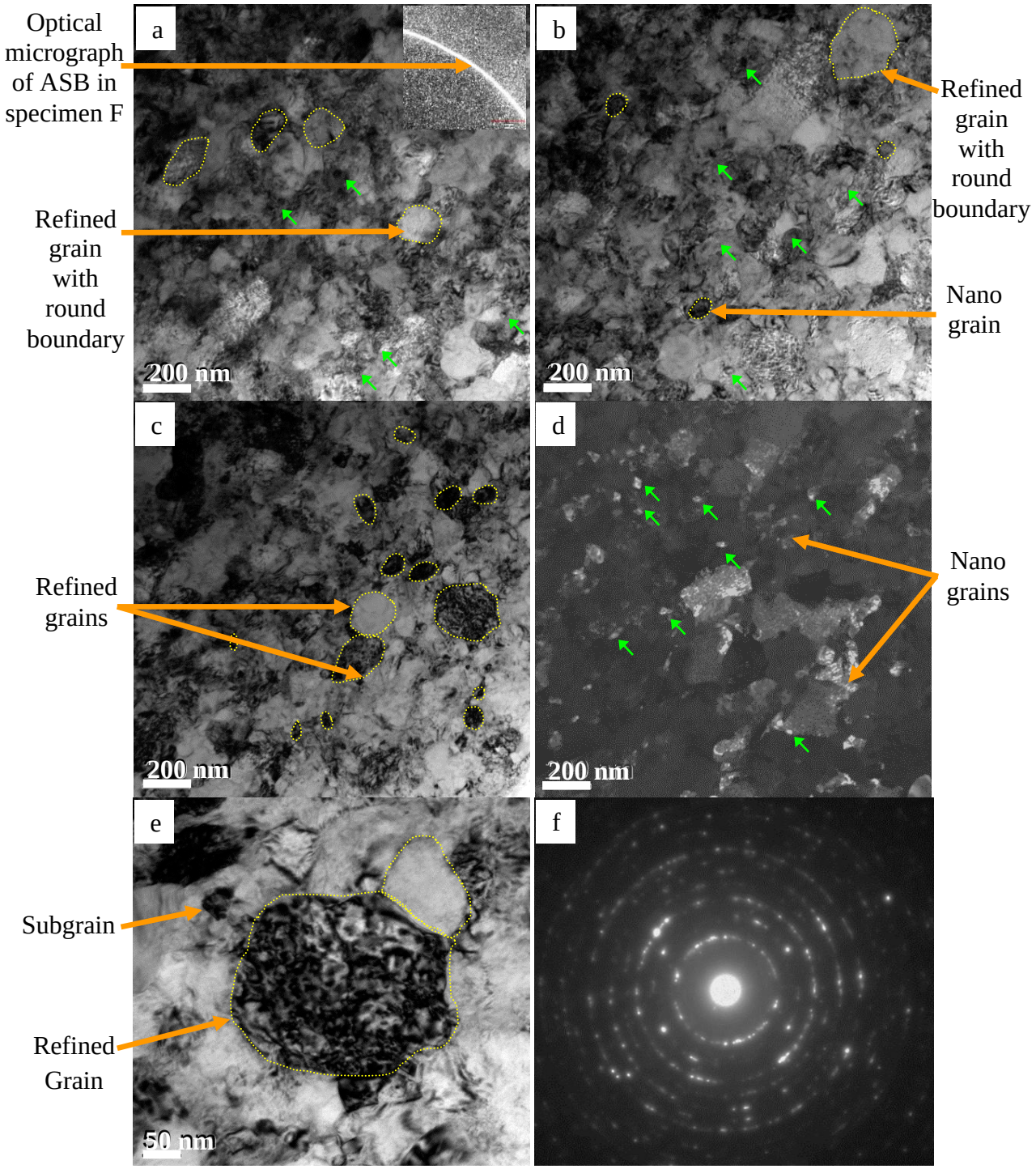

Figure 4- 39: Typical TEM micrographs of the steel specimen F after impact at 3853/S. (a), (b), (c) are bright field micrographs of the refined, and evolved nanograins and subgrains (d) dark field of (c) showing evolved nanograins, (e) bright field of a subgrain and a refined grain (f) Selected Area Diffraction Pattern (SADP) from the ASB.

The refined grains were decorated with dislocations and dislocation structures as shown in figure 4-40(a) and (b) which are two grains under a 2-Beam conditions. Figure 4-40(c) and (d) also show an evolved nanograins with dense dislocation structures within the grain. It is believed that the nanograins evolve during the breaking of the elongated grains such that the random dislocation boundaries that were observed at lower strain rates could lead to the formation of these nanograins based on the routes for breaking of the grains as indicated on figure 4-34(c) and (e). A single occasion of an elongated grain with transverse dislocations was observed coexisting with a refined grain and subgrains as shown in figure 4-40(e). Figure 4-40(f) shows a refined grain with a subgrain also under boundary refinement.

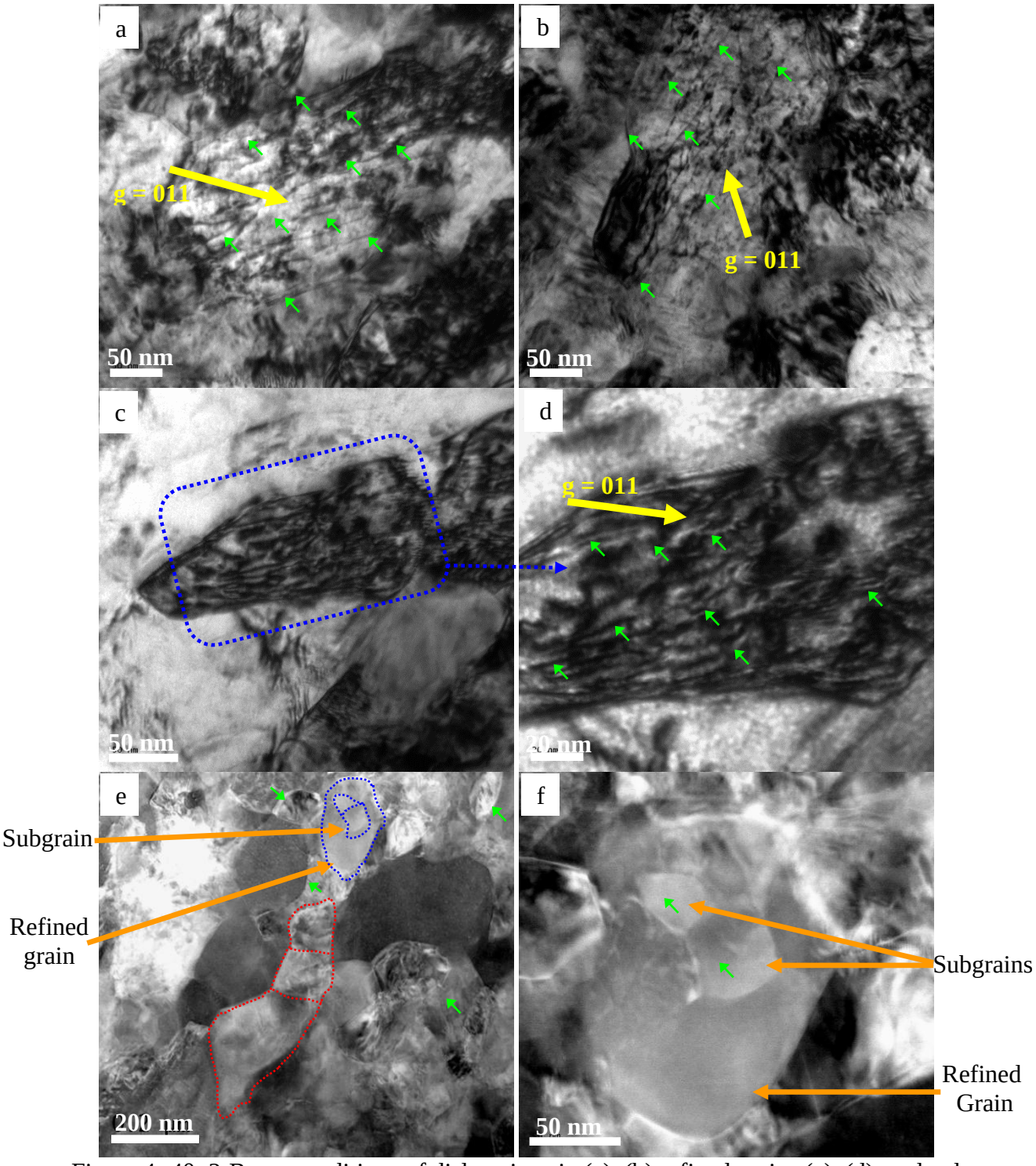

Figure 4- 40: 2-Beam conditions of dislocations in (a), (b) refined grains (c), (d) evolved nanograins. (e) HAADF image of elongated grain coexisting with a refined grain and subgrains (f) HAADF image of refined grain with subgrains in steel specimen F after impact at 3853/S.

4.3.1.5 Quantification and Statistical Analysis of the Evolved Grains within Adiabatic Shear Bands in the Impacted Steel Specimens

Quantification of the grains within the evolved adiabatic shear bands after impact were carried to determine the grain size distribution. It was observed that as the strain rate increases, the average size of the evolved grains within the shear bands decreases as shown on figure 4-41. The histograms in figure 4-42(a)-(d) show the distributions of the grain sizes within the adiabatic shear bands that evolved after impact at $3189S^{-1}$, $3246S^{-1}$, $3400S^{-1}$, and $3853S^{-1}$ respectively. Even though the histograms are all right skewed, the data spread shows that there was a significant reduction in the sizes of the grains that evolved within the shear band as the strain rate was increased. The elongated grains within the shear band that evolved after impact at $3189S^{-1}$ had an average length of 229nm and an average width of 91nm. An average grain size of 159nm was also measured for the grains within the shear band as shown on figure 4-42(a). The average length of the grains that evolved within the shear bands after impact at $3246S^{-1}$ was 195nm and a width of 93nm while the average size of the evolved grains was 145nm as shown on figure 4-42(b) representing a 9% decrease in the average grain size when compared to that of figure 4-42(a). The average size of the grains that evolved within the shear bands after impact at $3400S^{-1}$ was 133nm with an average length and width of 165nm and 99nm respectively as shown in figure 4-42(c). An average length of 112nm and a width of 75nm were measured for the grains that evolved after impact at $3853S^{-1}$. The average size of the grains was 94nm. The shear band that evolved after impact at $3853S^{-1}$ was approximately a 21% increase in strain rate compared to that which evolved after impact at $3189S^{-1}$. However, there was an approximate 41% reduction in the grain size of the grains that evolved after impact at $3853S^{-1}$ when compared to that after $3189S^{-1}$. That is a 21% increase in strain rate during the impact gave a 41% reduction in grain sizes within the shear bands.

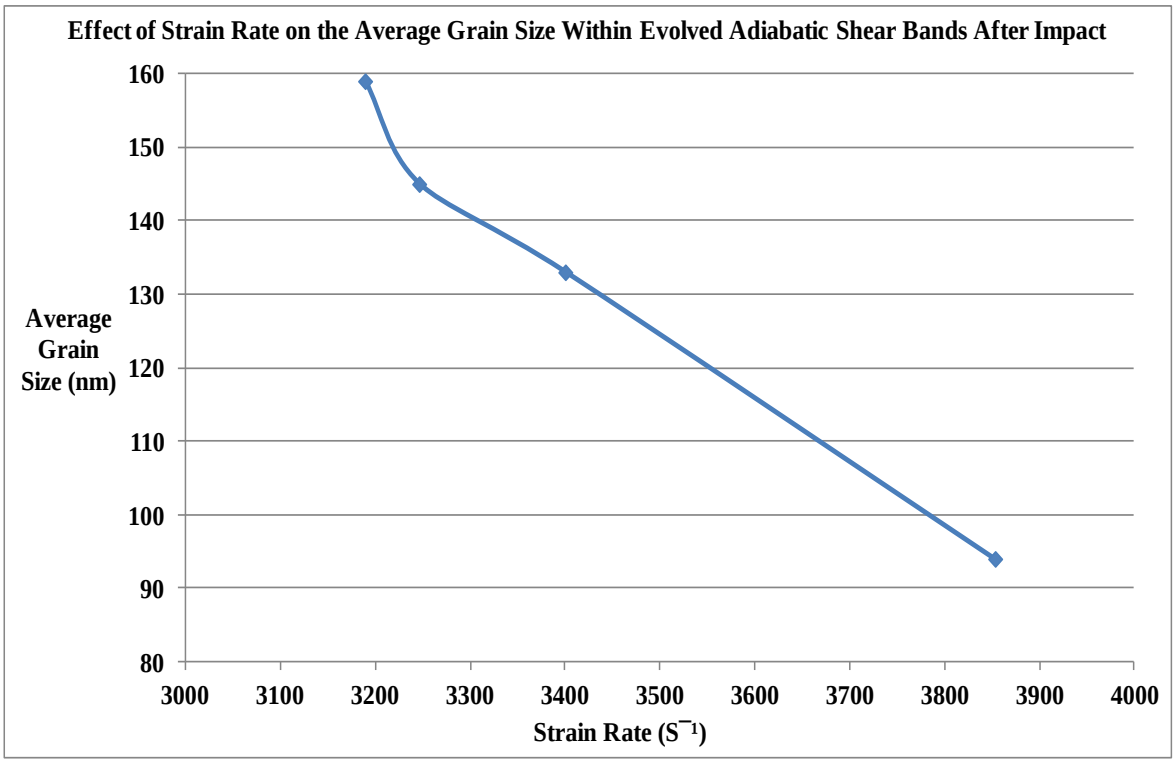

Figure 4- 41: Effect of strain rate on the average grain size within evolved adiabatic shear bands after impact

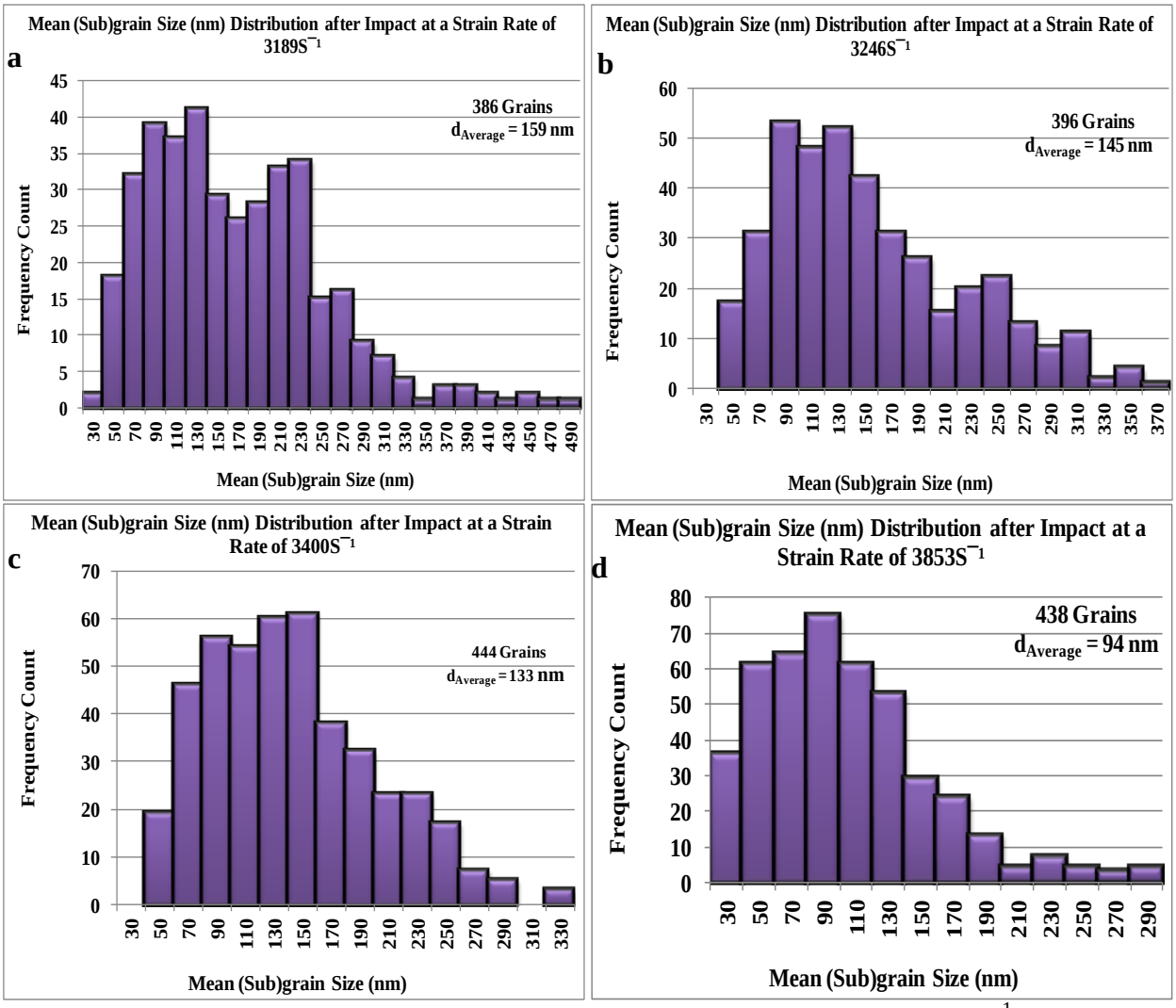

Figure 4- 42: Grain size distribution within the adiabatic shear bands. (a) C-3189S^{-1}, (b) D-3246 S^{-1}, (c) E-3400 S^{-1}, (d) F-3853 S^{-1}

Figure 4-43(a)-(d) show the distribution of the aspect ratios (d_L/d_T) of the grains within the adiabatic shear bands that evolved after impact at 3189S^{-1}, 3246S^{-1}, 3400S^{-1}, and 3853S^{-1} respectively. The average aspect ratios of the grains decreased from 2.6 for the grains within the shear bands in the specimen that was impacted at 3189S^{-1} to 1.6 for the grains within the shear bands that evolved after impact at 3853S^{-1} as shown on table 4-11. This also indicated that a 21%

increase in strain rate resulted in approximately a 39% reduction in the aspect ratios of the grains that evolved within the shear bands.

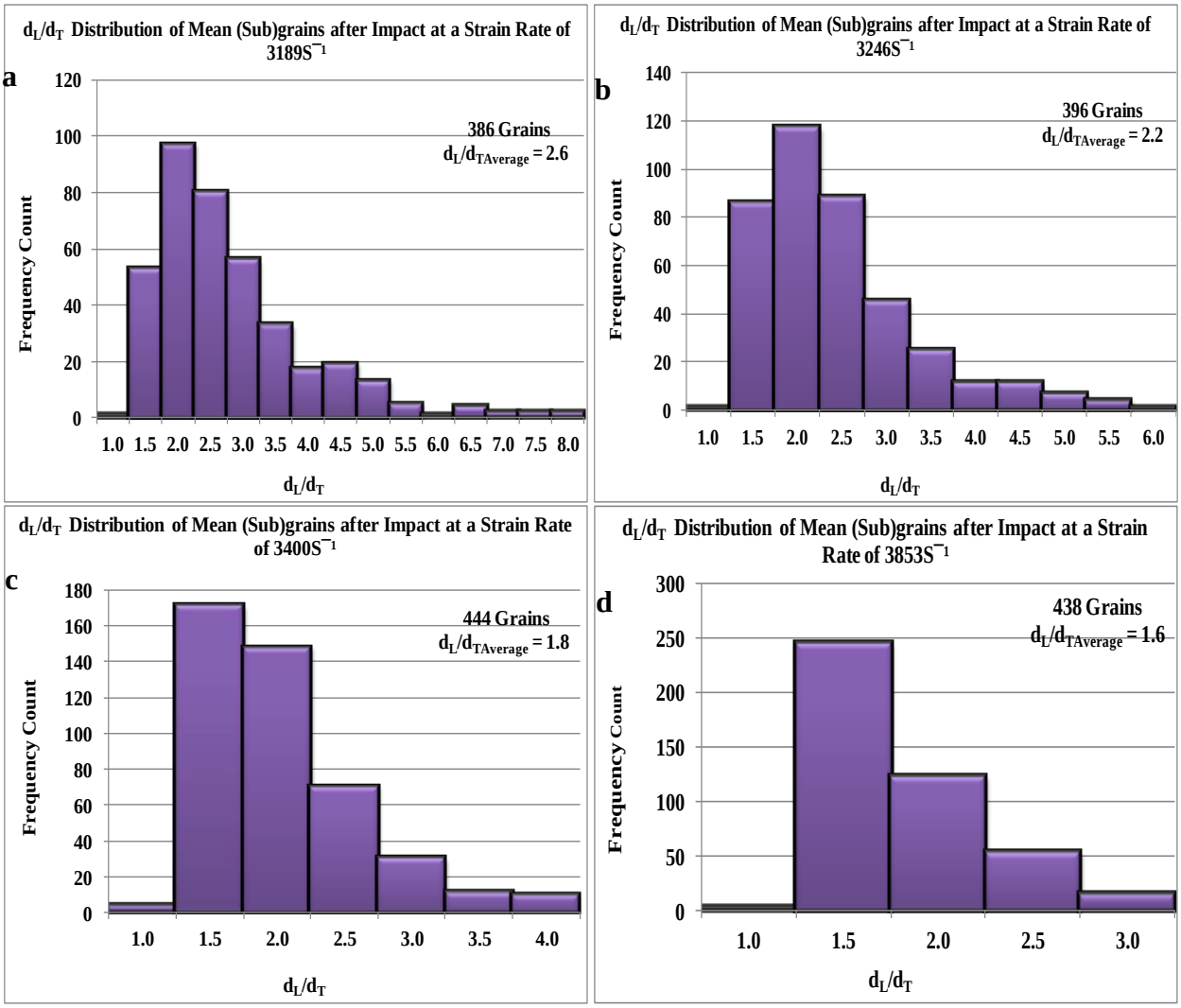

Figure 4- 43: Distribution of the aspect ratios (d_L/d_T) of the grains within the adiabatic shear bands. (a) C-3189S^{-1}, (b) D-3246 S^{-1}, (c) E-3400 S^{-1}, (d) F-3853 S^{-1}

Table 4- 11: Quantification of the grains within the evolved adiabatic shear bands

Specimen	Strain Rate	Number of Grains Measured	Average Length of Grains (nm)	Average Width of Grains (nm)	Average Grain Size (nm)	Average Angle of Grains	Average Aspect Ratio of Grains
C	3189/S	386	229	91	159	54°	2.6
D	3246/S	396	195	93	145	67°	2.2
E	3400/S	444	165	99	133	88°	1.8
F	3853/S	438	112	75	94	86°	1.6

Figure 4-44(a)-(d) show the angular distribution of the grain elongation axes and the impact direction for the grains within the adiabatic shear bands that evolved after impact at $3189S^{-1}$, $3246S^{-1}$, $3400S^{-1}$, and $3853S^{-1}$ respectively. For the impact from $3189S^{-1}$ to $3246S^{-1}$, the average angle between the grain elongation axis and the impact direction increased from 54^{O} to 67^{O} for the grains within the evolved shear bands. As the strain rate was increased from $3246S^{-1}$ to $3400S^{-1}$, the average angle increased to 88^{O}. This is attributed to the rotation of the grains as the imposed strain rate and strain increases. The refinements of the boundaries of the broken grains are thought to occur during this rotation process with thermal assistance due to the conversion of plastic work into heat. Moreover, most of the grains within the shear band that evolved after impact at $3853S^{-1}$ had round boundaries and large numbers of evolved nanograins and subgrains. This accounts for the recorded average angle of 86^{O} for these grains as shown on table 4-11.

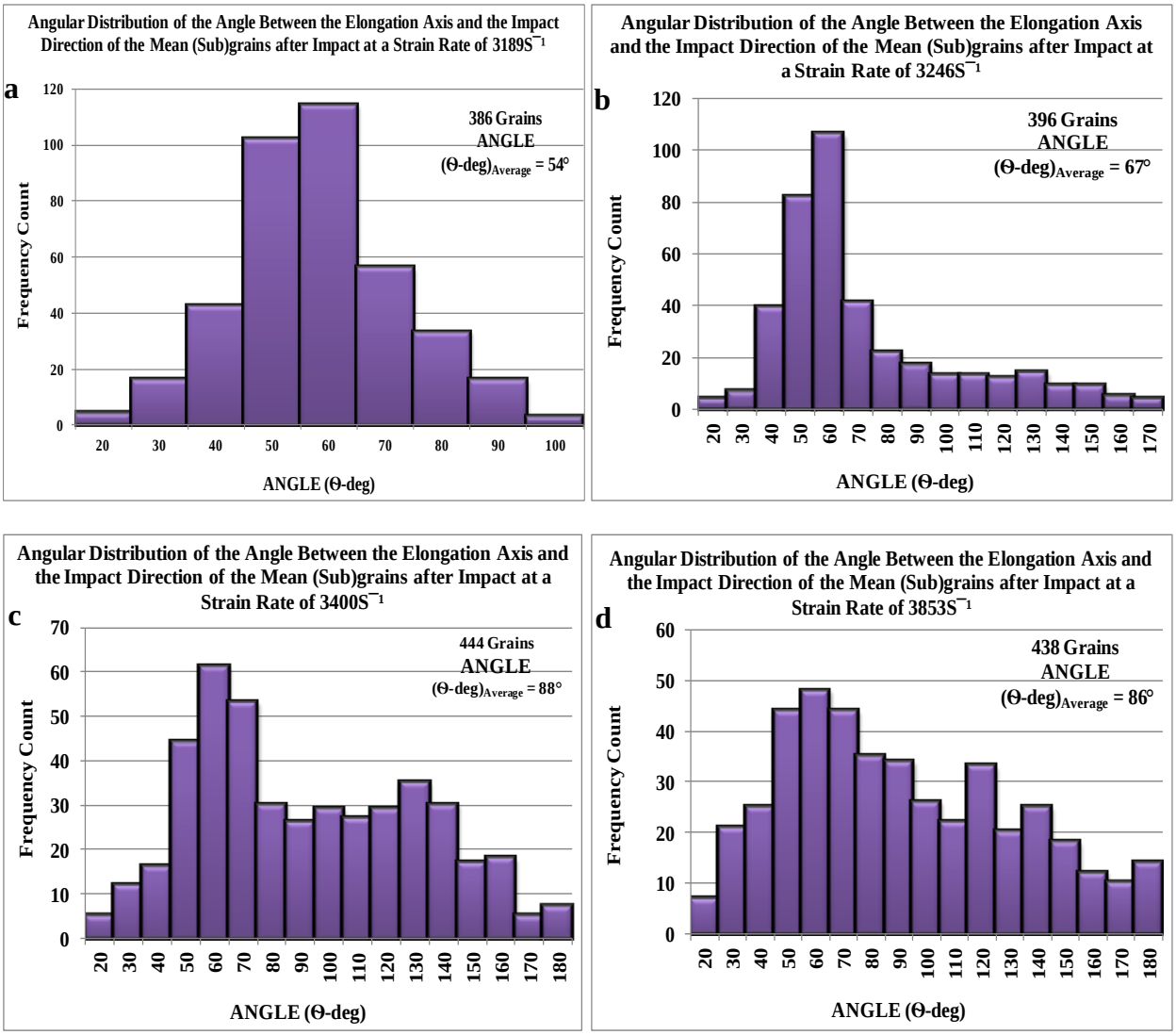

Figure 4- 44: Distribution of the angles between the shear band grain elongation axis and the impact direction. (a) C-3189S^{-1}, (b) D-3246 S^{-1}, (c) E-3400 S^{-1}, (d) F-3853 S^{-1}

4.3.2 Microstructure of Regions Outside ASBs in the Impacted Steel Specimens

TEM thin foils were prepared from regions close to ASBs and regions away from the ASB in the 620^{O}C-2hrs tempered specimen F impacted at $3853S^{-1}$. This was done to observe the microstructure in regions outside the ASB in order to document conditions that could precede the evolution of the structure within the ASB. Typical TEM Bright Field (BF) and Dark Field (DF) micrographs of regions outside the are shown in figure 4-45. Figure 4-45(a)-(b) show the micrographs of the regions away from the ASB while Figure 4-45(c)-(d) show micrographs of regions close to the ASB. During impact, regions away from the shear bands develop dense dislocation walls in the ferrite grains, evolving gradually into sub-boundaries and highly misoriented grain boundaries at increasing strains, leading to grain refinement of the ferrite. The evolved grains in regions away from the ASB had an average length of 449nm and a width of 321nm corresponding to an approximate aspect ratio of 1.4. The grains were bounded by "knitted" and interlocked dislocations. Carbides with reduced aspect ratios were observed in this region. The spherical carbides in the specimens prior to impact had an average diameter of 400nm which reduced to an average of 84nm in regions away from ASB after impact. Also the intralath platelet carbides reduced from an initial length of 203nm and a width of 51nm corresponding to an approximate aspect ratio of 4 to a length of 124nm and a width of 46nm, corresponding to an approximate aspect ratio of 2.7. The microstructure close to the ASB on the other hand were characterized by evolved grains immersed in dense tangles of dislocations as shown in figure 4-45(c) and (d). There were no observed spherical carbides in these regions. However, platelet carbides were observed under relatively high magnifications. SADPs from regions away from the ASB had diffused spots compared to the spotty rings from regions close to the ASB as shown in figure 4-45(e)-(f).

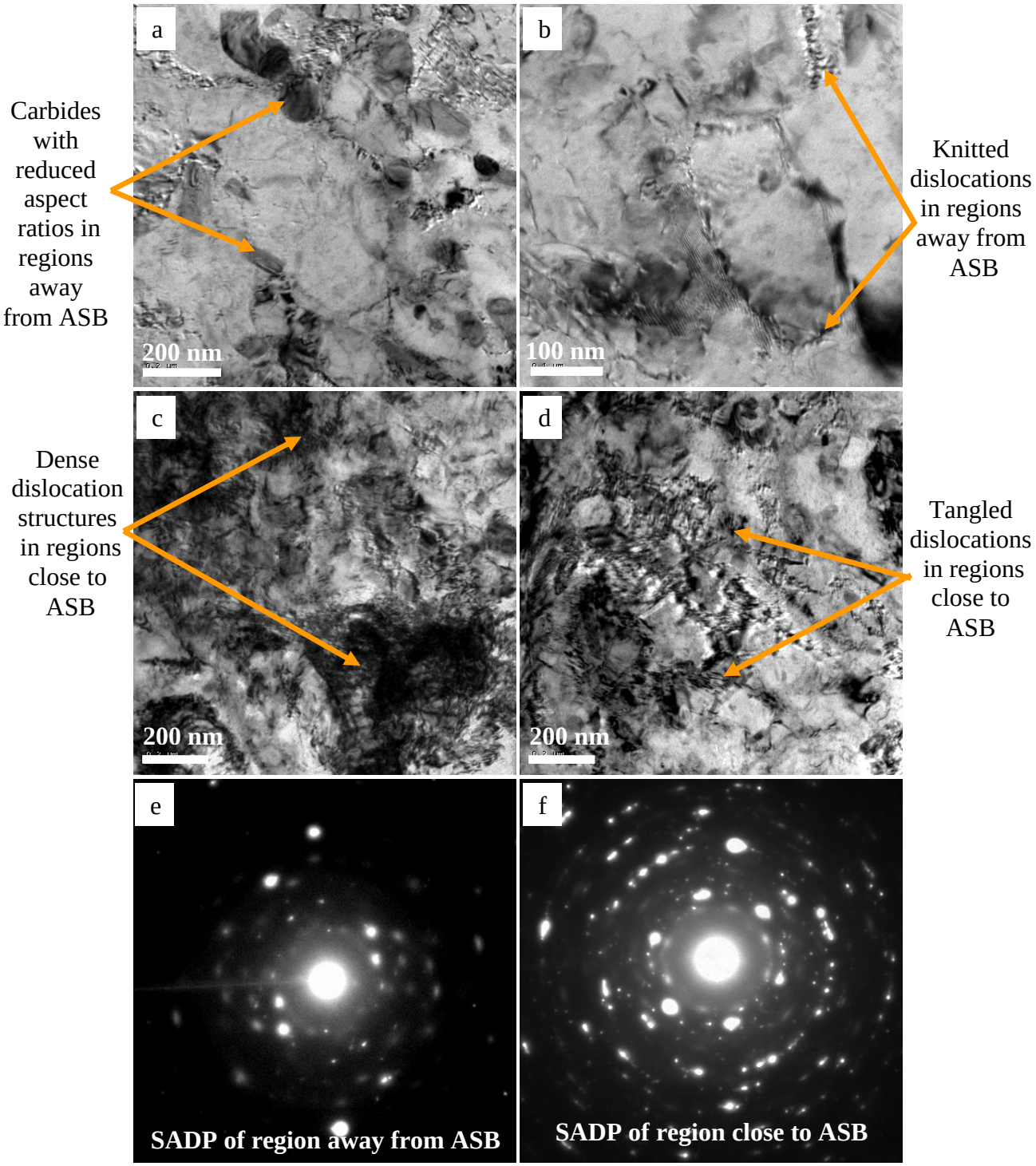

Figure 4- 45: TEM micrographs of the 620^{O}C-2hrs tempered specimen F impacted at 3853 S^{-1} showing (a) BF region away from ASB (b) DF region away from ASB (image taken with the (020) cementite reflection as shown on the inserted SADP). (c), (d) BF micrographs of regions close to ASB (e) SADP of region away from ASB (f) SADP of region close to ASB.

Figure 4-46 show dislocation tangles and structures in regions close to the evolved ASB compared to the knitted dislocations aligning grains developed in regions away from the ASB. The presence of the high density of dislocations in regions away from the ASB and in regions close to the ASB demonstrate that the emergence of dislocations is an integral part of the impact process and precede substructural evolutions that occur in highly strained regions of the impacted specimen.

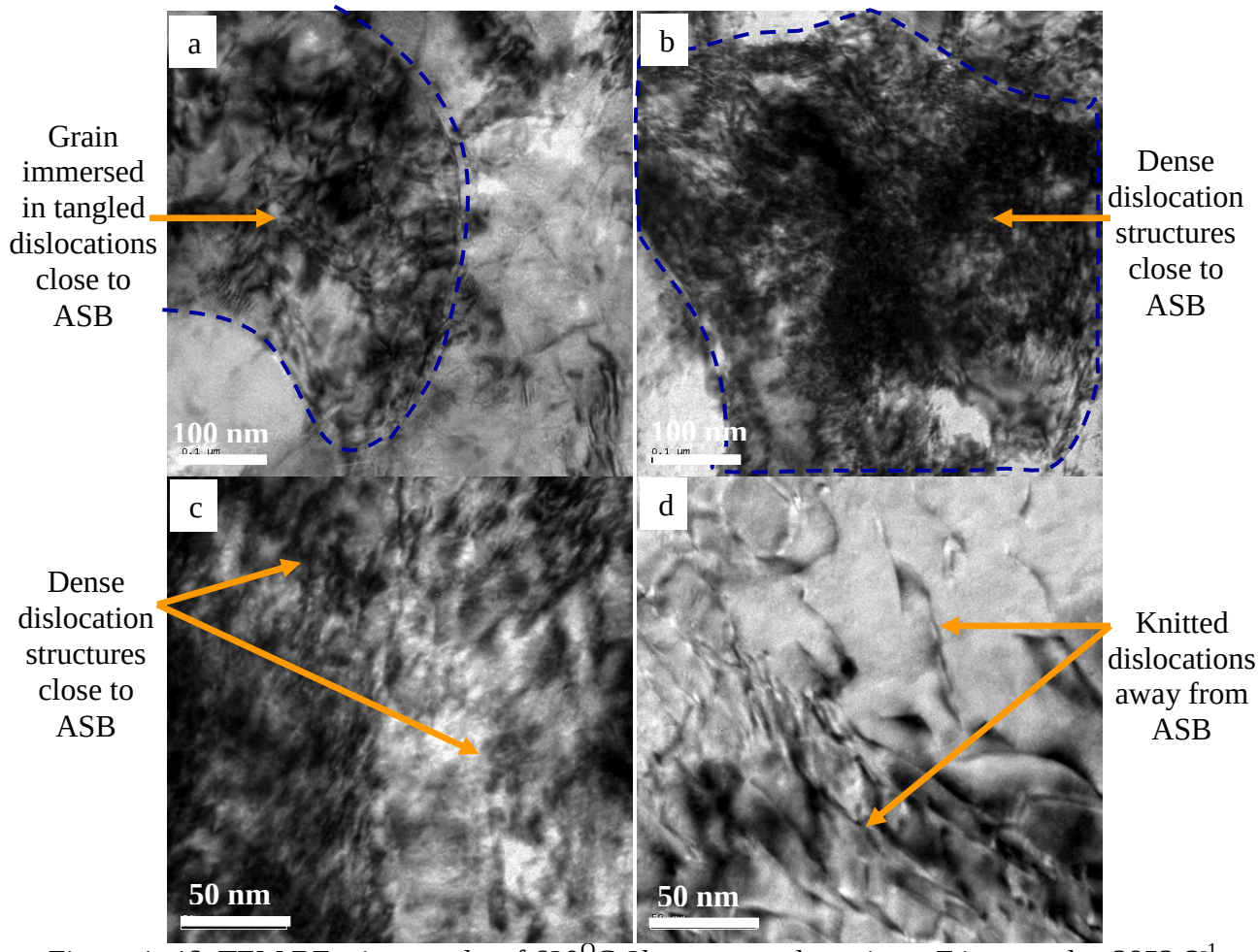

Figure 4- 46: TEM BF micrographs of 620^{O}C-2hrs tempered specimen F impacted at 3853 S^{-1} showing (a), (b), (c) dislocation tangles in regions close to ASB (d) "knitted" dislocations in regions away from ASB.

4.3.3 Carbide Fragmentation and Redistribution within the Impacted Steel Specimens

The structure of the tempered specimens prior to impact contained platelet and spherical carbides within a ferrite matrix. Nevertheless, there were no apparent platelet or spherical carbides in the regions within evolved ASBs. Backscattered Electron (BSE) micrographs of the evolved ASB in the 620^{O}C-2hrs tempered specimen E impacted at 3400 S^{-1}in is shown in figure 4-47. Residual carbides were observed within regions outside the ASB whereas none of these carbides were present within the shear bands.

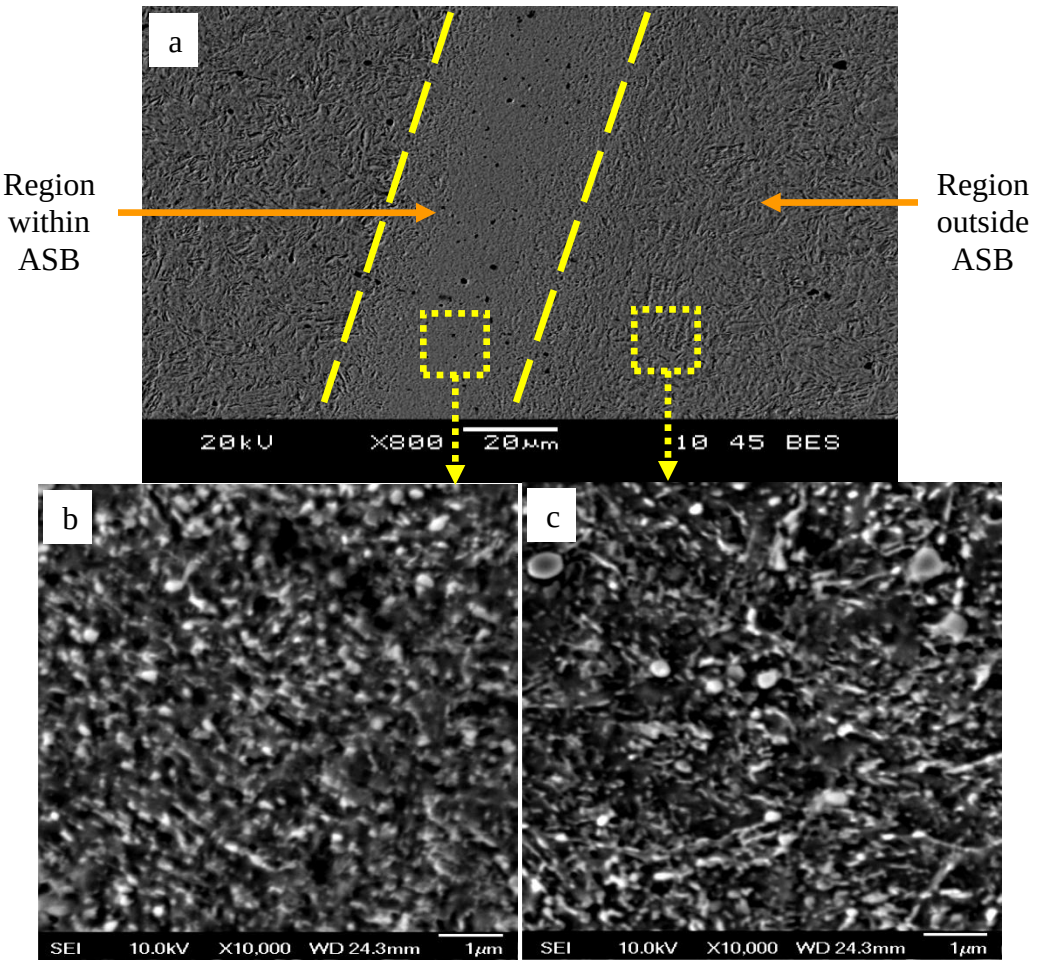

Figure 4- 47: SEM micrographs of (a) ASB (b) regions outside ASB (c) regions within ASB.

A detailed combination of imaging and diffraction analyses revealed that there were fine carbide particles within regions of the evolved shear bands. These fine particles were resolved to be residual carbide particles as shown in figure 4-48. The residual carbide particles were fine and virtually evenly distributed within the evolved structures of the ASBs. Figure 4-48(c) is a bright field micrograph of a region within the shear band while figure 4-48(d) is a dark field micrograph of figure 4-48(c) showing the presence of fine residual carbide particles within the grains of the shear band. Figure 4-48(e) shows a dark field image of a region within a shear band that evolved after impact at $3853S^{-1}$ taken with the (023) cementite reflection as shown on the Selected Area Diffraction Pattern (SADP) in figure 4-48(f). The residual carbide particles were finer than the structures within the evolved shear bands. Due to the brittle and harder nature of the carbides compared to the ferrite matrix, it is believed that plastic deformation occurs within the carbides during impact which results in carbide fracture and fragmentation.

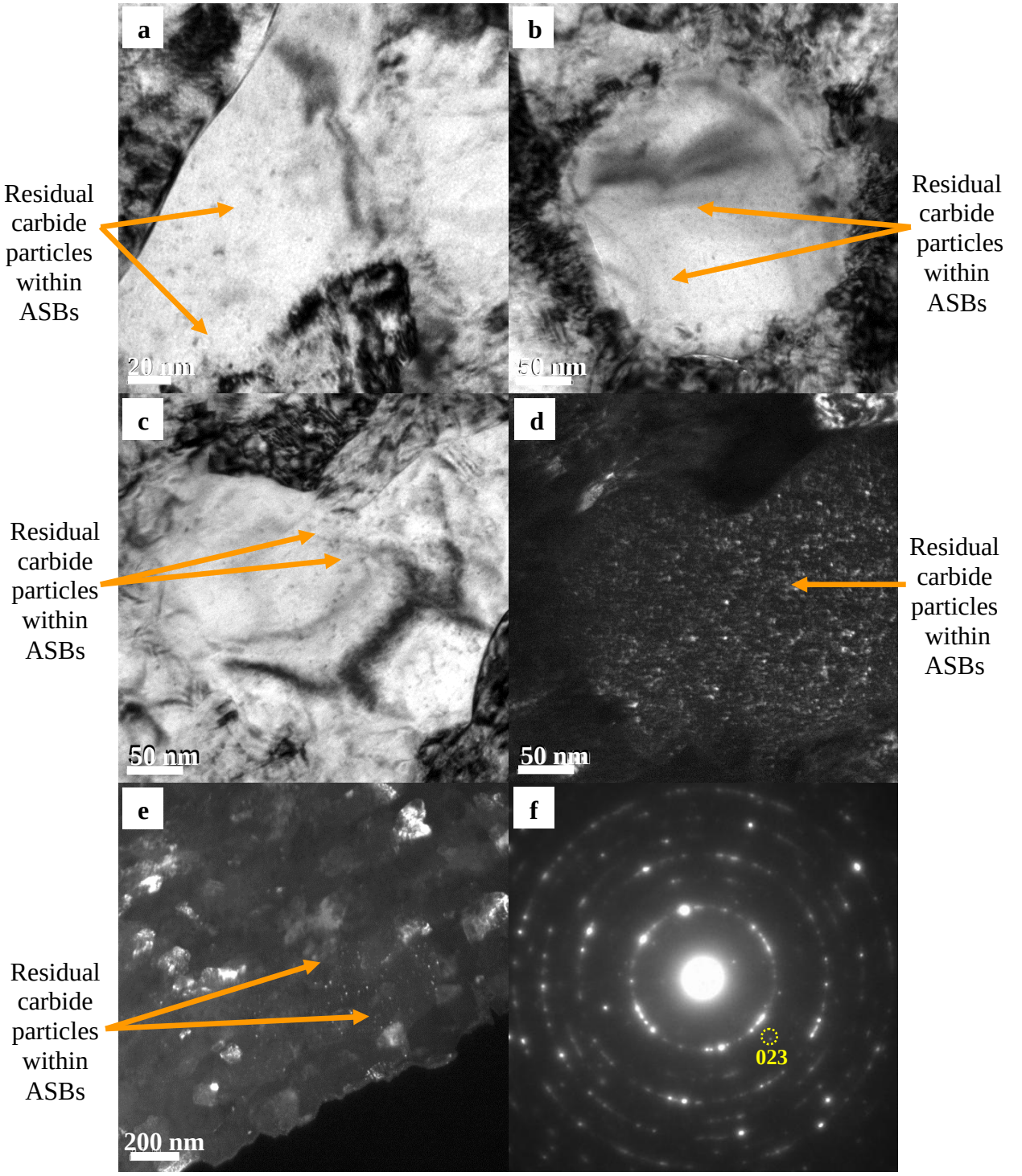

Figure 4- 48: (a), (b) Bright field micrographs of residual carbide particles within adiabatic shear bands. c) Bright field micrograph of a region within the shear bands showing carbide particles (d) dark field micrograph of (c) (e) Dark field image of a region within shear band taken with the (023) cementite reflection as shown on the Selected Area Diffraction Pattern (SADP) (f).

Figure 4-49 are bright field micrographs of regions outside the ASB that evolved after impact at $3853S^{-1}$ showing the existence of residual carbides and residual carbide particles. The residual carbide particles in appeared to have broken off from the residual carbides. Both residual platelet and spherical carbides were observed in regions away from the shear bands but with extensive reduction in their diameters (from 400nm to 84nm). Only residual platelet carbides were observed in regions close to the shear bands with a significant reduction in their aspect ratios from 4 to 2.2. The average diameter of the residual carbide particles in regions away from the ASB was 7nm while that of the regions close to ASB was 14nm. Strain localization results in higher local strain and strain rate within ASBs compared to regions outside the shear bands. The lower strain rates and strains within the regions away from ASBs produce partial carbide fragmentation with residual carbides and residual carbide particles. It is believed that extensive carbide fragmentation would have occurred for the carbides outside the shear bands if they were located within the shear band regions prior to deformation. The existence of residual carbides and residual carbide particles in regions outside the evolved shear bands affirms the occurrence of carbide fragmentation and redistribution within the ASBs during impact.

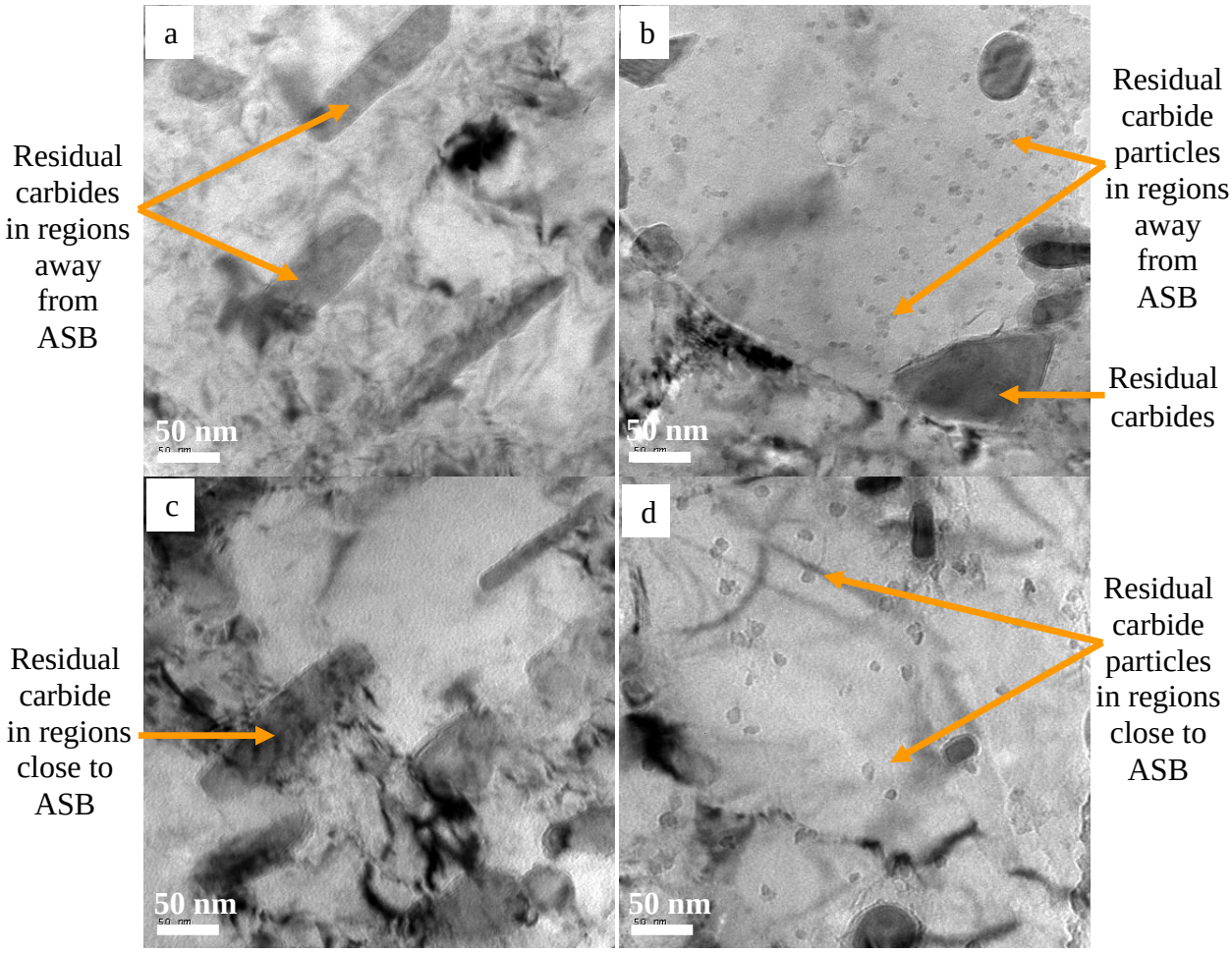

Figure 4- 49: TEM BF micrographs showing (a) residual carbides in regions away from ASB (b) residual carbide particles in regions away from ASB (c) residual carbides in regions close to ASB (d) residual carbide particles in regions close to ASB.

Prior to impact, it was observed that the precipitated carbides were surrounded by dislocations as shown by figure 4-50(a) and (b). The high density dislocation lines were intersecting the ferrite/cementite interface and surrounding the carbides. During impact, it is believed that the interface between the precipitated carbides and the ferrite matrix can serve as sources of dislocations and the generated dislocations cut through the carbide/ferrite interface regions causing plastic deformation of the carbides. This may also result in carbide fracture and

fragmentation. In addition, it was observed that the structures within the evolved ASBs were decorated with dislocations as shown by the 2-beam conditions of the shear band in figure 4-50(c) and (d). It is reported that the residual carbide particles that are redistributed within the shear bands are able to trap and pin dislocations which may account for the presence of dislocations within the evolved shear bands.

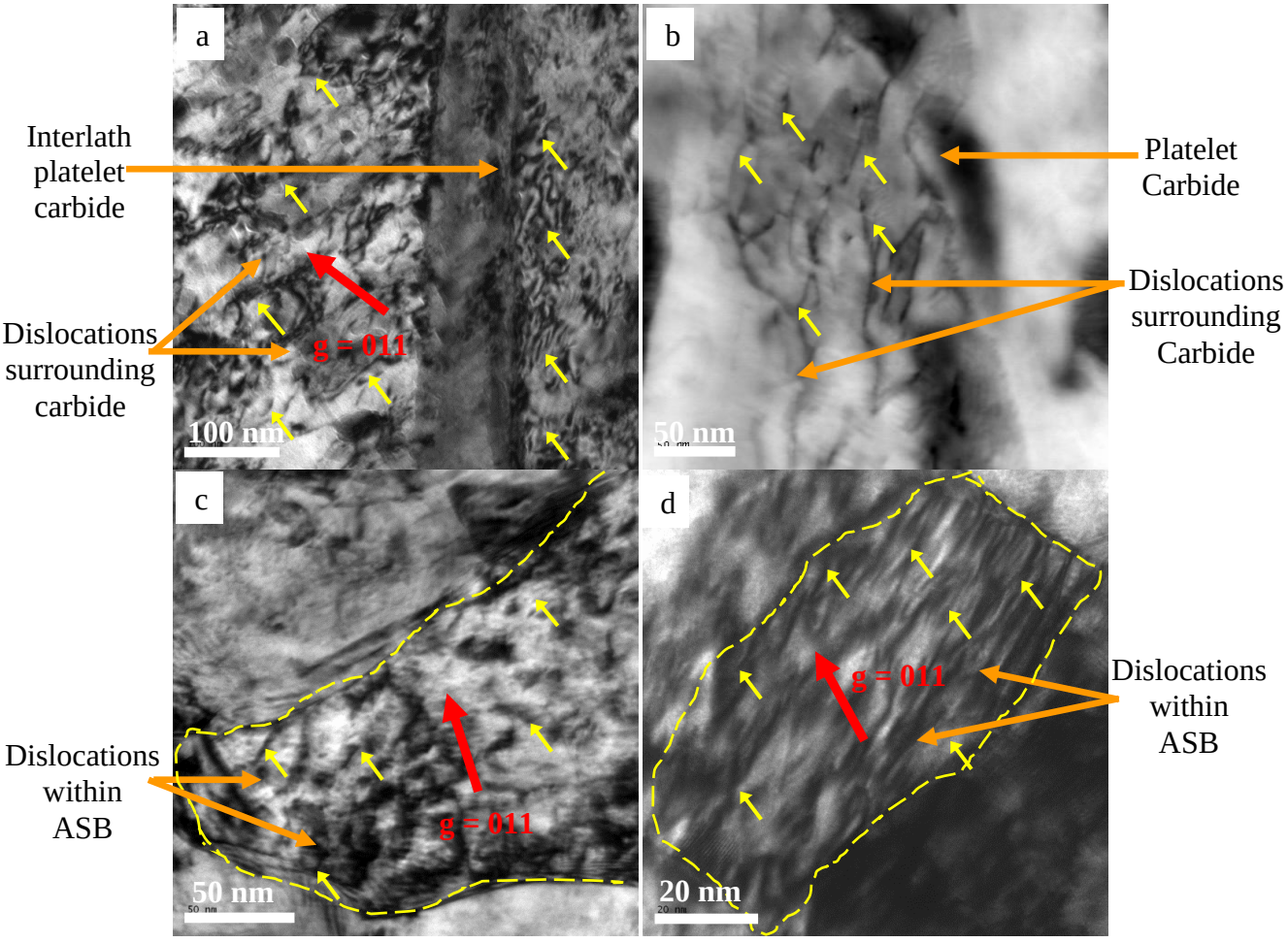

Figure 4- 50: (a) Dislocations (indicated by yellow arrows) surrounding platelet carbides under 2-Beam conditions prior to impact (b) STEM micrograph showing dislocations around platelet carbide. (c), (d) 2-Beam conditions of structure within evolved ASBs showing the presence of dislocations.

4.3.4 Lattice Displacement and Strain Fields within Adiabatic Shear Bands (ASBs)

Geometric Phase Analysis (GPA) was used to analyze High Resolution Transmission Electron Microscope (HRTEM) images of regions within the evolved ASBs. Quantitative measure of the two-dimensional strain tensors for each point in the field of view of the image was obtained. Figure 4-51(a) shows a [0-21] HRTEM image of platelet carbide while figure 4-51(b) shows the [400] HRTEM image of the ferrite matrix in a tempered specimen prior to impact. Figure 4-51(c) shows the total amplitude maps of the high resolution carbide micrograph while figure 4-51(d) shows the total amplitude of the high resolution ferrite micrograph with their corresponding inserted profile plots. The amplitude plots give the point by point amplitude of the intensity of the lattice fringes. This was used to control where the lattice fringes disappear, and to reduce errors, high intensity regions from the amplitude plots were used for analysis. Figure 4-51(e) shows the inverse FFT of the platelet carbide using the (200) carbide reflections while figure 4-51(f) shows the inverse FFT of the ferrite matrix using the (020) ferrite reflections. The high intensity regions from the amplitude plots is used to determine regions in the HRTEM images that have crystallographic lattices displaced by the imperfect contrast transfer of the TEM.

A schematic of a fibbed TEM foil from evolved ASB which was used for the GPA is shown in figure 4-52(a) while figure 4-52(b) shows the [200] high resolution electron micrograph of a region within evolved ASB in the specimen impacted at 45kg.m/s. The projected strains analyzed within the shear bands were parallel to the direction of impact as shown by the schematic. The high intensity regions of the HRTEM image was used for analysis as shown by the total amplitude plot in figure 4-52(d). Some lattice distortions and defects were observed in some of the high intensity regions from the amplitude plots as shown by figure 4-52(e) and (f).

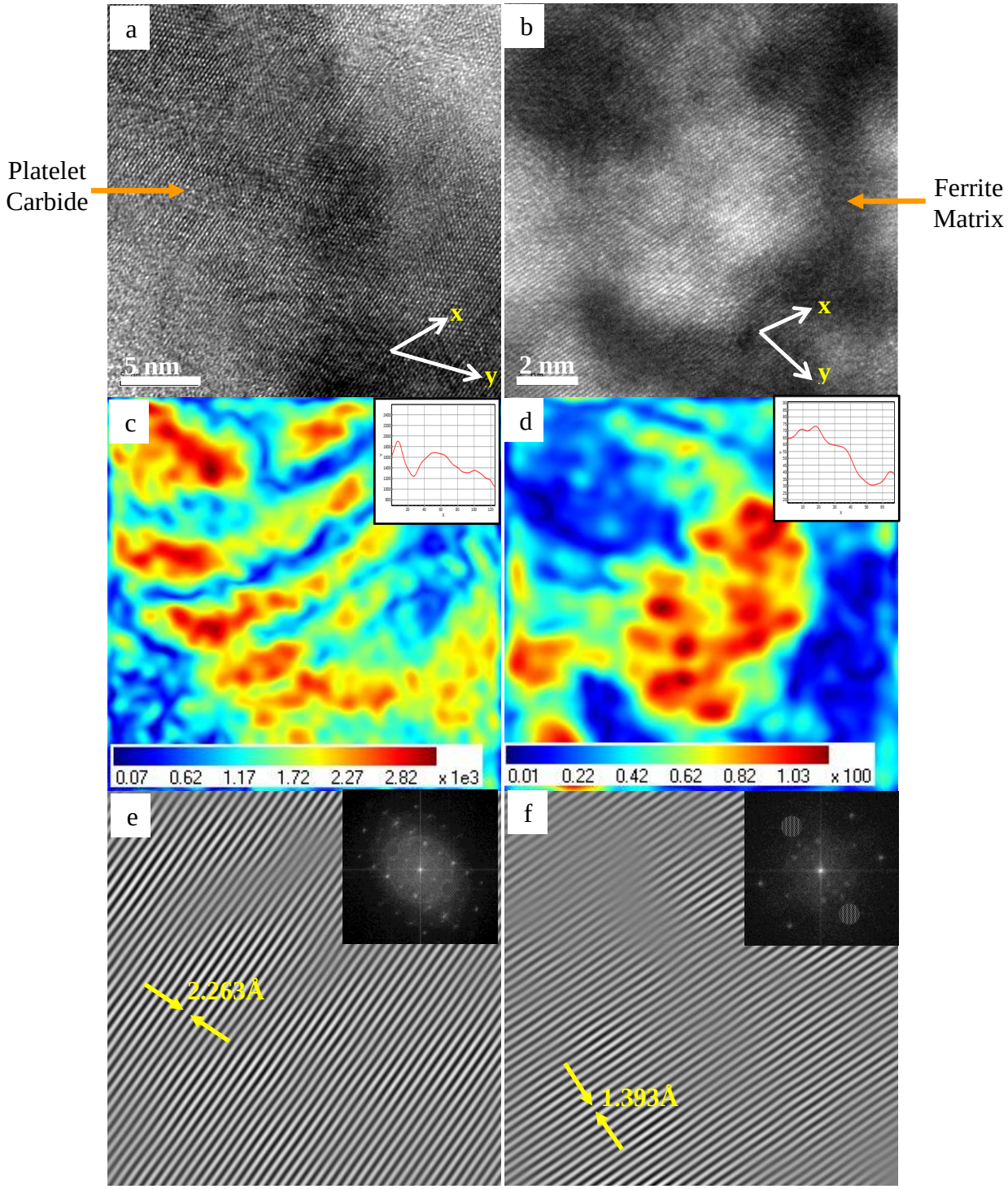

Figure 4- 51: (a) [0-21] HRTEM of pre-impact carbide (b) [400] HRTEM of pre-impact matrix (c) total amplitude of HRTEM carbide (insert-amplitude profile plot) ((d) total amplitude of HRTEM matrix (insert-amplitude profile plot) (e) Inverse FFT of carbide using (200) reflections (insert-FFT of carbide) (f) Inverse FFT of ferrite using (020) reflections (insert-FFT of ferrite)

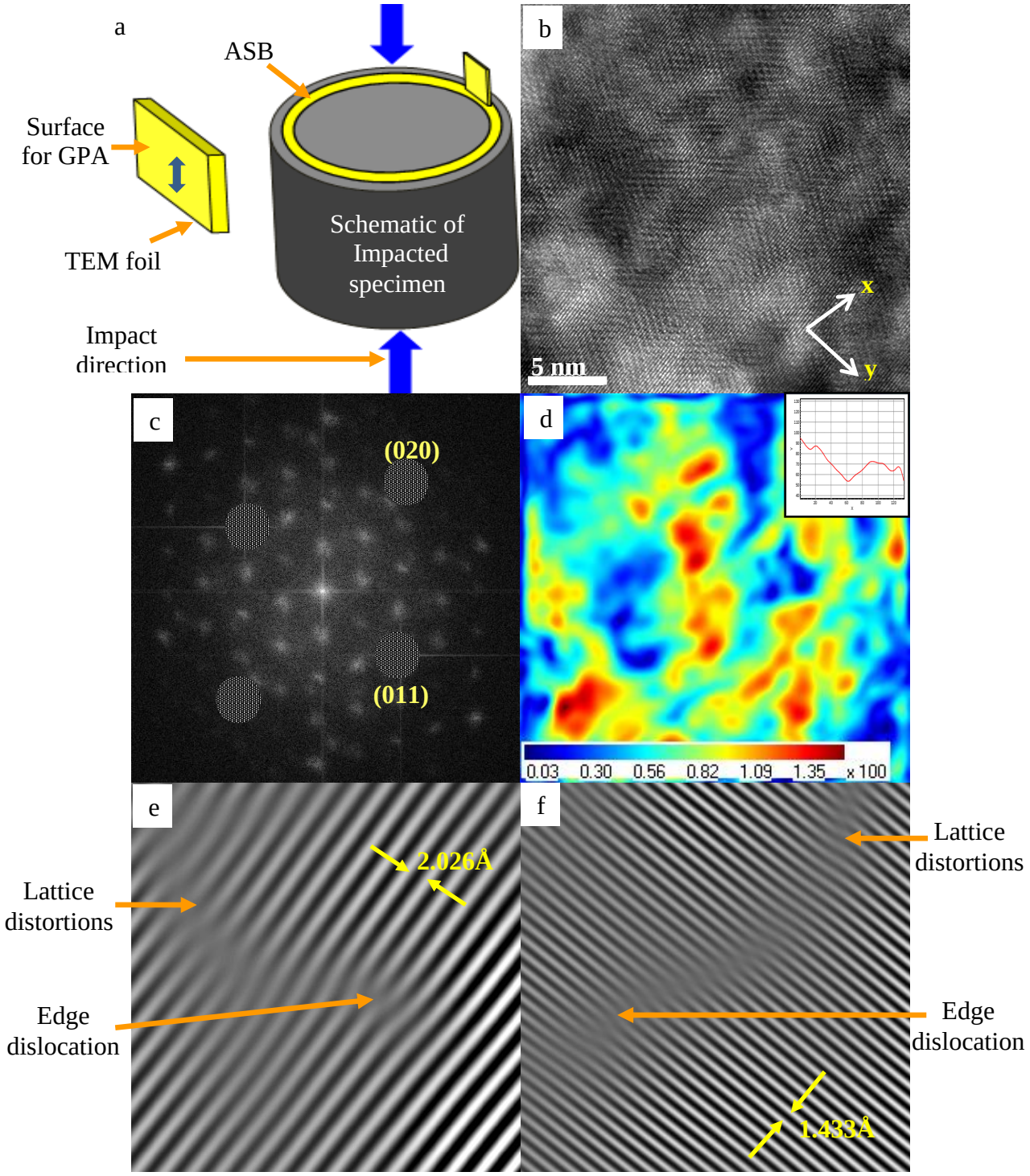

Figure 4- 52: (a) Schematic of TEM foil from ASB (b) [200] HRTEM of region within ASB in specimen impacted at 45kg.m/s (c) Fast Fourier Transform of (b). (c) Total amplitude of [200] HRTEM image (Insert-Profile plot of total amplitude) (e) Inverse FFT of HRTEM image using (011) reflections (f) Inverse FFT of HRTEM image using the (020) reflections.

The map of the internal rotations of the crystallographic lattice prior to impact and perpendicular to the direction of impact within the carbide is shown in figure 4-53(a). The map revealed some rotational gradients and disclination-like rotational distortions within the lattice. The rotational fields were comparatively thin and discontinuous with an indication of -1.09º to 1.12º rotations. On the other hand, the shear-strain distribution map of regions within the carbide prior to impact revealed longer shear strain fields with occasional shear gradients across lattices as shown in figure 4-53(b). The map had an indication of 0.56% to 1.42% shear strains. The lattice rotation map shown in figure 4-53(c) revealed that the ferrite matrix had comparatively irregular lattice rotational gradients with broader and longer rotational fields and indication of -5.29º to 5.65º rotations. Some disclination-like rotational distortions were observed within the internal lattice rotational map of the ferrite matrix prior to impact. Figure 4-53(d) shows the map of the shear-strain distributions within the ferrite matrix prior to impact. Comparatively, the ferrite matrix had broader and longer shear strain fields with irregular distribution of shear gradients across the lattices. The map had an indication of 0.77% to 1.19% shear-strains. Figure 4-53(e) shows the internal lattice rotational distributions within the evolved shear band parallel to the direction of impact. The rotational fields within the shear band were narrower and shorter than was observed for the ferrite matrix but broader and longer than was observed for the carbides. In addition, the lattice-rotational distortions, with an indication of -5.83º to 5.09º rotations, and the rotational fields were regularly distributed. Furthermore, the shear strains within the evolved shear band parallel to the direction of impact were comparatively regularly distributed with shear gradients across lattices and an indication of 0.80% to 1.18% shear strains as shown in figure 4-53(f). The shear strain fields within the ASBs were narrower and more regular than the broader shear strain fields within the ferrite matrix prior to impact.

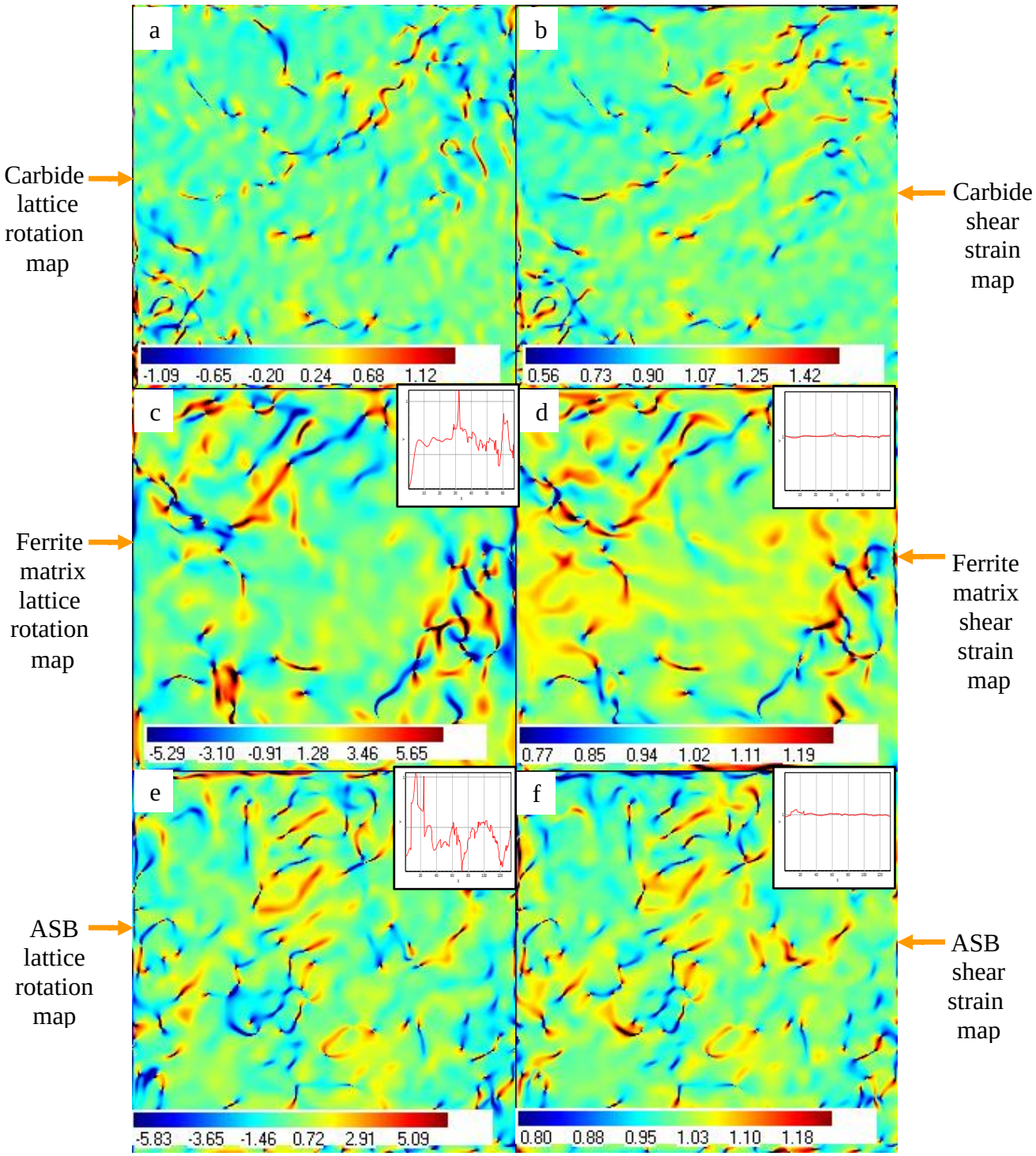

Figure 4- 53: Internal lattice-rotation and shear-strain distribution maps (inserted profile plots) of regions within (a),(b) carbide prior to impact (c),(d) ferrite matrix prior to impact (e),(f) Adiabatic Shear Band (ASB) respectively in the specimen impacted at 45 kg.m/s.

Figure 4-54(a) and (b) show the internal strain distribution maps in the x-direction (Exx) and y-direction (Eyy) respectively in regions within carbide prior to impact. The strain fields were mostly broader and continuous in the y-direction compared to the relatively narrow discontinuous fields observed in the x-direction. There were observed strain gradients across lattices with an indication of 0.58% to 1.47% strain in the x-direction and 0.82% to 1.20% strain in the y-direction. The internal strain distribution maps in the x-direction (Exx) and y-direction (Eyy) in regions within the ferrite matrix prior to impact are shown in figure 4-54(c) and (d) respectively. The strain fields in the y-direction were broader than the fields in the x-direction. The strain fields were mostly discontinuous in both directions with an indication of 0.86% to 1.18% strain in the x-direction and 0.87% to 1.10% in the y-direction. Figure 4-54(e) shows the internal strain distribution map in the x-direction (Exx) while figure 4-54(f) shows the strain distribution map in the y-direction (Eyy) for a region within the evolved shear band after impact at 45kg.m/s. The strain fields were broader and more continuous in the Eyy than the narrow discontinuous strain fields observed in the Exx. The Exx had an indication of 0.90% to 1.13% strains while the Eyy had 0.90% to 1.07% strains.

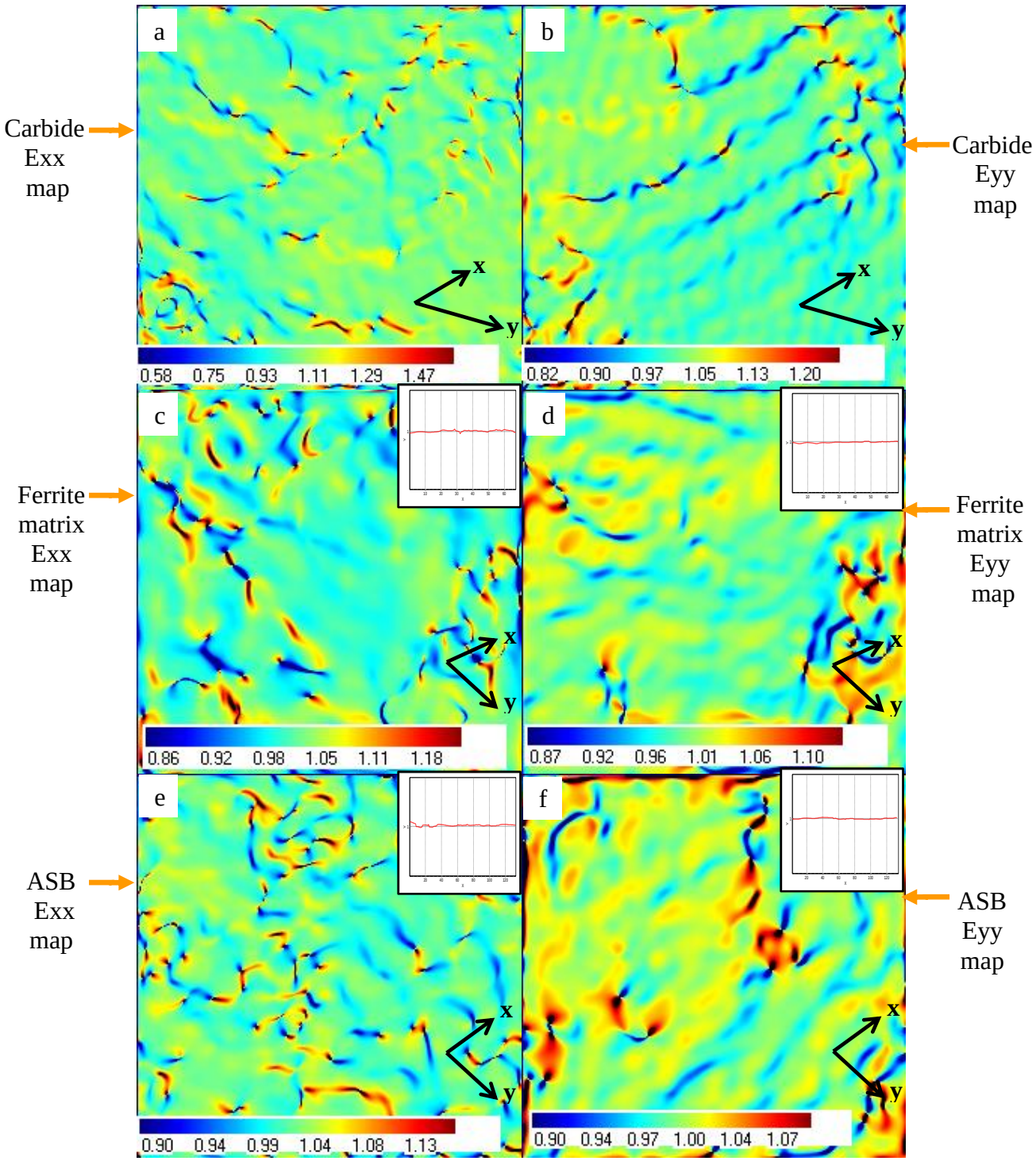

Figure 4- 54: Internal strain distribution maps in the x-directions (Exx) and y-directions (Eyy) (inserted profile plots) of regions within (a),(b) carbide prior to impact (c),(d) ferrite matrix prior to impact (e),(f) Adiabatic Shear Band (ASB) respectively in the specimen impacted at 45 kg.m/s.

4.3.5 Microstructural Changes during Post-Shear Band Formation Thermal Treatments

Impacted specimens with distinct ASBs were soaked at 350^{O}C to 650^{O}C for 30 minutes to 4 hours to investigate how post-impact annealing processes influence the microstructure of the shear bands which may relate to understanding the mechanism of evolution of ASBs. Figure 4-55 shows the microhardness distribution of specimens A, B and C, initially tempered at 425^{O}C-1hr before impact at 45, 50 and 52kg.m/s respectively. There was an increase in hardness for regions within and outside the ASBs in specimen A after annealing at 350^{O}C while significant reduction in hardness occurred in specimen C after annealing at 650^{O}C.

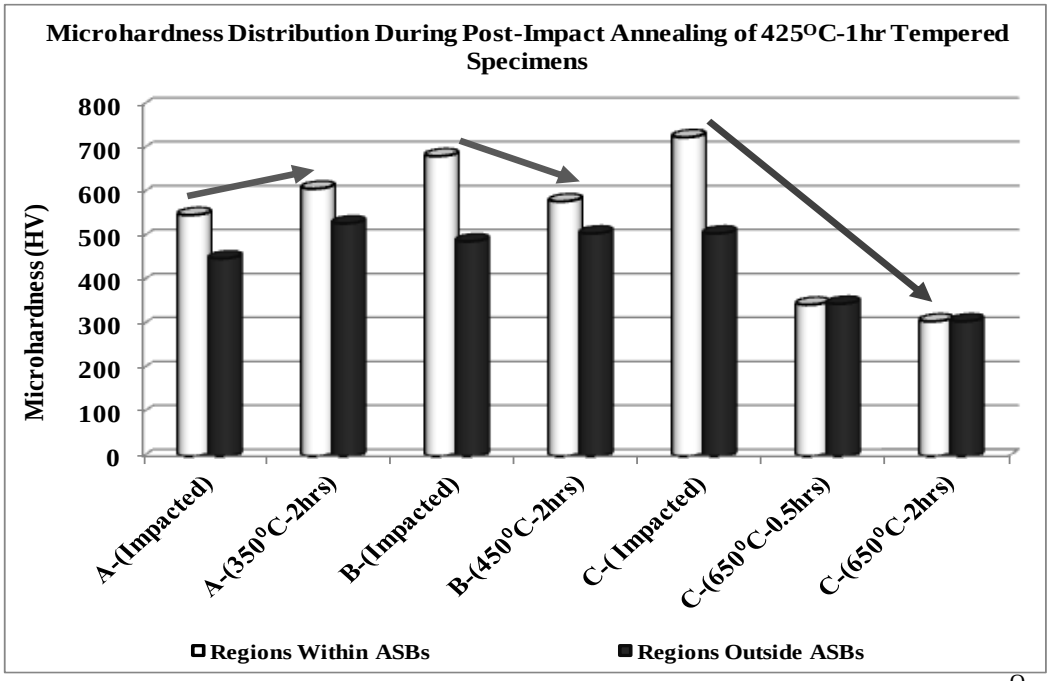

Figure 4- 55: Microhardness distribution during post-impact annealing of ASBs at 350^{O}C, 450^{O}C and 650^{O}C.

Annealing the impacted specimens with distinct ASBs at 350^{O}C resulted in an increase in hardness of the ASBs regardless of the pre-impact heat treatment, the amount of deformation and

time for annealing. Figure 4-56 shows increasing hardness distributions for regions within and outside ASBs during post-impact annealing at 350^{O}C. Specimens A-315^{O}C, A-425^{O}C and A-620^{O}C are from the 315^{O}C-1hr, 425^{O}C-1hr and 620^{O}C-2hrs pre-impact tempered groups impacted at 44, 45 and 50kg.m/s respectively.

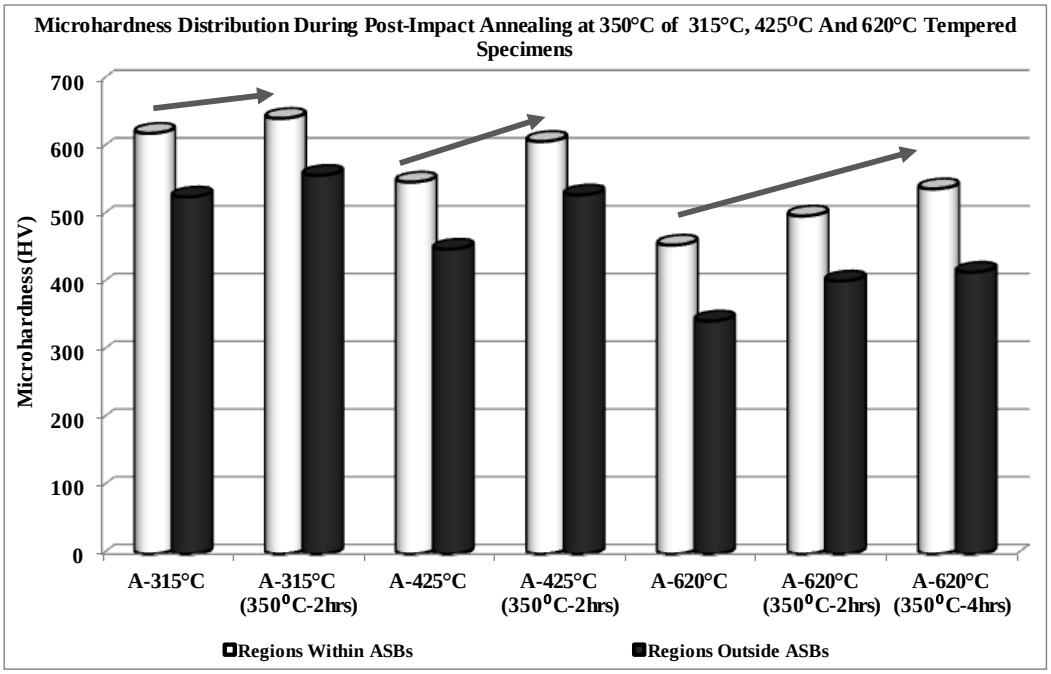

Figure 4- 56: Microhardness distribution during post-impact annealing of ASBs at 350^{O}C.

X-ray diffraction (XRD) analysis revealed that chemical and structural changes could have occurred during the post-deformation annealing at 350^{O}C. Figure 4-57 shows the various reflecting planes of specimen A-620^{O}C, from the 620^{O}C-2hrs pre-impact tempered group, impacted at 50kg.m/s and annealed at 350^{O}C for 4hrs compared to the pre-impact tempered specimen.

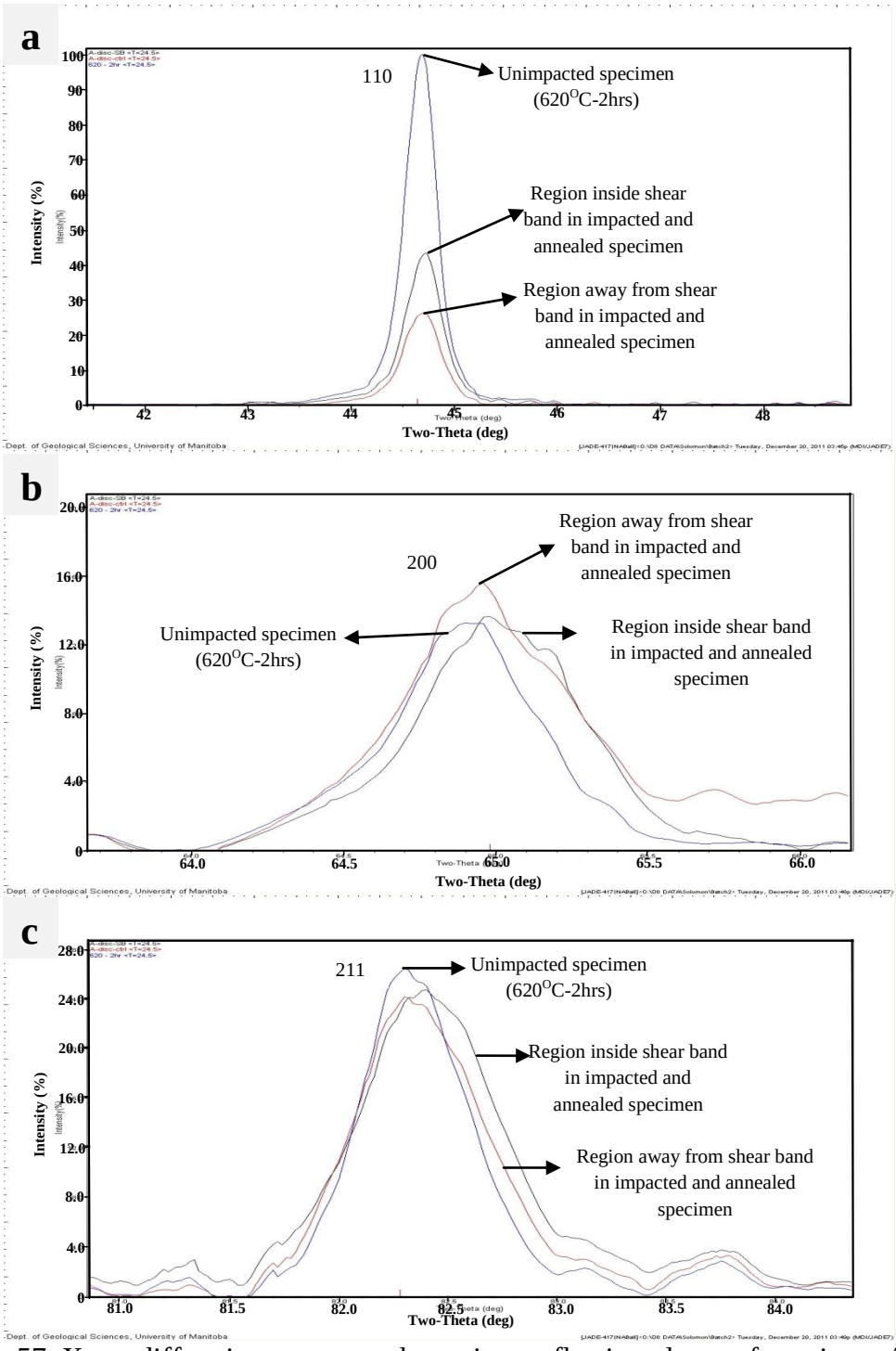

Figure 4- 57: X-ray diffraction spectra at the various reflecting planes of specimen A-620^{O}C impacted at 50kg.m/s and annealed at 350^{O}C for 4 hours compared to the pre-impact specimen.

TEM Bright Field (BF) micrographs of regions outside the shear bands showed a disappearance of the “knitted” and tangles dislocations that bounded the grains that developed in these regions after impact. This is attributed to static recovery processes which results in dislocation annihilation. Figure 4-58 shows the BF micrographs of regions outside ASBs after post-impact annealing of specimen A-620^{O}C at 350^{O}C for 4hrs. Reprecipitation of platelet and spherical carbides were observed. The reprecipitated carbides were well developed compared to the observed residual carbides and residual carbide particles observed after impact. Extensive reprecipitation of platelet and spherical carbides were also observed within the ASBs after post-impact annealing at 350^{O}C for 4hrs as shown on figure 4-59. The reprecipitated carbides were easily distinguishable and well developed. The reprecipitated platelet carbides after post-impact annealing had an average length of 163nm and width of 36nm corresponding to an approximate aspect ratio of 4.5. The reprecipitated spherical carbides after the post impact annealing at 350^{O}C for 4hrs had an average diameter of 87nm. The increasing hardness of the specimens after the post-impact annealing at 350^{O}C is as a result of the carbide reprecipitation during the annealing process. In addition, the residual carbide particles observed both outside and within the ASBs disappeared after the post-impact annealing which is attributed to diffusion processes due to thermal energy activation. From figure 4-59, the alignment of the reprecipitated carbides in the shear direction also lends credence to the fact that shear band formation in tempered 4340 steel involves an initial alignment of the tempered martensite microstructure in the shear direction.

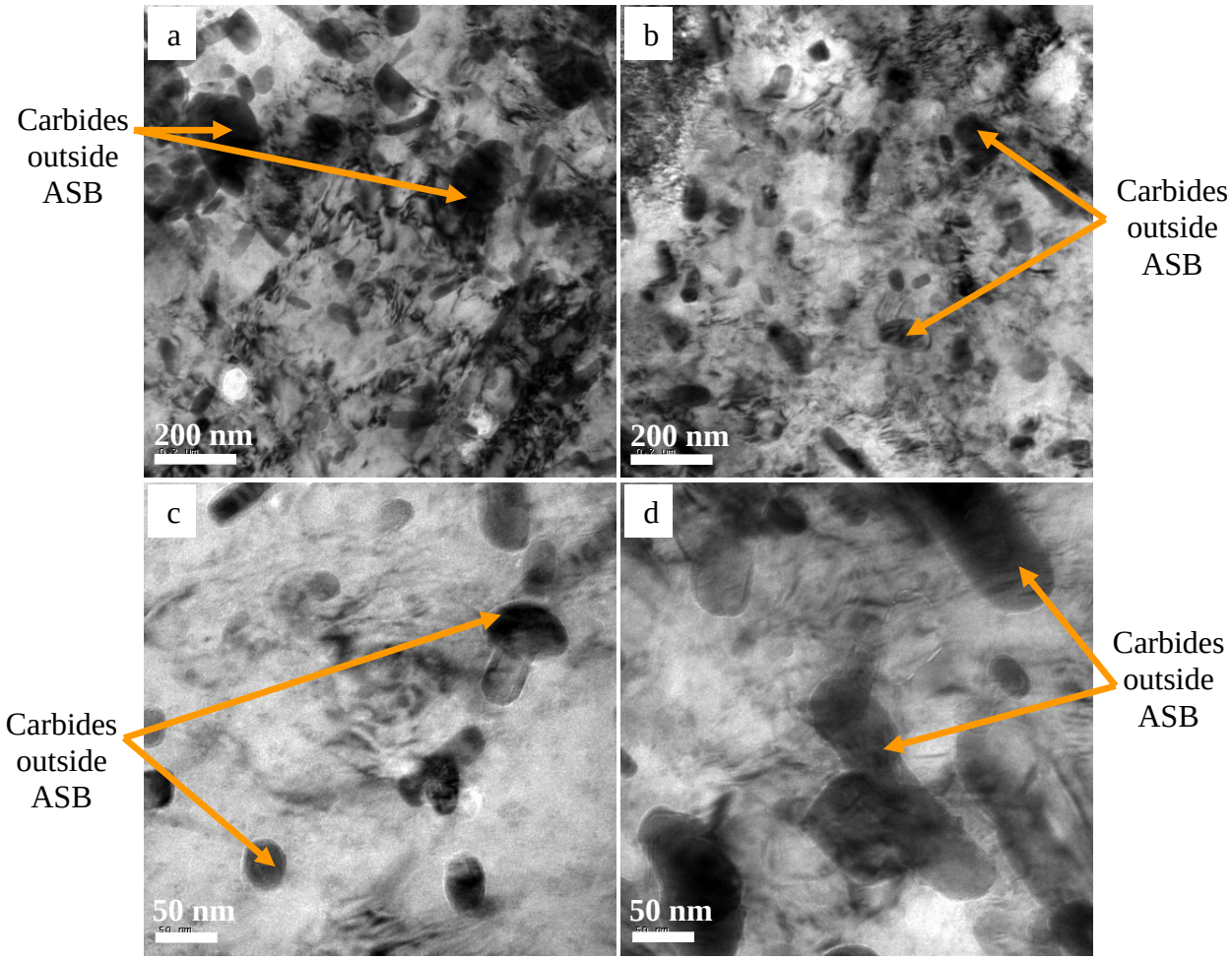

Figure 4- 58: TEM BF micrographs of regions outside ASB in specimen A-620^{O}C impacted at 50kg.m/s and annealed at 350^{O}C for 4hrs.

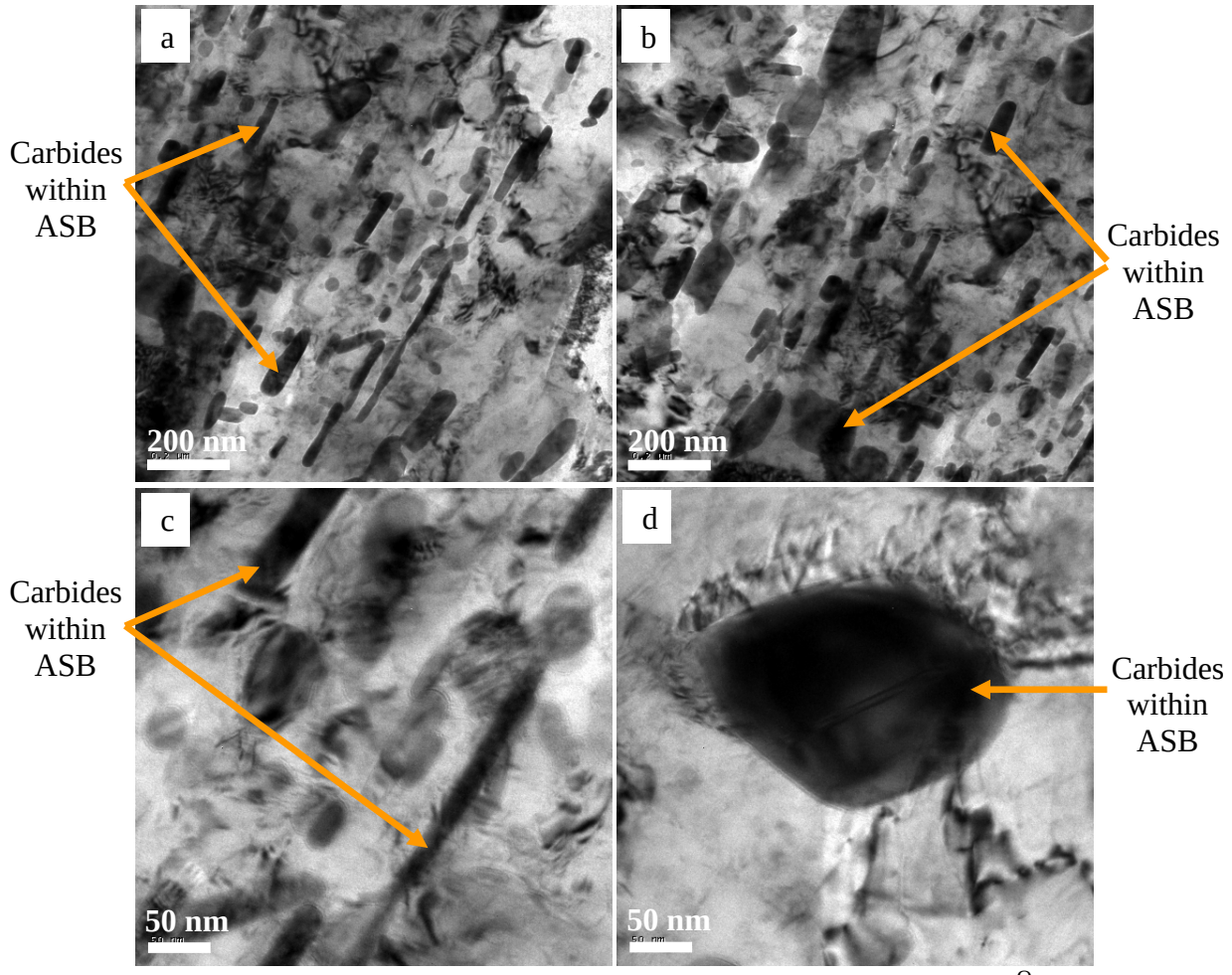

Figure 4- 59: TEM BF micrographs of regions within ASB in specimen A-620^{O}C impacted at 50kg.m/s and annealed at 350^{O}C for 4hrs.

Post-impact annealing of the ASBs above 450^{O}C resulted in a decrease in hardness with a significant decrease in hardness occurring after annealing at 650^{O}C. Hardness of the ASBs reduced to the same level as that of the impacted material outside the shear bands due to static recrystallization processes. Figure 4-60 shows Energy Dispersive Spectroscopy (EDS) analysis on spheroidized carbides within the ASBs after post-impact annealing at 650^{O}C for 2hrs which resulted in extensive softening. due to static recrystallization and grain growth mechanisms. Figure 4-61 shows TEM micrographs of regions within and outside ASBs after post-impact

annealing at 650^{O}C for 2hrs. The grain size of regions within the ASB was 1.4µm (1400nm) while those outside were 0.7µm (700nm). It is inferred that under the same annealing conditions, the high strain energy stored in the ASBs would trigger early static recrystallization within the ASBs as compared to the surrounding regions during the annealing process . This accounts for the large grain growth within the ASBs after the completion of static recrystallization.

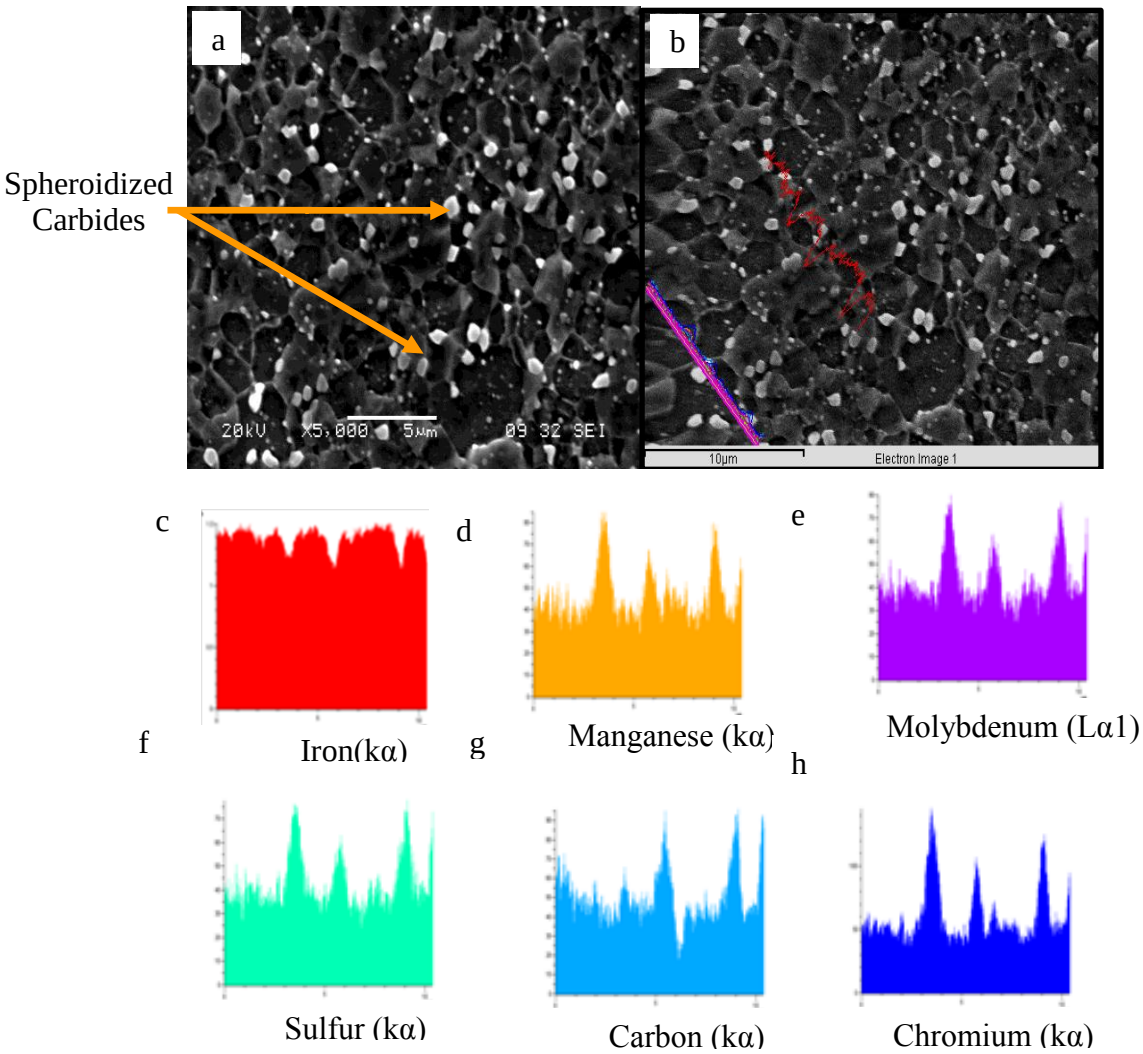

Figure 4- 60: EDS on spheroidized carbides within ASBs in specimen A-620^{O}C impacted at 50kg.m/s and annealed at 620^{O}C for 2hrs.

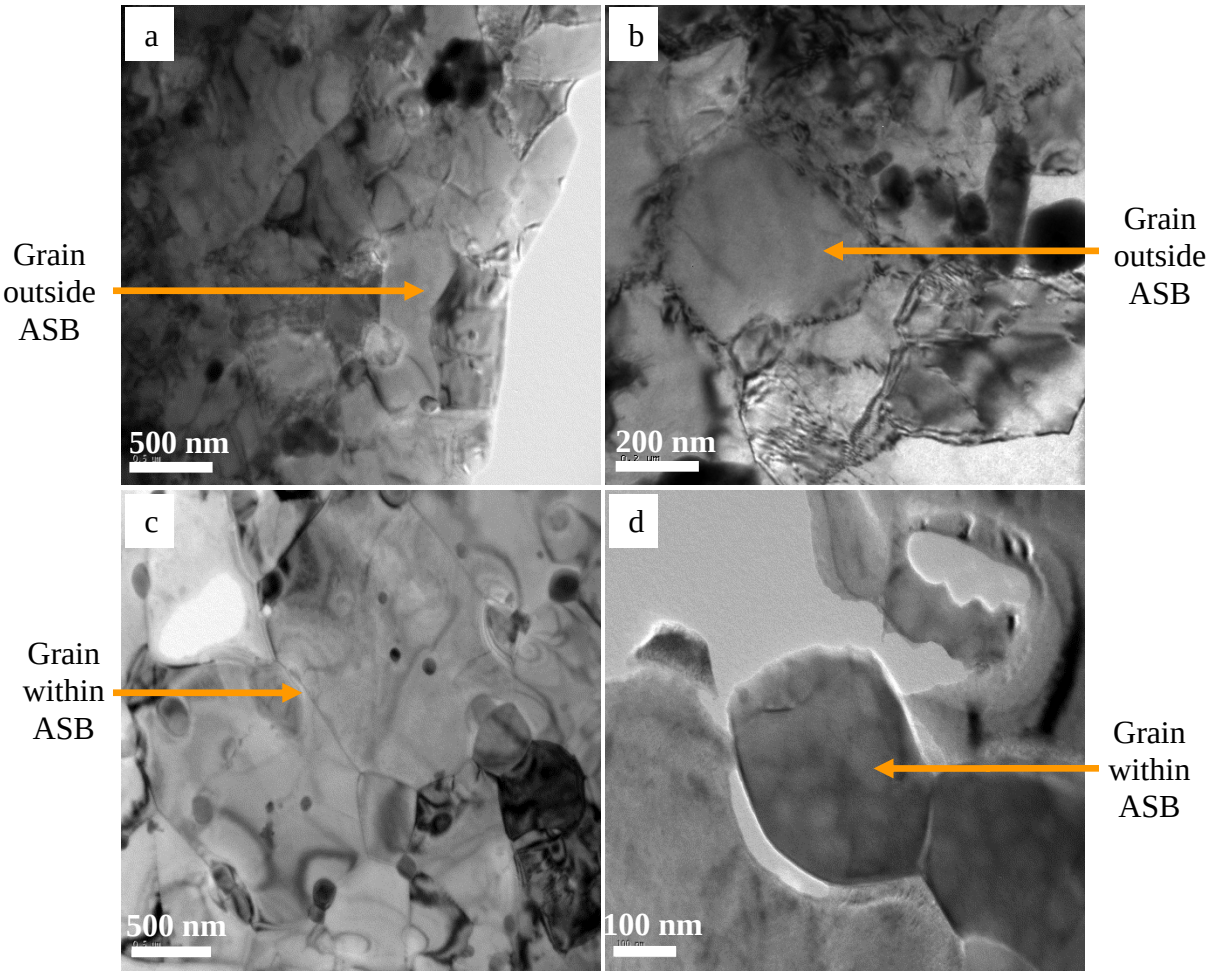

Figure 4- 61: TEM BF micrographs of regions (a), (b) Outside and (b), (c) within ASB in specimen A-620^{O}C impacted at 50kg.m/s and annealed at 650^{O}C for 2hrs

The experimental results from this study indicate that a more complex mechanism of nucleation and evolution of ASBs occur in 4340 steel during impact. The microstructures of the pre-impact specimens significantly influence the process of initiation and evolution of the ASBs during impact. Emergence of dislocations, texture development through elongation of grains in the shear direction, grain refinement due to grain boundary rotations, and carbide fragmentation and redistribution simultaneously contribute to the structure that evolves within the ASBs in 4340 steel during impact.

CHAPTER 5
DISCUSSION

Comprehensive systematic observation of the microstructure of AISI 4340 steel prior to impact, after impact and after post-impact annealing was performed to determine the effect of the pre-impact microstructure on the nucleation and initiation of Adiabatic Shear Bands (ASBs) and to determine the mechanism of evolution of ASBs during impact. This chapter discusses the main findings in the study based on the results reported in the previous chapter on the microstructural observations of the steel specimens. This chapter is divided into four sections, section 5.1 to 5.4. Section 5.1 discusses the effect of the pre-impact microstructure on the susceptibility of 4340 steel to the nucleation and initiation of ASBs during Impact. The mechanism of grain refinement and the evolution of ASBs in 4340 steel during impact are discussed in section 5.2. Section 5.3 discusses the role of carbides on the structure of ASBs and the results of the strain mapping. Finally, section 5.4 discusses how the current results can be applied in tailoring and designing microstructures of other steels that are resistant to the formation of ASBs.

5.1 The Effect of Pre-impact Microstructure on the Susceptibility of 4340 Steel to Nucleation and Initiation of ASBs during Impact

It has been reported experimentally and analytically that the instability criterion ($d\tau/d\gamma \leq 0$) and perturbations are necessary conditions for the occurrence of shear strain localization leading to the formation of ASBs [6, 17, 115]. Instability may occur homogenously throughout the specimen during high strain rate deformation and result in global distribution of deformation. However, the formation of ASB does not accompany a homogenous instability during impact [6, 115]. Geometrical stress concentration sites and/or microstructural inhomogeneities result in the

initiation and propagation of shear strain localization [6, 17, 19]. Many factors influence the transition from homogenous instability (globalization) to shear strain localization during impact. The current study shows that microstructural inhomogeneities within tempered steel specimens make them more susceptible to the formation of ASBs. Specimens tempered at lower temperatures had thin precipitated carbides with high aspect ratios densely distributed within the ferrite matrix. As the tempering temperature increased, the relative sizes of the carbides increased with associated reduction in their aspect ratios and distribution density within the matrix. In addition, the average lath sizes also increased at higher tempering temperatures as shown on table 4-10. The larger carbides with reduced aspect ratios sparsely distributed within the larger lath matrix makes the microstructure relatively more homogenous than the thin carbides with high aspect ratios densely distributed within smaller lath matrix. The higher susceptibility of the lower tempered specimens to ASB formation is attributed to their higher microstructural inhomogeneity associated with the precipitated carbides within and along the boundaries of the ferrite matrix.

Mechanisms that have been used to explain the evolution of ASBs are fundamentally based on the principle of dislocation nucleation, multiplication and/or annihilation due to the associated high strain rates/strains and the temperature rise due to the conversion of plastic work to heat during impact [6, 8-10, 115]. Empirical and phenomenological constitutive models such as the Johnson-Cook and Zerilli-Armstrong models use constitutive equations to relate macroscopic strain (γ), strain rate ($\dot{\gamma}$) and temperature (T) to macroscopic stress (τ) [50-53, 116]. Points of local imperfections and the magnitude of pre-existing defects prior to deformation have been reported by Feng and Bassim, and Duffy and Chi, respectively to predict the formation of ASBs

[47-48]. Consequently, the role of emergence and multiplication of dislocations and the rate of generation of dislocations are significantly vital to shear strain localization during high strain rate deformation.

The current study demonstrates that, misfit interfaces between carbides/boundary layers and boundary layers/ferrite matrix relatively increase the presence of misfit dislocations within the pre-impact specimens. This is because the atomic arrangements at the interfaces create misfit dislocations within the microstructure and a single interface between a carbide and matrix would have only one misfit interface. However, the existence of two misfit interfaces around each precipitate within the specimens in the current study, due to the presence of the boundary layer, increases the misfit dislocations. It has been reported that because of elastic misfit, long-range stresses exist in the surrounding matrix during precipitation prior to impact [39, 116]. These long-range stress fields are eliminated when the misfit dislocations capture the misfit at the interfaces [117]. The dislocations at the interfaces makes them more susceptible to act as dislocations sources when they are activated during impact. During the impact, activated dislocation sources result in the emergence and multiplication of dislocations. Since the interfaces ("fault regions") could act as sources of dislocations when activated during the impact, the volume fraction of these interfaces within a specimen prior to impact increases the sources for the emergence and multiplication of dislocations. It is inferred that these "fault regions" are the origins of microstructural inhomogeneities associated with the tempered steel specimens. An increase in the volume fraction of these “fault regions” increases the microstructural inhomogeneity of the specimen.

Various investigators have shown that carbide/ferrite interfaces in steel microstructures serve as dislocation sources during plastic deformation and cyclic loading [39, 118-119]. In addition, the Orowan equation relates the macroscopic strain rate to the mean dislocation velocity; the proportionality being the product of the mobile dislocation density and the mean dislocation velocity [39]:

$$\gamma' = b \rho \nu \quad \text{.....5-1}$$

where γ' is the macroscopic strain rate, b is the burger's vector, ρ is the mobile dislocation density and ν is the mean dislocation velocity [39, 116-117]. The effective stresses on the dislocation source and its size influences the nucleation and movement of dislocations which also influences the macroscopic strain rate [117]. This implies that if the evolution of the shear band structure are initially driven by the emergence of dislocations, then the sources of dislocations within the specimens coupled with the effective stresses on the dislocation sources and the rate of generation of dislocations during impact, are significantly necessary conditions prior to the nucleation of shear strain localization. Thus, the activation and the volume fraction of activated dislocation sources during impact, is a necessary condition for the nucleation of strain localization depending on the rate of dislocation generation, local strain and strain rate.

A recent study by Ghomi et. al. [120] reported that the trajectory of shear bands on the transverse section of cylindrical and cubical specimens followed the shape of the cross-section: cylindrical specimens resulted in the evolution of circular-shaped (conical hourglass) shear bands while cubical specimens formed rectangular path (pyramidal hourglass shape). Also, shear bands

induced in hat-shaped specimens by Meyers et al. [115, 121] resulted in the formation of ASBs along the thin regions of the specimen (geometrical stress concentration sites). Accordingly, upon impact of the projectile on a specimen; the geometry of the specimen, the direction and surfaces of impact, define a specific direction of maximum shear within the specimen. Considering the direction of maximum shear (regions of stress concentrations) within a specimen under impact, it is proposed that a dislocation source ("fault region") could be a possible nucleation site for the initiation of ASB when the dislocation source is activated and it intersects the direction of maximum shear within the specimen. Thus, the points of intersection of an activated dislocation source with the direction of maximum shear (regions of stress concentrations) within the specimen, can serve as nucleation sites for the initiation of ASBs. The presence of a dislocation source (region of local imperfection), within the microstructure of the steel specimen, is a necessary condition for the source to act as a possible site for the emergence and multiplication of dislocations when the source is activated during impact. However, it is inferred that the intersection of an activated dislocation source with the direction of maximum shear (regions of stress concentrations) within the specimen during impact, is a necessary condition for the points of intersection to act as regions or sites for the nucleation of ASBs depending on the rate of dislocation generation, local strain and strain rate.

Figure 5-1(a) is a schematic of the test specimen prior to impact while figure 5-1(b) is a typical fractured specimen after impact showing the fracture path. The fracture path shows that cracks propagate along the trajectory of the evolved shear band leading to fracture and fragmentation. A schematic of the trajectory of the evolved shear band based on the appearance of the observed ASBs in the transverse and longitudinal sections of the impacted specimens is shown in figure 5-

1(c). The point of impact between the projectile and the specimen (projectile/specimen interface) in addition to the specimen and the transmitter bar (specimen/transmitter bar interface) create regions of stress concentrations within the specimen upon impact of the projectile. This means that the direction of maximum shear within the specimen under impact, defined by the geometry of the specimen and the impact direction, in conjunction with the regions of stress concentrations at the surfaces of the specimen, create the trajectory of the observed shear band as shown in figure 5-1(c). A schematic of a single ferrite matrix modelled as a cylindrical specimen is shown in figure 5-1(d) to (f). Figure 5-1(d) is a schematic representation of the typical carbide distribution in the steel specimens tempered at the lowest temperature (315°C-1hr) which resulted in the precipitation of thin carbides densely distributed within the matrix while figure 5-1(e) and (f) represents approximated carbide sizes and their distribution densities in the 425°C-1hr and 620°C-2hrs tempered specimens respectively. For simplicity, a single matrix has been approximated by a cylindrical specimen and the carbides as spheroids. It is also assumed that, within the matrix, the volume fraction of the carbides is constant because all the specimens have the same chemical composition. The only variation between the different tempered groups is approximated to be the difference in the size of the precipitated carbides and their distribution density within the matrix. The yellow circles represent the precipitated carbides after tempering while the red circles represent the 1^{st}, 2^{nd} misfit interfaces and the boundary layers (dislocation sources/"fault regions") observed around the precipitated carbides. It is also assumed that all the dislocation sources would be activated during impact. It is schematically shown, in figure 5-1(g) that, the intersection of a red circle (an activated dislocation source), with the direction of maximum shear/stress concentration within the specimen, is a necessary condition for the point of intersection to act as a possible site for the nucleation and initiation of ASBs during impact.

The black arrows in figure 5-1(g) represent the point of intersection of an activated dislocation source with the direction of maximum shear/stress concentration. Figure 5-1(h)-(j) shows the probability of intersection of an activated dislocation source with direction of maximum shear in the 315°C-1hr, 425°C-1hr and 620°C-2hrs tempered specimens respectively. From the carbide distribution densities shown in figure 4-30, the 315°C-1hr tempered specimens have higher probability of an activated dislocation source to intersect the direction of maximum shear/stress concentrations during impact than in the 425°C-1hr and 620°C-2hrs tempered specimens.

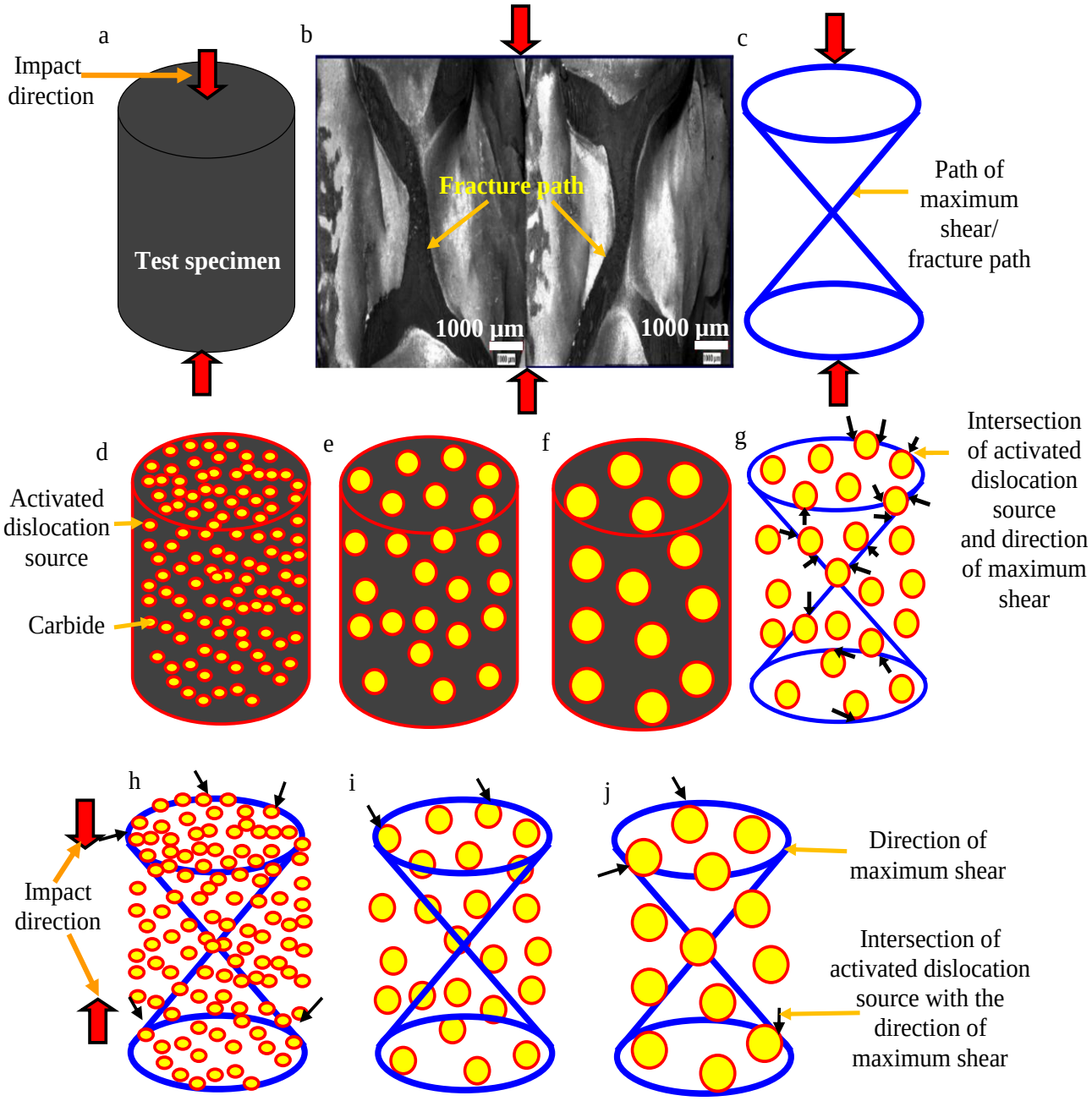

Figure 5- 1: Schematic of (a) test specimen (b) fractured specimen showing the fracture path (c) trajectory of shear band/direction of maximum shear. Single matrix in (d) 315°C-1hr (e) 425°C-1hr (f) 620°C-2hrs tempered specimens. (g) Intersection of activated dislocation source with the direction of maximum shear/stress concentration within a specimen during impact. Intersection of a dislocation source with direction of maximum shear in the (h) 315°C-1hr (i) 425°C-1hr (j) 620°C-2hrs tempered specimens. Black arrows represent the point of intersection of an activated dislocation source with the direction of maximum shear

Thus, at a constant carbide volume fraction, the thinner precipitated carbides with higher aspect ratios densely distributed within the small lath matrix, typical of the lower tempered steel specimens, have higher probabilities for activated dislocation sources intersecting the direction of maximum shear (regions of stress concentration) compared to the larger carbides, with reduced aspect ratios sparsely distributed within the larger lath matrix. The higher susceptibility of the lower tempered specimens to shear band formation, is attributed to the volume fraction of points of intersection between activated dislocation sources and the direction of maximum shear (regions of stress concentrations) within the specimens during impact.

It has been reported that high strength structural materials are more susceptible to the formation of ASBs and a reduction in their grain sizes typically result in a significant increase in their susceptibility to ASB formation [7, 12-13, 17]. In the absence of precipitates or reinforcing particles, i.e. a more homogenous material, reduction in grain sizes will result in higher probability of grain boundaries intersecting the direction of maximum shear during impact. Grain boundaries are also regions of local imperfections and can serve as dislocation sources during deformation when they are activated. The higher susceptibility of a homogenous material to the formation of ASBs when grain sizes are reduced (increasing their strength) prior to impact, is attributed to the increased probability of an activated dislocation source (grain boundary) intersecting the direction of maximum shear in the specimens during impact.

Furthermore, high strain gradient has been reported to be a strong driving force for strain localization due to the stress/strain partitioning characteristics between matrix and precipitates [122-125]. Zhu et al. [126] reported that the strain gradient coefficient significantly influences

the structure of the shear bands as compared to the effect of thermal conduction. Owolabi et al. [127] and Dai et al. [122] studied the effect of particle size on the formation of ASBs in particle reinforced metal matrix composites and reported that the composite reinforced with smaller particles were more susceptible to the formation of ASBs. Dai et al. attributed the size-dependency phenomenon to strain gradient effects and reported that high strain gradient is a strong driving force for the formation of ASBs in particle reinforced metal matrix composites (MMCp). In the current study, the harder brittle carbides immersed in the ductile ferrite matrix create high strain gradients during impact due to inhomogeneous stress/strain partitioning characteristics between the carbides and the matrix. The smaller carbides with their higher aspect ratios and high distribution density increase the microstructural inhomogeneity due to the inhomogeneous stress/strain partitioning. Al-Rub et al. [124] showed that at a constant volume fraction, decreasing the interparticle spacing or the size of reinforcing particles/precipitates results in a stronger and more sensitive average stress-strain response. They attributed the occurrence of plastic strain gradient hardening to the distribution and evolution of geometrically necessary dislocations which depends on the reinforcing particle size and shape. Liu et al. [123] used dislocation models by considering the mismatch of elastic modulus between matrix and reinforcing particles based on the Taylor relation and the kinetics of dislocation multiplication to determine the effective strain gradients for particle reinforced metal matrix composites. They demonstrated that the smaller the reinforcing particle size, the higher the strain gradient.

In addition, the steel specimens tempered at lower temperatures had relatively narrower shear bands than the steel specimens tempered at higher temperatures. The spacing between precipitates has been observed to influence the thickness of ASBs such the occurrence of shear

strain localization results in the concentration and retention of high residual stresses in the spaces between the reinforcing particles. It has been shown that the dislocation structures associated with large plastic deformation, interparticle spacing and grain size are the major factors that influence the width of ASBs [128-129]. Thus, the interparticle spacing has a significant influence on the thickness of the evolved ASBs. The densely distributed carbides reduces the interparticle spacing in the specimens tempered at lower temperatures which could account for the narrower shear bands with higher microhardness observed in these specimens. The increase in the microhardness of the regions within the shear bands as the thickness decreases is attributed to the very high stresses which are accommodated in narrower bands when the strain rate increases.

5.2 Mechanism of Grain Refinement and Evolution of ASBs in 4340 Steel during Impact

Thermomechanical or microstructural mechanism have been used to explain the formation of ASBs during dynamic deformation. The thermomechanical mechanism attributes the occurrence of strain localization leading to the formation of ASBs to the competition between strain hardening and thermal softening [2-5, 8-9]. In the microstructural mechanism, there is a significant change to the original microstructure and its constituents during the passage of the stress waves leading to a new microstructure due to the absorption of the strain energy [19-25]. In the case of impact, the situation is much more complicated because the deformation occurs so rapidly that it is almost impossible to observe the actual changes in properties due to the short duration between deformation and failure.

In this study, a systematic deformation coupled with a comprehensive microscopic analysis was used to establish the link between the original pre-impact microstructure and the impacted

specimen. The initial structure of the tempered steel specimens prior to impact consisted of lenticular laths of α-ferrite with interlath and intralath platelet and spherical M_3C carbides. It is observed that the structure and thickness of the shear bands become better defined and distinct as the strain rate/strain increases during the impact. This is attributed to the increase in the energy of deformation as the impact momentum increases due to the increase in the impact velocity during the passage of the stress waves through the material. The material absorbs the impact energy and the evolution of the shear bands through strain localization are ways of accommodating the absorbed impact energy**.** The material under impact is considered to have failed when ASBs form, regardless of whether it is a metallographically diffused or distinct ASB as was observed in the current study. Thus, there is no difference between the diffused and distinct ASBs that evolve after impact if the ASBs are considered as a damage mechanism.

On the microstructural level, it was observed that the structure of the ASBs that evolve during the impact after the initiation of strain localization starts out with the elongation of the grains in the shear direction. The grain elongation in the shear direction is attributed to strain localization due to the imposed local strain and strain rate which results in the change from global to localized distribution of deformation. As the local strain and strain rate increases, transverse dislocation boundaries form along the elongated grains. At the same time, random dislocation boundaries are also formed along the elongated grains. With increasing local strain and strain rate, the elongated grains break along these dislocation boundaries. However, as the imposed local strain and strain rate increase, these grains rotate leading to refinement of the boundaries of the broken grains. Moreover, it is inferred that due to the conversion of plastic work into heat, thermal assistance occurs concurrently with the grain rotation during boundary refinement which

accounts for the decrease in dislocations on the boundaries of the refined grains compared to that of the broken grains. The boundary refinement leads to grains with round boundaries compared to the straight boundaries of the broken grains.

It was observed that the evolved shear band microstructure was not uniform at any of the stages of the impact because several types of grains and structures were observed coexisting within the ASBs. At relatively lower impact momentum/strain rates, after the initiation of strain localization, the structure is comprised of mainly elongated grains and few broken grains within the ASB. After this stage, the structure that evolved after increasing the impact momentum/strain rate was made of predominantly broken grains; a few refined grains and nanograins, while yet another structure after increasing the strain rate was made of dominant refined grains, nanograins and subgrains. Table 5-1 is a summary of the types of grains and observed features within the evolved ASBs with increasing strain rate/strain. The sizes and types of the grains present within the evolved ASB after the initiation of strain localization is dependent on the ensuing strain and strain rate within the specimen during impact. Since a material is considered to have failed once a shear band forms, regardless of the type of shear band, it is inferred that the stages of grain elongation in the shear direction (texture development), breaking of the grains along initiated dislocation boundaries, grain rotation and refinement, represent a unique state of imposed local strain and strain rate within the specimen.

Table 5- 1: Microstructure of Evolved ASBs with Increasing Strain Rate/Strain

Specimen	Strain Rate	Microstructure of Evolved ASB	Grain Orientation Within ASB
C	$3189S^{-1}$	(a) Dominant elongated grains with initiated transverse and random dislocation boundaries (b) Cluster of dislocations along the prominent transverse dislocation boundaries	Grains oriented in the direction of shear (texture development)
D	$3246S^{-1}$	(a) Mixture of broken and elongated grains (b) Broken grains had straight boundaries and smaller sizes compared to the elongated grains (c) Transverse and random dislocation boundaries serve as routes for breaking of the grains and boundary refinement during grain rotation (d) Dislocations were within the broken grains compared to the elongated grains which had the dislocations clustered on the initiated boundaries	Decreasing texture/increasing random orientation
E	$3400S^{-1}$	(a) Predominant broken grains with smaller sizes and straight boundaries coexisting with evolved nanograins (b) Broken grains were predominant in this structure compared to the evolved nanograins (c) Observed subgrains and grains had dislocations within them than on the boundaries	Decreasing Texture/Increasing random orientation
F	$3853S^{-1}$	(a) Dominant refined grains, coexisting with evolved nanograins and subgrains (b) Refined grains relatively smaller than the broken grains and had round boundaries (c) Nanograins were smallest, followed by subgrains and then refined grains (d) Grains were decorated with dislocations and dislocation structures	Random Orientation

Figure 5-2 is a schematic showing the stages of grain evolution that occurs within the evolving shear band structure during impact based on the observations of the appearance of the ASB structure as a function of strain rate/impact momentum. It is emphasized here that each of the stages represent an already failed material because of the presence of either a diffused or distinct ASB within the impacted material. After the nucleation and initiation of an ASB, the occurrence of strain localization starts with texture development and the emergence of dislocations as shown in figure 5-2(a) and (b) which depicts the elongated grains with initiated transverse and random dislocation boundaries. At this stage, the elongated grains are decorated with high density of dislocations including clusters of dislocations along the predominant transverse dislocation boundaries. This represent a unique structure of ASB which corresponds to the observed metallographically diffused ASB shown in figure 5-2(c).

Figure 5-2(d) and (e) illustrates a later stage after grain elongation prior to the breaking of the elongated grains along the initiated dislocation boundaries. The observed boundaries at this stage have thin clusters of dislocations along the initiated random and transverse boundaries and corresponds to the shear band in figure 5-2(f). The broken grains with smaller sizes and straight boundaries are shown in figure 5-2(g). At this stage, the observed dislocations were within the broken grains and not concentrated on the boundaries. Rotation and boundary refinement of the broken grains results in refined grains with round boundaries as shown in figure 5-2(h) which corresponds to the distinct ASB in figure 5-2(i). Thus, each of the observed stage and ensuring structures distinctly defines the microstructure within an ASB, be it a diffused or distinct shear band and depicts the evolution of ASB based on the imposed local strain and strain rate after the initiation of strain localization during impact.

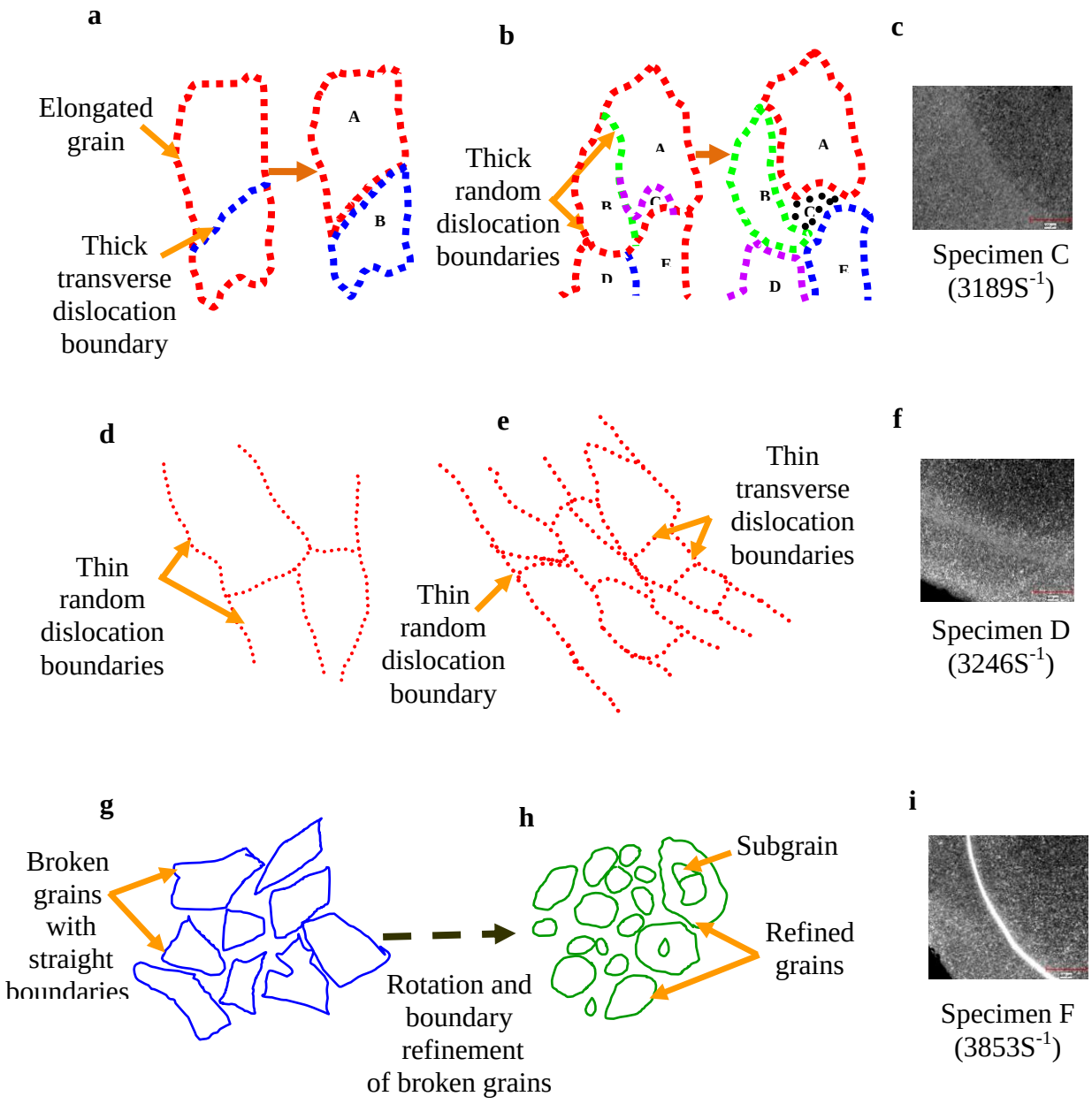

Figure 5- 2: Schematic of the stages of grain refinement during the evolution of ASBs. (a), (b) occurs after the initiation of strain localization which corresponds to the diffused ASB in (c). (d), (e) Occur prior to breaking of the elongated grains which corresponds to the ASB in (f). (g) Represents broken grains which undergo rotation and boundary refinement to produce refined grains (h) Refined grains and subgrains which corresponds to the ASB in (i).

Fine equiaxed grains with low dislocation density and well-defined grain boundaries are the microstructural characteristics of the occurrence of Dynamic Recrystallization (DRX) [6, 17]. DRX has been defined as a structural rearrangement as a result of refinement of initial grain structures of materials to a point where new nanograins form and grow [17]. Thus, the new grains that nucleate and grow based on the phenomenon of DRX would generally be dislocation free and the sizes of the final evolved grains would be dependent on diffusion and time. It has been reported that the kinetics of the existing recrystallization models are too slow than the deformation time and/or the cooling time of the shear bands during dynamic deformation [58, 63]. Progressive Subgrain Misorientation (PriSM) recrystallization model is widely accepted as a model for DRX that explains the evolution of the structure within ASBs [58, 63, 65]. It has been demonstrated that the PriSM recrystallization model is based on mechanically-assisted subgrain rotation that is kinetically feasible in the stringent time and temperature profile of an ASB and may enable dynamic recrystallization to progress at very high strain rates with little or no thermal assistance [58, 63]. In the current study, elongated grains, broken grains, refined grains, subgrains and nanograins decorated with high density of dislocations were observed within the shear band structures. This demonstrate that different mechanisms occur simultaneously including the emergence of dislocations, breaking of grains, and grain refinement during the evolution of the shear bands. Thus, dynamic recovery and dynamic recrystallization alone cannot explain the observed structure within the evolved ASBs. The observed mechanism of emergence of refined grains agrees well with the PriSM model by Hines et al. [58]. However, the PriSM model accounts for only the refined grains observed within the ASB and does not explain the presence of the heavily dislocated nanograins and subgrains. The occurrence of the nanograins in the current study is attributed to the emergence of the random dislocation boundaries along the

elongated grains after the initiation of strain localization. It is inferred that the arrangement of dislocations which results in the initiation of random dislocation boundaries may result in the creation of nanograins as was observed in figure 4-34. This would account for the reason why these nanograins were heavily dislocated as shown by the micrographs in figure 4-40. The observations in the current study also agree well with the study by Yang et al. [130] on the microstructural evolution and nanograins formation during shear localization in cold-rolled titanium. They reported that the alignment of grains in the shear direction forms the early stages of shear localization and continuous thermally assisted lath and concurrent lateral sliding and lattice rotations lead to the formation of the structure within the shear bands at large strains [130]. It is concluded that the evolution of the shear band structure can be considered as a simultaneous layering of microstructures initially driven by dislocations which produce the final structures observed in the shear bands.

5.3 The Effect of Carbides on the Microstructure of Evolved ASBs and Strain Mapping

It has been shown earlier that the precipitated carbides in the pre-impact microstructures of the tempered steel have a marked effect on the nucleation and initiation of ASBs during impact. The precipitated carbides were surrounded by network of dislocations at the carbide/ferrite interfaces. After impact, the structure of the evolved ASBs comprised elongated grains, recrystallized grains and refined grains with no apparent traces of the platelet and spherical carbides. The evolved structure within the ASBs was also decorated with high density of dislocations. The absence of the precipitated platelet and spherical carbides from the evolved structure within the ASBs is attributed to the occurrence of carbide fragmentation and redistribution during the evolution of the shear bands. It is inferred that the high local strain rate and strains within the regions of the

ASBs because of strain localization induce plastic deformation of the carbides which result in carbide fragmentation. It has been reported that dislocations generated at the ferrite/carbide interface during plastic deformation cut the carbides and drag the carbon atoms out of the carbides [131-135]. In the current study, the extensive carbide fragmentation is attributed to the movement of high density of dislocations, because of the associated high strain and strain rates during strain localization. The plastic deformation of the carbides produces the residual carbide particles. These particles may then be dragged along with the dislocations within the evolving structure causing their redistribution within the evolved shear bands. Carbide dissolution has been used to explain the disappearance/decomposition of carbides within pearlitic steel during loading by several investigators [131-135]. Wittman et al. [25] proposed that carbide dissolution occurs inside adiabatic shear bands leaving residual carbon in solution contributing to local hardening during high strain rate deformation. In addition, residual carbide particles in regions away from the ASBs appeared to have been broken off from the residual carbides. The existence of the residual carbides together with the residual carbide particles in regions away from the shear bands are attributed to the relatively lower strain and strain rates in these regions. This also affirms the theory of carbide fragmentation and redistribution.

Furthermore, the evolved structure within the shear bands were decorated with dislocations and dislocation structures which may be attributed to the presence of residual carbide particles observed within the shear bands. It is reported that the residual carbide particles locally trap and pin dislocations within the evolved shear bands. It has been shown that the binding enthalpy between carbon and iron atoms in cementite is lower than the binding enthalpy between carbon atoms and dislocations in ferrite [132, 134-135]. Gavrilyuk [134] reported that during cementite

decomposition, carbon atoms are transferred to dislocations near the interface because of the higher binding enthalpy between carbon atoms and dislocations in ferrite than the enthaply of dissolution of cementite. Chakraborty et al. [132] recently showed that the lattice parameter of ferrite does not change after cementite dissolution and that the dissociated carbon atoms do not diffuse into the ferrite lattice to form Fe-C interstitial solid solution. This affirms the carbide fragmentation and redistribution observed in the current study since the redistributed carbides do not diffuse into the ferrite lattice. It is inferred that the higher degree of carbide fragmentation and redistribution, together with the high density of trapped/pinned dislocations within the evolved shear bands account for the higher residual stresses/strains within the shear bands which increases their local hardness and susceptibility to crack nucleation and propagation during subsequent loading.

The extensive carbide reprecipitation that occurs during the post-impact annealing at $350^{O}C$ reinforces the theory of carbide fragmentation and redistribution. The reprecipitated carbides were aligned in the direction of shear, demonstrating that texture development occurs during the dynamic loading. Moreover, the observed carbide particles inside the shear bands disappeared during the post-impact annealing due to diffusion as a result of thermal activation. During the post-impact annealing, bright field TEM images of regions away from the shear bands also showed a disappearance of most of the "knitted" dislocations that bounded the subgrains developed in these regions after deformation. This is attributed to dislocation annihilation mechanisms that occur during static recovery processes. Post-impact annealing above $450\ ^{O}C$ shows static recrystallization and grain growth. Because the amount of strain energy stored in the shear band regions after impact is comparatively higher than in regions away from the shear

bands, this higher stored strain energy may trigger static recovery mechanisms and the extensive carbide reprecipitation which is observed during the post-deformation annealing process.

The local deformation mappings showed that the internal lattice rotational fields and the shear strain fields were more homogenous within the ASBs compared to the ferrite matrix within the pre-impact specimens. The local displacement and deformation gradients quantify the change in shape of infinitesimal line elements of the crystallographic lattice. The irregular distribution of lattice rotational gradients and the broader lattice rotational and strain fields associated with the ferrite matrix is attributed to the lattice-invariant deformation and shape deformation processes that occur during martensitic transformation [136]. These deformation processes occur on specific crystallographic planes such as the habit plane [73-74, 76]. This may result in higher stress and strain distribution fields on the specific crystallographic planes compared to other regions which do not contain these specific planes. On the other hand, it has been shown that the points of intersection of dislocation sources with the direction of maximum shear/stress concentration are possible sites for the nucleation and initiation of ASBs which are independent of crystallographic planes. Thus, strain localization does not occur on specific crystallographic planes which results in a more homogenous distribution of crystallographic lattice rotation and strain fields within the evolved ASBs after impact

5.4 Application of the Current Results in Tailoring and Designing Microstructures that are Resistant to the Formation of ASBs

The microstructure of the pre-impact 4340 steel specimens used in this study consisted of a ductile ferrite matrix reinforced with precipitated carbides. Even though the steel develops high strength when heat-treated, the presence of the precipitated carbides within the matrix create nucleation sites for the initiation of ASBs during impact. The current study showed that the amount, sizes and defects around the precipitated carbides in the pre-impact steel determine their susceptibility to the formation of ASBs during impact. Microstructures with thin precipitated carbides that have high aspect ratios densely distributed within the matrix are easily susceptible to the formation of ASBs. As the relative size of the carbides increase with a corresponding reduction in their aspect ratios and their distribution density within the matrix, they become more resistant to the formation of ASBs. These results for 4340 steel can be projected to other steels that have similar physical properties and microstructures such as other hardenable steels. Hardenable steels frequently used in structural applications and loadings that subject them to high strain rate and large strains of deformation have similar microstructures to the microstructures of the pre-impact 4340 steel used in this study. It is inferred that hardenable steels that can achieve yield strengths of over 2000MPA will exhibit similar behavior as that observed in the 4340 steel during impact. Thus, the results from the current study provide the knowledge and understanding to model and design materials with higher resistance to the formation of ASBs by using knowledge about heat treatment, and controlling its composition and grain size. Similarly, although the current results are specific to the behavior of BCC ferritic pearlitic hardenable steels, the response of Metal Matrix Composites (MMCs) to shear strain localization during high strain rate deformations could also be predicted by controlling the size, amount and distribution of reinforcements within the MMCs.

Additionally, the current numerical models that include the nucleation and initiation of ASBs such as the work by Erlich et al. [103] assume a blank microstructure and applies to materials with simple microstructures. However, most of the materials used for structural applications that are susceptible to the formation of ASBs have complex microstructures with constituents including carbides, solutes and hard particles/second phases. Thus, the starting microstructures of the materials used for high strain rate applications are not blank and simple as is assumed in numerical models that predict the formation of ASBs. In the case of structural steels, while heat treatment procedures are used to strengthen the steels by producing a complex microstructure with different constituents and phases, it is these complex microstructures that are easily susceptible to the formation of ASBs. Moreover, from the results of the current study, it is inferred that a critical parameter in any numerical model that predicts the microstructural evolution of ASBs in hardened steels should start with the emergence of dislocations and texture development after the initiation of strain localization. After the occurrence of strain localization and texture development, the presence of extra strain energy due to increasing impact momentum/strain rate would result in the reduction in grain sizes and evolution of refined grains through grain rotation and boundary refinement. The knowledge and understanding from this study can be used to develop theoretical and numerical models which take into account these complex microstructures and better depict the microstructures of materials used for structural applications. Such plastic models would provide more accurate results for the nucleation and propagation of ASBs during high strain rate applications.

CHAPTER 6
SUMMARY AND CONCLUSIONS

It was established in the previous chapter that the initiation and formation of ASBs in 4340 steel during impact undergo complex mechanisms that depends on the pre-impact microstructure. In order to determine the effect of the pre-impact microstructure on the nucleation and initiation of ASBs and to determine the mechanism of evolution of ASBs during impact, it is imperative to systematically study the microstructure of the specimens prior to impact, after impact and after post-impact annealing. Following this procedure, it was observed that concurrent occurrence of different mechanisms including the emergence of dislocations, texture development, grain rotation and refinement result in the evolution of the microstructure within ASBs in impacted 4340 steel specimens. This agrees well with recent findings on the mechanism of evolution of ASBs [12, 63, 130]. It was demonstrated that the occurrence of Dynamic Recovery (DR) and Dynamic Recrystallization (DRX) alone would not be sufficient to explain the observed microstructure within the evolved ASBs in impacted 4340 steel specimens because of the presence of refined and nano-grains with high density of dislocations. This was established when the microstructure within the ASBs was compared with the microstructure in regions outside the ASBs. In addition, the current study demonstrated that the points of intersection of activated dislocation sources and the direction of maximum shear or regions of stress concentrations (as defined by the impact direction and the geometry of the specimen) within the impacted steel, are possible sites or regions for the nucleation and initiation of ASBs during impact depending on the rate of generation of dislocations, imposed local strain and strain rate. This is the first time experimental observations have been used to predict regions within the microstructure of 4340 steel that could serve as sites for the nucleation and initiation of ASBs during impact. These

results are specific to the behavior of BCC ferritic pearlitic hardenable steels. A summary of the findings and conclusions from this research are presented below:

1. The initiation of ASBs in AISI 4340 steel during impact occurs when the microstructure is highly inhomogeneous. Specimens tempered at lower temperatures are more susceptible to the formation of ASBs because of the higher inhomogeneities as established by the amount, sizes and defects around precipitated carbides and the prevalence of these carbides at lower tempering temperatures in the pre-impact microstructures.

2. For the three tempering temperatures employed in the current study, misfit interfaces and semi-crystalline boundary layers with random arrangement of atomic columns observed around precipitated carbides increase the volume fraction of dislocation sources within the pre-impact microstructures.

3. The steel specimens tempered 315°C had thin precipitated carbides with high aspect ratios densely distributed within the matrix and were susceptible to the formation of ASBs. As the tempering temperature increased to 425°C and 620°C, the relative size of the carbides increased with a corresponding reduction in their aspect ratios and their distribution density within the matrix and they were resistant to the formation of ASBs.

4. The volume fraction of the sources of emergence and multiplication of dislocations within the specimens coupled with the rate of dislocation generation are very significant to the initiation of strain localization during impact.

5. Upon impact of the projectile on a specimen, the geometry of the specimen, direction and surfaces of impact define a specific direction of maximum shear within the specimen. The presence of a dislocation source (region of local imperfection) within the microstructure of a specimen is a necessary condition for the source to act as a possible site for the emergence and multiplication of dislocations provided the source is activated during deformation. However, the intersection of an activated dislocation source with the direction of maximum shear (regions of stress concentration) within the specimen during impact, is a necessary condition for the points of intersection to act as a possible site for the nucleation of ASBs depending on the rate of dislocation generation, local strain and strain rate.

6. The higher susceptibility of the 315°C-1hr tempered specimens to ASB formation is attributed to the volume fraction of the points of intersection of activated dislocation sources with the direction of maximum shear (regions of stress concentrations) within the specimen during impact. At a constant carbide volume fraction, the thinner precipitated carbides with high aspect ratios densely distributed within the small lath matrix, have higher probability for an activated dislocation source to intersect the direction of maximum shear (regions of stress concentration) compared to the larger carbides with reduced aspect ratios sparsely distributed within the larger lath matrix.

7. The structure of the shear bands that evolve after strain localization starts out with elongation of the grains due to grain reorientation in the shear direction with the initiation of random and transverse dislocation boundaries along the elongated grains. The transverse and random dislocation boundaries serve as possible routes for breaking of the elongated grains.

8. Boundary refinement of the broken grains occurring through grain rotation and adiabatic heating results in the evolution of refined grains, subgrains and nanograins. However, this adiabatic heating which results in a temperature rise of the specimen during impact is not high enough to cause a phase transformation as has been reported by some investigators.

9. The presence of highly dislocated elongated grains, broken grains, refined grains, subgrains and nanograins within the shear band structure demonstrates that the emergence of dislocations, texture development, grain rotation and refinement occur concurrently within the localized regions during impact.

10. The sizes and types of the grains present within the evolved ASB after the initiation of strain localization is dependent on the ensuing strain and strain rate during impact. Thus, since a material is considered to have failed once a shear band forms, the stages of grain elongation in the shear direction (texture development), breaking of the grains along initiated dislocation boundaries, grain rotation and boundary refinement, represent a unique state of imposed local strain and strain rate within the specimen.

11. Extensive carbide fragmentation and redistribution occurs within ASBs because of plastic deformation of carbides during impact. The carbide fragmentation produces fine residual carbides within the ASBs. This is attributed to strain localization which results in high strain rates and strains within the ASBs when compared to regions away from the shear bands.

12. Partial carbide fragmentation and redistribution occurs in regions outside the ASBs because of the associated lower strain rates and strains. The partial carbide fragmentation produces smaller residual carbides and residual carbide particles in regions outside the ASBs.

13. Residual carbide particles trap and pin dislocations within the shear bands which account for the presence of dislocations within the evolved ASBs. Additionally, the residual carbide particles increase the residual stresses/strains and contribute to local hardening within the ASBs.

14. Post-impact annealing at $350^{O}C$ resulted in an increase in hardness of both regions outside the shear bands and regions within the shear bands regardless of the heat treatment before impact, amount of deformation, and the time of annealing which is attributed to carbide reprecipitation during the post-impact annealing.

15. A more homogenous distribution of narrower and shorter rotational and shear strain fields were revealed by the local deformation maps within the evolved ASBs. It is concluded that strain localization does not occur on specific crystallographic planes during impact. This results in a more regular distribution of internal lattice rotational and strain fields within the ASBs.

16. It is concluded that the evolution of the shear band structure can be considered as a simultaneous layering of microstructures initially driven by dislocations which produce the final structures observed in the shear bands at the end of passage of the stress wave.

REFERENCES

[1] J. A. Zukas, Impact Dynamics, John Wiley & Sons Inc. (1982)

[2] J. Hopkinson, Original Papers By J. Hopkinson, And B. Hopkinson, Cambridge University Press 2 (1901) 316-324

[3] R. W. Armstrong And S. M. Walley, High Strain Rate Properties Of Metals And Alloys, International Materials Reviews 53 (2008) 105-128

[4] F. J. Zerilli And R. W. Armstrong, Dislocation-Mechanics-Based Constitutive Relations For Material Dynamics Calculations, Journal Of Applied Physics 61 (1987) 1816-1825

[5] C. Zener And J. H. Hollomon, Effect Of Strain Rate Upon Plastic Flow Of Steel, Journal Of Applied Physics 15 (1944) 22-32

[6] Y. Xu, J. Zhang, Y. Bai And M. A. Meyers, Shear Localization In Dynamic Deformation: Microstructural Evolution, Metallurgical And Materials Transactions A 39 (2008) 811-841

[7] N. Bassim, Mesoscale Manifestations Of Damage In Metallic Materials, 13th International Conference On Mesomechanics (2011) 1-3

[8] L. E. Murr, E. A. Trillo, S. Pappu And C. Kennedy, Adiabatic Shear Bands And Examples Of Their Role In Severe Plastic Deformation, Journal Of Materials Science 37 (2002) 3337-3360

[9] C. M. Glass, G. M. Moss And S. K. Golaski, Response Of Metals To High Velocity Deformation, Wiley Interscience (1961)

[10] M. A. Meyers, B. Y. Cao, V. F. Nesterenko, D. J. Benson And Y. B. Xu, Shear Localization Martensitic Transformation Interactions In Fe-Cr-Ni Monocrystal, Metallurgical And Materials Transactions A 35 (2004) 2575-2586

[11] M. E. Backmann And S. A. Finnegan, Metallurgical Effects At High Rates Of Strain, Plenum Press, New York (1973) 531-543

[12] Q. Wei, Z. L. Pan, X. L. Wu, B. E. Schuster, L. J. Kecskes And R. Z. Valiev, Microstructure And Mechanical Properties At Different Length Scales And Strain Rates Of Nanocrystalline Tantalum Produced By High-Pressure Torsion, Acta Materialia 59 (2011) 2423-2436

[13] B. E. Schuster, J. P. Ligda, Z. L. Pan And Q. Wei, Nanocrystalline Refractory Metals For Extreme Condition Application, Journal Of Metals 63 (2011) 27-31

[14] J. Peirs, W. Tirry, , B. Amin-Ahmadi, F. Coghe, P. Verleysen, L. Rabet, D. Schryvers And J. Degrieck, Microstructure Of Adiabatic Shear Bands In Ti-6al-4v, Materials Characterization 75 (2013) 79-92

[15] D. Rittel, G. Ravichandran And A Venkert, The Mechanical Response Of Pure Iron At High Strain Rates Under Dominant Shear, Material Science And Engineering A 432 (2006) 191-201

[16] D. Rittel, A Different Viewpoint On Adiabatic Shear Localization, Applied Physics 42 (2009) 1-6

[17] B. Dodd And Y. Bai, Adiabatic Shear Localization: Frontiers And Advances, Elsevier (2012)

[18] J. A. Hines, K. S. Vecchio And S. Ahzi, A Model For Microstructural Evolution In Adiabatic Shear Bands, Metallurgical And Materials Transactions A 29 (1998) 191-203

[19] S. Boakye -Yiadom, Effect Of Heat Treatment On Stability Of Adiabatic Shear Bands In 4340 Steel, Master of Science Thesis, University Of Manitoba (2010)

[20] S. Boakye-Yiadom And M. N. Bassim, Effect Of Heat Treatment On Stability Of Impact-Induced Adiabatic Shear Bands In 4340 Steel, Materials Science And Engineering A 546 (2012) 223– 232

[21] M. N. Bassim And A. G. Odeshi, Shear Strain Localization And Fracture In High Strength Structural Materials, Archives Of Material Science And Engineering 31 (2008) 69-74

[22] K. A. Zurek, The Study Of Adiabatic Shear Band Instability In A Pearlitic 4340 Steel Using A Dynamic Punch Test, Metallurgical Transactions A Volume 25 (1994) 2483

[23] K. M. Cho, S. Lee, S. R. Nutt And J. Duffy, Adiabatic shear band formation during dynamic torsional deformation of an HY-100 steel, Acta Metallurgica et Materialia 41 (1993) 923-932

[24] A. G. Odeshi, M. N. Bassim And S. Al-Ameeri, Effect Of Heat Treatment On Adiabatic Shear Bands In High Strength Low Alloy Steel, Materials Science And Engineering A 419 (2006) 69–75

[25] C. L. Wittman, M. A. Meyers And H. R. Pak, Observation Of An Adiabatic Shear Band In AISI 4340 Steel By High-Voltage Transmission Electron Microscopy, Metallurgical Transactions A 21 (1990) 707-716

[26] S. Boakye-Yiadom, M. N. Bassim and S. Al-Ameeri, On The Persistence Of Adiabatic Shear Bands, 10th International Conference on the Mechanical and Physical Behaviour of Materials under Dynamic Loading, EPJ Web Of Conferences 26 (2012) 1-4

[27] B. Zhang, W. Shen And Y. Liu, Adiabatic Shear Bands In Impact Wear, Journal Of Material Science 17 (1998) 765-767

[28] X. W. Chen, Q. M. Li And S. C. Fan, Initiation Of Adiabatic Shear Failure In A Clamped Circular Plate Struck By A Blunt Projectile, International Journal Of Impact Engineering 31 (2005) 877-893

[29] A. L. Wingrove, A Note On The Structure Of Adiabatic Shear Bands In Steel, Department Of Supply, Australian Defense Scientific Service, Defense Standard Laboratories, Technical Memo 33 (1971)

[30] R. Nakkalil, Formation Of Adiabatic Shear Bands In Eutectoid Steels In High Strain Rate Compression, Acta Metallurgica et Materialia 39 (1991) 2553-2563

[31] P. W. Leech, Observations Of Adiabatic Shear Band Formation In 7039 Aluminum Alloy, Metallurgical Transactions A 16 (1985) 1900-1903

[32] W. S Lee, T. H. Chen, C. F. Lin And G. T. Lu, Adiabatic Shearing Localisation In High Strain Rate Deformation Of Al-Sc Alloy, Materials Transactions 51 (2010) 1216 – 1221

[33] S. Boakye-Yiadom And M. N. Bassim, Effect Of Prior Heat Treatment On The Dynamic Impact Behavior Of 4340 Steel And Formation Of Adiabatic Shear Bands, Materials Science And Engineering A 528 (2011) 8700-8708

[34] G. A. Li, L. Zhen, C. Lin, R. S. Gao, X. Tan And C. Y. Xu, Deformation Localization And Recrystallization In Tc4 Alloy Under Impact Condition, Materials Science And Engineering A 395 (2005) 98-101

[35] Y. Bai And B. Dodd, Adiabatic Shear Localization, Pergamon Press (1992)

[36] V. E. Panin, V. E. Egoweshkin And A. V. Panin, Proceedings Of Mesomechanics (2010) 215-229

[37] N. K. Bourne, J.C.F. Millett And G.T. Gray Iii, On The Metallurgy Of Shock Deformation In Simple Metals, Proceedings Of The Scanning Electron Microscopy Annual Conference (2009)

[38] J. J. Gilman, Micromechanics Of Shear Banding, Lawrence Berkeley Laboratory, 32810 DE93-002568 (1992)

[39] D. Hull And D. J. Bacon, Introduction To Dislocations, 3rd Ed, International Series On Materials Science And Technology, Pergamon Press (1984)

[40] A. N. Holden, The Yielding Behavior Of Iron Single Crystals, Journal Of Applied Physics 22 (1951) 1290-1297

[41] M. A. Meyers, A. Mishra And D. J. Benson, Mechanical Properties Of Nanocrystalline Materials, Progress In Materials Science 51 (2006) 427–556

[42] R. Z. Valiev, R. K. Islamgaliev And I. V. Alexandrov, Bulk Nanostructured Materials From Severe Plastic Deformation, Progress In Materials Science 45 (2000) 103-189

[43] L. S. Costin, E. E. Crisman, R. H. Hartley And J. Duffy, On The Localization Of Plastic Flow In Mild Steel Tubes Under Dynamic Torsional Loading, 2nd Conference On The Mechanical Properties Of Materials At High Rates Of Strain, Institute Of Physics (1979) 90-96

[44] K. A. Hartley, J. Duffy And R. H. Hawley, Measurement Of The Temperature Profile During Shear Band Formation In Steels Deforming At High Strain Rates, Journal of the Mechanics and Physics of Solids 35 (1987) 283-301

[45] A. Marchand And J. Duffy, An Experimental Study Of The Formation Process Of Adiabatic Shear Bands In A Structural Steel, Journal of the Mechanics and Physics of Solids 36 (1988) 251-283

[46] J. Duffy, Temperature Measurements During The Formation Of Shear Bands In A Structural Steel, In Mechanics Of Material Behavior, The Daniel C. Drucker Anniversary Volume, Elsevier (1984) 75-79

[47] J. Duffy And Y. C. Chi, On The Measurement Of Local Strain And Temperature During The Formation Of Adiabatic Shear Bands, Materials Science And Engineering A 157 (1992) 195–210

[48] H. Feng And M. N. Bassim, Finite Element Modeling Of The Formation Of Adiabatic Shear Bands In AISI 4340 Steel, Material Science And Engineering A 266 (1999) 255-260

[49] K. L. Johnson And K. M. Smith Jr., Failure Analysis Of The Estonia, Advanced Materials And Processes (2009) 29-33

[50] G. R. Johnson And W. H. Cook , A Constitutive Model And Data For Metals Subjected To Large Strains, High Strain Rates And High Temperatures, 7th International Symposium On Ballistics (1983) 541-547

[51] G. R. Johnson And W. H. Cook, Fracture Characteristics Of 3 Metals Subjected To Various Strains, Strain Rates, Temperatures And Pressures, Engineering Fracture Mechanics 21 (1985) 31-48

[52] G. R. Johnson And T. J. Holmquist, Evaluation Of Cylinder-Impact Test Data For Constitutive Model Constants, Journal Of Applied Physics 64 (1988) 3901-3910

[53] L. Anand, Constitutive Equations For Hot-Working Of Metals, International Journal Of Plasticity 1 (1985) 213-31

[54] J. Delorme, Extension Of A Finite Element Model To 2d For The Prediction Of Adiabatic Shear Bands, Master Of Science Thesis, The University Of Manitoba (2012)

[55] I. Polyzois, Finite Element Modeling Of The Behavior Of Armor Materials Under High Strain Rates And Large Strains, Master Of Science Thesis, University Of Manitoba (2010)

[56] D. Rittel, A. Bhattacharyya, B. Poon, J. Zhao And G. Ravichandran, Thermomechanical Characterization Of Pure Polycrystalline Tantalum, Material Science And Engineering A 447 (2007) 65-70

[57] D. Rittel And Z. Wang, Thermo-Mechanical Aspects Of Adiabatic Shear Failure Of Am50 And Ti6al4v Alloys, Mechanics of Materials 40 (2008) 629-635

[58] J. A. Hines And K. S. Vecchio, Recrystallization Kinetics Within Adiabatic Shear Bands, Acta Materialia 45 (1997) 635-649

[59] G. Ravichandran, A. J. Rosakis, J. Hodowany And P. Rosakis, On The Conversion Of Plastic Work Into Heat During High-Strain-Rate Deformation, Shock Compression Of Condensed Matter (2001), American Institute Of Physics (2002) 557-562

[60] R. C. Glenn And W. C. Leslie, The Nature Of "White Streaks" In Impacted Steel Armor Plate, Metallurgical Transactions 2 (1971) 2945-2947

[61] C. Z. Duan, Y. J. Cai, M. J. Wang And G. H. Li, Microstructural Study Of Adiabatic Shear Bands Formed In Serrated Chips During High-Speed Machining Of Hardened Steel, Journal Of Material Science 48 (2009) 897–902

[62] Y. Yang, F. Jiang, B. M. Zhou, X. M. Li, H. G. Zheng And Q.M. Zhang, Microstructural Characterization And Evolution Mechanism Of Adiabatic Shear Band In A Near Beta-Ti Alloy, Materials Science And Engineering A 528 (2011) 2787–2794

[63] M. T. Perez-Prado, J. A. Hines And K. S. Vecchio, Microstructural Evolution In Adiabatic Shear Bands In Ta And Ta-W Alloys, Acta Materialia 49 (2001) 2905-2917

[64] J. R. Trelewicz And C. A. Schuch, The Hall-Petch Breakdown At High Strain Rates: Optimizing Nanocrystalline Grain Size For Impact Applications, Applied Physics Letters 93 (2008) 171916

[65] J. A. Hines And K. S. Vecchio, Dynamic Recrystallization In Adiabatic Shear Bands In Shock-Loaded Copper, Proceeding Of The 1995 International Conference On Metallurgical And Materials Applications Of Shock-Wave And High-Strain-Rate Phenomena, EXPLOMET, Elsevier (1995) 421-428

[66] D. Jia, Y. M. Wang, K. T. Ramesh, E. Ma, Y. T. Zhu And R. Z. Valiev, Deformation Behavior And Plastic Instabilities Of Ultrafine-Grained Titanium, Applied Physics Letters 79 (2001) 611–613

[67] J. E. Bailey And P. B. Hirsch, The Recrystallization Process In Some Polycrystalline Metals, Proceedings Of The Royal Society Of London A 267 (1962) 11-30

[68] J. M. Li, Possibility Of Subgrain Rotation During Recrystallization, Journal Of Applied Physics 33 (1962)

[69] H. Hu, In Recovery And Recrystallization Of Metals, Interscience Publishing (1963)

[70] U. Andrade, M. A. Meyers, A. H. Chokshi, And K. S. Vecchio, Dynamic Recrystallization And Grain Size Effects In Shock- Hardened Copper, Journal De Physique 4 (1994) 361-366

[71] R. D. Doherty And J. A. Szpunar, Kinetics Of Sub-Grain Coalescence—A Reconsideration Of The Theory, Acta Metallurgica 32 (1984) 1789–1798

[72] D. Lehmhus, M. Busse, A. Herrmann And K. Kayvantash, Structural Materials And Processes In Transportation, Wiley (2013)

[73] G. Krauss, Steels, Processing, Structure And Performance, ASM International (2005)

[74] G. F. Vander-Voort, Metallography In Principles And Practice, McGraw-Hill Book Company (1984)

[75] M. A. Grossmann And E. C. Bain, Principles Of Heat Treatment, American Society Of Metals (1964)

[76] W. S. Lee And T. T. Su, Mechanical Properties And Microstructural Features Of AISI 4340 High-Strength Alloy Steel Under Quenched And Tempered Condition, Journal Of Materials Processing Technology 87 (1999) 198-206

[77] F. C. Campbell, Elements Of Metallurgy And Engineering Alloys, ASM International (2008)

[78] D. P. Koistinen And R. E. Marburger, A General Equation Prescribing The Extent Of The Austenite-Martensite Transformation In Pure Iron-Carbon Alloys And Plain Carbon Steels, Acta Metallurgica 7 (1959) 59-60

[79] K. R Kinsman And J. S Shyne, Thermal Stabilization Of Austenite In Iron-Nickel-Carbon Alloys, Acta Metallurgica 15 (1967) 1527-1543

[80] M. S. Wechsler, D. S. Lieberman And T. A Read, Theory Of The Formation Of Martensite, Transactions AIME 197 (1953) 1503-1515

[81] J. S Bowles And J. K. Mackenzie, The Crystallography Of Martensite Transformations, Acta Metallurgica 2 (1954) 129-147, 224-234

[82] C. Zhu, Tempering Of Engineering Steels, Oxford Materials (2005) 1-32

[83] C. S. Roberts, B. L. Averbach And M. Cohen, The Mechanism And Kinetics Of The First Stage Of Tempering, Transactions ASM 45 (1953) 576-585

[84] P. G. Winchell And M. Cohen, The Strength Of Martensite, Transactions ASM 55 (1962) 347-361

[85] G. Krauss, Deformation And Fracture In Martensitic Carbon Steels Tempered At Low Temperatures, Metallurgical And Materials Transaction A 32 (2001) 861-877

[86] A. R. Marder And G. Krauss, The Morphology Of Martensite In Iron-Carbon Alloys, Transactions ASM 60 (1967) 651-660

[87] M. G. Mendiratta, J. Sasser And G. Krauss, Effect Of Dissolved Carbon On Microcracking In Martensite Of An Fe-1.39C Alloy, Metallurgical Transactions 3 (1972) 351-353

[88] J. M. Marder And A. R. Marder, The Morphology Of Iron-Nickel Massive Martensite, Transactions ASM 62 (1969) 1-10

[89] G. R. Speich, Tempering Of Low–Carbon Martensite, Transactions TMS-AIME 245 (1969) 2552-2564

[90] J. Pesicka, R. Kuzel, A Dronhofer And G. Eggeler, The Evolution Of Dislocation Density During Heat Treatment And Creep Of Tempered Martensite Ferritic Steels, Acta Materialia 51 (2003) 4847-4862

[91] S. Morito, J. Nishikawa And T. Maki, Dislocation Density Within Lath Martensite In Fe-C And Fe-Ni Alloys, Transactions Of Iron And Steel Institute Of Japan 43 (2003) 1475-1477

[92] ASTM STP 407, Temper Embrittlement In Steels, A Symposium Presented At A Meeting Of Committee A-1 On Steel, American Society For Testing And Materials (1967) 1-19

[93] ASTM STP 499, Temper Embrittlement Of Alloy Steels, American Society For Testing And Materials (1971) 1-33

[94] D. H. Herring, The Embrittlement Phenomena In Hardened & Tempered Steel, The International Journal Of Thermal Technology (2006)

[95] A. Reguly, T. R. Strohaecker, G. Krauss And D. K. Matlock, Quench Embrittlement Of Hardened 5160 Steel As A Function Of Austenitizing Temperature, Metallurgical & Materials Transactions A 35 (2004) 153

[96] R. A. Grange, C. R. Hribal And L. F. Porter, Hardness Of Tempered Martensite In Carbon And Low-Alloy Steels, Metallurgical Transactions A 8 (1977) 1775-1785

[97] G. Kurdjumov And G. Sachs, Uber Den Mechanismus Der Stahlhartung," Zeitschrift Für Physik 64 (1930) 225

[98] D. Brandon And W. D. Kaplan, Microstructural Characterization Of Materials, Wiley (2008)

[99] C. A. Volkert And A. M. Minor, Focused Ion Beam Microscopy And Micromachining, Bulletin MRS 32 (2007) 389-399

[100] D. B. Williams And C. B. Carter, Transmission Electron Microscopy, Springer Science (2009)

[101] B. K. Kad , J.-M. Gebert , M. T. Perez-Prado, M. E. Kassner And M. A. Meyers, Ultrafine-Grain-Sized Zirconium By Dynamic Deformation, Acta Materialia 54 (2006) 4111–4127

[102] N. Bassim , K. Scott And L. A. Giannuzzi, Recent Advances In Focused Ion Beam Technology And Applications, Bulletin MRS 39 (2014) 317-325

[103] D. C. Erlich, L. Seamen And D. A. Shockley, Development Of A Computational Shear Band Model. Aberdeen Proving Ground, U.S. Army Ballistic Research Laboratory (1980)

[104] M. J. Hÿtch, Geometric Phase Analysis Of High Resolution Electron Microscope Images, Scanning Microscopy 11 (1997) 53-66

[105] M. J. Hÿtch, E. Snoeck And R. Kilaas, Quantitative Measurement Of Displacement And Strain Fields From Hrem Micrographs, Ultramicroscopy 74 (1998) 131-146

[106] M. J. Hÿtch And T. Plamann, Imaging Conditions For Reliable Measurement Of Displacement And Strain In High-Resolution Electron Microscopy, Ultramicroscopy 87 (2001) 199-212

[107] D. R. G. Mitchell, Difftools: Software Tools For Electron Diffraction In Digital Micrograph, Microscopy Research And Technique 71 (2008) 588-593

[108] J. Chung And L. Rabenberg, Effects Of Strain Gradients On Strain Measurements Using Geometrical Phase Analysis In The Transmission Electron Microscope, Ultramicroscopy 108 (2008) 1595-1602

[109] V. Grillo And F. Rossi, STEM_CELL: A Software Tool For Electron Microscopy. Part 2 Analysis Of Crystalline Materials, Ultramicroscopy 125 (2013) 112-129

[110] V. Grillo And E. Rotunno, STEM_CELL: A Software Tool For Electron Microscopy: Part I-Simulations, Ultramicroscopy 125 (2013) 97-111

[111] A. Guinier, X-Ray Diffraction In Crystals, In: Imperfect Crystals And Amorphous Bodies, Dover Publications (1994)

[112] A. L. Patterson, The Scherrer Formula For X-Ray Particle Size Determination, Physical Review 56 (1939) 978–982

[113] N. S. Lim, C. W. Bang, S. Das, H. W. Jin, R. Ayer And C. G. Park, Influence Of Tempering Temperature On Both The Microstructural Evolution And Elemental Distribution In AISI 4340 Steels, Metals And Materials International 18 (2012) 87-94

[114] S. Abrate, Impact dynamics: Impact engineering of composite structures, Springer 526 (2011)

[115] M. A. Meyers, G. Subhashb, B. K. Kada And L. Prasada, Evolution Of Microstructure And Shear-Band Formation In -Hcp Titanium, Mechanics Of Materials 17 (1994) 175-193

[116] A. Roos, J. Th.M. De Hosson And E. V. Der Giessen, High-Speed Dislocations In High Strain-Rate Deformations, Computational Materials Science 20 (2001) 19-27

[117] A. Roos, J. Th.M. De Hosson, H. H. M. Cleveringa And E. V. Der Giessen, Fast-Moving Dislocations In High Strain-Rate Deformation, Computational Materials Science 18 (2000)

[118] L. Yumen, Low-Energy Dislocation Structures In Cyclically Deformed Quench-Tempered Steel, Material Science And Engineering A 113 (1989) 237-244

[119] L. Yumen, Plastic Deformation In Quench-And 650oc Tempered Steel, Chinese Journal Of Metal Science And Technology 5 (1989) 333-338

[120] H. M. Ghomi And A. G. Odeshi, The Effects Of Microstructure, Strain Rates And Geometry On Dynamic Impact Response Of A Carbon–Manganese Steel, Materials Science And Engineering A 532 (2012) 308– 315

[121] L. W. Meyer And S. Manwaring, Critical Adiabatic Shear Strength Of Low Alloyed Steel Under Compressive Loading in Metallurgical Applications Of Shock-Wave And High-Strain-Rate Phenomena, Marcel Dekker (1986) 657-674

[122] L. H. Dai, L. F. Liu And Y. L. Bai, Effect Of Particle Size On The Formation Of Adiabatic Shear Band In Particle Reinforced Metal Matrix Composites, Materials Letters 58 (2004) 1773-1776

[123] L. F. Liu, L. H. Dai And G. W. Yang, Strain Gradient Effects On Deformation Strengthening Behavior Of Particle Reinforced Metal Matrix Composites, Materials Science And Engineering A 345 (2003) 190 – 196

[124] R. K. A. Al-Rub And M. Ettehad, Modeling Interparticle Size Effect On Deformation Behavior Of Metal Matrix Composites By A Gradient Enhanced Plasticity Model, Journal Of Engineering Materials And Technology 133 (2011)

[125] X. Zhang, K. Matsuura And M. Ohno, Effect Of Strain Rate On The Plastic Strain Gradient Beneath The Deformed Surface Of Iron, Journal Of Physics 419 (2013) 1-4

[126] H. T. Zhu, H. M. Zbib And E. C. Aifantis, On The Role Of Strain Gradient In Adiabatic Shear Banding, Acta Mechanica 111 (1995) 111-124

[127] G. M. Owolabi, A. G. Odeshi, M. N. K. Singh And M. N. Bassim Dynamic Shear Band Formation In Aluminum 6061 And Aluminum 6061-T6/Al_2O_3 Composites. Materials Science And Engineering A 457 (2007) 114-119

[128] B. C. Batra And C. H. Kim, Analysis Of Shear Banding In Twelve Materials, International Journal Of Plasticity 8 (1992) 425 - 452

[129] J. P. Hirth, A Model For A Propagating Shear Band On The Basis Of A Tilt Wall Dislocation Array, Applied Mechanics Review 45 (1992) 71-74

[130] D. K. Yang, P. Cizek, P. D. Hodgson And C. E. Wen, Microstructure Evolution And Nanograin Formation During Shear Localization In Cold-Rolled Titanium, Acta Materialia 58 (2010) 4536 – 4548

[131] Y. Ivanisenko, W. Lojkowski, R. Z. Valiev And H. -J. Fecht, The Mechanism Of Formation Of Nanostructure And Dissolution Of Cementite In A Pearlitic Steel During High Pressure Torsion, Acta Materialia 51 (2003) 5555–5570

[132] J. Chakraborty, M. Gosh, Rajeev Ranjan, G. Das, D. Das And S. Chandra, X-Ray Diffraction And Mossbauer Spectroscopy Studies On Cementite Dissolution In Cold-Drawn Pearlitic Steel, Philosophical Magazine 93 (2013) 4598-4616

[133] V. N. Gridnev, V. G. Gavrilyuk, I. Y. Dekhtyar, Y. Y. Meshkov, P. S. Nizin And V. G. Prokopenko, Investigation Of Carbide Phase In Strained Steel By The Method Of Nuclear Gamma Resonance, Physica Status Solidi (1972) 689-694

[134] V. G. Gavrilyuk, Decomposition Of Cementite In Pearlitic Steel Due To Plastic Deformation, Materials Science And Engineering A (2003) 81-89

[135] X. Sauvage, C. Opreauxf, F. Danoix And D. Blavette, Atomic-Scale Observation And Modelling Of Cementite Dissolution In Heavily Deformed Pearlitic Steels, Philosophical Magazine (2000) 781-796

[136] J. W. Christian, The Theory Of Transformations In Metals And Alloys, Pergamon, Elsevier Science Ltd (2002)

RESEARCH CONTRIBUTIONS

Journal Articles

[1] S. Boakye-Yiadom, A. K. Khan And N. Bassim, Effect of Pre-impact Microstructure on the nucleation and initiation of Adiabatic Shear Bands (ASBs) During Impact, Materials Science And Engineering A (2014) 373-394

[2] S. Boakye-Yiadom, A. K. Khan And N. Bassim, Deformation Mapping and the Role of Carbides on the Microstructure and Properties of Evolved Adiabatic Shear Bands, Metallurgical And Materials Transaction A 45 (2014) 5379-5396

[3] S. Boakye-Yiadom, A. K. Khan And N. Bassim, A Systematic Study Of Grain Refinement During Impact Of 4340 Steel, Materials Science And Engineering A 605 (2014) 270–285

[4] S. Boakye-Yiadom, N. Bassim And A. K. Khan, Microscopical Study Of The Formation Of Adiabatic Shear Bands In 4340 Steel During Dynamic Loading, Philosophical Magazine 93 (2013) 4544-4568

[5] S. Boakye-Yiadom And M. N. Bassim, Effect Of Heat Treatment On Stability Of Impact-Induced Adiabatic Shear Bands In 4340 Steel, Materials Science And Engineering A 546 (2012) 223-232

[6] S. Boakye-Yiadom And M. N. Bassim, Effect Of Prior Heat Treatment On The Dynamic Impact Behavior Of 4340 Steel And Formation Of Adiabatic Shear Bands, Materials Science And Engineering A (2011) 8700-8708

Conference Proceedings

[1] S. Boakye-Yiadom And N. Bassim, Use Of Focused Ion Beam (FIB) To Study The Impact Properties Of Materials, 6th Annual FIB SEM User Group Meeting, Harvard University, Cambridge, Massachusetts (March 2013)

[2] S. Boakye-Yiadom And N. Bassim, Methodologies For The Study Of The Formation Of Adiabatic Shear Bands During Impact, 16th International Conference On Advances In Materials & Processing Technologies Taipei, Taiwan (September 2013)

[3] S. Boakye-Yiadom And N. Bassim, Microstructural Mechanisms During Impact And Evolution Of Adiabatic Shear Bands In Steel, Microscopical Society Of Canada Annual Meeting, University Of Victoria In British Columbia (June 2013)

[4] N. Bassim And S. Boakye-Yiadom, The Role Of Dislocation Structures In Assessment Of Damage In Metallic Materials, Proceedings Of The 19th International Symposium On Plasticity & Its Current Applications 2013, Neat Press (2013) 109-111

[5] S. Boakye-Yiadom, M. N. Bassim and S. Al-Ameeri, On The Persistence Of Adiabatic Shear Bands, 10th International Conference on the Mechanical and Physical Behaviour of Materials under Dynamic Loading, EPJ Web Of Conferences 26 (2012) 1-4

[6] M. Nabil Bassim, S. Boakye-Yiadom, And Mannon Bolduc, Microstructural Evolution From Shaped Charge Through Steel Plates, Applied Mechanics and Materials 566 (2014) 344-349